NASA Contractor Report 165861

(NASA-CR-165861) A NEW VIEW ON ORIGIN, ROLE AND MANIPULATION OF LARGE SCALES IN TURBULENT BOUNDARY LAYERS Interim Report (Illinois Inst. of Tech.) 378 p HC A17/MF A01 CSCL 20D G3/34

N83-15588

Unclas 02350

A NEW VIEW ON ORIGIN, ROLE AND MANIPULATION OF LARGE SCALES IN TURBULENT BOUNDARY LAYERS

T. C. Corke, H. M. Nagib, and Y. G. Guezennec

ILLINOIS INSTITUTE OF TECHNOLOGY
Chicago, Illinois 60616

Grant NSG-1591
February 1982

National Aeronautics and Space Administration

Langley Research Center
Hampton, Virginia 23665

TABLE OF CONTENTS

	Page
LIST OF TABLES	v
LIST OF FIGURES	vi
NOMENCLATURE	xix
ABSTRACT	xxii
CHAPTER	
I. INTRODUCTION	1
Relevant Literature	2
Objectives	14
II. EXPERIMENTAL FACILITIES AND TECHNIQUES	17
Facilities	17
Instrumentation	27
Digital Acquistion and Processing System	30
Flow Visualization	36
III. DATA ACQUISITION	38
Hot-wire Calibration	38
Acquisition for Mean Measurements	45
Simultaneous Hot-Wire Rake and Digital Image Acquisition	47
IV. PROCESSING OF TRANSDUCER OUTPUTS	57
Boundary Layer Profile Calculations	57
One-dimensional Processing	67
Two-dimensional Processing	75
V. PROCESSING OF IMAGES	85
Image Enhancement and Processing	85
Pattern Recognition	96
VI. PARAMETRIC INVESTIGATION OF MANIPULATORS	98
Four Plate Manipulator: Preliminary Results	99
Family of Parallel-Plate Manipulators	102

Page

VII. MEAN CHARACTERISITICS OF TURBULENT BOUNDARY LAYERS 109

VIII. MEAN CHARACTERISTICS OF MANIPULATED BOUNDARY LAYERS 122

IX. UNSTEADY CHARACTERISTICS OF WALL LAYER . . 148

One-dimensional Analysis of Velocity: Time-Series Data 149
Two-dimensional Analysis of Velocity: Space/Time Data 162
Two-dimensional Analysis of Images . . . 168

X. DISCUSSION 174

Mechanisms Governing Operation of Parallel-Plate Manipulators 174
Drag Reduction and Reynolds Number Effects on Boundary-Layer Large Scales 182
Wall Layer Instability 186

XI. CONCLUSION 193

Conclusions 194
Recomendations 198

APPENDIX

A. INSTRUMENTATION DESIGN CONFIGURATION . . . 201

B. SUMMARY OF RESULTS FROM A PARALLEL EXPERIMENT 205

C. FIGURES 213

BIBLIOGRAPHY 346

LIST OF TABLES

Table		Page
1.	Sampling Rate Parameters for Simultaneous Acquisition	50
2.	Mean Boundary Layer Characteristics at Rake Location	149

LIST OF FIGURES

Figure		Page
1.	Plan-View Schematic of IIT Environmental Wind Tunnel Showing Newly Lengthened High-Speed Test Section	213
2.	Side-View Schematic of High-Speed Test Section	214
3.	Schematic of Boundary-Layer Plate Showing Measurement Stations and Two Tandem Manipulator Plates	215
4.	Photographs of Series Manipulator (top) Suspended Above Boundary Layer Plate in Wind Tunnel, and of Surface Plug with Rake of Hot-wires and Shear-Wire	216
5.	Circuit Diagram of Constant Temperature Anemometer Used in 12-Channel System	217
6.	Circuit Diagram of DC Power Supply Used for 12-Channel C.T.A.	218
7.	Circuit Diagram of Variable DC Bias Amplifiers and Low-Pass Filters Used to Preprocess Analog Signals Before Digitization	219
8.	Frequency Response Curves for Second-Order Butterworth Low-Pass Filters Shown in Figure 7	220
9.	Schematic of PDP-11 Based Fast Acquisition System	221
10.	Schematic of PDP-11 Based Software Development and Data Processing System	222
11.	Schematic of Special Purpose Module Containing Microprocessor-Controlled Array and Display Processors	223
12.	Calibration Curve for Surface Mounted Hot-wire Shear Stress Sensor	224
13.	Schematic of Instrumentation Used in Mean Profile Measurements	225

Figure Page

14. Schematic of Instrumentation Used in Simultaneous Acquisition of Outputs from Hot-Wire Rake and Digital Camera 226

15. Circuit Diagrams of Threshold Detector (a) and Strobe Output Signal Conditioner (b) for Instrumentation Schematic of Figure 14 227

16. Timing Diagram for Conditioned Acquisition Sequence of Outputs from Hot-Wire Rake and Digital Camera 228

17. Flow Chart Representation of Computational Method Used to Determine the Wall Shear from Momentum Balance 229

18. Schematic of Data Handling of One-Dimensional Match Filtering Method for Detection of Wall Events 230

19. Spectrum of One-Dimensional Low-Pass Digital Filter Function 231

20. Spectrum of Two-Dimensional Low-Pass Digital Filter Function Generated from One-Dimensional Filter of Figure 19 232

21. Schematic of Data Handling for Two-Dimensional Processing of Hot-wire and Image Data 233

22. Parameter Values for Optimized Manipulator Configurations 234

23. Plate Configurations for Boundary Layer Manipulators 235

24. Effect of Varying Number of Plates on Reduction of Large-Scale Turbulence for Optimized Manipulators 236

25. Comparison Between Optimized Parallel and Tandem Plate Arrangements for Reducing Large-Scale Turbulence 237

26. Effect of Single-Plate Angle of Attack on Large-Scale Turbulence 238

27. Comparison of Mean Velocity and Turbulence Intensity Profiles for Boundary Layer Alone and with Optimized Manipulators 239

Figure

Page

28. Visualized Flow Without and With the Addition of Two-Plate Manipulator Showing Streamwise Extent (70δ) of Large-Scale Turbulence Suppression 240

29. Non-dimensional Mean Velocity Profiles at Various Streamwise Stations in Regular Boundary Layer for Low Reynolds Number Range 241

30. Non-dimensional Mean Velocity Profiles at Various Streamwise Stations in Regular Boundary Layer for High Reynolds Number Range 242

31. Non-dimensional Fluctuating Velocity Profiles at Various Streamwise Stations in Regular Boundary Layer for Low Reynolds Number Range 243

32. Non-dimensional Fluctuating Velocity Profiles at Various Streamwise Stations in Regular Boundary Layer for High Reynolds Number Range 244

33. Streamwise Development of Non-dimensional Free-Stream Pressure Difference 245

34. Comparison of Wall-Friction Coefficient Values Obtained by Three Methods for Data of Wieghardt 246

35. Comparison of Wall-Friction Coefficient Values Obtained by Three Methods for Regular Boundary Layer 247

36. Wall-Unit Non-dimensionalized Mean Velocity Profiles at Various Streamwise Stations in Regular Boundary Layer for Low Reynolds Number Range 248

37. Wall-Unit Non-dimensionalized Mean Velocity Profiles at Various Streamwise Stations in Regular Boundary Layer for High Reynolds Number Range 249

38. Wall-Unit Non-dimensionalized Fluctuating Velocity Distribution at Various Streamwise Stations in Regular Boundary Layer for Low Reynolds Number Range 250

Figure Page

39. Wall-Unit Non-dimensionalized Fluctuating Velocity Distribution at Various Streamwise Stations in Regular Boundary Layer for High Reynolds Number Range 251

40. Wake Function Distribution at Various Streamwise Stations in Regular Boundary Layer for Low Reynolds Number Range 252

41. Wake Function Distribution at Various Streamwise Stations in Regular Boundary Layer for High Reynolds Number Range 253

42. One-dimensional Spectra of the Streamwise Velocity Component at Different Self-Similar Heights at Station 2 in the Regular Boundary Layer for Low Reynolds Number Range 254

43. One-dimensional Spectra of the Streamwise Velocity Component at Different Self-Similar Heights at Station 5 in the Regular Boundary Layer for Low Reynolds Number Range 255

44. One-dimensional Spectra of the Streamwise Velocity Component at Different Self-Similar Heights at Station 9 in the Regular Boundary Layer for Low Reynolds Number Range 256

45. One-dimensional Spectra of the Streamwise Velocity Component at Different Self-Similar Heights at Station 2 in the Regular Boundary Layer for High Reynolds Number Range 257

46. One-dimensional Spectra of the Streamwise Velocity Component at Different Self-Similar Heights at Station 5 in the Regular Boundary Layer for High Reynolds Number Range 258

47. One-dimensional Spectra of the Streamwise Velocity Component at Different Self-Similar Heights at Station 9 in the Regular Boundary Layer for High Reynolds Number Range 259

Figure | Page

48. Vertical Distribution of Non-dimensional Streamwise Integral Length Scale at Various Downstream Stations in Regular Boundary Layer for Low Reynolds Number Range 260

49. Vertical Distribution of Non-dimensional Streamwise Integral Length Scale at Various Downstream Stations in Regular Boundary Layer for High Reynolds Number Range 261

50. Reynolds Number Dependence of Non-dimensional Streamwise Integral Length Scale at Different Self-Similar Heights in the Regular Boundary Layer 262

51. Two Realizations of Smoke-wire Visualization Photographs of Flowfield in Regular Boundary Layer (Top) and Manipulated Boundary Layer (Bottom) Representative of Final Data Runs 263

52. Non-dimensional Mean Velocity Profiles at Various Streamwise Stations in Manipulated Boundary Layer for Low Reynolds Number Range 264

53. Non-dimensional Mean Velocity Profiles at Various Streamwise Stations in Manipulated Boundary Layer for High Reynolds Number Range 265

54. Non-dimensional Fluctuating Velocity Profiles at Various Streamwise Stations in Manipulated Boundary Layer for Low Reynolds Number Range 266

55. Non-dimensional Fluctuating Velocity Profiles at Various Streamwise Stations in Manipulated Boundary Layer for High Reynolds Number Range 267

56. Comparison Between Streamwise Distribution of Integral Thicknesses in Regular and Manipulated Boundary Layers for Low Reynolds Number Range 268

57. Comparison Between Streamwise Distribution of Integral Thicknesses in Regular and Manipulated Boundary Layers for High Reynolds Number Range 269

Figure Page

58. Reynolds Number Dependence of Shape Factor for Regular and Manipulated Boundary Layers 270

59. Correlation of Energy to Momentum Thickness Ratio with Shape Factor for Regular and Manipulated Boundary Layers 271

60. Comparison of Wall-Friction Coefficient Values Obtained by Three Methods in Manipulated Boundary Layer and Average Distribution in Regular Boundary Layer 272

61. Wall-Unit Non-dimensionalized Mean Velocity Profiles at Various Streamwise Stations in Manipulated Boundary Layer for Low Reynolds Number Range 273

62. Wall-Unit Non-dimensionalized Mean Velocity Profiles at Various Streamwise Stations in Manipulated Boundary Layer for High Reynolds Number Range 274

63. Wall-Unit Non-dimensionalized Fluctuating Velocity Distribution at Various Streamwise Stations in Manipulated Boundary Layer for Low Reynolds Number Range 275

64. Wall-Unit Non-dimensionalized Fluctuating Velocity Distribution at Various Streamwise Stations in Manipulated Boundary Layer for High Reynolds Number Range 276

65. Wake Function Distribution at Various Streamwise Stations in Manipulated Boundary Layer for Low Reynolds Number Range 277

66. Wake Function Distribution at Various Streamwise Stations in Manipulated Boundary Layer for High Reynolds Number Range 278

67. Reynolds Number Dependence of Wake Strength Parameter for Regular and Manipulated Boundary Layers 279

68. Reynolds Number Dependence of Normalized Wake Strength Parameter for Regular and Manipulated Boundary Layers 280

Figure | Page

69. Reynolds Number Dependence of Non-dimensional Entrainment Velocity and its Correlation to Wall-Friction Coefficient 281

70. One-dimensional Spectra of Streamwise Velocity Component at Various Stations Behind Manipulator Plate for Low Reynolds Number Range 282

71. One-dimensional Spectra of Streamwise Velocity Component at Various Stations Behind Manipulator Plate for High Reynolds Number Range 283

72. One-dimensional Spectra of the Streamwise Velocity Component at Different Self-Similar Heights at Station 1 in the Manipulated Boundary Layer for Low Reynolds Number Range 284

73. One-dimensional Spectra of the Streamwise Velocity Component at Different Self-Similar Heights at Station 4 in the Manipulated Boundary Layer for Low Reynolds Number Range 285

74. One-dimensional Spectra of the Streamwise Velocity Component at Different Self-Similar Heights at Station 8 in the Manipulated Boundary Layer for Low Reynolds Number Range 286

75. One-dimensional Spectra of the Streamwise Velocity Component at Different Self-Similar Heights at Station 1 in the Manipulated Boundary Layer for High Reynolds Number Range 287

76. One-dimensional Spectra of the Streamwise Velocity Component at Different Self-Similar Heights at Station 4 in the Manipulated Boundary Layer for High Reynolds Number Range 288

77. One-dimensional Spectra of the Streamwise Velocity Component at Different Self-Similar Heights at Station 8 in the Manipulated Boundary Layer for High Reynolds Number Range 289

Figure Page

78. One-dimensional Spectra of Wall-Shear Stress for Regular and Manipulated Boundary Layers at Both Free-Stream Speeds 290

79. Normalized Probability Distribution of Wall-Shear Fluctuations for Regular and Manipulated Boundary Layers at Low Free-Stream Speed 291

80. Normalized Probability Distribution of Wall-Shear Fluctuations for Regular and Manipulated Boundary Layers at High Free-Stream Speed 292

81. Vertical Distribution of Skewness of Streamwise Velocity in Regular and Manipulated Boundary Layers 293

82. Vertical Distribution of Kurtosis of Streamwise Velocity in Regular and Manipulated Boundary Layers 294

83. Vertical Distribution of Non-dimensional Streamwise Integral Length Scale at Various Downstream Stations in Manipulated Boundary Layer for Low Reynolds Number Range 295

84. Vertical Distribution of Non-dimensional Streamwise Integral Length Scale at Various Downstream Stations in Manipulated Boundary Layer for High Reynolds Number Range 296

85. Reynolds Number Dependence of Non-dimensional Streamwise Integral Length Scale at Different Self-Similar Heights in the Manipulated Boundary Layer 297

86. Normalized Time Series Outputs From Hot-wire Rake and Surface Mounted Shear Wire for Regular Boundary Layer at Low Reynolds Number 298

87. Normalized Time Series Outputs From Hot-wire Rake and Surface Mounted Shear Wire for Regular Boundary Layer at High Reynolds Number 299

88. Normalized Time Series Outputs From Hot-Wire Rake and Surface Mounted Shear Wire for Manipulated Boundary Layer at Low Reynolds Number 300

Figure Page

89. Normalized Time Series Outputs From Hot-wire Rake and Surface Mounted Shear Wire for Manipulated Boundary Layer at High Reynolds Number 301

90. Normalized Burst-Conditioned Ensemble-Average Time Series Obtained from VITA Detection in Regular Boundary Layer at Low Reynolds Number 302

91. Normalized Probability Distributions of Burst Periods from VITA Detection with Different Thresholds in Regular Boundary Layer at Low Reynolds Number 303

92. Normalized Velocity Time Series From Sensor at y+ = 15 and Corresponding Match Filter Output in Regular Boundary Layer for Low Reynolds Number 304

93. Normalized Velocity Time Series From Sensor at y+ = 15 and Corresponding Match Filter Output in Regular Boundary Layer for High Reynolds Number 305

94. Normalized Velocity Time Series From Sensor at y+ = 15 and Corresponding Match Filter Output in Manipulated Boundary Layer for Low Reynolds Number . . . 306

95. Normalized Velocity Time Series From Sensor at y+ = 15 and Corresponding Match Filter Output in Manipulated Boundary Layer for High Reynolds Number . . 307

96. Normalized Burst-Conditioned Ensemble Average Time Series Obtained from Match Filter Detection in Regular Boundary Layer at Low Reynolds Number 308

97. Normalized Burst-Conditioned Ensemble Average Time Series Obtained from Match Filter Detection in Regular Boundary Layer at High Reynolds Number 309

98. Normalized Burst-Conditioned Ensemble Average Time Series Obtained from Match Filter Detection in Manipulated Boundary Layer at Low Reynolds Number 310

Figure | Page

99. Normalized Burst-Conditioned Ensemble Average Time Series Obtained from Match Filter Detection in Manipulated Boundary Layer at High Reynolds Number 311

100. Normalized Probability Distributions of Burst Periods for VITA (1.2) and Match Filter Detections in Regular Boundary Layer at Low Reynolds Number 312

101. Normalized Probability Distributions of Burst Periods from Match Filter Detection at Both Reynolds Numbers in Regular Boundary Layer 313

102. Normalized Probability Distributions of Burst Periods from Match Filter Detection at Both Reynolds Numbers in Manipulated Boundary Layer 314

103. Normalized Probability Distributions of Burst Periods from Match Filter Detection in Regular and Manipulated Boundary Layers at Low Reynolds Number 315

104. Normalized Probability Distributions of Burst Periods from Match Filter Detection in Regular and Manipulated Boundary Layers at High Reynolds Number 316

105. Two-Dimensional Reconstructions of Normalized Streamwise Velocity Time-Series for Regular (Top) and Manipulated (Bottom) Boundary Layers at Low Reynolds Number 317

106. Two-Dimensional Reconstructions of Normalized Streamwise Velocity Time-Series for Regular (Top) and Manipulated (Bottom) Boundary Layers at High Reynolds Number 318

107. Ensemble-Averaged Two-Dimensional Reconstructions of Normalized Streamwise Velocity for Time Instant of Digital Image Acquisition in Regular Boundary Layer 319

108. Ensemble Averaged Two-Dimensional Reconstructions of Normalized Streamwise Velocity for Time Instant of Digital Image Acquisition in Manipulated Boundary Layer . . 320

Figure Page

109. Burst-Conditioned Ensemble Average of Normalized Two-Dimensional Velocity Reconstructions Obtained From Match Filter Detection in Regular Boundary Layer at Low Reynolds Number 321

110. Burst-Conditioned Ensemble Average of Normalized Two-Dimensional Velocity Reconstructions Obtained From Match Filter Detection in Regular Boundary Layer at High Reynolds Number 322

111. Burst-Conditioned Ensemble Average of Normalized Two-Dimensional Velocity Reconstructions Obtained From Match Filter Detection in Manipulated Boundary Layer at Low Reynolds Number 323

112. Burst-Conditioned Ensemble Average of Normalized Two-Dimensional Velocity Reconstructions Obtained From Match Filter Detection in Manipulated Boundary Layer at High Reynolds Number 324

113. Ensemble Average of Normalized Two-Dimensional Velocity Reconstructions for Events with Periods Greater than Three Standard Deviations from Distribution Mean at Low Reynolds Number 325

114. Ensemble Average of Normalized Two-Dimensional Velocity Reconstructions for Events with Periods Greater than Three Standard Deviations from Distribution Mean at High Reynolds Number 326

115. Normalized Two-Dimensional Spectrum of Reconstructed Streamwise Velocity Distributions for Regular Boundary Layer at Low Reynolds Number 327

116. Normalized Two-Dimensional Spectrum of Reconstructed Streamwise Velocity Distributions for Regular Boundary Layer at High Reynolds Number 328

117. Normalized Two-Dimensional Spectrum of Reconstructed Streamwise Velocity Distributions for Manipulated Boundary Layer at Low Reynolds Number 329

Figure Page

118. Normalized Two-Dimensional Spectrum of Reconstructed Streamwise Velocity Distributions for Manipulated Boundary Layer at High Reynolds Number 330

119. Digitized Realization of Visualized Flow Conditioned on Wall Event (Top) and Corresponding Two-Dimensional Match-Filter Enhancement in Regular Boundary Layer 331

120. Digitized Realization of Visualized Flow Conditioned on Wall Event (Top) and Corresponding Two-Dimensional Match-Filter Enhancement in Manipulated Boundary Layer 332

121. Ensemble Average of Enhanced Images Conditioned on Match Detection in Regular (Top) and Manipulated (Bottom) Boundary Layers 333

122. Digitized Realization of Visualized Flow Conditioned on Wall Event (Top) and Corresponding Two-Dimensional Match-Filter Enhancement (Bottom) Viewing 10δ in Regular Boundary Layer 334

123. Digitized Realization of Visualized Flow Conditioned on Wall Event (Top) and Corresponding Two-Dimensional Match-Filter Enhancement (Bottom) Viewing 10δ in Manipulated Boundary Layer 335

124. Reynolds Number Dependence of Wall-Friction Coefficients in Regular and Manipulated Boundary Layers 336

125. Reynolds Number Dependence of Wall-Layer Strouhal Frequency in Regular and Manipulated Boundary Layers 337

126. Reynolds Number Dependence of Wall-Layer Strouhal Frequency for Present Investigation and Results of Other Investigations 338

127. Correlation of Wall-Layer Strouhal Frequency with Reynolds Number for Results in Figure 126 339

Figure | Page

128. Etch Patterns for Printed Circuits Used in Constructing Constant-Temperature Anemometers (Top), Square-Wave Generator (Middle) and Bias/Filter/Gain Signal Conditioners (Bottom) 340

129. Mean Velocity and Turbulence Intensity Profiles in Regular and Manipulated Boundary Layers Upstream of Device Position 341

130. Mean Velocity and Turbulence Intensity Profiles in Regular and Manipulated Boundary Layers at Location Approximately 2 Device Heights Downstream 342

131. Mean Velocity and Turbulence Intensity Profiles in Regular and Manipulated Boundary Layers at Location Approximately 21 Device Heights Downstream 343

132. Mean Velocity and Turbulence Intensity Profiles in Regular and Manipulated Boundary Layers at Location Approximately 90 Device Heights Downstream 344

133. Wall-Friction Coefficient Distribution in Regular and Manipulated Boundary Layers and Comparison with Present Results from Figure 60 345

NOMENCLATURE

Symbol	Definition
C_f	Skin friction coefficient = $\tau_w/1/2\rho U_\infty^2$
F	Pixel intensity of digitized image
f_c	Filter cutoff frequency
G	Equilibrium shape factor = $\int_0^\delta \left(\frac{U_\infty - \bar{U}}{u_\tau}\right)^2 d\left(\frac{Y}{\Delta}\right)$
h	Height of manipulator plates away from wall
H	Shape factor = δ_1/δ_2
IL	Integral Length Scale
k	Von Karman's constant
ℓ	Chord dimension of parallel plate manipulator
Re_L	Reynolds Number = $U_\infty L/\upsilon$, where L = x or θ
s	Spacing between tandem manipulator plates
St	Strouhal number = fL/U, where L and U are a characteristic length and velocity, respectively
T_B	Time period between wall burst events
U	Streamwise velocity component $\equiv \bar{U} + u$
u	Fluctuating component of streamwise velocity, U
$\bar{U}$	Time-averaged mean of streamwise velocity component
U_∞	Time-averaged free-stream velocity
u'	rms value of fluctuating velocity, u
u^+	$\bar{U}/u_\tau$
u_τ	Wall shear velocity = $\sqrt{\tau_w/\rho}$

Symbol	Definition
V_p	Entrainment velocity = $V_p = \frac{d}{dx} U(\delta-\delta_1)$
v	Fluctuating component of vertical velocity
x	Cartesian coordinate in streamwise direction; origin at leading edge of plate
x_0	Downstream distance between leading edge of plate and turbulence manipulator
y	Cartesian coordinate taken normal to flat plate; origin at plate surface
y^+	yu_τ/ν
z	Cartesian coordinate taken parallel to flat plate; origin along plate centerline
β	Equilibrium parameter = $\frac{\delta_2}{\tau_w}\frac{dp}{dx}$
Δ	Clauser thickness = $\int_0^\delta \frac{U_\infty-\bar{U}}{u_\tau} dy$
δ	Boundary layer thickness = y value where U equals 0.995 U_∞
δ_1	Displacement thickness = $\int_0^\delta \frac{U_\infty-U}{U_\infty} dy$
δ_2	Momentum thickness = $\int_0^\delta \frac{\bar{U}}{\bar{U}_\infty}\left(1-\frac{\bar{U}}{\bar{U}_\infty}\right)dy$
δ_3	Energy thickness = $\int_0^\delta \frac{\bar{U}}{\bar{U}_\infty}\left(1-\left[\frac{\bar{U}}{\bar{U}_\infty}\right]^2\right)dy$
ξ	Distance downstream of manipulator where measurements were taken
Π	Wake strength coefficient
ρ	Fluid density

Symbol	Definition
τ_w	Wall shear stress
ν	Kinematic viscosity
ζ	Non-dimensional damping coefficient

ABSTRACT

The potential of passive "manipulators" for altering the large-scale turbulent structures in boundary layers was investigated. Utilizing smoke-wire visualization and multi-sensor probes, the experiment verified that the outer scales, defined by the intermittent excursions of potential fluid into the boundary layer could be suppressed by simple arrangements of parallel-plates. A parametric investigation of different types of parallel-plate devices verified that optimum designs existed for the different configurations of stacked and tandem plate arrangements. A final optimized design consisting of two single plates residing at a height of 0.8$ in the boundary layer and spaced 8$ apart in the streamwise direction was chosen for the final set of measurements to document the characteristics of the "manipulated" layers.

As a result of suppressing the outer scales in the turbulent layers, a decrease in the streamwise growth of the boundary layer thickness was achieved and was coupled with a 30 percent decrease in the local wall-friction coefficient. After accounting for the drag on the manipulator plates, the net drag reduction reached a value of 20 percent within 55 boundary layer thicknesses downstream of the device. No evidence for the

reoccurrence of the outer scales was present at this streamwise distance thereby suggesting that further reductions in the net drag are attainable. The manipulated layers also exhibited a 17 percent thickening of the wall sublayer. In turn, the frequency of the wall "burst" process was reduced by a comparable amount.

Utilizing new techniques, many of them introduced in this investigation, the objective detection and description of the two-dimensional velocity field near the wall was achieved. These included match filtering, two-dimensional velocity reconstruction as well as digital image processing and pattern recognition. The results of these established that the frequency of occurrence of the wall events is simultaneously dependent on the two parameters, $Re_{\hat{c}_2}$ and Re_x. The correlation of the inner layer Strouhal frequency for these events with the two parameters resulted in a simple relation which correlates wall-layer event (or "burst") results of this investigation as well as those in the literature, covering a range of Reynolds numbers from 600 to 38000. As a result of being able to independently control the inner and outer boundary layer characteristics with these manipulators, a new view of these layers emerged. It now appears that the large outer scales in laboratory turbulent boundary layers are remnants of the transition process, i.e., slowly decaying turbulent spots that are

embedded in the boundary layer. The manipulators in effect remove this link with the "birth" of the turbulence and therefore hasten the Reynolds number "aging" of the turbulence.

CHAPTER I

INTRODUCTION

The use of screens, grids and honeycombs for "managing" turbulence has been an ongoing interest at I.I.T. for some time. The application of such devices for controlling free stream turbulence in wind tunnels is best summarized in the publications by Loehrke and Nagib (1972 and 1976) and Tan-atichat et al. (1982). Through careful scaling of mesh sizes and in-depth appreciation of the various suppression and generation mechanisms that control the turbulent flow, these techniques have been quite successful in this application.

Recently, a growing energy consciousness has generated interest in developing techniques for reducing viscous drag on aerodynamic bodies. Recent work conducted by NASA's Langley Research Center by D. Bushnell and J. Hefner and their colleagues has focused on this subject. Their work is best summarized in the reference by Bushnell (1978). In a majority of applications, this would involve removing or altering, in some way, the turbulent boundary layers that exist on their surfaces. It was the latter of these two alternatives that was of interest to us and which lends itself as a natural extension to turbulence management techniques. To be most effective, however, it is essential that these "turbulence manipulators" be

tailored to the particular mechanisms governing the flowfield of interest. Devices such as screens and honeycombs are not necessarily the suitable ones here. This warranted a review of the current experimental and theoretical information on wall-bounded turbulent shear flows.

Relevant Literature

In the last 20 years, the research on turbulent boundary layers has transformed the picture given by earlier long-time average statistics. Once perceived as quasi-steady turbulent eddies transported by a mean shear, such flows now appear, as a result of space-time velocity correlations and short-time conditioned measurements, to be highly unsteady coherent motions of strongly interacting scales. This revolution in thinking was primarily set forth by Townsend (1956) and Grant (1958) who, while being primarily interested in turbulent wake flows, viewed the turbulent flowfield as one where turbulent fluid is moved about by the motions of a system of large coherent eddies whose dimensions scaled with the width of the flow. The motions of these large scales carried eddies of smaller comparative size but which contained most of the turbulent energy. Townsend in particular inferred from velocity correlation measurements, the presence of characteristic eddies of finite length with a structure inclined in the flow

direction. He surmised that these large eddies in turbulent shear flows form coherent and identifiable groups and control the overall rate of spreading by contorting the layer between the turbulent and the non-turbulent fluid and by affecting the bulk convection of turbulence energy from regions of maximum production. Later Townsend (1970) described these structures as an inclined pair of double-roller eddies, a picture which was consistent with the eddy pattern perceived by Grant (1958).

At about the same time, Kline and others at Stanford University were studying turbulent boundary layers with the then new hydrogen bubble visualization technique. The culmination of that work was the 1967 paper by Kline et al. which revealed the presence of surprisingly well-organized motions in the near-wall region of a turbulent boundary layer. These motions lead to the formation of low-speed wall "streaks" which eventually interacted with the outer portions of the flow through a process "of gradual lift-up, sudden oscillation, bursting and ejection". This sequence of events later became known as "bursting". It was felt that this process played an important and dominant role in the production of new turbulence and the transport of turbulence away from the wall.

The turbulent boundary layer is uniquely different from any of the other turbulent flowfields in that its

mean velocity profile can be divided into four main parts. The first of these is the wall region in which the flow processes are dominated by the presence of the wall. Within the wall region in the near vicinity of the wall is the viscous sublayer ($0 \leq y+ \leq 7$). In this region, viscosity plays a dominant role, however turbulent fluctuations are still large relative to the local mean velocity. Scaling analysis in that region yields the result that $u+ = y+$ in the sublayer and subsequently is also used to define it. Further from the wall, $50 \leq y+ \leq 200$, there is a region of nearly homogeneous turbulent flow which is often referred to as the constant stress layer. In this region the velocity is found to vary with height in a logarithmic manner defined by $u^+ = \frac{1}{\kappa} \ln y^+ + B$. The viscous sublayer and constant stress layer are smoothly matched by the buffer layer which can take a number of implicit forms to define the velocity distribution (Whitfield, 1979; Spalding, 1981). The buffer layer typically exhibits the greatest amount of turbulence production. Measurements by Klebanoff (1954) showed that the peak production occurred in that region just at the edge of the sublayer. Beyond the constant stress layer, the turbulence is bounded by the potential flow outside the boundary layer. Coles (1956) designated this as the wake region because of its similarity to flow characteristics exhibited in a wake flow. He further developed an empirical formulation of

the mean velocity distribution in that region which was found to work well for a variety of boundary layer flows with pressure gradients. At the outer edge of the wake region, there exists a thin interfacial region separating the turbulent and the non-turbulent flow. This interface was termed the superlayer by Corrsin and Kistler (1955). It is across this region that vorticity is acquired by the potential flow and eventually is incorporated into the wake flow.

Each of these regions has a characteristic length scale. In the viscous sublayer that length is ν/u_τ. The wake region has a characteristic length on the order of the boundary layer thickness. Kovasznay (1967) estimates the thickness of the superlayer to be $10\nu/V_p$ where V_p is the entrainment velocity.

The fact that the maximum turbulence production coincided with the region of large coherent activity, discovered by Kline et al., prompted more investigations of this near wall phenomena. For example, Corino and Brodkey (1969) visualized the near wall motions in a turbulent pipe flow. In their paper they reported that the most important and distinguishing characteristic of the wall region was the intermittent ejection of discrete fluid elements away from the wall. They catagorized the process as a local deceleration of the fluid near the wall followed by the appearance of faster moving fluid which approached from the outer parts upstream resulting

in eruptions of low velocity fluid away from the wall. The ejection of low velocity fluid was always found to be followed by a sweep of upstream fluid from the previous ejection event. They also investigated the Reynolds number dependence of these events and found that their frequency of occurrence increased like the 1.7 power of Re_x. Corino and Brodkey (1969) further estimated that the wall ejections accounted for 70 percent of the $\overline{uv}$ Reynolds stress in the boundary layer. This amount was substantiated by the visual study made by Kim et al. (1971). The "burst" process examined by that reference may be somewhat altered in boundary layer flows over large roughness elements as pointed out by Grass (1971). Using a $\overline{uv}$ quadrant discrimination Willmarth and Lu (1972) determined that 60 percent of the $\overline{uv}$ Reynolds stress is produced when the sublayer velocity is less than the mean and that the largest contribution occurs when $u<0$ and $u>0$.

A growing issue at that time was how the frequency of occurrence of these events scaled with the boundary layer characteristic lengths and velocities. In the initial studies by Kline et al.(1967) the "bursting" was associated with the wall streaks and, therefore, thought to scale with the inner variables u_τ and ν. The results of Rao et al. (1971), which utilized narrow band-pass filtering of a differentiated velocity time series to detect the intermittent turbulent fluctuations associated

with these events, indicated that their frequency scaled with the outer variables, U_∞ and δ. Kim et al. (1971) tried to reconcile the difference in their proposed mechanism by suggesting that the low-speed streak lifting was triggered by large scale disturbances. There was, however, no explanation for the clear dependence of the burst period on the wall friction velocity in that reference. Through some dimensional arguments and assumptions about the boundary layer profile shape, Laufer and Narayanan (1971) suggested that the nondimensional burst frequency $U_\infty T/\delta \simeq 5$, was approximately 5, which is in near agreement with the value of 6 obtained by Rao et al.(1971). They further pointed out that the average wavelength of the turbulent-laminar interface is approximately $2\delta/U_\infty$ suggesting an interaction between this outer flow structure and the inner layer regular events.

In a recent review article by Cantwell (1981) he states that "it appears fairly well established that the mean time between bursts scales with outer variables". However, he prefaces his statement by saying that the interaction process that creates conditions under which the bursts occur is far from understood. Blackwelder and Haritonidis (1981), however, in their recent paper in which they utilize a locally high variance as a burst discriminator (see also Blackwelder and Kaplan, 1976), claim that the bursting period scales with inner

variables which is in support of the Kline et al. (1967) concept based on the lift up of the low-speed wall streaks. A more detailed investigation of this aspect was performed by Blackwelder and Eckelmann (1979), where they identified the low-speed streaks as the regions between pairs of counter-rotating streamwise vortices. This verified an earlier result obtained by Bakewell and Lumley (1967) who performed an eigenfunction decomposition of space-time correlations of streamwise velocity fluctuations in the wall region and obtained a dominant eigenfunction structure consisting of counter-rotating eddy pairs of elongated streamwise extent.

In order to form a conceptualized view which would lead us to distinguish between inner and outer variable dependence of the wall "bursting" process, we must review the available data on the organized motions in the outer part of the turbulent boundary layer. Since the measurements of Corrsin and Kistler (1955) of intermittency in the outer parts of the boundary layer, it became clear that the turbulent/non-turbulent interface extends well into the boundary layer. The studies of intermittency by Fiedler and Head (1966) gave visual evidence of this. This region is of interest because it is the interface for energy transfer from the external flow into the turbulence producing region. Kaplan and Laufer (1969) utilized a rake of hot-wires

spanning the whole boundary layer and came to the conclusion that the non-turbulent intermittent regions did not appear to be surrounded by turbulent fluid but were connected to the free-stream fluid. The interface also seemed to be highly corrugated. Kovasznay (1970), utilizing conditional sampling techniques, defined "fronts" and "backs" to these turbulent "bulges". He found that the "front" velocity was approximately 5 percent faster than that for the "back". The average velocity of the turbulent bulges was of the order of $0.93U_\infty$ which suggested that the outer flow rides over these structures. From velocity correlations Blackwelder and Kovasznay (1972) later defined a mean motion inside a turbulent "bulge" which was rotational with a mean vorticity component in the same direction as the mean strain rate. Furthermore, they gave these features a travel life-time, estimated from a 1/e correlation decay, to be from 5 to 10 boundary layer thicknesses. From their measurements they estimated that these large eddies contribute as much as 80 percent of the Reynolds stress for $y>0.2\delta$. The conditioned measurements of Antonia (1972) were in substantial agreement with them. In addition he determined that the maximum $\overline{uv}$ distribution within the turbulent bulges represents approximately 45 percent of the wall shear value. This provided support to the Bradshaw et al. (1967) theory that the strength of the large scale eddies is closely

related to the wall shear stress, τ_w.

On the trailing edge or "back" of the large scale eddies, Falco (1977) noticed predominant small-scale eddies, with sizes on the order of 100 to 200 ν/u_τ, which he associated with Reynolds-stress-producing motions. Head and Bandyopadhyay (1981) present a picture of the large eddy structures as being an amalgamation of elongated hairpin vortices. It was suggested by them that Falco's (1977) small scale eddies are actually tips of these hairpin structures.

In spite of the well established existence of these large scale motions and their obvious importance to the entrainment of potential fluid, turbulence energy transfer and wall friction, the mechanisms for their generation are still in question. Zilbermann et al. (1977) and Wygnanski (1978) generated turbulent spots (Emmons, 1951) in a transitional boundary layer flow and followed their development downstream. They concluded that the turbulent spots were related to the large scale motion in a turbulent boundary layer. Schraub and Kline (1965) suggested that these bulges are the same as or at least formed from the ejected wall streaks. This was similarly conjectured in the results of Kovasznay et al.(1970). Later Offen and Kline (1975) suggested that the large-scale outer bulges might be a consequence of vortex pairing between the vortices associated with two or more wall bursts. They prefaced this concept by

stating that it was related to data taken at fairly low Reynolds numbers. However, they suggested that the basic structure should be the same at high and low Reynolds numbers. Taneda (1981) proposes that the large scale bulges might be a preferred eigenmode of the outer flow.

The suggestion by Offen and Kline (1975) that the large outer scales are a result of the pairing of old bursts is only part of their hypothesis. They further say that the circulatory flow or vortex in a "burst" can impose an adverse pressure gradient at the wall as it is convected downstream, thereby resulting in the lift-up of a newly formed wall streak. This defined a regenerative process for the wall bursts. Coles (1978) discussed and evaluated a large volume of boundary layer and ducted flow data based on a Görtler-like instability mechanism. This mechanism would lead to the streaks and may be triggered by the flow curvature associated with the large scales.

Theoretical models for a regenerative bursting process based on the instability of the sublayer were proposed by Hanratty (1956), Einstein and Li (1957) and Black (1966). According to their analysis the bursting frequency should scale with the inner variables ν/u_τ^2. This view cannot, however, be easily reconciled with the findings of Rao et al. (1971) which indicate that the bursting period shows Reynolds number independence when scaled with outer variables. This suggests the influence

of the outer large-scale eddy motions. The dependence of the semi-regular wall events on the passage of an outer large-scale eddy was also supported by Piaturi and Brodkey (1978), based on their interpretation of visualization results. Doligalski et al. (1980) proposed a model for the lift up of low-speed fluid from the wall which was based on the interaction with an eddy structure which originated in the outer part of the flow. Blackwelder and Woo (1974) investigated the bursting process while applying a pressure perturbation on the flow of a type exhibited by a passing large scale eddy. Those results indicated no changes in the wall bursts as a result of the pressure excitation. Chen and Blackwelder's (1978) temperature measurements above a heated wall highlight an internal shear layer by which the large scale outer structure may be related to the wall bursting. Brown and Thomas (1977) suggest that an organized structure, inclined in the flow direction at an angle of 18 degrees and is on the order of 2δ long, relates the outer flow to the wall bursts. This structure, they believe, may be connected with the interaction of turbulent spots.

If we summarize these results into one picture for the process governing the turbulent boundary layer, we can point to the existence of two types of coherent motions, one associated with the wall layer and the other with the outer flow. Each of these has been observed to

contribute a large percentage of the Reynolds stress in the boundary layer. The wall layer is associated with the generation of low-speed streaks which lift away from the wall, interact with faster moving fluid and eventually break-up. This process has been associated with the generation of as much as 70 percent of the net turbulence production. Away from the wall, the outer turbulent bulges maintain a net circulation which plays an important role in the entrainment of potential fluid and the extraction of turbulence energy from the mean flow. The strength of these large scale eddies has been found to be related to the wall shear stress, although the mechanism for their generation is not clear. Through a conceptualized view it has been thought that these two coherent motions should interact, however, the method by which this occurs is again not clear. Of primary importance to this is the manner in which these events scale. From an intuitive standpoint, it would seem that the period of these wall layer events or "bursts" should scale with wall units. The data in this regard seem to be contradictory, although it is safe to say that no clear trend has been put forth. There is also little agreement in the literature as to the source of the large-scale outer eddies. It is undeniable, however, that these features of the flow are important in sustaining the generation of new turbulence and in the growth of the boundary layer.

Objectives

In light of the fundamental questions that remain unanswered about the coherent processes which have been observed to play a major role in the growth and evolution of a turbulent boundary layer, we undertook an experiment which would separate the two classes of coherent features and point to the mechanisms of their interrelations. Loehrke and Nagib (1976) and Tan-atichat et al. (1982) had a great deal of success with this approach. This involved altering the outer part of the turbulent boundary layer by suppressing the large-scale intermittent turbulent bulges. Based on some of the conjectures previously cited, the absence of this feature in the outer part of the flow would either interrupt or impede the "bursting" process. On the other hand, another view may suggest that these wall layer events would continue undisturbed and their outer interaction would generate new large scale bulges, or some new equilibrium would be established and remain throughout the lifetime of the boundary layer. Also of extreme importance from a technological point of view is the prospect of reducing skin-friction drag beneath turbulent boundary layers by removing the intermittent excursion of higher velocity potential fluid near the wall. We proposed to use two-dimensional "boundary layer

manipulators" formed from thin, stacked parallel plates which would be suspended in the boundary layer parallel to the wall. This concept to reduce drag was first proposed by H. M. Nagib in 1977 (see Bushnell, 1978). These plates would present a minimum obstruction to the flow and provide us with the greatest amount of design freedom for matching the device to the scales of interest. Other devices for altering the large scale turbulence in a boundary layer are summarized by Hefner et al. (1980). A parametric study was first planned in order to pinpoint the important criteria for controlling the large scale motions.

To aid as tools for understanding this complex process we initiated our research intent on utilizing advanced flow visualization and velocity measurement techniques. These included digital processing techniques which could provide consistent detection and statistical analysis of these coherent events. The techniques would include one- and two-dimensional analysis of single velocity sensors and rakes of sensors, along with the simultaneous acquisition of digitized images of the smoke-wire visualized flowfield. Signal processing techniques such as one-dimensional match filtering and two-dimensional reconstruction and match filtering would be employed to isolate coherent features in the velocity time series and digital images.

The results of this study are aimed at documenting a

method by which net drag reduction could be obtained in fully turbulent boundary layer flows. We further intended to document the coherent features in the turbulent boundary layer and to try to answer some of the outstanding questions about their interaction.

Many thanks are due to John L. Way for his ready advice on the signal processing aspects as well as the expert work he has done in building the data processing system. The expert craftsmanship of Edward D. Nieman exhibited in the modification of the wind tunnel and in the other fabrications needed throughout the experiment is also acknowledged. The careful work of Jeffrey A. Corke in helping to fabricate the analog preprocessing circuitry is appreciated. Special thanks to Amy H. Lee and Dennis J. Koga for helping to prepare the final figures. Finally, special appreciation is due to Roberta J. Corke and Thelma T. Grymes for their help in typing the manuscript.

It is obvious that work such as this is built on and shaped by the efforts and accomplishments of others who have preceded us. To them we extend a special thanks. The authors would like to especially acknowledge the efforts and stimulating discussions with Dennis Bushnell and Jerry Hefner, the technical monitor of the grant, of the NASA Langley Research Center.

CHAPTER II

EXPERIMENTAL FACILITIES AND TECHNIQUES

Facilities

The experiment was performed in the high-speed test section of the I.I.T. Environmental Wind Tunnel. The tunnel runs in a closed return configuration with the return leg being used as a low-speed test-section for atmospheric boundary layer simulations. In the high-speed section, honeycombs and screens upstream of a 4:1 contraction give a turbulence intensity level of 0.03 percent over a range of velocities from 1 to 30 m/s. The rectangular test section is 0.61 m wide and 0.91 m high with plexiglass back and front walls to allow for easy flow visualization. In addition, the front walls are hinged in two sections to allow easy access to the test section.

Wind Tunnel Modifications. During the experiment, between the preliminary and final data runs, modifications were made in the high-speed leg of the wind tunnel to accommodate the addition of 1.83 m. to the streamwise dimension of the test-section. To accomplish this, a 2.44 m. long section from the 4.88 m. long diffuser, downstream of the test section, was removed. The existing 3.05 m. long instrumented test section was moved back toward the remaining diffuser and a 1.83 m. long parallel-wall section made the connection to the

contraction. A removable 0.5 by 1.3 m. plexiglass window was incorporated into the new section and all of the other walls were painted black to aid in flow visualization.

A 0.58 m. long square diffuser section was made to connect the test section to the remaining diffuser section. This "quick" diffuser was bolted to the test section. A 2.54 cm. gap was left between the two diffuser sections to allow air to enter the tunnel and maintain its internal pressure above the room atmospheric pressure. A schematic of the wind tunnel and the new 4.88 m. long high-speed test section is shown in Figures 1 and 2.

Without the boundary layer plate inside the test section, measurements were made to determine if these modifications had any detrimental effects on the tunnel performance. Using a digital, real-time spectrum analyzer, special attention was given to the free-stream turbulence level and especially its low frequency content, where we felt the effects of any diffuser separation would appear. These measurements indicated that the tunnel modifications had no adverse effect on its performance and actually appear to have improved the tunnel efficiency as indicated by a lower operating air temperature rise and aerodynamic noise levels.

The reason for these improvements may be in the diffuser design. Before the modification, air entered

the tunnel through a 0.6 cm. slot in the wall perimeter just downstream of the test section. It now appears that the air was jetting sufficiently enough to have caused the flow in the long diffuser to separate. Since this flow leads directly into the fan assembly, non-uniformities in the flow could result in inefficient fan operation. In the present case, the combination of the "quick" diffuser and the four times wider slot results in lower velocity air to enter in a direction more tangent to the "slow" diffuser wall.

Traversing Mechanism. The downstream 3 m. length of the tunnel test-section is equipped with a motorized traversing mechanism. Using this, two probes can be moved to any position in a plane 0.6 m. high and 3 m. long respectively along the test-section vertical centerplane. The two-dimensional probe positions are monitored through the linear outputs of two 10 turn potentiometers acting as voltage dividers. The potentiometers are mounted on the movable beds carrying the probes and their translational motion is transferred through rack and pinion gears. This ensures that the outputs are proportional only to the relative locations of the probes and not sensitive to the tolerances in the traversing drive mechanism. In the vertical direction, a probe can be repeatably positioned with 0.03 mm. accuracy.

Boundary Layer Plate. A 5.16 m. long, 0.57 m. wide flat plate served as the boundary layer plate for the experiment. To be able to place the plate inside the test-section, it was broken up into three parts with lengths 1.68, 1.85 and 1.63 m. respectively, from the leading edge. This arrangement is shown in the schematic of the plate in Figure 3.

The first plate was fabricated from a 1.6 cm. thick aluminum plate. The leading edge of the plate is machined to a razor edge. In addition, the noise is sloped downward so as to fix the stagnation point on the measurement side of the plate. The other two plates are made from 1.3 cm. thick clear plexiglass which were mounted to a metal frame made from 2.5 cm. square aluminum channel to maintain a flat surface. Each plate section was suspended on four independently adjustable legs. The vertical placement of the plates partitioned the test section so that 0.61 m. by 0.61 m. square cross-section was formed above the plate. The seams between the three plates were glued together with epoxy and drawn tight by threaded rods attached to each end of adjoining plates. To guarantee a smooth surface across the seams, they were covered with a plastic filling compound and wet-sanded to provide a smooth, flush surface.

With the boundary layer plate inside the test

section, the flow at its leading edge was observed using smoke-wire visualization. As a result of the greater blockage below the plate due to the support legs, the stagnation point was observed to occur on the underside of the plate which resulted in flow separation on the top measurement side. In order to equalize the blockage, a number of perforated plates were tested at the exit of the test-section across the part of the cross-section above the plate. A 40 percent solidity plate was found to give the best results. With this plate, a slightly higher pressure was maintained on the measurement side of the test-section so that the stagnation streamline impinged on the downward sloping leading edge. This slight pressure difference was further utilized by leaving a .16 cm. gap along the intersection of the boundary layer plate and side walls. This resulted in a very slight flow from this intersection to the underside of the plate. As observed by injecting smoke into the corner, the influence of this downflow only extended out to approximately 1 cm. from the side walls. Since the corners are likely sites for the generation of longitudinal vorticity from the merging of the plate and side-wall boundary layers, we wanted to draw off as much of the boundary layer there as possible, without interrupting the two-dimensionality of the test boundary layer.

Surface Plug. A 6.03 cm. circular hole was machined through one of the plexiglass plates to accommodate a removable plexiglass flush-surface plug. The instrumented plug shown in the photograph of Figure 4 was made up of a larger plug which fit snugly the hole in the plate and a smaller, 1.27 cm. diameter removable plug placed off-center, 0.16 cm. from the edge of the larger plug. An O-ring filled a groove cut into the circumference of each plug to ensure an air-tight fit when they were in place.

The smaller plug was designed to hold the surface wire. In order to minimize heat conductivity through its surface, it was constructed of wood. Two gold plated terminals were imbedded in its surface, 1.3 cm. apart, and connected to copper leads which extended out through the underside of the plug. The surface wire, designed to measure wall shear velocity, consisted of a 10 micron diameter tungsten wire which was copper plated on both ends and soldered to the terminals. Care was taken here to ensure that the wire was taught and that it rested on the surface. The unplated portion of the wire was approximately 1 mm. long. This results in a maximum non-dimensional sensor length, $l^+ = lu_\tau/\nu$, for the range of shear velocities encountered approximately 20. This value is approximately half of the width of the wall-streak structures (Blackwelder and Eckelmann, 1979).

The larger plug was designed to hold a rake of 10

hot-wires so that their sensors were aligned in a vertical plane on top of the shear wire. The rake was made by soldering the ends of jeweler's broaches to a double-sided, copper clad p.c. board. Separate conduction lines were etched into both sides of the board by exposing the photo-sensitized surfaces to ultraviolet light through a photo-negative mask of the network. The broaches have a minimum length of 3.1 cm. and their diameters tapered from 0.3 mm. to 0.08 mm. at the sensor.

The sensor spacing was selected for specific non-dimensional heights in the low Reynolds number boundary layer case at that downstream station. Because of the high mean shear near the floor, the wires are more closely spaced there. The non-dimensional heights of the sensors vary slightly from the design values in the other boundary layer, because of the change in the wall shear velocity. However, there was always a minimum of six wires below y+ of 100 in all cases.

The exact alignment of the broaches for soldering onto the p.c. board was accomplished on a specially made jig. The jig held the sensor ends of the broaches at the precise spacing and angles so that the opposite ends could be soldered to the p.c. board. After mounting the broaches, thin glass fibers were glued across broach pairs to reduce vibration which could result in strain-gaging of the velocity sensors. Ten micron, copper-plated tungsten wire was soldered onto the tips of

the broaches. As with the shear sensor, the unplated portion of the wires gave a maximum sensor length, l^+, of approximately 20.

The p.c. board carrying the probes extended up through the plug in a 2.9 cm. long, 0.15 cm. wide slot cut in the side diagonally opposite to the shear-wire plug. With the sensors on the top of the plug, the bottom of the board was fixed to a micrometer mounted to the underside of the plug. When the plug was placed in the boundary layer plate in the test section, the micrometer was used to lower the wire rake into position near the floor. In all cases, the lowest wire was positioned to be at $y^+ = 7$. A twenty two conductor ribbon cable and connector carried the power to the eleven hot wires in the plug. As with the boundary layer plate, the seams around the plug were filled with plastic filler and wet-sanded smooth.

Boundary Layer Manipulator. In the course of this study, a number of boundary layer manipulators were studied. All of these were configured from thin, flat plates which were suspended above the boundary layer plate and spanned the tunnel test section. The plates were used singly, vertically stacked or placed in tandem in the streamwise direction. Because of the number of parameters involved in the configuration of these manipulators (namely, the chord length and thickness of

the plates, the vertical spacing between them, their angle of attack and the distance between tandem plates as well as the relationship of all of these to the boundary layer characteristic length scales) a method was needed to "optimize" their design. This was accomplished by holding the plates of various dimensions in a low disturbance rig inside the tunnel test section. The rig consisted of two sets of vertical, slotted rods which were supported on either side of the test section in a rail on the test section ceiling and in the small gap between the boundary layer plate and the side wall. Each manipulator plate was clamped in a streamlined holder which could slide in the slotted rods. The plates were positioned and tightened in place so that they were tensioned to remove any sagging or ripples. Various sizes of manipulator plates were placed in the rig for different spacings in three different turbulent boundary layers. Using a smoke-wire to visualize the flow, we adjusted the parameters for four different basic plate configurations to obtain a maximum visible reduction in the large-scale, intermittent structures.

The final design for the manipulator used in the quantitative measurements was optimized in the manner previously described. The placement along the boundary layer plate was chosen so that the minimum Reynolds number Re_{θ}, was sufficiently large (2000) so that the layer is fully turbulent past the transition stage and

containing a full spectrum of scales. The streamwise chosen location also provided a sufficient number of boundary layer thicknesses (approximately 60) from the start of the manipulator along which we could observe any regeneration of the large scale structures. Also, since measurement station 1 of Figure 3 was the farthest upstream location that could be conveniently measured from the traversing mechanism, it was necessary that the manipulator be placed at a point where the approaching flow field was well documented.

The final manipulator consisted of two, 0.2 mm. thick brass plates. The chord of each of the plates and its elevation above the floor was equal to 80 percent of the boundary layer thickness at the location of the upstream most plate, i.e., equal to 3.2 cm. In the high Reynolds number case the boundary layer thickness at that station did not change sufficiently enough to change any of the design values. The two plates were spaced 25.4 cm. apart or eight times the boundary layer thickness at the upstream plate. The manipulator plates were held at one end by a 3.2 cm. wide, 0.7 mm. thick steel bracket which wrapped around the end of the plexiglass boundary layer plate, and was secured to the aluminum frame below. On that end the brass manipulator plates were bent over the brackets and fixed by three small machine screws. The opposite end of each manipulator plate was attached to a 0.7 mm. thick steel bracket which pivoted on a small

threaded rod. The rod protruded through the back wall of the test section and a nut on the outside was used to draw up the slack on the plates and put them under tension. Special care was taken to make sure that the manipulator plates were not sagging, twisted or under an angle of attack. In addition they were observed under a strobe light to ensure that they were not vibrating under the operating conditions. A photograph of the two tandem manipulators mounted in the wind tunnel for the final set of measurements is shown in the top portion of Figure 4.

Instrumentation

A variety of analog and digital instrumentation was used in the investigation. In general, the analog instrumentation was used to pre-process the data before the digital acquisition by a PDP-11/10 mini-computer controlling an A/D converter and other peripherals. Processing of the data was performed later on a variety of computer systems including a larger UNIVAC 11/08. The analog instrumentation and peripherals used in the data acquisition and processing will be described in the following.

Multi-channel Anemometers. To control the rake of 11 hot wires, a system of 12 constant temperature anemometers based on a variation of the design first introduced by Kreider (1973) was constructed. The

circuit diagram for the anemometer is shown in Figure 5. The system represents a low cost alternative to commercially available CTA's while giving comparable performance to a DISA 55D01 anemometer (Wlezien,1981). The anemometers were grouped into two sets of six channels each. Two 15 volt, ±1 Ampere power supplies, whose circuit diagram is shown in Figure 6, provided ample power for the anemometer operation. The circuits utilized CA3140 high-precision operational amplifiers which are pin for pin replacements for more traditional 741 op-amps, but which require only a few milliamps to power and provide a near ideal input impedance of 10^9 ohms and frequency response bandwidth of 1MHz. To guard against cross-talk between channels, all of the power inputs were AC coupled with 0.1 uF capacitors to ground. Each set of six anemometers also utilized a built in square wave generator which was used to adjust the feedback in the servo loop.

The operation of the anemometers involved measuring the resistance of the hot-wire and adjusting the overheat resistance to equal R_w times the overheat ratio times 20, where the 20 accounts for the 20:1 bridge ratio. With the switch set to the +15 volt side, the 10 ohm resistance is adjusted to provide an output voltage of approximately 10 volts. With the servo loop closed and the square wave supplied to the bridge, the 10 ohm resistance is adjusted to give a slightly underdamped

response. The square wave generator was turned off during the normal operation of the anemometer channels.

Multi-channel Signal Conditioners. Prior to digitization of the analog outputs, the signals were d.c. biased, amplified and low-pass filtered by the circuit shown in Figure 7. The bias and amplification was necessary to minimize the quantization error in the analog to digital conversion. The low-pass filtering was necessary to remove the amplitude energy in the signals above the Nyquist frequency for spectral analysis.

The bias and gain are accomplished in the first two stages of the op-amp circuit. The gain in each stage is set by plug-in feed-back resistors. In this experiment, the first stage operated as a unity gain amplifier so as not to saturate the op-amp, and a majority of the d.c. was subtracted from the signal. The second stage amplification was normally 10 or 15 and any remaining d.c. was subsequently subtracted from the signal. The exact amplification was determined by applying a precisely known d.c. voltage into the channel and measuring the output value. The last two stages of the circuit are two second-order low-pass butterworth filters. In series they give the fourth order response shown in Figure 8 with an amplitude decay rate of 60dB/decade for frequencies above the filter cutoff. The damping values for these filters were fixed by the

capacitors in the circuit to give the desired amplitude response with frequency. The cutoff frequency was changed by switching in dual pairs of precision resistors to give nominal cutoff values of 2.5, 5.0, 8.0 and 10.0 K hertz. The resistance values corresponding to these frequency cutoff values are given in the table of Figure 7. Provisions were made in the design to allow for setting of other cutoff values through the equation

$$f_c = 1/2\pi RC_1\zeta$$

Digital Acquisition and Processing System

The digital system (D.A.P.S.) for acquiring analog data and performing digital processing consists of three systems: The Fast Acquisition System (F.A.S.), the Processing and Development System (P.D.S.), and the Special Purpose Module (S.P.M.). Each of these systems, schematically shown in Figures 9, 10, and 11 was used in the experiment to develop software, to perform the digital acquisition, to process the data or in many cases, to display or plot results. For some of the results, processing was also performed on a UNIVAC 1108. The FAS and PDS systems are based around PDP-11/10 and PDP-11/04 mini-computers, respectively. Information could be passed between the three systems through external PDP-11 bus lines, but typically the SPM was connected to either the FAS or PDS at one time. All these systems are portable, thereby allowing them to be

moved to the laboratory during data acquisition. These systems will be described in the following with more detailed attention being given to those devices which are an integral part of this experiment.

Fast Acquisition System. The FAS, schematically shown in Figure 9, was used along with the Special Purpose Module to acquire the data during the experiment. It consists of a PDP-11/10 processor with 28 K, 16 bit words of RAM memory. The analog signals are acquired by a micro-processor controlled, 16 channel, 100 kHz analog-to-digital converter which is designated as the MIP. This device features its own 4K words of dual ported memory. The memory is double buffered so that one of the 2K buffers can be written to tape by the PDP-11 processor while the MIP microprocessor fills the other buffer, thereby allowing continuous, uninterrupted acquisition of data. The high speed digital magnetic tape drive in the FAS allows fast, continuous storage of 8 mega-words of data.

Special Purpose Module. The SPM, schematically shown in Figure 10, is made up of a number of special purpose peripherals which are used both in data acquisition and processing. Data from and control of these peripherals are handled by one of the PDP-11 processors through the bus. Digital acquisition of analog signals is done in this module by a 100 kHz, 16

channel, 12 bit, A/D converter. Unlike the micro-computer controlled MIP, acquisition here is controlled by the PDP-11 processor. Acquisition rates are set with the programmable clock in the SPM. The acquisition software is written in computationally efficient PDP-11 assembly language which handles the A/D control, clock interrupts and data conversion at a rate which makes full use of the 100 kHz A/D. As in the case of the other assembly language software written for this experiment, the macro acquisition software was configured as subroutines which were called from less efficient but more I/O compatible Fortran programs. Computer control of analog devices is made through the 3 channels of 12 bit D/A conversion in the SPM. Again the D/A converter is controlled through Fortran callable, assembly language subroutines.

The other three peripherals in the SPM, i.e., the digital camera, color display processor and array processor, performed very important functions in this experiment. Because of their unique nature and importance, they will be given a more detailed discussion in the following.

Digital Camera. A model 659F optical data digitizer which is interfaced to the PDP-11 bus was used to digitize the smoke-wire visualized flowfields. The camera incorporates a Vidicon imaging tube which stores

an electron charge pattern proportional to the luminous energy of an image focused on the tube. As contrasted with a scanning type video tube in which the image data is retrieved by sequential sweeps, the vidicon tube has 4096 x 4096 randomly addressable picture elements (pixels) from which intensity information can be retrieved. As a result of some spatial averaging of adjacent pixels, the number of resolvable points for the tube is 512 x 512. The analog intensity information is converted to an 8 bit parallel binary intensity word through an A/D converter in the camera. This gives 256 resolvable levels of intensity. Since the PDP-11 word is two 8 bit bytes, the image data was packed into double bytes to reduce storage requirements. The vidicon tube is sensitive to light energy in the range of 10^{-6} to 10^{-4} footcandle-seconds which gives it an equivalent ASA rating of approximately 3000. The exposure time is program controllable from 15 ms to 60 s.

The camera also has an analog video and position D/A output and a 30 frame/sec sweep generator so that the image can be viewed on a black and white monitor. This feature is useful for setting up the camera before digitizing runs. The camera is equipped with a Nikon lens mount so that a complement of conventional lenses can be used. The camera data and control lines are interfaced to the PDP-11 bus through a DR-11C camera interface and a merging logic unit. Camera control and

data transfer were handled by a Fortran callable, assembly language subroutine. The image data is stored on digital magnetic tape for processing later.

Display Processor. An MDP/3 display processor is used to display the image data retrieved from the digital camera. The MDP is a micro-processor controlled image processor having 64K x 18 bits words of refresh memory with 16 bits for graphics display and 2 bits for 2 graphic overlays in each processor word, as well as 1K by 16 bit RAM memory and 4K by 16 bit EPROM memory. Image data is stored in the graphics memory, assigned a gray level intensity value or a pseudo color through programmable look-up tables and displayed on a color monitor. The monitor screen formats are 512 x 512 pixels x 4 bits to give 16 levels of intensity or colors and 256 x 256 x 8 bits to give 256 levels of intensity or colors. In addition, special firmware allows rapid manipulation of displayed data such as level windowing, zoom and linear interpolation to 128 x 128 or 64 x 64 as well as animation.

A library of Fortran callable, assembly language subroutines was written in order to load up the MDP processor registers and to execute the desired firmware programs. In addition, programs were written in MDP micro assembly language and loaded into the MDP memory to allow data to be written directly into and retrieved from

the MDP graphics memory. Thus we were able to utilize the 65K words of MDP memory as a temporary storage media or "scratch pad". This was especially important because the PDP-11/04 and 10 can support only 28K words of memory.

Array Processor. An MSP-3X array processor was used to perform the floating point arithmetic on the digital image and hot-wire signal arrays. The MSP is a block-floating dedicated array processor with 4K words of 24 bit data memory which is controlled by a high speed microprocessor. As with the MDP, 4K x 16 bit EPROMS contain firmware to support the execution of a comprehensive array function library. These functions include real and complex number addition, multiplication, magnitudes and forward and inverse fast Fourier transforms. As an indication of the processing speed of the MSP, it can perform a 1024 complex FFT in 26 milliseconds. This is extremely important since it requires 512 256-point one-dimensional row and column FFT's to transform a typical 256 x256 image into the spatial frequency domain for filtering and pattern recognition. As with the MDP, a library of Fortran callable, PDP-11 assembly language subroutines were written to transfer data into the MSP memory and to execute the array arithmetic.

Processing and Development System. The PDS system shown in Figure 11 was used to develop programs and process image and hot-wire data. This system is controlled by a PDP-11/04 mini-computer with 28 K words of 16 bit memory. Efficient use of the processor, hard and floppy disks, magnetic tape drive and input/output devices is made through the DEC RT-11 operating system. Under this system programs can be created, edited, compiled, linked with subroutine libraries and executed.

Flow Visualization

A "smoke-wire" was used to visualize the boundary layer flow at the lower freestream speed of approximately 6 m/s in this investigation. The smoke-wire, described by Corke, et al. (1977), consists of a 0.1 mm. diameter stainless steel wire which is coated with oil by letting a drop run down the wire. As a result of a capillary instability, the oil forms droplets along the wire so that when the wire is resistively heated the vaporized droplets generate discrete streaklines of smoke. The heating of the "smoke-wire" and triggering of a camera and strobe light are controlled by a synchronization circuit. Digital logic in the circuit allows visualization records to be taken which are conditioned on an "event" in the flow.

In this experiment a smoke wire, oriented normal to the boundary layer plate, was placed midway between

stations 6 and 7. The upper support arm was placed well into the free-stream so as not to disturb any part of the flow in the boundary layer. The stainless steel "smoke-wire" was connected to the upper support arm and passed through a small hole drilled through the boundary layer plate to its underside. That end of the wire was clamped and earth grounded through a connection to the metal frame of the wind tunnel. When the smoke wire was not in the tunnel, the small hole in the boundary layer plate was filled and wet-sanded smooth so that it would not create any disturbance to the flow.

The streamwise position of the smoke-wire allowed us to visualize approximately the last 15 boundary layer thicknesses of the flow. Also, the smoke wire was sufficiently upstream of the plug station so as not to influence the hot-wire rake by its thermal wake.

CHAPTER III

DATA ACQUISITION

The digital data acquisition of the analog signals for this experiment can be broken up into the relatively straightforward process used in the calibration of the hot-wires and time-mean measurements in the boundary layer, and into the much more complicated acquisition for the instantaneous unsteady measurements and digital image retrieval. All of the data acquisition software was written for this experiment in a manner to make the most use of the computer core available and to optimize the use of the various peripherals described in the previous chapter. These experimental setups and methods will be described in the following sections of this chapter.

Hot-wire Calibration

The calibration of the single hot-wire used in the mean measurement runs and the rake of 11 wires used in the unsteady measurement was done in the wind tunnel test-section. A schematic of the hot-wire rake is shown in the corner of Figure 3. Even though the tunnel heating problem was improved by the test section modifications, the test section air temperature would still increase by approximately 4°C for the low Reynolds number runs and approximately 6-8°C during the high Reynolds number runs. The absolute tunnel temperature

was,however, dependent on the laboratory room temperature which could vary about 3 to 4°C from day to day. For this reason, all calibration and data runs required that the hot-wire outputs be compensated for low frequency temperature variations.

For the single-sensor measurements, the hot-wire, sensitive to the streamwise velocity, U, was operated in a constant temperature mode by a DISA 55D01 anemometer. In this case and in the multiple wire case, a 1.8 overheat was used to provide the minimum amount of ambient temperature sensitivity of the output voltage proportional to velocity. Two separate calibration runs were made for the low and high Reynolds number cases so as to calibrate over each range of velocities with the two different mean operating temperatures. The overheat temperature was set after the tunnel temperature had reached its equilibrium value. Since the absolute temperature varied from day to day, the calibration temperature as referenced to an average long term temperature from which the compensated, true velocity could be determined.

During the calibration run for a single hot-wire, three channels of analog signals were digitized. One was the analog output of a Digatec 5810 temperature transducer proportional to the wind-tunnel air temperature. This signal was pre-processed through the bias/filter/gain circuitry to obtain an output equal to

the temperature in degrees Celsius divided by 10 . A minimum, pre-designed cutoff frequency of 2.5 KHz. was used to low-pass filter the signal prior to digitization. With the minimum resolution of 4 mv. for the A/D converter, an accuracy of .1°C was obtained.

The absolute test-section velocity was measured by a pitot-static probe connected to a Validyne DP103 pressure transducer. This transducer has a sensitivity of 2.65 V/kg/m in pressure, thereby giving it a sensitivity of 2.52 V /m/s in velocity. This signal was directly digitized to give a resolution of approximately .002 m/s over the range of operating velocities.

The output of the anemometer was d.c. biased, amplified nominally by 15 times and low-pass filtered at 5 KHz prior to being input to the A/D converter. The exact bias voltage and amplification factors were determined with a test signal to account for tolerance limits of the op-amp circuitry. These three sensor probes were placed at the same streamwise location along the mid-span of the tunnel test section for calibration. The three signals were simultaneously sampled and simple statistics were computed on line during the calibration run.

With the tunnel "pre-heated" to one of the operating temperatures, the fan speed was controlled to give a range of steady velocity readings. At each of these settings, acquisition was initiated and a sampling of

points was taken until the voltage values converged to steady means. This typically involved 1024 points taken over 4 seconds. Along with the mean values, the maximum and minimum values in the sample were ouptut to give an indication of the sample distribution. Each of the digitized voltages, proportional to temperature, was converted to temperature through the calibration and the average temperature was computed. Given the average temperature, the digitized voltages proportional to the pitot-static pressure were converted to velocity and the average free-stream velocity was computed.

From each of the voltages proportional to the streamwise velocity, the gain and bias were removed to give the actual bridge voltage. The temperature corrected voltage was then computed from the relation given by Bearman (1971).

$$E(T)_{corr} = \left[1 - \frac{\alpha_c}{r_{o-1}} (T-T_o) \right]^{-1/2} E(T)$$

where

r_o = overheat ratio at the reference temperature

α_c = resistance sensitivity to temperature of tungsten $(^oC)^{-1}$

T = actual temperature

T_o = reference temperature

The value for α_c was experimentally determined by

allowing the tunnel to heat up at a fixed velocity. A typical value was approximately .0034°C. The average corrected bridge voltage was computed for each velocity setting to generate voltage-velocity data pairs.

Given the data pairs, a squared, third order polynomial least-squares curve fit was performed to find the "best-fit" coefficients. This fit had been demonstrated by Drubka and Wlezien (1979) to better represent the output from a hot-wire than King's Law and to be computationally more efficient. A typical average error in the fit was 0.006 m/s.

In the case of the rake of hot wires, the 10 wires mounted to the p.c. board were held in the free-stream for calibration. The hot-wires were operated by 10 of the 12 CTA channels built for the experiment. The 10 analog outputs were d.c. biased, amplified nominally by 10 times and low-pass filtered at 5 KHz. These 10 channels were simultaneously sampled with the signals proportional to temperature and pressure as with the single wire calibration. The bridge voltage outputs were temperature compensated and 10 sets of velocity-voltage data pairs were fit to determine their calibration polynominal-coefficients.

Shear-wire Calibration. A single hot-wire mounted to the tunnel floor was calibrated to measure the streamwise component of the surface shear stress. The

wire, which was operated in a constant temperature mode, was calibrated in a turbulent boundary layer at different Reynolds numbers. An estimate of the mean wall shear was inferred from a single wire placed in the sublayer above the shear wire, which measured the slope of the velocity distribution near the wall. Although there is evidence from measurements in the thick sublayers of turbulent boundary layers in oil (Ekelmann,1974) that the sublayer velocity distribution is not linear, for sufficiently small non-dimensional heights, the error in assuming a linear distribution is small. For this reason the calibration was performed in the manipulated boundary layer which, as a result of its lower wall-friction velocity, has a thicker sublayer in which a probe can be placed at a smaller non-dimensional distance from the wall. The height of the probe was carefully measured using a cathatometer. The results of the calibration are shown in Figure 12. This calibration was considered satisfactory for the present study, since the main purpose for using the shear wire was to obtain information on the fluctuating shear stresses at the wall. High reliability for absolute values of the shear stress was not a primary requirement for this method.

The analysis of heat transfer from a heated strip in a linear velocity distribution which was removed by Sandborn (1972), suggests a 1/3 power relation between the shear stress and heat loss, or

$$\tau_\omega^{1/3} = Ag + B$$

where B is related to the energy lost into the surface substrate on which the sensor is mounted. For constant temperature operation, the i^2R_w heating equals E^2/R_w which equals CE^2 since R_w is constant. Therefore,

$$\tau_\omega^{1/3} = CE^2 + B$$

was used to normalize the axis of Figure 12. Sandborn (1981) points out through a perturbation analysis that τ_w is a function not only of E but also of the moments of fluctuations up to $\overline{e^6}$. Therefore, the mean value of the anemometer output voltage is composed of a mean value from conditions when no fluctuations are present plus higher order mean terms due to fluctuations in the shear as in the case of the turbulent boundary layer. These conclusions point to the fact that the calibration must be done where the conditions, such as the turbulence levels and scales, are similar to those in which measurements are to be taken.

It is obvious in Figure 12 that the calibration would not be best fit by a straight line, and as in the case of the velocity sensing wires, a squared third-order polynomial was found to provide the best fit to the voltage-shear distribution. The average error in the calibration fit was 0.8 percent.

Acquisition for Mean Measurements

The digital acquisition of data for time-mean results was broken up into profile runs which utilized relatively slow acquisition rates for the calculation of the first and second moments of the stream-wise velocity fluctuations, and into relatively high acquisition rates for the calculation of one-dimensional power spectral density, auto correlations and integral time scales.

Profile Data Runs. The instrumentation schematic for the acquisition of the boundary layer profile data is shown in Figure 13. As in the case for the single-wire calibration, the voltages proportional to the tunnel temperature, free-stream velocity and instantaneous velocity from the hot-wire were digitally sampled. In addition to these, the voltage proportional to the vertical position of the hot-wire was also simultaneously sampled. This voltage was pre-processed to give an output of 1V/12.5 mm. so as to give a resolution of 0.05 mm. through the A/D conversion.

Since the profile runs were intended to calculate only the mean and rms velocity values, it was necessary only to have enough samples taken over a sufficiently long period of time, equivalent to the passage of a sufficient number of the integral scales of interest, for the quantities to reach steady values. As contrasted with the spectra, the moments are not aliased in any way

by the sampling rate. For these data runs, a sequence of four channels, sampled 64 times a second for 30 seconds was found to be sufficient.

Profile data was taken by starting at the first upstream station and digitally acquiring and storing on digital magnetic tape the 6012 values comprising a tape record for each of 30 vertical heights from the surface of the boundary layer plate. Nearer to the plate, in that region of greater mean shear, the vertical sampling intervals were more closely spaced. In all but the first and last profiles, the streamwise intervals between the data stations was 0.3 m., as shown in Figure 3.

To ensure that the voltage corresponding to the vertical position of the probe accurately indicated the relative distance from the plate surface at each station, the lowest point was always set to be at x=0.5 mm. and to correspond to zero volts output. This was done by sighting the probe and its reflection in the plate in a graticuled cathetometer. By this technique, the probe sensor could be positioned to an accuracy of .01 mm.

Spectra Runs. The data runs for spectra calculations were done for half of the streamwise stations. In order to be able to make comparisons between the regular and manipulated boundary layers at the different stations, the data were taken at the same self similar heights of y^+ = 8, 15, 30, 50, 75, 100, 200, 400 and 800.

The highest frequency of interest in the velocity fluctuations was 5 KHz so that a sampling frequency of 10 KHz was necessary to ensure that the spectra would not be aliased. To further ensure no aliasing the signal was low-pass filtered at 5 KHz. For each height at each station, 100 records of 2052 pts/record were acquired and stored on digital magnetic tape. Each record contained 0.21 seconds of continuous data so that scales as large as 0.7 m. (a minimum of 9 boundary layer thicknesses) being convected at 70 percent of the free-stream velocity could be resolved. In regards to the turbulence, the 100 records were statistically independent, however, the acquisition program was written so that the data be acquired in phase with the 60 Hz clock. In this way any 60 cycle line noise and all of its harmonics could be removed if necessary as demonstrated by Way (1975).

Simultaneous Hot-Wire Rake and Digital Image Acquisition

The simultaneous acquisition of the rake of 10 wires, the shear wire and the digitized image of the smoke-wire visualized flowfield was designed to look in detail at the relationship between the large-scale outer structures and the wall "burst" mechanism in the turbulent boundary layers. The design of the probe concentrated as many as 7 sensors below $y^+=100$ which has been observed to bound the influence of the wall events. Although other sensors as high as $y^+=800$ would provide

some information about the large scale turbulence, the digital images, viewing the whole boundary layer over a number of boundary layer thicknesses, would be primarily used for that information.

The method by which the data was acquired reflects the type of information we wanted to extract and the limitations of the equipment. For example, we wanted the sampling rate to be fast enough to give sufficient resolution of points during a "burst" event and to be continuous for a sufficient amount of time to ensure more than one event per sampling record. For a number of statistically independent samples, the second criterion was necessary to compute frequency of events. The first criterion was limited only by the speed of the A/D converter and controlling assembly language software. For 13 input channels a maximum sequence sampling rate of approximately 2000 Hz could be attained. The second criterion was limited by sampling rate and the amount of computer memories available. Since the 65 K bytes of image data could not be retrieved from the digital camera fast enough to keep pace with the hot-wire acquisition, only one image per sampling was possible. Therefore, the images had to be "conditioned" on the event. Since we wanted the images and hot-wire data to coincide, the detection ot the event had to also initiate the hot-wire acquisition. However, we were also interested in the pre-event history of the flow. The acquisition strategy

was designed to allow for all these requirements.

The results of Rao et.al. (1971), Laufer and Narayanan (1971), Blackwelder and Kaplan (1976) and others have suggested that in the range of Reynolds numbers of this investigation the non-dimensional period between "burst" events is $TU_e/\delta \approx 5$. In the case of the low Reynolds number regular boundary layer, a sampling frequency of approximately 1800 Hz would resolve this period into 100 points. Approximately 400 words of memory were available to store each of the 11 channels of anemometer outputs, temperature and pressure so that at this sampling rate an average of 4 events could be detected. The acquisition rate was adjusted to maintain this resolution over the range of boundary layer parameters. Table 1 lists the acquisition rates for all of the boundary layer cases.

The analog and digital instrumentation setup for the simultaneous acquisition is shown in Figure 14. The 11 channels of anemometer outputs are d.c. biased, amplified nominally by 10 and low-pass filtered at 5 KHz before being input to channels 1 - 11 of the A/D converter in the support processing module. The analog signal proportional to the free-stream pitot-static pressure difference was input to channel 13 of the A/D.

The analog signal output of channel 10 of the anemometer was used to detect the "burst" events. This signal, which was proportional to the instantaneous

Table 1. Sampling Rate Parameters for Simultaneous Acquisition

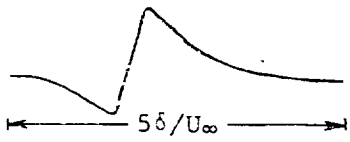

B. L. Case	U_∞(m/s)	δ(cm)	T(s)	f(Hz)	SSR	PTS/T
Regular	6.71	8.08	.0590	16.96	1694	100
Regular	10.36	7.42	.0356	28.10	2000*	71
Manipulated	6.71	7.16	.0536	18.66	1865	100
Manipulated	10.36	6.71	.0323	30.92	2000*	65

*Upper acquisition rate limit for 13 channels

velocity at $y^+ = 7$ in the boundary layer, would be examined for occurrences of high variance compared to the long-time background values. Although it has been common for investigators to use a sensor at $y^+ = 15$, the results of Blackwelder and Kaplan (1976) show that the velocity signature of these events remains coherent in the whole portion of the boundary layer below $y^+ = 100$. The signal at $y^+ = 15$, being near the peak in the vertical distribution of turbulence intensity, has considerably more turbulence fluctuations thereby making the detection more difficult. The (Blackwelder and Kaplan, 1976) VITA technique in effect low-pass filters the velocity data to perform the detection. However in this case, analog

filtering would be undesirable since it would introduce a phase shift in the detection signal. The signal from the $y^+ = 7$ sensor allowed easy detection without low-pass filtering. In all of the boundary layer cases, with the changing free-stream velocities and the addition of the manipulator, the vertical position of the hot-wire rake was adjusted to compensate for the different values of the wall shear velocity so as to always locate the lowest wire (channel #10) at $y^+ = 7$.

The anemometer output of the detection wire was linearized with a DISA 55D10 linearizer and input to a DISA 55D35 rms meter to measure the long-time average rms and to output a signal proportional to the instantaneous variance. The analog signal was fed to the variable threshold level detection circuit schematically shown in Figure 15a. The output from the l detection circuit consisted of a TTL logic status cc onding to

$$\text{CONDITION} = \begin{cases} 0: \; u'^2_{10} < ku'^2 \\ 1: \; u'^2_{10} \geq ku'^2_{10} \end{cases}$$

where k is an adjustable threshold coefficient. The logic output was connected to the condition logic in the smoke-wire control.

The smoke-wire circuit is made up of timing chips which control the duration of heating of the wire and the delay needed for the smoke to be convected into the field of view before triggering a camera and/or strobe light.

In addition, digital logic in the circuit allows photographs to be taken when the smoke is in view and when an external condition is satisfied. The conditioned photographs are necessary to do ensemble image averaging. The timing diagram for the smoke-wire control circuit is shown in part in Figure 16. The sequence is initiated by a positive pulse which can be manually applied or, as in this case, was software controlled through the output of channel 0 of the D/A converter.

The experiment was run in a darkened lab so that the image was recorded at the instant of the strobe flash The flash is approximately 1 ms. in duration which was sufficiently short to "freeze" the motion of the smoke image. In order to be able to mark that instant on the sequence of data, the trigger output pulse was multiplexed onto the slowly varying signal proportional to the wind tunnel air temperature. Before this could be done however, it was necessary to "shape" the pulse using the circuit schematically shown in Figure 15b. This circuit was designed to transform the syncing pulse from the strobe light into a -10v amplitude, 10 ms. duration square wave pulse. The 10 ms. guaranteed a minimum of 20 detection points at the A/D conversion rates used in the acquisition. The shaped pulse was added to the temperature signal through the second stage of the op-amp amplifier section of the bias/filter/gain circuit. The combined signal was fed to channel 12 of the A/D

converter.

The digital camera, which was mounted on a tripod, was connected to the PDP-11 bus through the merging logic unit and DR11-C interface. Under software control, the camera was operated in the 30 Hz scanning mode while the D/A outputs of the camera were viewed on a Tektronix 614A black/white monitor which sat on top of the camera. During this operation, the camera performed like a conventional television camera which made it easy to position and focus. For both of the low Reynolds number boundary layer cases the camera was set up to record two views of the flow. One view (zoomed out view) which encompassed approximately 8 boundary layer thicknesses utilized a 50 mm., f:1.4 lens. The other (zoomed in view) encompassed approximately 2 boundary thicknesses and utilized a 210 mm., f:3.5 macro/zoom lens. In both cases, the rake of hot wires was visible in the image. The camera was not moved throughout this phase of the acquisition. To be able to compare the image results with future data runs, the camera always viewed two LED lamps which were precisely spaced to provide a scale. During the retrieval and storage of the image data, the digital numbers were copied into the MDP-3 display processor graphics memory and displayed on the Conrac 5211C color display monitor. The MDP-3 graphics memory was also used for temporary storage of the digitized 13 channels of data.

The acquisition was directed by the PDP-11/04 processor in the fast acquisition system as controlled by the acquisition software. The timing diagram for the simultaneous acquisition is shown in Figure 16. After the smoke-wire is coated with oil, the sequence is initiated by a keyboard command. Prior to this, the digital camera is in a prime mode which erases any previous images. After initiation, the camera expose lines are enabled awaiting a flash from the strobe to store an image. A start pulse is sent to the smoke-wire control circuit to begin the generation of the smoke streak-lines. The duration of the smoke and the delay time to allow for the smoke to be convected had been preset in the smoke-wire control. It is within this "window" of time that the smoke is in the field of view and during which we search for a condition. The "window" was typically 1-2 seconds wide. The condition is only valid if it occurs when the smoke is in view.

Since we do not know a priori where in this window an event will occur, the acquisition of the 13 channels began at the initiation of the sequence and the data were stored in computer memory. For the sampling rates used, the amount of available data storage was too small to accommodate the time interval within our conditional window. Therefore, the software configured the space into a "circular" buffer so that old data were overwritten. Between each sequence of 13 channels, and

before the next interrupt of the programmable clock, the data value of channel 12 of the A/D was checked to see if the condition, marked by a -10V pulse, had occurred. If the condition was detected, 50 points, or one half of an average "burst" cycle, preceding the event were kept and the remaining 350 points following the event were acquired to fill the buffer. Also at the instant the condition occurred, the strobe flashed and the smoke image was stored on the digital camera. The 13 channels of data were then copied into a file on digital magnetic tape. The digital image was retrieved from the camera and copied to the next file on the digital magnetic tape. The camera was subsequently put in the prime mode awaiting the next sequence.

Depending on the delay time allowed for the convection of the smoke, it was possible that 50 points were not acquired before an event was detected. In such a case, the data set was discarded. It was also possible that no events be detected inside the "window". In this case, the acquisition loop was halted by manually applying a -10 V signal from the pulse shaping circuit into the channel 12 A/D input to terminate the acquisition cycle. Again the data set was discarded.

The threshold for the detection was set using an HP digital Spectrum Analyzer. The output of the threshold detector circuit was connected to the external trigger input of the spectrum analyzer to conditionally sample

the events. The threshold was raised until the educted ensemble average resembled the signature for the "burst" process. The ratio of the instantaneous threshold variance level to the long-time average variance used in the regular and manipulated boundary layers was 3.5. This number is not to be confused with the threshold used in the VITA technique since those values are the local average over $10Tu^2/\nu$ points.

For the high Reynolds number boundary layer cases, the velocity was too high to operate the smoke wire. In those cases, where the digital camera was not used, the acquisition was not initiated by the detection of a "burst" event. Rather, 256 statistically independent records of 400 points per channel for the 13 digitized analog signals were sequentially acquired and stored on digital magnetic tape.

Acquisition runs were also made for use in computing the power spectrum, auto-correlation and probability density of the signals from the 10 rake sensors and shear wire. In this case, the output of each wire was independently acquired at a 10 KHz sampling rate and stored on digital magnetic tape. The methods and acquisition software were identical to those described earlier in this chapter.

CHAPTER IV

DIGITAL PROCESSING OF TRANSDUCER OUTPUTS

This chapter is intended to describe the various types of digital processing performed on the hot-wire data. These include the methods for the boundary layer profile calculations, and for determining integral boundary layer properties, as well as the approach used in calculating the momentum balance for obtaining the wall friction of the boundary layer. Special one-dimensional time sequence processing is next examined. This includes one-dimensional power spectrum, auto-correlation, probability density and integral length scale calculations. Also included is one-dimensional match filtering for pattern recognition of the signature associated with the regular wall phenomena. The latter will provide information about the frequency of their occurrence, i.e., their distribution in time. The two-dimensional processing will demonstrate two-dimensional sampling and reconstruction techniques which allowed comparisons to be made between the hot-wire rake data and the digital images. Techniques for processing of the images based on smoke-wire visualization are described in the next chapter.

Boundary Layer Profile Calculations

The boundary layer profile data were made up of 30 discrete data points, spaced in the vertical direction

normal to the flat plate, taken at 10 (or 9 in the manipulated boundary layers) streamwise stations. The data were stored in raw form on four channels of digital magnetic tape as time series of unlinearized anemometer output and values proportional to the vertical probe position, tunnel air temperature and free-stream velocity for each of the discrete profile points. The first step in performing the profile calculations was to put the data in a more manageable form. For each profile point, this involved computing the mean air temperature, free-stream velocity and vertical probe position through their respective calibration equations. The anemometer output was compensated for any drift in tunnel temperature from the calibration temperature, in the manner described in Chapter III, and the mean and rms velocities were computed. These five values were written on another digital magnetic tape where they would be used for further processing. Since this processing, as well as the other processing on the profile data and raw data calibration for the hot-wire rake, required many floating point operations and tape-to-tape data transfers, they were performed on a large main frame UNIVAC 11/08 computer which handled these more efficiently than our PDP-11 systems. With the average profile values stored on digital tape, the integral characteristics of the boundary layers were calculated. Since we were particularly interested in the friction coefficient, a

number of these integral quantities were calculated in the same program which computed C_f.

A number of empirical relations exist for determining the wall shear from velocity profile data in a turbulent boundary layer. One of the most commonly used involves fitting the "log law" relation

$$u^+ = A \log y^+ + B$$

Here A and B are experimentally determined and universally accepted constants. A number of values for these coefficients have been reported, and there is some evidence that they may be weakly dependent on pressure gradient (Hinze, 1975). The values of 2.439 for A and 5.0 for B have been recommended by Coles (1969) and are most commonly used.

In a zero pressure gradient turbulent boundary layer flow, Coles' "Law of the Wake" (1960, 1969) relations

$$\frac{U_\infty}{u_\tau} = \frac{1}{k} \log\left(\frac{\delta u_\tau}{\nu}\right) + B + \frac{2\Pi}{k}$$

and

$$\frac{\frac{\delta_1 U_\infty}{\nu} - 65}{\frac{\delta u_\tau}{\nu}} = \frac{1 + \Pi}{k}$$

can be combined to remove the effect of boundary layer thickness to obtain

$$\frac{U_\infty}{u_\tau} = \frac{1}{k} \log \frac{\frac{\delta_1 U_\infty}{\nu} - 65\,k}{1 + \Pi} + B + \frac{2\Pi}{k}$$

Given δ_1 and U_∞ from the velocity profile, and using the value for Π given by Coles (1960), the wall shear velocity u_τ can be obtained. The value for k and B are those given by the log relation. The value of Π has been observed (Hinze, 1976) to be strongly dependent on the streamwise pressure gradient.

The empirical relation of Ludwig and Tillmann (1945)

$$C_f = .246\ Re_{\delta_2}^{-.268}\ 10^{-.678\ H_{12}}$$

has also been used to infer the friction coefficient from the integral profile properties. This relation was derived by correlating the experimental results from boundary layer measurements of different investigators.

Although these relations could be used to infer the friction velocity from the profiles of the boundary layers without the manipulator, there is no reason to expect that the empirical constants used in any of these formulations would take the same values in the manipulated boundary layer. Rather than using any of these, we undertook to measure the balance of momentum from which we could obtain the shear force on the plate. This was done for both the manipulated and non-manipulated boundary layers with the empirical relations being used only for comparison purposes.

If we solve the momentum equation for a two-dimensional, incompressible turbulent boundary layer we can obtain the integral form

$$\frac{d}{dx}\,(U_\infty{}^2\delta_2) + \delta_1\, U_\infty \frac{dU_\infty}{dx} = \frac{\tau_w}{\rho}$$

which was first formulated by von Karman in 1921 (see Hinze, 1975). The contribution of turbulent fluctuations to the balance are trivial and neglected in this formulation. The terms δ_1 and δ_2 are the integral displacement and momentum thicknesses

$$\delta_1 = \int (1 - \frac{U(y)}{U_\infty})dy$$

and

$$\delta_2 = \int \frac{U(y)}{U_\infty} (1 - \frac{U(y)}{U_\infty})dy$$

The computational method for solving this equation with the prescribed profile data is given in the flow-chart of Figure 17 and described in the following.

For each particular boundary layer case, the mean velocity and turbulence intensity values corresponding to the vertical y positions at each streamwise station were read from digital magnetic tape into a computer array. For use in comparing τ_w values to those determined by the momentum balance, the U,y data pairs were least-squares curve fit to the log relation over the range from y+ = 50 to 200 to determine $\tau_w(x)$ for the profiles. This was done in an iterative manner by initially guessing a value for u_τ and computing the average deviation of the points from the equation

$$u^+ = 2.44 \log y^+ + 5.0$$

A correction to the previous u_τ was computed and the solution continued to loop until a "best fit" was obtained.

The free-stream velocity, U_∞ , at each station was computed from the top portion of each profile. Since the value for U_∞ appears inside the integral for δ_1 and δ_2, small errors in measuring that quantity are summed up in the area under the distribution. We therefore formulated an accurate general method for determining the free-stream velocity, which used the fact that at the top of the profile the slope is a constant. This involved computing the cumulative average velocity starting from the top most point of the profile which is well into the free-stream. The contribution of each point to the cumulative average is determined and compared to a tolerance. If the contribution is less than the tolerance, the contribution of the next point down the profile is computed and the tolerance is reduced by an amount proportional to the number of points in the cumulative average. When a point's contribution exceeds the tolerance, the value of the cumulative average taken two points previous to that one was assigned the value of U_∞. The sensitivity of the final result to the choice of the two parameters, namely, the initial tolerance and number of points to be stepped back after the tolerance

had been exceeded was investigated and used to provide consistent results. The values of U_∞ from each measurement station constituted the streamwise distribution of $U_\infty(x)$.

For a particular boundary layer case, the acquisition of the profiles, starting at the upstream most station, required data runs which lasted approximately six hours. During those runs, a very slow free stream velocity drift was detected. This resulted in the free-stream velocity for the last profiles being slightly lower than that for the first profiles. To compensate for this, so that it would not be interpreted as pressure gradient effect, the free-stream velocity time dependence was computed from the digitized output of the free-stream reference pitot-static probe and used to correct the free-stream velocity values. This involved increasing the U_∞ values by an amount equal to the difference between the free-stream velocity read by the pitot-probe at the beginning of the data run and the average value over the time when each set of profile points was taken. The velocity values of the profile points were suitably increased by an amount proportional to their percentage of the free-stream speed so as to preserve the profile shape.

If one is to use the momentum balance for determining the wall-shear stress, it is very important that any time dependent changes in the tunnel operating

conditions be accounted for. A great deal of effort has been spent over the last ten years quantifying the wind tunnel used in this investigation. Additional hot-wire diagnostics and flow visualiation experiments were conducted early in this study. The excellent agreement achieved in regular boundary layers between this approach and several well accepted formulas, as discussed in Chapter VII, was a prerequisite to proceeding with this method in the manipulated boundary layers.

To obtain a functional representation of the $U_\infty(x)$ distribution, the values obtained from the above technique were fit with a least squares cubic spline fit with weighting and damping. The advantage of the cubic spline is that it fits a smooth function through the data points rather than fitting the points to some pre-described function. In the limits, a zero damped spline function will pass through all of the data points, while an infinitely damped spline will fit a straight line through the data. In its application here, all of the points were equally weighted and the damping was adjusted to obtain a smooth distribution through the data values. After smoothing, the velocity values of the profile points were raised or lowered by a proportional amount so that the free-stream value equaled the spline smoothed value at that streamwise position. The streamwise distribution of the dU_∞/dx was obtained from the direct differentiation of the spline function. The local dU_∞/dx

values were further smoothed by a spline fit for use in the momentum computation.

Since we placed less confidence on the accuracy of the points taken closest to the floor we developed an iterative method for computing the quantities needed in the solution of the momentum equation. Initially, for each velocity profile, the datum point closest to the surface of the flat plate was chosen as an "initial guess" for y corresponding to y+ = 10. The velocity profile was subsequently taken to be linear to that height and to pass through the data points at all higher elevations. The profiles were then integrated to obtain $\delta_1(x)$, $\delta_2(x)$ and the energy thickness $\delta_3(x)$. In the process of integration, the profiles were smoothed by fitting a parabola through successive groups of three data points. Two data points of each group were overlapping. The integral values of the parabolic profiles taken across the overlapping regions were subsequently averaged and summed to obtain the total integral value for the complete mean profile. Given values for $\delta_2(x)$, the Ludwig-Tillmann relation was computed at this point to be used later for comparison to the u_τ values obtained by the momentum balance.

For use in the momentum equation, a functional relation for $\delta_2(x)$ was obtained from a least squares cubic spline fit. Discrete values of $d\delta_2(x)/dx$ were obtained from direct differentiation of the cubic spline

function. The $d\delta_2(x)/dx$ values were further smoothed by fitting the values with a cubic spline.

The values taken from the "initial guess" were substituted into the momentum equation to generate new values of $\tau_w(x)$. The values of τ_w were used to compute new values of y at y+ = 10 and the corresponding velocity values at that height taken from the linear velocity distribution

$$u^+ = y^+$$

Using these values the profiles containing new bottom points were again integrated to compute $\delta_2(x)$ and $d\delta_2(x)/dx$ and used to solve the momentum equation for $\tau_w(x)$. The solution continued to loop until consecutive τ_w values differ by less than 10^{-8}. Convergence typically occurred after three iterations.

To substantiate this method for determining the wall shear stress from the momentum equation, the boundary layer data taken by Wieghardt (1951) were used and the results compared to those obtained from other empirical formulas. The results of this comparison are discussed in Chapter VIII.

In order to determine the wake component, Π, for the outer part of the boundary layers, the transcendental equation

$$f(\Pi) = \frac{1}{2}\log\left[\left(\frac{\delta_1 U_\infty}{\nu} - 65\right)k\right] + B + \frac{2\Pi}{k}$$

was solved using a Newton-Raphson iteration method. New

k and C were determined from the log portion of the velocity profile. In the case of the non-manipulated boundary layers the standard values of k and C, 2.44 and 5.0 respectively, were found to represent the data well and were used in the "law of the wake" solution. In the manipulated boundary layers, a least-squares curve fit was performed on the u+ vs. log y+ data to determine the "best" k and C values. These coefficients, which differed from the non-manipulated case, were then used in the solution for Π.

One-dimensional Processing

In order to obtain a statistical description of the digitally acquired turbulent velocity fluctuations, one-dimensional time-series digital processing was performed on the data. The processing included calculation of the first four moments, probability density, one-dimensional Fourier transforms, energy spectrum, auto correlation and integral length scale. In regard to studying the wall layer phenomena, one-dimensional detection using the average local variance as a discriminator is presented along with one-dimensional match filtering methods for the velocity signature pattern recognition. The one-dimensional processing was performed on the time series velocity data of the single hot-wire sampled at 10 KHz and of the individual rake sensors as well as the

data from the shear wire.

In the case of the 10 KHz sampled data, the tunnel air temperature was not digitized along with the anemometer output. In order to compensate for temperature differences from the calibration reference temperature, the hand-recorded temperatures were used to correct the voltage values. Since the change in temperature results in an apparent change in the d.c. offset and gain in the anemometer voltage, the temperature differences were compensated for by modifying these two values which were input for the digital calibration of each data file. In order to recover the actual anemometer voltage value from the digitized value, the equation

Sample value = (E - OFFSET) x GAIN x ADGAIN

is solved where

OFFSET = Analog d.c. bias

GAIN = Analog amplifier gain

ADGAIN = Analog-Digital conversion factor.

In correcting for temperature changes which result in changes in E, the processed, corrected voltage is EC where,

$$EC = \left(\frac{E(U,T)}{GAIN \times ADGAIN} + OFFSET\right) / K(T)$$

and

$$K(T) = \left[1 - \frac{a_c}{r_o - 1}(T - T_o)\right]^{1/2}$$

If we put the equation into the original form we obtain

Sample value = (EC - OFFSET') GAIN' x ADGAIN

where

$$OFFSET' = OFFSET/K(T)$$

and

$$GAIN' = GAIN \times K(T)$$

Therefore the gain and offset values could be adjusted file by file to account for changes in temperature away from the reference.

The one-dimensional spectra were obtained by taking the discrete real valued forward FFT of the 2048 point time series and constructing the one-sided power spectral density by multiplying the values in the frequency domain by their complex conjugate and summing symmetric points. The power spectra were normalized by the area under their distribution, which is the variance. The auto-correlation is obtained by taking the inverse FFT of the one-sided spectral function. The integral length scale was calculated from the area under the auto-correlation function, where it is defined as the time lag intercept of a rectangle of equal area with a height equal to the zero lag correlation value, or variance. Since each time series constituted a number of integral time scales, their correlation functions should approach zero for long time delays. As pointed out by Wigeland (1979), very low frequency fluctuations, which are not related to the flow characteristics, but rather to quasi-steady changes in the laboratory environment,

can cause the correlation functions to not asymptote toward zero. Since the integral time is computed from the area under the curve, this can cause significant errors. To remedy this, the method detailed by Wigeland (1979) was used to calculate the contribution of these very low frequencies and remove these effects from the determination of the integral time scale and variance.

The probability density calculations are actually the number density distribution where

$$P_j = \text{SAMPLE probability that } [\, d_{j-1} \leq u < d_j]$$

and d_j specifies the width of a bin. Before sorting the numbers, the values were scaled by a variable amount corresponding to 10/rms(u) in order to increase their significance and to make the bin width a function of the rms of the velocity fluctuations. In the distribution for the wall shear for each boundary layer case, 200K data values were sorted into 300 bins of width 1/10 rms(τ).

"Burst" Signature Detection. In order to determine the velocity signature for the wall events, so called "bursts", the variable-interval time-averaging (VITA) technique introduced by Blackwelder and Kaplan (1976) was employed. This technique utilized the localized short-time variance defined as

$$VAR(x_i,t,T) = u^2(x_i,t,T) - [u(x_i,t,T)]^2$$

as a discriminator, where T is an averaging time which is

on the order of the event duration. The detection function is defined as

$$D(t) = \begin{cases} 1 & \text{if VAR} < k.u^2_{rms} \\ 0 & \text{otherwise} \end{cases}$$

where k is a threshold level and u_{rms} is the long-time-average root mean square of the record of the series, namely,

$$u^2_{rms} = \lim_{T \to \infty} \text{VAR}$$

In essence we are searching for correlated events which stand out above the background (Blackwelder, 1977; Antonia, 1972). Except for detection purposes, the method has serious flaws. The first of these is that the frequency of occurrence of events detected by this technique is dependent on the threshold and local averaging time. In addition the technique does not always detect the same "class" of events. The "burst" event has been classified as a local deceleration (ejection) of the streamwise velocity followed by a rapid acceleration (sweep). The large local variance results from the large deceleration to acceleration sequence. Nishioka et al. (1980) show that although some of the latter class of events occur, the majority are of the deceleration/acceleration type. Therefore, the VITA technique only yields the signature of the most coherent event linked to a large local variance. It is with this application in mind that the technique was utilized here.

In keeping with the results of Blackwelder and Kaplan (1976), a threshold value, k, of 1.2 and a non-dimensional averaging time, $Tu_\tau^2/\nu=10$ was used. Also, the detection was made at a non-dimensional height of $y^+ = 15$.

The detection was performed on the outputs from the rake of hot-wires. In order to determine any Reynolds number effect on the frequency of events, the technique was also applied to the 10 KHz acquired outputs of the traversed single wire. The raw anemometer outputs were calibrated on the UNIVAC 11/08 computer and written to digital tape. These tapes, containing the instantaneous velocity values were then processed on the PDP-11/04 mini-computer. The processing involved scanning each record of 400 points for a local variance greater than the threshold. The locations of the detected points were subsequently stored on floppy disks for later processing. The educted ensemble average of the velocity distribution at the time of the event was constructed by averaging each velocity time series centered around the detection point. In the case of the rake of wires, the pattern was educted not only at the detection wire but also for the other sensors. In this manner, the ensembled signature of the events for all of the boundary layer cases and Reynolds numbers were generated for use as a "pattern" in the one-dimensional match filtering which is described in the following section.

One-dimensional Pattern Recognition. Given the most coherent velocity signature which was linked to a high local variance, one-dimensional pattern recognition processing was done to obtain unbiased statistics for the frequency of occurrence of these events. This is contrasted to other "pattern recognition" schemes such as used by Wallace et al. (1972), which do not have the same statistical basis. The pattern recognition was accomplished by match filtering the time series of the detection wire with the educted velocity signature. The match filter has an impulse response equal to the time-reverse version of the signal waveform to which it is matched so that the response is identical to an autocorrelation function. The peak in the autocorrelation, marking the match, occurs at a zero lag time and is proportional to the total energy of the signal waveforms. It can be shown theoretically (Lynn, 1973) that the improvement in signal-to-noise ratio caused by a match filter is the best possible.

The match filter was constructed by centering the one-dimensional educted time series, obtained from the method of the previous section, in a 64 point array. In order to eliminate the circular effect in the time limited autocorrelation function, the time series was extended to twice its original length with zeros. The real 128 point FFT of the time series was taken and

stored in the resulting 128 point complex array. In order to form the correlation functions, the imaginary part of the complex filter function was multiplied by -1 to form the complex conjugate.

The velocity time series of each record was broken into six 64 point segments which were each time extended with zeros to 128 points. The real FFT was taken of each segment and the real and imaginary parts of the filter function and data were multiplied (convolved) in the frequency domain. The inverse complex FFT was taken of each of the convolved segments to obtain the correlation function. In order that the zero time lag would correspond to the center of the 128 point correlation function, the two 64 point sections were interchanged. The match filtered output was constructed from the filtered segments by the so-called overlap-add method which accounts for the fact that the linear convolution of each section with the sample response is larger than the section length. As illustrated in Figure 18, adjacent segments were overlapped by an amount equal to the filter width and the autocorrelation values in this region were summed to generate a smooth transition between segments. The first and last half filter width of points in the correlation function are filled with zeros and therefore discarded. The original record length of points was then retrieved.

Each record was analyzed to locate the positive

correlation peaks corresponding to a match with the pattern for the "burst" event. The match locations for each time series were stored and the difference in time between peaks, computed using the sequence sampling rate, was used to compute the frequency statistics.

Two-dimensional Processing

The two-dimensional space-time processing of the outputs from the hot-wire rake was initiated to allow a comparison between the flow structures deduced from the velocity field and those marked by smoke and stored as digital images. A number of the processing techniques described here are similar to those used in the processing of the two-dimensional image data (see Chapter V) and, therefore, some overlap will be encountered in the discussion.

If we consider the digital acquisition of the analog outputs of the rake of hot-wires they can be represented by the sample function

$$u(y,t) = u(y + qY(y), t + rT)$$

where q and r are arbitrary positive integers. Here the data are sampled simultaneously in time at the A/D acquisition rate with a constant period, T, and in space by the variably spaced, Y(y), sensor wires. We would like to reconstruct the discreetly sampled velocity data into the low-frequency wave number distribution analogous to the digital image. As will be explained,

C-2

low-frequency is a relative quantity which depends on the sampling rate.

If we consider the sampling theorem for the discrete sampling of continuous data, which can be found in any number of texts on digital processing, (Lynn (1973)), Bendat and Piersol (1971 and 1980), Oppenheim and Schafer (1975), it states that for data sampled at a frequency 1/T, the highest frequencies that can be realized in processing is half of that value or

$$f_c = 1/2T = 1/\omega_o$$

Here f_c is the well-known Nyquist frequency or folding frequency. Furthermore, the sampling theorem guarantees that a properly sampled band-limited signal can be reconstructed by a properly designed reconstituting filter. The reconstituting filter must have the frequency response $F(\omega)$ such that

$$F(\omega) = \begin{cases} T & |\omega| \leq \frac{\omega_o}{2} \\ 0 & |\omega| > \frac{\omega_o}{2} \end{cases}$$

or in other words the filter response must guarantee no aliasing in the spectrum. In the time domain, this function would have an impulse response equal to the inverse transform of $F(\omega)$ or,

$$I(t) = \frac{1}{2\pi} \int F(j\omega) e^{j\omega t} \, d\omega$$

$$I(t) = \frac{1}{2\pi} \int T e^{j\omega t} \, d\omega$$

$$I(t) = \frac{\sin \omega_o t}{\omega_o t}$$

If we convolve this function with our sample function,

$$u_f(t) = u_s(t) * \frac{\sin \omega_0 t}{\omega_0 t}$$

it can be shown (Lynn (1973)) that an exact reconstruction of the continuous time series is obtained. In practice we can reconstruct the continuous data function for a range of frequencies below the Nyquist frequency by choosing a low-pass filter which band-limits above that frequency. Although a sin(t)/t function was used in this analysis, in practice it cannot be applied. In this application a finite impulse response filter was specifically designed to reconstruct the two-dimensional data space.

Two-dimensional Filter Design. In the case for the space-time analysis of the rake of hot-wires, the sampling frequencies of interest are the A/D rate and wire spacings. If we consider first the A/D rate, we can choose an integral convection velocity to convert that frequency to a spatial passage of a coherent eddy. A typical value based on the acquisition rates which was used in the experiment is 2.8 mm./sample. The largest spacing between sensors was 11.8 mm. so that the latter is the limiting value for the design of a two-dimensional low-pass spatial filter.

The two-dimensional FIR filter was generated from a 64 point one-dimensional low-pass filter whose impulse response was symmetrically expanded into a 64 x 64 two-dimensional plane. In the 64 point array, the maximum sensor spacing corresponded to 12 points so that for $.5f/f_c$ equal to the total 64 points, the maximum cutoff frequency for proper reconstruction was 0.05f. The linear phase FIR filter was designed using the program written by Mcleilan et al. which was one of a number of programs for the processing of digital signals (IEEE Press, 1979). This program allows the design of up to 128 point, multiple stop-band filters with multiple weighting of ideal response characteristics. In this case the 64 point filter had a pass band from 0 to $0.05f/f_c$ and a stopband from 0.08 to $0.5f/f_c$ with an equal weighting of 5 for both bands. The weighting and edge cutoff frequencies of the bands were designed to give a minimum amount of ripple and the greatest amount of amplitude cutoff. In this design the amplitude in the stopband is reduced by 60dB.

The program returns the impulse response which was subsequently used to generate a two-dimensional symmetric response by $R(x,y) = R(x) * R(y)$. The 64 x 64 array was time extended to 128 x 128 by adding zeros to the top and right to ensure linear convolution filtering and the 128 point two-dimensional FFT was taken. The frequency domain representation of the filter was stored for later

use in the reconstructive processing. The one- and two-dimensional spectral function of the low-pass filter is shown in Figures 19 and 20. In the two-dimensional representation, only the positive frequency quadrant of the digital filter is shown.

Two-dimensional Discrete Fourier Transform. The discrete Fourier transform representation of two-dimensional sequences is of considerable computational importance in the digital processing of two-dimensional signals such as the digital photographs and in the reconstruction of the space-time velocity features in the boundary layer. In two dimensions, the Fourier transform is applied over a finite area corresponding to a block of data or part of an image. Because of the separable nature of the Fourier transform, (see Oppenheim and Schafer, 1975) the two-dimensional DFT can be implemented by using a one-dimensional DFT on the rows and then on the columns or vice versa.

In its application, as shown in Figure 21, the 64 x 64 blocks of data were time extended by adding zeros to form a 128 x 128 real array of which the two-dimensional FFT was taken. The 128 x 128 real-valued array requires 32K words of storage and its transform at the worst case requires 65K words. Even with the 65K words of MDP display memory, this would only allow one transform to be stored in RAM at one time and furthermore leave no room for

intermediate and final results of the processing sequence. If the transforms were stored on disk, the time required for disk access would increase the processing time by an order of magnitude. Therefore, we utilized the symmetry properties of the Fourier transform to reduce the storage requirements. The real part of the transform is conjugate symmetric and the imaginary part is conjugate antisymmetric. Therefore, we need only store half of the transform and the other half can be reconstructed. The redundant transform domain samples resulting from the symmetry properties are shown in Figure 21. It must be noted that these symmetry properties only apply to the Fourier transforms of real functions (Oppenheim and Schafer, 1975). In the case of the two-dimensional transform the first transform is done on a real valued data, the second is done on the result of that transform which is complex-valued so that the symmetry only applies in the first direction. The savings, however, reduce the storage from 65K words to 32K words so that both the transformed two-dimensional filter function and the data block being transformed can be stored in the fast access MDP memory. In terms of computations, we also reduce the number of FFTs taken in the second direction by a factor of two.

The 128 x 128 real array of data to be transformed initially resided in the upper or lower half of the MDP display memory. The first transform was done in rows by

reading the individual "sticks" of data into the MSP array processor and taking the real one-dimensional 128 point FFTs. The transforms were packed into 64 complex values by taking the symmetric half and placing the symmetry point into the complex part of the d.c. bin. They were subsequently stored in non-bitreversed form in place in the MDP memory. The 64 cclumns of 128 word long complex values were each transformed by reading in those "sticks" of data and perfcrming the complex 128 point FFTs. The 128 point transforms were written back in place in non-bitreversed form in the MDP memory.

The inverse two-dimensional transform was performed by inverting the procedure in the forward transform. The 64 columns of complex valued numbers were read into the MSP array processor, put into bitreversed order, and the complex inverse FFTs were taken. The columns were then replaced by their bitreversed transform, in place, in the MDP graphics memory. The 123 rows of complex values were each read from the graphics memory into a one-dimensional PDP array. The symmetric half was then reconstructed and the 128 point array was complex inverse transformed in the MSP. The real values of the result were taken and optimally scaled to an integer format where they were written for storage and display purposes in the display processor memory.

In order to reduce execution time, any processing which was repeated a number of times, for example the

symmetric reconstruction, was handled by specifically written assembly language subroutines. Also, whenever possible, the PDP, MDP and MSP processors were allowed to run in parallel. The total execution time for a forward or reverse 128 x 128 point FFT was approximately 30 seconds.

Two-dimensional Reconstruction. As with the one-dimensional analysis of the rake data, the continuous time series was broken up into six segments, each 64 points long. In the space direction the simultaneous data from the nine sensors furthest from the wall were placed in the array rows 0, 1, 2, 3, 4, 6, 12, 19, and 31. The spacings in the array represent their proportional spacing in the rake. Any further spacing of the sensors to accommodate more of the 64 point space dimension was not possible because a suitably low ripple, low-pass filter could not be designed. The array was not reduced to 32 x 32 because the reduction in points used in the design of the impulse response for the digital filter degraded the performance. The shear wire and hot wire at $y^+ = 7$ were not used in the reconstruction. However, since the data is over-specified in that region of the array for the low-pass filter cutoff designed by the largest spacing, their influence would have been minimal. Zero values filled the space between the rows where data values were specified. The arrangement is

shown in Figure 21.

Since we wished to highlight flow structures, the velocity data for the two-dimensional reconstruction were normalized by removing the ensemble mean value and dividing by the ensemble rms of each of the sensors. We therefore intended to give emphasis to parts of the flow which stood out above the background turbulence or "noise". These structures were assumed to remain reasonably intact as they were being convected past the probe. Furthermore, we expected that these structures would be the same as the coherent features visualized by smoke and stored as digital images.

Each segment of data was read into the MDP memory and the two-dimensional FFT was taken with the spacial frequency representation being stored in place in memory. The convolution was performed by multiplying the real and imaginary parts of the column values of the transformed data block and filter function. The result then replaced the transformed data. The inverse two-dimensional FFT was taken of the convolved data and the result was stored away. As with the one-dimensional match filter, the segmented data were smoothly connected using the overlap-add method.

The result of the convolution is left in the center of the 128 x 128 array. Since these are segments in the time series, the overlap-add is done in that direction

only. As illustrated in Figure 21, the segments are overlapped by an amount equal to the filter width in the time direction where the values were added. The top and bottom half filter widths of the two-dimensional arrays were discarded along with the first and last half filter widths of each 400 point long continuous realization.

Using the match points from the one-dimensional analysis, the two-dimensional representations were ensembled about those instants in time to obtain an "average" view of the "burst" sequence. Also the two-dimensional spectral function was calculated for the reconstructed data. In that case the spectra were formed by taking the two-dimensional FFT of a reconstructed segment of data. The transformed data columns were multiplied by their complex conjugate and the real valued function formed the positive and negative frequency spectra. The spectrum was normalized by the volume under the distribution, i.e., its two-dimensional variance.

CHAPTER V

PROCESSING OF IMAGES

The methods documented in this chapter describe the two-dimensional processing techniques which were applied toward systematically extracting information from the digitally acquired images of the smoke-wire visualized flowfield. These images, whose acquisition was conditioned on a so-called "burst" event, are intended to provide visual information about any coherent flow structures linked to the process. This chapter will first discuss the methods used for the visual enhancement of the images and the special processing techniques to convert the images to a form better suited to machine analysis. Later, two-dimensional pattern recognition using match filtering will be discussed in order to extract and mark coherent features appearing in the images.

Image Enhancement and Processing

The image enhancement process consisted of methods that sought to improve the visual appearance of an image or to convert the image to a form better suited to human interpretation or machine analysis. In terms of visual appearance, one method of enhancement consisted of the application of pseudo-colors to an otherwise gray level image. Another application of image enhancement was to

emphasize salient features of the original image in order to simplify the processing task. For example, the images could be high-pass filtered in order to emphasize the smoke-wire streaklines thereby simplifying streakline following routines like those used by Nagib et al. (1978).

The digital images were stored on a digital magnetic tape for post processing after acquisition. In order to reduce storage space, each pair of 8 bit pixel intensity values were packed into a single double byte PDP word. During processing, the images were "unpacked" and the pixel values were read into the display memory for viewing on the color monitor. The images consisted of white smoke on a black background and were recorded in a maximum of 256 gray levels. Therefore, an exact black and white reconstruction was accomplished by loading the red, green and blue color lookup tables in the display processor with identical color intensity ramps from 0 to 255. In this way, a pixel value is translated into a gray level intensity proportional to its original luminance. After processing for image detection it was often helpful to display the results in pseudo-color which were designed to enhance the detectability of features in the image. The pseudo-color mapping of the original image is not a color image but rather a two-dimensional array of values that is converted to a color plane. In this application a color table consisting

of 16 bands of color hues and saturation levels was generated to represent the data.

Although the digital-camera output values ranged over 8 bits, the display processor was capable of displaying unsigned integer values of up to 15 bits. Therefore we often would rescale the pixel values to occupy the full 32K integer range. The easiest way of doing this is to compute the maximum and minimum pixel values and to do a linear rescaling so that

$$F(j,k) = \frac{F(j,k) - F_{min}}{F_{max} - F_{min}} \times 32767$$

This in effect performs a histogram expansion of the original image and thereby increases its contrast.

Because of the extreme light sensitivity of the digital camera, the images were very sensitive to slight differences in background illumination. Differences from image to image could come about as a result of non-consistent flash intensities from the strobe light or non-uniform vaporization of oil from the smoke-wire. Within an image, low-frequency variations in lighting arising from shadows or reflections or slight non-uniformities in the sensitivity of the Viticon tube, were imperceptible in a single realization but they were brought out as strongly coherent features in the ensemble averaged images. Therefore, before applying pattern recognition techniques to these images it was necessary to remove any non-uniformities which were not related to

the flow structures.

In order to remove any stationary variations in the image luminance the pixel values were corrected by adjusting their values by an amount proportional to the "average" background values. The average background illumination was obtained by ensemble averaging all of the digital images. The random nature of the smoke in the images canceled their contribution to the average so that only the average stationary background features remained. The value of each pixel in an image array was changed by an amount corresponding to the average background pixel value at that array point. This can be written as

$$F(j,k) = \frac{F(j,k)}{\bar{F}(j,k)} \times K$$

where K is a coefficient of adjustment used to expand the result over a large usable range. In effect, this procedure digitally "dodges" the images in a more systematic way than can be done by hand in the dark room. This process was performed on all of the images before pattern recognition processing.

In some cases it was beneficial to remove a dominant feature from the images, such as the hot-wire rake, in order to better see the smoke around an otherwise hidden region. In the case of the sensor rake, this was accomplished by recording an image of the probe alone without smoke. It was necessary that this image was

perfectly scaled and its position was perfectly registered with that in the standard images. The two-dimensional FFT was taken of the rake image alone to obtain its spacial frequency representation. A corresponding portion of a smoke plus the probe image was similarly transformed to the two-dimensional spacial frequency domain. The two arrays were then subtracted on a point by point basis to remove the frequency content associated with the probe. The inverse two-dimensional FFT was taken of the result to leave the smoke image without the probe.

Another method for removing or highlighting image features which are oriented with some directional coherence was a digital implementation of another dark room technique. The pixel values of a digital image are linearly rescaled to utilize the full 15 bits available in the display processor and then a "negative" of the image was generated by the transfer function:

$$\hat{F}(j,k) = 32767 - F(j,k)$$

The negative image was translated in a direction normal to the oriented feature of interest and the pixel values were averaged and rescaled to obtain a new pixel value

$$\bar{F}(j,k) = F(j,k) + F(j + \Delta j, k + \Delta k)$$

The resulting image brought out the edges of the features in the translation direction and everything else not coherent in that direction was left as a uniform gray background.

Two-dimensional high-pass and low-pass filtering of the images was performed by convolving the images with a digital filter function. This was done either by a discrete convolution of the form

$$Q(m_1,m_2) = \Sigma_{n_1}\Sigma_{n_2} F(n_1, n_2)\ H\ (m_1-n_1 + 1, m_2-n_2 + 1)$$

or by array multiplication in the spatial frequency domain. The criteria for the choice of methods was based on the size of the impulse response array, H(i,j). In our case, if the dimensions of the filter array exceeded 3 x 3, it became more computationally efficient to do the convolution in the frequency domain. The low-pass filter masks (taken from Pratt, 1978) that were implemented here are

$$H = \frac{1}{9}\cdot\begin{vmatrix} 1 & 1 & 1 \\ 1 & 1 & 1 \\ 1 & 1 & 1 \end{vmatrix}$$

and

$$H = \frac{1}{10}\begin{vmatrix} 1 & 1 & 1 \\ 1 & 2 & 1 \\ 1 & 1 & 1 \end{vmatrix}$$

These are essentially noise cleaning masks with normalized weighting so that they would not introduce a brightness bias into the processed image.

The high-pass filter masks were utilized to highlight edges in the images. The masks utilized in the discrete convolution were

$$H = \begin{vmatrix} 0 & -1 & 0 \\ -1 & 5 & -1 \\ 0 & -1 & 0 \end{vmatrix}$$

and

$$H = \begin{bmatrix} -1 & -1 & -1 \\ -1 & 9 & -1 \\ -1 & -1 & -1 \end{bmatrix}$$

These possess the property that the sum of their elements is unity. The filter masks were implemented in an interactive way to enhance visual interpretation of the images after processing.

Another form of edge enhancement that was used to highlight features of the match filtered results is called statistical differencing (Rosenfeld, 1969). This involves the generation of an image by accounting for its statistical deviation from its neighbors. The transfer function implemented in the processing was suggested by Wallis (1976)

$$G(j,k) = F(j,k) - \bar{F}(j,k) \quad \frac{A\sigma_o}{A\sigma(j,k) + \sigma_D} + [\alpha m_D + (1 - \alpha)\ \bar{F}(j,k)]$$

This function enhances the image by forcing a form on the first and second order central moments. In this case m_d and σ_d are the desired mean and standard deviation factors. The coefficient A is a gain factor which prevents overly large values when $\sigma(j,k)$ is small, and α is a proportionality factor controlling the edge enhancement. To apply this function, the processed image was divided into non-overlapping pixel blocks in which the block mean and standard deviation were computed. Bilinear interpolation of the four nearest block values was used to compute the mean and standard deviation at

each point. Along the image border, the mirror image of the blocks was used in the interpolation. The block size influenced the size of features that were enhanced. In the case of the zoomed images in which we viewed approximately two boundary layer thicknesses in 128 x 256 points, we utilized a block size of 16 x 16.

Ensemble Averaging. Since the images were conditioned on the detection of a "burst" event, the first processing that was performed was to ensemble average the images. In this case not only the average image was computed, but also the rms of the differences between the images. Regions of low rms signified features that were coherent between realizations. The same procedure had been done for the phase conditioned images of the visualized wake of a cylinder (Nagib et al., 1978). The mean and variance of N related digital images was formed in the usual way through the relations

$$\frac{1}{N}\sum_{n=1}^{N}\left[F_n(j,k) - M(j,k)\right]^2$$

and

$$\frac{1}{N}\sum_{n=1}^{N} F_n(j,k) = M(j,k)$$

where $F_n(j,k)$ is the pixel intensity at point (j,k) in realization n.

As indicated in Chapter IV, the detection method used to acquire the images was based on a high local variance and was not always a reliable indicator. In order to make the averages converge more quickly, we

included in the ensemble only those images which corresponded to an event detected by the more reliable match filtering technique applied to the hot-wire sensor outputs acquired at the same instant.

Two-dimensional Spatial Filtering. As in the case of the two-dimensional Fourier processing for the hot-wire rake signals, spacial filtering was employed in the processing of the digital images. Just as the individual hot-wires spatially sampled the velocity field in the boundary layer, the digital image is a two-dimensional spatial sampling of points of a physical image. In its application with smoke visualization, each sample point or pixel is a measure of the image intensity only. The pixel intensity is related in some non-linear fashion to the density or concentration of smoke particles which emanate from a line source and are convected downstream. In the boundary layer, the transport capability of the turbulence is represented (see Tennekes and Lumley, 1972) by the momentum flux $-\rho\overline{uv}$. In a turbulent boundary layer, the three-dimensional eddies maintain a good correlation between the u and v velocity fluctuations. Indeed, the largest uv correlation values are associated with the wall "burst" events (Lu and Willmarth, 1973). Since the transport of the smoke is related to the relative distribution and energy of the turbulent scales, we might expect that the

spacial distribution of smoke is an indication of these scales. Therefore, rather than looking at the relative intensities of the picture elements, we proposed to look at their relative groupings to infer information about the turbulence structures. This was be done using Fourier filtering techniques.

In the discretely sampled images, the sampling frequency is the spacing between pixels. In line with the sampling theorem, the smallest scales that could be spectorally resolved are two pixels on edge. In the case of the zoomed view, the images corresponing to two boundary layer thicknesses are made up of 256 x 128 pixels, so that scales as small as .02δ are resolvable. In these images, however, we were mainly interested in larger scales so that in order to speed the computations, the images were bilinearly interpolated to 64 x 128 pixels thereby cutting our resolution in half.

In the case of the ensemble averaged images, in order to remove the streaklines and enhance the large scales, the images were low-pass filtered. A number of 64 x 64 point two-dimensinal low-pass filters were designed from a set of one-dimensional filter impulse response functions which were symmetrically developed over a two-dimensional rectangular area. The design of the impulse response utilized the same computer program developed by McClellan and used in the two-dimensional velocity reconstructions.

The filtering was implemented by dividing the 64 x 128 images into two 64 x 64 blocks which were stored in MDP graphics memory. The area to the top and right of the 64 x 64 image blocks was zero filled in order that the circular convolution will be identical to the desired linear convolution. The 128 x 128 two-dimensional FFT was taken of the two image halves and stored in place in the display memory. The FFT subroutine was identical to that used in the velocity reconstruction so that the reader is directed to that section of Chapter IV for a detailed description. The filter function which was already transformed and stored, was convolved with the image halves by complex multiplying columns. The convolved parts replaced the originals and the inverse FFT was performed to return the images to the spatial domain. The two image halves were smoothly connected using the overlap-add method described in the previous chapter.

In order to increase the dynamic range of the image domain upon reconstruction, the generalized Cepstrum was formed. This is a method of nonlinear transform image enhancement which consists of taking the logarithm of each real transform coefficient. The imaginary part of the transform domain datus points were left untouched so as not to destroy the phase information. Qualitatively, this processing reduces the dynamic range within the transform domain and provides a stretching of the

resultant dynamic range in the reconstructed image.

The two-dimensional spectrum of the images was computed by taking the FFT of the 64 x 128 images and multiplying the Fourier coefficients by their complex conjugates. The real valued spectrum functions were normalized by their volume, ensemble arranged and plotted as two-dimensional level contours with positive and negative spatial frequencies. The volume under the spectra corresponded to the statistical variance of scales in the image and were saved for comparison.

Pattern Recognition

In order to search for structures in the visualized flowfield which were associated with the wall layer events and to obtain the frequency of these events from the images viewing 10 boundary layer thicknesses, two-dimensional match filtering was performed on these zoomed out records. The patterns used for the match were the ensemble averaged two-dimensional structure shapes obtained from the zoomed in images conditioned on the wall layer events. These two sizes of images were scaled properly to the same physical size by expanding the zoomed back views by padding each pixel with neighboring zero value points and low-pass filtering these images to reconstruct the intermediatel points. As in the one-dimensional pattern recognition described in the previous chapter, the two-dimensional application.

utilized a correlation match technique to determine if and where a match occurred.

The computational procedure consisted of transforming the 64 x 128 images into wave-number space as described in the previous section on spatial filtering. A 64 x 64 representation of the two-dimensional structures was similarly transformed. The imaginary part of the Fourier coefficients of the matching function was multiplied by -1 to form the complex conjugate and the columns were complex multiplied with those of the transformed image to form the transformed correlation function. An inverse transform was taken of the result to obtain the two-dimensional spatial correlation function. Any peaks in the distribution corresponded to location where a match occurred. The pattern recognized images were later ensemble averaged to obtain the average visual representation of the flowfield approaching the point where a wall layer event has been detected.

CHAPTER VI

PARAMETRIC INVESTIGATION OF MANIPULATORS

In the preliminary stages of this study we chose to move toward our objectives in a number of steps. The first of these was to verify that the outer intermittent structure of a turbulent boundary layer could be substantially removed. In this aspect we were concerned primarily with altering specific scales of turbulence in the boundary layer. Initially, we were not overly concerned with the device drag. However, minimizing the drag was part of the overall objective, so we chose a device which potentially could provide a minimum obstruction, when compared to the screens of Yajnik and Acharya (1977), various types of honeycombs or even perforated plates.

Early on it was recognized that the initial design should allow some flexibility based on a sufficient number of parameters so that one can to match the device to the turbulence scales of interest. This is important for trying to sort out the complex interaction between the inner and outer scales of turbulence in the boundary layer. We were also interested in how turbulence generation near the wall is influenced by the outer scales, or lack of them. Therefore, the device had to be capable of directly modifying, in a controlled way, a

narrow spectrum of scales. An arrangement of stacked parallel plates suspended above the wall of the boundary layer at different elevations satisfied these design criteria.

Four-Plate Manipulator: Preliminary Results

Our first attempt at removing the large-scale intermittent structures in a turbulent boundary layer was reported by Corke et al. (1980). The turbulence manipulator utilized in that study consisted of four plates, vertically stacked in a parallel arrangement and spanning the tunnel test section. All of the plates were 0.7 mm. thick and had a streamwise chord of 75 mm. This manipulator was designed to remove a wide range of the scales in the turbulent boundary layer. Therefore, the manipulator plates were spaced successively closer at lower y values. The dimensions of this device relative to the boundary layer thickness at the streamwise station where it was placed is shown in the top line of the table of Figure 22. Here the four-plate manipulator, being the first tested, is designated M-1.

The effects of placing M-1 in the turbulent boundary layer was recorded by photographs of the smoke-wire visualized flowfield and digitally acquired velocity profiles taken with a traversing hot-wire probe. The photographs revealed the lack of the large-scale intermittent structure and a redistributing of fine

scales of turbulence in the manipulated boundary layers. As will be described later in this chapter, these photographs will be used as a standard to judge the effectiveness of other simpler devices in removing large scale.

The velocity surveys of this study recorded an approximate 10 percent reduction in the value of u'/U_∞ below y+ = 100 when the M-1 device was introduced. The streamwise distribution of the friction coefficient, C_f, was determined from a momentum balance similar to that used in the current study. There were, however, several key differences between the computational procedures used in the preliminary study and those used in the present study.

As described in Chapter IV, the solution of the momentum equation required obtaining functional expressions for the streamwise distribution of $U_\infty(x)$ and $\delta_2(x)$. In the previous study, values of U_∞ were "fitted" with a second order polynomial. Its derivative was subsequently fit by a linear function which was necessary to "smooth" the values of dU/dx. The values of $\delta_2(x)$ in the preliminary work were fitted with a power-law equation as suggested from two-dimensional boundary layer analysis (Schlichting, 1968). The derivative of the power-law function, which is used in the momentum balance is ever decreasing for increasing streamwise distances. In the simplified case of a zero streamwise pressure

gradient, the momentum equation reduces to

$$U_\infty^2 \; A_o \; P \; x^{P-1} = \frac{\tau_w}{\rho} \; ; \; o < P < 1$$

so that the streamwise distribution of τ_w directly follows the power-law distribution which the data prescribe. In the case of the regular boundary layers the use of the power-law representation for the growth of the momentum thickness provided good agreement with the accepted friction coefficients at comparable Reynolds numbers, however, for the manipulated boundary layers the limitations of the power-law fit resulted in an erroneous shear distribution from the momentum balance calculation. The main reason for this error is the local influence of the manipulator which results in an initially higher momentum thickness. The resulting streamwise distribution is not well represented by a power-law function in this case.

In the present results, the functional representations of $U_\infty(x)$ and $\delta_2(x)$ were obtained by fitting the data with a cubic spline with weighting and damping. The formulation of the spline is given by Greville (1969). The spline approximates a continuous and differentiable function over an interval in a piecewise fashion using third order polynomials in non-overlapping subintervals formed by the data pairs. The spline function possesses continuous first and second

order derivatives over the full interval. In the limits of very high damping the cubic spline will "best fit" the data by a straight line. Contrasted with a standard least-squares fit, which fits the data to a prescribed function, the cubic spline formulation fits the function to the data. In its application here, the damping was adjusted to smooth the variations in the streamwise values of $U_\infty(x)$ and $\delta_2(x)$ and their derivatives. The smoothed values were then used in the momentum balance computation.

The results of this preliminary study gave visual evidence that the large intermittent turbulent scales in the boundary layer were removed by the four-plate manipulator. Near the wall ($y+ < 100$) the streamwise turbulence intensity was reduced by approximately 10 percent. However, as a result of the large momentum deficit produced by the device, no net reduction in the friction drag was observed. We therefore undertook a parametric study of a family of parallel-plate manipulators which could comparatively suppress the large scale while exhibiting a lower device drag.

Family of Parallel-Plate Manipulators

Having documented the effectiveness of a four-plate "turbulence manipulator" for removing the intermittent large-scale eddies in a turbulent boundary layer (albeit

with an excessive device drag) we documented, primarily through visualization records, the effects of a family of such devices that require a fewer number of plates to suppress the large scale to the same degree as that exhibited by M-1. This parametric investigation was aimed at developing a better understanding of the mechanisms by which the manipulators work and hence schemes for minimizing the device drag. This is an essential ingredient in the performance of such manipulators since our ultimate goal is to obtain net drag reduction for the turbulent boundary layers. The summary of results from this investigation is presented in the following. These experiments were performed prior to the extension of the wind-tunnel test section discussed in Chapter II.

Parametric Study. The manipulators utilized in this study were made up of one, two or four plates in parallel or series configurations as shown in Figure 23. In the single plate condition, plate angle of attack was also taken into consideration. The different parameters for each configuration, such as manipulator plate elevation in the boundary layer, streamwise spacing, plate chord length and angle of attack were adjusted to optimize the device effectiveness. This was done while observing the smoke-wire visualization in the boundary layer downstream of the manipulator. The relevent parameters were

systematically varied to obtain a flow which exhibited the least amount of large-scale turbulence. The final values obtained for this set of devices is tabulated in Figure 22. The flow conditions from these optimum configurations are recorded by smoke-wire visualization photographs and mean velocity and turbulence intensity profiles in Figures 24 through 28. It should be pointed out that for the sake of clarity, the scales of the photographic records and the velocity profiles in the combined figures are not the same. In these figures, the distance y on the velocity profiles is approximately three times the geometric scale of the photographs.

The results presented here represent the visually observed changes in the large-scale turbulent structure of the boundary layer, and the differences in some of the mean quantities of the flow caused by the addition of each of the manipulators. Except for the cases with parametric variation of angle of attack, these results are for the devices which have been optimized with respect to the downstream boundary layer conditions.

The results presented in Figures 24 through 26 demonstrate the effectiveness of each of the devices in controlling the intermittant large-scale turbulence. To aid as a reference, these figures include at the top, a typical realization of the visualized boundary layer before the addition of a manipulator. The right portion of these figures contains a schematic representation of

the different device types with manipulator plates shown at their relative heights with respect to the mean boundary layer profile. The boundary layer profiles shown are those obtained in the unmanipulated boundary layer at the two positions where the devices are installed and where the comparison is carried out downstream. The visualized flow resulting from these devices is presented in the opposite left part of these figures. It should be noted that the streamwise dimensions of the device in the schematics of these figures are not drawn to scale so as not to obscure the profiles.

In Figure 24, a comparison is made between manipulators having one, two or four vertically stacked plates. The four plate manipulator is the same device used in our early work. The boundary layer within which this family of devices was studied, however, had somewhat different characteristics from that previously used. Device M-1 was found to behave in an identical manner.

If we compare the results from the two-plated (M-3) and single-plate (M-2) devices, in Figure 24, with those of M-1, we observe that the introduction of a single plate has some effect on the large scale eddies. However, at least two plates are necessary to approach the effectiveness of M-1. As expected, we found that these plates should reside in the outer portion of the boundary layer, where the larger scales are being

convected.

In Figure 25 , the result of spacing two single plates in the streamwise direction is presented. In this case, a quite comparable reduction of the intermittant eddies, as with M-1, is observed. This configuration is quite appealing since the drag on the downstream plate is reduced by being in the wake of its upstream partner. Also, in terms of studying the effects of the lack of the large-scales on turbulence production and the so called "bursting" phenomenon, the placement of this device high in the boundary layer limits any direct influence of their wakes on the flow near the wall.

Figure 26 demonstrates the effect of the angle of attack of a single plate on the intermittant large-scale. Depending on the sign of the angle used, the plate generates a wake dominated by eddies which rotate in the same sense (negative angle of attack) or opposite sense of direction to the large structures in the boundary layer. In the former case this tends to augment the large scales, instead of suppressing them. Another mechanism of large scale suppression is similar to that active in honeycombs and documented in earlier studies at IIT (Loehrke and Nagib, 1976); i.e., the inviscid inhibition of the transverse velocity fluctuations by the solid boundaries.

As was demonstrated with manipulator M-1, a measured reduction in the streamwise turbulence intensity in the

boundary layer is found below y+ = 100. In Figure 27, the turbulence intensity profiles for devices M-1, -3 and -4 exhibit the same characteristic reduction in that quantity near the wall. Also included in this figure are the mean velocity profiles for the same cases. The velocity defects in the profiles with the devices give an indication of the device drag when compared to the profile of the unmanipulated boundary layer. Both manipulators with only two plates, either in parallel or in series, result in less device drag compared to the case of M-1.

In order to extend our measurements to farther downstream distances from the manipulator in the same fetch of wind tunnel test section, we generated a turbulent boundary layer approximately one-third as thick as that used in previous cases. Using a properly scaled two-plate manipulator of the M-2 design, we observed the flow to approximately 70 boundary layer thicknesses downstream of the device. The result of that experiment are summarized in Figure 28. As far as we can judge with the visualization and the u' profiles, the effectiveness of the manipulator seems to persist for the entire downstream fetch.

As a result of this simple parametric study of various flat-plate manipulator configurations, we have verified that an optimum exists for the placement of single or multiple plates in parallel or series

arrangements. The optimum is based on minimum device drag for the comparable effectiveness in suppressing the large-scale turbulent structures in the boundary layer. The results suggest that two plates spaced in the streamwise direction, i.e., in tandem, give a reduction in large-scale intermittant eddies in a turbulent boundary layer which is comparable to a stacked, four-plate manipulator with a much less cost in device drag. With the newly extended wind-tunnel test section, we utilized these conclusions to establish the degree of net drag reduction that may be achieved by such passive devices in turbulent boundary layers as well as documented some changes in the mechanisms of turbulence production in the wall region.

CHAPTER VII

MEAN CHARACTERISTICS OF TURBULENT BOUNDARY LAYERS

In order to demonstrate the changes which occurred in the boundary layers as a result of the suppression of the intermittent outer scales, the time-mean and unsteady characteristics of the naturally developed turbulent boundary layers, into which the manipulator was placed, were first documented. These measurements not only serve for comparison to the manipulated boundary layers, but also act as a bench mark for comparisons to the classical literature and as a reference for the reader to judge the quality of the present measurements.

This chapter depicts the mean and turbulent velocity distributions of these boundary layers for the range of momentum thickness Reynolds numbers from 2000 to 5500. This range was achieved by operating at two different free-stream speeds of 6.7 and 10.4 m/s. The "burst" conditioned measurements for these layers will be presented in Chapter IX where a more direct comparison with the "manipulated" boundary layers is made. For the figures to be referenced in the following chapters, we used a Cartesian coordinate system that has its origin at the leading edge of the boundary layer plate on the center plane of the test section. The x, y and z axis are in the streamwise, vertical and transverse directions, respectively. The data were taken at 10 streamwise, x,

stations along the plate centerline (z equals zero) as depicted in the schematic of Figure 3. The figures in this chapter will typically show data from alternating stations for clarity purposes, although the processed data exists for all of the measurement locations. Furthermore, all of the digitized raw data time series as well as the processed results are stored on digital magnetic tape to be used for any further processing.

The non-dimensionalized mean velocity and turbulence intensity profiles for the boundary layers at different streamwise stations for the two free-stream speeds is shown in Figures 29-32. The vertical, y, distribution of the mean velocity in Figures 29 and 30 is non-dimensionalized with the local free-stream velocity, U_e, and the momentum thickness δ_2. We chose the outer variable δ_2 to non-dimensionalize the vertical distance rather than the boundary layer thickness, δ, because the former is an easily determined physical characteristic of the flow unlike the somewhat vague definition for the boundary layer thickness. Whenever possible, non-dimensionalization with outer variables will be in terms of the momentum thickness. Exceptions will be those cases where comparisons are made to the results of other investigators which involve the boundary layer thickness as a parameter. For the readers reference, the ratio of the boundary layer thickness to momentum thickness is approximately 10. The rms of the

fluctuating velocity distribution for the boundary layers, presented in Figures 31 and 32, is non-dimensionalized with the local wall-friction velocity u_τ . The values for u_τ were determined from the momentum balance and will be discussed later in this chapter. The friction velocity was chosen to non-dimensionalize the fluctuating streamwise velocity distributions because it provided a collapse for the full vertical extent of the boundary layer. Non-dimensionalizing this quantity with the outer free-stream velocity would only provide a collapse of the downstream development of the fluctuating velocity at the outer portion of the vertical distribution. This was expected since the turbulence stresses are linked to the production at the wall and proportional to the friction velocity u_τ.

Utilizing these non-dimensional forms, the streamwise development of the mean velocity and turbulence intensity for the two ranges of Reynolds numbers show a high degree of collapse that demonstrates their self-similar behavior. Included for reference in Figures 31 and 32 is the turbulence intensity distribution taken from the results of Klebanoff (1954) for a Reynolds number of 7500. Comparing the turbulence distributions in these two figures we observe that the higher Reynolds number flow case results in a slightly greater distribution of turbulent stress fluctuations away from the wall and thereby a better comparison to the

higher Reynolds number flow case of Klebanoff (1954).

The values for the wall-shear velocity used in the previous figures were obtained by a balance of the momentum flux along the boundary plate. As a result of the extremely mild streamwise pressure gradient, which is shown in non-dimensional form in Figure 33, the functional form for the momentum balance included the streamwise rate of change of the total pressure. The pressure gradient is mainly a result of the pressure field generated by the perforated plate at the end of the test section which maintained the slightly higher pressure on the measurement side of the plate and ensured parallel flow at the leading edge. In this respect the perforated plate acted like the flap often used to control the circulation on test boundary layer plates. The reduced streamwise growth exhibited in the manipulated boundary layers had no measurable effect on the streamwise pressure gradient for the two operating free-stream velocities. The consistent agreement and calculation approach allowed us to maintain comparable accuracy in using the momentum balance for the determination of skin friction in regular and manipulated boundary layers.

In order to test the software program for calculating the values of wall-shear stress from the momentum balance, the data of Wieghardt (1944), as presented by Coles and Hirst (1968), were utilized. Since in the latter reference a number of the parameters

for this data were calculated, including the wall-shear stress, this offered a good comparison of the results from different computational techniques. In particular, for the determination of the friction velocity, the values obtained from the empirical log-relation and the Ludwig-Tillmann relation were compared with the results from the momentum balance. The number of profiles and their streamwise spacing was chosen from the Wieghardt data so as to be representative of the two parameters in this study. In the momentum balance the damping of the spline fits to the distributions of dU_e/dx and $d\delta_2/dx$ were adjusted to obtain the "best" correlation of friction coefficient values with those provided by Coles and Hirst (1968). The point of best agreement was also found to coincide with the best collapse of the mean velocity profile values in the log-linear region. Varying the spline dampings also provided us with a measure for the dependence of the results on these parameters.

The results for the calculation of the friction coefficients for Wieghardt's data (1944) are shown in Figure 34. The distribution of the friction coefficient values for the range of Reynolds numbers in this figure show a good collapse of the results from the Ludwieg-Tillmann relation and the momentum calculation. Below a Reynolds number of 6000 the comparison is not as satisfactory. However less emphasis was placed on results from the the fit of the log portion of the

profile because the small number of data values taken in that region (typically 2 to 3) added to the uncertainty of the fit. Furthermore, since the data of Wieghardt (1944) was used in part to obtain the Ludwieg-Tillman form for the friction velocity, the degree of agreement between their relation and the momentum balance was taken as a more satisfactory indication of the performance of the program. In addition to the friction velocity, the integral properties of the boundary layer of Wieghardt were compared to the results published by Coles and Hirst (1968) and found to be in close agreement.

After satisfactorily exercising the momentum calculation with the Wieghardt data (1944), the profile data from the present experiment were analyzed. The results for the distribution of the local friction coefficient versus Reynolds number are presented in Figure 35. The values for C_f presented in this figure were obtained in three manners: a least squares curve fit of the log portion of the profile from y+ equal to 50 to 200, the Ludwieg-Tillmann relation, and the solution of the momentum equation. Also shown on this figure the corresponding distribution from Wieghardt's (1944) data over a comparable Reynolds number range. The data is presented with individual symbols corresponding to each of the 10 streamwise stations for the two ranges of Reynolds numbers.

An important feature of the data is that three of

the stations have overlapping Reynolds number values based on the momentum thickness. In the lower free-stream velocity, this corresponds to stations at the downstream end of the plate and in the higher free-stream velocity case to points at the upstream end. Any property of the flow which exhibits only a Reynolds number dependence should present a smooth distribution through this overlapping range In the C_f distribution of Figure 35, all three methods gave values within 5 percent of a mean distribution drawn through the points. As a result of the scatter of points in this figure that average was chosen to represent the results.

The values of the friction velocity taken the results in Figure 35 were used in the non-dimensionalization with inner variables of the mean velocity distributions presented in Figures 36 and 37 for the two Reynolds number ranges. Drawn for comparison in these figures is the log-law relation using the coefficient values suggested by Coles (1963). In both figures, the collapse of the data in the log region, $50 \leq y^+ \leq 200$, is quite good. It should be pointed out that in this approach we have determined the value of the von Karman constant and the log-linear intercept constant from the momentum balance. This in contrast to the often used approach of determining the skin friction velocity from these two constants, i.e., by a fit of the log-linear profile. This result is significant in that it

substantiates our application of a careful momentum balance for determining the wall shear stress. The agreement with the law-of-the-wall relation is, however, not very satisfactory in these figures. The lack of similarity in this range is most likely a result of the accuracy of positioning the traversing probe in the thin sublayers of these boundary layer flows in air.

The wall-unit non-dimensionalization of the fluctuating velocity distributions is shown in Figures 38 and 39 for the two ranges of Reynolds numbers. As indicated by these figures the approximate similarity in wall units of the rms values of the streamwise velocity fluctuations is maintained only out to an y+ equal to 15. A similar trend with Reynolds number was presented by Purtell, Klebanoff and Buckley (1981). They suggest that the decrease in the u'/u_τ values at lower Reynolds numbers is a result of the suppression of all but the largest scales of turbulence. The maximum in the distribution occurs at y+ values between 15 and 20. It was at y+ of 15 that Blackwelder and Kaplan (1976) observed the largest effect on their "burst" conditioned averages. This region of the flow field has been pinpointed by Corino and Brodkey (1969) as the site for the ejection of low-speed fluid near the wall during a "burst" event, and as contributing as much as 60 percent of the total $\overline{uv}$ Reynolds stress (Willmarth and Lu, 1972) in the boundary layer.

We focus on the wake portion of the boundary layer profile in Figures 40 and 41. In this figure the wake component

$$W(y/\delta) = \frac{k}{\Pi} \quad u^+ - (\frac{1}{k} \log y^+ + B)$$

is plotted versus the non-dimensional boundary thickness y/δ. The respective values of k and B of 0.41 and 5.0 presented in the log distributions of Figures 36 and 37, were used in this formulation. For reference purposes wake distribution suggested by Coles (1956) is included in these figures. At the lower Reynolds number range the agreement with Coles' wake distribution is very satisfactory. At higher Reynolds numbers in Figure 41, the agreement is not as good below half the boundary layer thickness. Close inspection of the wake function, $w(y/\delta)$, reveals that it is not entirely antisymmetric with respect to $y/\delta = 0.5$. Actually we expect (see Hinze, 1975), deviations from the $\sin^2$ distribution at the top and bottom of the profiles. In the representation of Figures 40 and 41, the deviation from the antisymmetric distribution appears to display some Reynolds number dependence.

Normalized one-dimensional spectra of the streamwise velocity component at different self-similar heights along alternating measurement stations is shown in Figures 42 to 47 for both Reynolds number ranges. The power spectral energy in these distributions is

non-dimensionalized by the area under them which is equal to the variance of the instantaneous velocity fluctuations. The frequency axis is normalized by the local mean velocity at each respective height in the boundary layer to obtain the wave number, k. Also included in these figures for reference purposes are the lines with slopes of -1 and -5/3 corresponding to the viscous-convective and inertial subranges, respectively, for one-dimensinal velocity spectra. The spectral distributions exist for the non-dimensional heights between those shown on these figures but were omitted for clarity purposes. However, they did reinforce the trends exhibited in these figures.

At any of the streamwise stations, the changes in the energy spectrum with non-dimensional height reveals that the contribution to the turbulence energy in the low-wave-number range, which is made up by larger eddies, decreases as the wall is approached. However the spectra indicate that the large scale, low-wave-number energy decreases only slightly down to y+ equal to 30, thereby indicating the influence of the large eddy structure very near to the wall. In a compatible way, as the wall is approached, the contribution to the turbulence energy in the high-wave-number range is increased.

In the outer part of the boundary layer, y+ greater than 200, the -5/3 law is followed rather closely over a discernable wave-number range. In the case for the

lowest Reynolds number in Figure 42 the wave-number range having a -5/3 distribution correspondance extends from approximately k equal to 50 to 200 m^{-1}. With increasing Reynolds number we observe a growth in the extent of the inertial subrange to encompass a wave number range between 5 and 200 m^{-1}. Nearer to the wall, y+ less than 200, the spectrum shows a range where E(k) varies nearly according to k^{-1}, indicating a strong interaction between the mean and turbulent flow. It is at these heights in the boundary layer where we also have strong production of turbulent energy. Comparing the extent of the viscous-convective subrange in these spectra indicates no discernable Reynolds number dependence.

The vertical distribution of the integral length scale at alternating streamwise stations for the range of Reynolds numbers is shown in Figures 48 and 49. The length scales were determined by multiplying the integral time scales, obtained from the one-dimensional autocorrelations, by the local mean velocity at each respective streamwise location and height in the boundary layer. That is, obtaining these from a local application of Taylor's hypothesis. In Figures 48 and 49 the integral scales and vertical y positions are non-dimensionalized with the outer characteristic length, δ_2. These distributions show that the maximum length scales occur at a height approximately 20 percent of the

boundary layer thickness. This suggests the presence of turbulence structures which are elongated in the streamwise direction and which reside fairly near the wall. This interpretation is consistent with the space-time correlation measurements of Grant (1958) and Blackwelder (1970). Near the wall, the streamwise extent of the turbulence structures is observed to lengthen with increasing Reynolds numbers.

The integral length scales are not observed to behave in a self-similar manner with Reynolds number when non-dimensionalized with outer variables as in Figures 48 and 49. To evaluate the growth with Reynolds number of the scales at different self similar heights in the boundary layers, the data are presented in the manner of Figure 50. In this figure the integral length scales, which were non-dimensionalized with the momentum thickness, are plotted versus Reynolds number along constant y+ lines. The actual data were "best fit" by a linear distribution and for clarity purposes only these lines are presented on the figure to show the trends. The typical correlation for the fit was approximately .6 - .7, where 1.0 represents a perfectly correlated numerical fit of the function to the data. The data as presented in Figure 50 can be interpreted as the streamwise growth of the average scales along self similar paths in the boundary layer.

With increasing Reynolds number, near the wall below

y+ equal to 30, the turbulent scales are observed to decrease with streamwise position. Between y+ values of 50 to 200 the scales are not growing appreciably with increasing Reynolds number. This corresponds to the log-region in the mean velocity distribution. At y+ equal to 400 we see a rapid growth of the streamwise scales with Reynolds number. This most likely reflects the growth of the constant stress layer. At higher elevations, y+ = 800, there is a continued growth of the streamwise scale although at a less rapid rate than in the initial wake region of the mean profile.

To summarize this chapter, these boundary layers, developed over two ranges of Reynolds numbers, exhibit mean and turbulent characteristics which are comparable to similar flows reported in the literature. The streamwise development of these quantities also demonstrates the desired self-similar behavior. Importantly, they display a full spectrum of turbulent scales which follow the expected wave number distributions. Other statistical quantities providing further documentation of these turbulent boundary layers will be presented in Chapter VIII where they will be directly compared to the results from the manipulateld boundary layers.

CHAPTER VIII

MEAN CHARACTERISTICS OF MANIPULATED BOUNDARY LAYERS

The time-mean velocity measurements in the manipulated boundary layers are presented in this chapter so as to document the effects of suppressing the intermittent outer structures on the mean characteristics of the flow. This chapter depicts their mean and turbulent velocity distributions for the range of momentum thickness Reynolds numbers from 2400 to 4900 corresponding to the two free-stream speeds of 6.7 and 10.4 m/s. In addition to the Cartesian coordinate system utilized in the results presented in Chapter VII, additional laboratory coordinates, which are related to the position of the manipulator, are introduced in this chapter. The coordinate length x_0 is the streamwise distance between the manipulator and the leading edge of the boundary-layer plate and ξ denotes the downstream distance of a measurement station from the trailing edge of the manipulator. The data were taken at nine streamwise, x, stations along the plate centerline, z equals zero. This is in contrast to the data runs without the manipulator in which measurements were recorded at 10 streamwise locations. For the results in the boundary layer with the turbulence manipulator, the first measurement station falls between stations 2 and 3 of the data runs without the device. In the manipulated

layers data station 2 corresponds to station 3 of the other case and the remaining streamwise stations correspond to their N + 1 equivalents. As in the previous chapter, the data will typically be presented at alternating stations although the processed data exist for all of the measurement locations.

The turbulence manipulator utilized in this final set of measurements was oriented in the series arrangement, M-4 of Figure 23, and optimized for the boundary layer characteristics depicted in Chapter VII. As described in Chapter VI, the optimization involved varying the different parameters to obtain the maximum suppression of the intermittent outer scales in the boundary layer. The degree of large-scale removal was judged visually with the aid of the smoke-wire technique. In this final set of results, the manipulator was placed at the streamwise distance, x_0=2.25 m., corresponding to the x-location of measurement station 1 in the regular boundary layer case. The manipulator plates were made from 0.2 mm. thick brass shim stock and each was placed at a height from the wall of 80 percent of the boundary thickness in the regular boundary layer at station 1. The streamwise chord length was equal to their distance from the wall which was 0.8. The streamwise spacing of the manipulator plates was 8 at that location. The arrangement of the manipulator plates is represented in the schematic of Figure 3 and shown in the photograph of

Figure 4.

The boundary layer characteristics, visualized using the smoke-wire, before and after use of this series manipulator are shown in the photographs in Figure 51. The top two photographs correspond to the regular boundary layer and the bottom two correspond to the boundary layer with the final series manipulator. The free-stream velocity at which these photographs were taken corresponds to the low Reynolds number range with Re_{δ_2} ranging from approximately 2800 to 3700 over their streamwise extent. Although these photographs represent one instant in the turbulent flowfields, their overall characteristics are representative of features of the boundary layer with and without the manipulator. Quantitative analysis of digitized image records of the visualized flow for the two types of boundary layers will be presented in Chapter IX. The photographs in Figure 51 allow comparison to the visualized flows presented in Chapter VI, which were obtained in a boundary layer with different characteristics than that utilized in this final set of results. The photographs of Figure 51, as well as those discussed in Chapter VI indicate that if the large scales are being reformed downstream of the manipulator, their return process is extremely slow. In Figure 51 no strong evidence of their rebirth is found as far as far as more than 40 boundary layer thicknesses downstream.

Qualitative examination of the photographs in Figure 51 clearly reveals the suppression of the larger outer bulges in the turbulent/non-turbulent interface with the addition of the series manipulator. Close inspection of the top two photographs in this figure and other related photographs reveals regions of potential flow, visible as intact streaklines, extending well into the bulk of the boundary layer and marking the intermittent non-turbulent portions of the flow. This mechanism is clearly inhibited by the removal of the outer scales as evidenced in the bottom two photographs. As will be demonstrated later in this chapter, this effect reduces the entrainment of irrotational fluid into the boundary layer.

The non-dimensionalized streamwise mean velocity distributions over a range of momentum thickness Reynolds numbers from 2400 to 4900 are presented for the manipulated layers in Figures 52 and 53. For comparison, a line corresponding to the non-dimensionalized velocity distributions of the boundary layer without the manipulator is also included in these figures. Also, the manipulator height, normalized with the characteristic length of the boundary layer at the first streamwise station, is shown for reference in the figures.

The wake of the manipulator plates is evident in the profiles approximately 36 momentum thicknesses downstream of the device in Figures 52 and 53. At the next

downstream station, ξ/δ_2 approximately equal to 136, the turbulent velocity fluctuations have smeared out the mean wake profile of the device.

In the lower 50 percent of the mean profile taken closest to the device, the non-dimensional distribution looks like that for the regular boundary layer. In the outer part of the distribution, $y/\delta_2 > 6$, the lack of the larger scale is immediately evident by 36 momentum thicknesses downstream, as indicated by the higher velocities at the edge of the layer with the device. The lack of the large scales is felt in the lower 50 percent of the boundary layer by 136 momentum thicknesses downstream where we observe a self-similar distribution having lower mean velocities than in the regular boundary layer.

The distribution of the rms of the streamwise component of the velocity fluctuation, non-dimensionalized with the friction velocity u_τ, is shown in Figures 54 and 55 for the manipulated layers. The streamwise distribution for u_τ was obtained from the momentum balance in the manner described in the previous chapter. That distribution will be presented later in this chapter. Included in these figures is the distribution taken from Klebanoff (1954) which was shown, in Figures 31 and 32, to represent quite well the fluctuating velocity profiles in the regular boundary layer. Clearly, the streamwise turbulence fluctuations do not

display the self similar behavior exhibited by the regular boundary layer. Nearer to the device, up to 136 momentum thicknesses downstream, we observe a reduction in the streamwise velocity fluctuations except in the vicinity of the wake where higher fluctuations, suggestive of a vortex street, result in locally higher rms values. Further downstream, higher turbulent stresses are observed to be filling the boundary layer up to approximately 60 percent of its thickness. This redistribution of turbulence stresses away from the wall is reminiscent of the Reynolds number dependence observed in the low Reynolds number range of the regular boundary layer. In that case, the distributions in Figure 31 demonstrated lower u'/u_τ values in the constant stress layer portion of the profile when compared to the higher Reynolds number case of Klebanoff (1954). Near the floor, at the edge of the sublayer, the maximum values are approximately 16 percent higher in the manipulated boundary layer than in the regular boundary layer. The maximum u'/U_∞ values in the manipulated boundary layers are, however, reduced as presented in the preliminary work on these manipulated boundary layers by Corke et al. (1980). This is also demonstrated in the results from a parallel study which is presented in Appendix B of this manuscript.

A comparison of the streamwise growth of the integral thicknesses, δ_1, δ_2 and δ_3 between the regular

and manipulated boundary layers for both Reynolds number ranges is presented in Figures 56 and 57. Included for the momentum thickness distribution, $\delta_2(x)$, are the lines corresponding to the spline function fit used in the momentum calculation for the friction velocity, u_τ. The figures demonstrate an initial thickening of the boundary layer with the manipulator. However, the streamwise rate of change of those quantities is less than in the regular boundary layer case. After approximately 250 momentum thicknesses, based on δ_2 at station 1 which corresponds to the leading edge of the manipulator, the momentum and energy thickness distributions cross their counterparts in the regular boundary layer. The displacement thickness requires somewhat farther distance for the distributions to cross.

The ratio values of the integral lengths are shown in Figures 58 and 59. In Figure 59, the ratio of the displacement to momentum thicknesses, is presented for a range of momentum thickness Reynolds numbers in the regular and manipulated boundary layers. As demonstrated by Purtell et al. (1981), the shape factor for the regular boundary layer is solely dependent on Reynolds number, Re_{δ_2}. This, however, is not the case for the boundary layer with the manipulator. As evidenced by the δ_1 distributions in Figures 56 and 57, the displacement thickness is disproportionately larger than the momentum thickness in the manipulated layers.

This is opposite to the effect of adding large surface roughness which results in a reduction in the displacement thickness (see Hinze, 1980, Figures 7-15). As will be further supported in the following parts of this chapter, this has led us to conceptualize these manipulated layers as boundary layers with "negative" roughness.

The ratio of the energy thickness to momentum thickness, δ_3/δ_2, is plotted versus the shape factor in Figure 59. Included are the data from Wieghardt with the integral values given by Coles and Hirst (1968) and obtained from the present computational scheme. Also included in Figure 59 are the lines corresponding to the analytic expression relating H_{32} with H_{12} and given by Wieghardt and Tillmann (1941)

$$H_{32} = C_1 H_{12}/(H_{12} - C_2)$$

which was obtained from the velocity law $U/U_\infty = (y/\delta)^{1/n}$. These distributions are presented for the constants given by Wieghardt and Tillmann (1941), which they had adjusted to give agreement to their data, as well as constants obtained by a "best fit" of the relation to Wieghardt's as well as the present data. The shape factors clearly follow a unique relationship of the form obtained from the analysis, including the manipulated boundary layers. However, over this range of values, new constants were necessary to best represent the present data as well as

Wieghardt's data which was, in part, the basis for the Wieghardt-Tillmann (1941) constants.

The Reynolds number distribution of the wall friction coefficients, C_f, for the manipulated boundary layers is shown in Figure 60. The line in the figure designates the corresponding distribution for the regular boundary layer. The open symbols in the figure indicate the values obtained from the momentum balance and the half-open symbols indicate the values of C_f obtained from the log-linear and Ludwig-Tillmann relations. In the latter two cases, the same coefficients as those presented for the analysis of the regular boundary layer, were used to calculate the streamwise distribution of the wall-shear stress.

It is clear from Figure 60 that the shear stress distributions obtained from the analytic expressions are not valid since neither demonstrates the necessary smooth Reynolds number dependence. This behavior was, however, anticipated and prompted the use of the momentum calculation to determine the wall shear stress. As was stated earlier, there is no reason to expect that either of the methods used in Figure 60 other than the momentum balance work in the manipulated layer. They have been included here only for purpose of comparison and illustrations. In the manipulated case, the last point from the low Reynolds number range is the furthest streamwise station from the manipulator while its

neighboring datum point corresponds to the streamwise station closest to the manipulator in the high free-stream velocity experiment.

Comparing the local $C_f(x)$ distributions between the regular and manipulated boundary layers in Figure 60 we observe an approximate 30 percent reduction in the local drag on the wall as a result of the suppression of the large intermittent outer scales. This reduction in drag is evident in the momentum thickness growth which was shown in Figures 56 and 57. Here we observed a decrease in the rate of change of $\delta_2(x)$ which, in absence of a pressure gradient, is proportional to the local values. That decrease in the slope is approximately 30 percent, which compares well to the reduction in the magnitudes of u_τ obtained from the momentum balance which had included the contribution of the extremely mild pressure gradient.

The net reduction in the drag must include the device drag of the manipulator. This can be obtained by calculating the net loss of momentum which, because of our near zero pressure gradient, is

$$\text{Percent Reduction} = \frac{(\delta_{2,9})_M - (\delta_{2,10})_R}{(\delta_{2,10} - \delta_{2,1})_R}$$

By this definition, we obtain a net reduction in the wall drag of 21 percent. The $\delta_2(x)$ distributions, however, are still diverging at the last streamwise station so

that greater net reductions may be achievable at larger x dimensions.

The values of $u_\tau(x)$ were obtained from the momentum calculation and used in the non-dimensionalization with inner variables of the mean velocity profiles which are shown in Figures 61 and 62 for both Reynolds number ranges in the manipulated boundary layers. It is evident from these figures that a log-linear region exists in these profiles. However, the coefficients of the analytic expression have changed. Drawn for comparison is the solid line in the figure which corresponds to the log-linear relation with the coefficients, $1/K = 2.44$ and $B = 5.0$, which were given by Coles (1968) and found to represent the boundary layer profiles without the manipulator. The dashed line is the "best fit" of the log-linear relation to the data over the range $50 \leq y^+ \leq 200$. This fit yields the coefficient values,

$$1/k = 2.87$$

$$B = 6.53 \text{ and } 7.56$$

over the range of Reynolds numbers for the manipulated layers.

If we draw on the analogy of the increasing wall roughness which results in a downward shift in the log linear distribution corresponding to a reduction in the value of the coefficient B, the boundary layers without the large outer scales emulate the qualities of a hypothetical "negative" roughness flow. Rotta (1950)

connected the value of B with the thickness of the viscous sublayer for large values of $u_\tau y/\nu$ to obtain the form

$$B = \frac{1}{k} (\log 4k - 1) + \frac{u_\tau \delta_\ell}{\upsilon}$$

where δ_ℓ is the sublayer thickness. Therefore, an increase in the value of B can be associated with a thickening of the sublayer. Using the values for k, B and u_τ for the regular and manipulated boundary layers the sublayer thickness is estimated to have increased by approximately 17 percent in the manipulated boundary layers. The value of y+ corresponding to δ_ℓ is 6.6.

The thickening of the sublayer has also been observed in boundary layer flows with drag reducing polymers (Donohue et al., 1972; Achia and Thompson, 1977; Hanratty et al., 1977). The mechanisms, however, are clearly different since the drag reducing polymers work by inhibiting momentum transport through viscoelastic action near the wall.

To account for the change in the value of the von-Karman constant in the manipulated boundary layers we consider the Reynolds number dependence of that quantity which was examined by Tennekes (1968) in turbulent pipe flow. In that reference, Tennekes obtains a second-order friction law and a Reynolds number dependent correction to the "universal" slope of the logarithmic velocity profile. This correction takes the form

$$1/K = 2.95 - 4.4\ Re_{*}^{-1/3}$$

If we take R_* to be $\delta u_\tau/\upsilon$ we obtain values of 1/K of 2.55 and 2.87 for the middle ranges of Reynolds numbers in the regular and manipulated boundary layers respectively. Although this theory has generally been unaccepted by others (see Yaglom, 1979) it predicts the observed change in the value for k in this case with surprising accuracy.

It is important to realize that the log-linear portion of the velocity profile and its coefficients were verified and presented in all cases with values of taken from a momentum balance. Therefore, no a priori bias was applied to the results except that momentum must be conserved. Thus the logarithmic region was found to exist in the boundary layers both with and in the absence of large outer turbulent structures. Based on the persistence of the logarithmic region down to momentum thickness Reynolds numbers of at least 465, where the larger scales of the turbulent fluctuations become increasingly dominant, Purtell, Klebanoff and Buckley (1981) suggest some form of Reynolds number independence of the large-scale structures. The results of the present investigation do not appear to support this conclusion since the manipulated boundary layers lack these large intermittent scales. Another explanation is that the large scales are a result of the transition process to turbulent flow and are actually composed of other smaller scales such as inclined hairpin eddies

(Klebanoff, 1962) which are generated through a wall instability process and which are sustained even in the fully turbulent flow. The logarithmic region would reflect the character of these eddies and, because they are related to a wall instability, would display some Reynolds number dependence. Further evidence toward this concept will be presented in results to follow.

The wall-unit non-dimensionalization of the fluctuating velocity distributions for the manipulated boundary layers is shown in Figures 63 and 64. Comparing these figures to the distributions for the regular boundary layer in Figures 38 and 39 indicates that the peak in the fluctuations in the streamwise velocity is at a lower wall unit in the manipulated layers. In the outer part of the profile there also appears to be a much sharper cutoff of the streamwise fluctuations near the edge of the boundary layer in Figures 63 and 64. The wake function for these manipulated layers is presented in Figures 65 and 66. For this case, the "best fit" values of k and B taken from log-linear distributions in Figures 61 and 62 were used in the determination of W. Included in these figures is the $\sin^2$ distribution suggested by Coles (1960). Although the wake strength, Π, was determined by prescribing that $W(y/\delta)=2$ at $y=\delta$, the peak in those values is observed to occur at y/δ approximately equal to 0.8. This would indicate that the

wake in the manipulated boundary layers is associated with structures which scale with an intermediate length smaller than the boundary layer thickness.

The Reynolds number dependence of the wake strength parameter, Π, is shown in Figure 67 for regular and manipulated boundary layers. Besides the dependence on Re_{δ_2} displayed in the figure, it is also a function of the streamwise pressure gradient. It was proposed by Coles (1968) that the strength of the wake component is Πu_τ, and that it might be an indicator of the local rate of production of large-scale turbulent energy. This quantity, non-dimensionalized with the free-stream velocity, is plotted versus momentum thickness Reynolds number in Figure 68. In this figure we observe a reduction in this quantity in the manipulated boundary layers. There is, however, a discontinuity in the distribution between the two Reynolds number ranges in the manipulated case indicating a dependence on the initial conditions imposed by the device on the flow.

Another indication of the strength of the large outer scales is to consider the velocity of entrained fluid into the boundary layer. In a self-preserving boundary layer, the velocity of propogation of turbulent fluid into the free-stream, namely the entrainment velocity, Vp, is

$$V_p = \frac{d}{dx} U(\delta-\delta_1)$$

which was shown by Bradshaw in his 1967 paper. It was

also found empirically by Bradshaw et al. (1967), that the quantity, Vp/U_∞ is very nearly proportional to $\tau_{max}/\rho U^2$ both in equilibrium and non-equilibrium boundary layers. In that reference, they also imply that the ratio of the large-eddy velocity fluctuation to the small-scale velocity fluctuations in the central part of the boundary layer is proportional to $(\tau_{max}/\rho U^2)^{\frac{1}{2}}$. Furthermore, the ratio of advection or diffusion to production in the outer part of the layer is shown to be proportional to $\delta V_p^2/\tau$ and thereby proportional, by the previous form, to $\tau_{max}/\rho U^2$.

In Figure 69, the ratio, V_p/U_∞ is plotted versus Re_{θ_2} for the regular and manipulated boundary layers. The top most dashed line represents the distribution of the friction coefficient, $C_f = \tau/\frac{1}{2}\rho U^2$, for the regular boundary layer. This distribution was fit to the data to obtain the proportionality constant between the entrainment velocity and the non-dimensional shear at the wall. In this figure

$$\frac{V_p}{U_\infty} \times 10^2 = 0.86\ (C_f \times 10^3) - 1.3$$

is found to provide a smooth distribution through the data values.

In the manipulated boundary layers, the suppression of the large outer scales results in lower proportional entrainment velocities. The solid line in this figure corresponds to the C_f distribution for the manipulated layers when scaled with the same proportionality constant

as in the regular layers. In this case the line does not represent a best fit to the V_p/U_∞ values indicating the proportionality constant is not exactly the same for both cases. In the case of the manipulated boundary layer, the relation

$$\frac{V_p}{U_\infty} \times 10^2 = 1.16\ (C_f \times 10^3) - 1.6$$

best represents the data values. The average V_p/U_∞ difference between the latter distribution and that obtained using the coefficient values for the regular boundary layer is approximnately 20 percent. The average reduction in the entrainment velocity in the manipulated boundary layers is observed to be approximately 40 percent.

The results of Figure 69 show some interesting trends. The first of these is that the entrainment velocity is becoming smaller with increasing Reynolds number. This would indicate that the strength of the large-outer scale turbulence structures is decreasing with increasing Re_{δ_2}. The ratio of diffusion to production in the outer part of the layer is decreasing like $\tau/\rho U_\infty^2 = 2C_f$ in the figure. This is a result of the decrease in the ratio of the large-eddy velocity fluctuations to the small-scale velocity fluctuations proportional to $(2C_f)^{\frac{1}{2}}$. Thus the outer part of the boundary layer is filling with smaller scale turbulence at higher Reynbolds numbers that are more quickly

dissipated by viscosity. By removing the large outer scales in the boundary layer we have hastened this process. This is evident in the visualization records of the manipulated boundary layers which appear to be filled with finer scales of turbulence than in the corresponding regular boundary layer cases. This gives some evidence that the manipulated boundary layers emulate higher Reynolds number layers.

The wave-number distribution of energy in the manipulated boundary layers is shown in Figures 70 to 78. In Figures 70 and 71, the development of the frequency associated with the vortex street generated by the manipulator plates is presented. At the closest streamwise station, a peak corresponding to a strouhal frequency of approximately $ft/U_\infty = 0.03$ is evident for both Reynolds number ranges. The scale of eddies associated with this peak is approximately 0.5 cm. The peak is observed to be less dominant at the higher Reynolds number. By the next measurement station, approximately 17 plate heights or approximately 10[illegible] downstream of the device, we observe no spectral peak, corresponding to a regular vortex pattern, in the one-dimensional spectra. Other differences in the spectral distributions are a result of taking the spectra at a constant y-value equal to the device height rather than along self-similar y-values in the boundary layer.

The normalized one-dimensional spectra of the

streamwise velocity component at different self-similar heights along alternating measurement stations is shown in Figures 72-78. Included in these figures are the lines with slopes of -1 and -5/3 corresponding to the viscous convective and inertial subranges, respectively, for one-dimensional velocity spectra. The corresponding spectral distributions for the regular boundary layers were presented in Figures 42 to 47.

For both Reynolds number ranges in the manipulated boundary layer we observe a better collapse of the spectral distributions taken at different heights at the station just downstream of the device (Figures 72 and 75). This would indicate more even distribution of turbulence scales across the boundary layer. Furthermore we observe that each of the profiles has a range of wave numbers over which they follow a -1 distribution. In the regular boundary layer, only the spectra taken very near to the wall (below y+ = 30) exhibited a -1 distribution. This would indicate that the viscous-convective interaction, and therefore greater turbulence production, is occurring over a greater portion of the boundary layer close to the manipulator. Indication of the inertial subrange is only evident in these figures at $y^+ \leq 600$. In the regular boundary layer the -5/3 portion in the spectral distribution could be observed down to y+ = 200.

At the farthest downstream station from the manipulator for the low Reynolds number range in Figure

74, we still observe a fairly good collapse of the spectral distributions for wave numbers greater than 100 at y+ values less than 200. At a comparable Reynolds number in the regular boundary layer, the inertial subrange was evident in the spectra taken at y+ values greater than 200, where it ranged between wave numbers of 50 to 200 m^{-1}. In Figure 74, the spectral distributions demonstrate a -5/3 slope down to $y^+ = 75$. The wave number range corresponding to the inertial subrange in this case is a much lower 5 to 50 m^{-1}. A k^{-1} distribution is observed in this figure for a range of wave numbers between approximately 8 to 100 at $y^+ = 30$.

At the highest Reynolds number, shown in Figure 77, the inertial subrange is observed to expand to encompass wave numbers between 5 and 100 m^{-1}. This is still an order of magnitude lower in wave numbers compared to the regular boundary layer at a comparable Reynolds number. This would indicate that the constant stress layer has extended over a larger portion of the boundary layer. There is still evidence of the viscous-convective interaction near the wall, below y+ of 75 at the higher Reynolds number. This would indicate that the events occurring near the wall in regard to turbulence production are reasonably unchanged in the boundary layers without the large outer scales.

The one-dimensional spectra of the wall shear, τ_w, for the regular and manipulated boundary layers at two

Reynolds numbers are shown in Figure 78. The wave-numbers are computed in this figure by using the average value of the shear velocity, u_τ, for each case. These distributions show a small range of wave numbers over which a k^{-1} energy change is evident. The emaining distribution exhibits a k^{-7} behavior indicating strong viscous dissipation of turbulent energy. In the manipulated boundary layer, which corresponds to the lowest Reynolds number in Figure 77, the wave-number distribution of the normalized spectra follows more closely the high Reynolds number distribution. This is especially more evident for lower wave-numbers, less than 1000 m^{-1} in this figure.

A comparison of the normalized probability distributions of the instantaneous shear stress for the manipulated and regular boundary layers is shown in Figures 79 and 80 for both Reynolds number ranges. In these figures, the distributions are normalized by removing the sample mean and dividing the distribution axis by 0.1 times the sample rms. Therefore every 10 bins correspond to one rms increment from the mean. This normalization provides an excellent collapse of the distributions even though the mean shear at the wall and the rms of its fluctuations are significantly reduced in the manipulated boundary layers. As is evident from these figures, the distribution of the surface shear fluctuations is skewed so that the most probable value is

less that the mean. A similarly skewed shear stress distribution was presented by Sandborn (1981) for a fully developed open channel flow. The probability distribution is, however, Reynolds numbe dependent, as shown in Figure 80 where the skewness ha decreased by approximately 50 percent for an increase in Re_{δ_z} of approximately 30 percent. Also with increasing Reynolds number, the $\tau'/\bar{\tau}$ shear stress intensity is observed to decrease by approximately 17 percent. In the manipulated boundary layers at a comparable Reynolds number, $\tau'/\bar{\tau}$ is higher by 22 percent over the regular boundary layer case. This was similarly true for the u'/u_τ values near the wall in the distributions in Figure 54. However, it should be pointed out that the absolute value of the wall-shear fluctuations is reduced when the boundary layer is manipulated. As the Reynolds number is increased in the manipulated layers we observe a 25 percent decrease in this value, which is about half of the decrease demonstrated for the regular boundary layer.

The shape of the distribution, indicated by the kurtosis, is also Reynolds number dependent. In the case of the regular boundary layer, the kurtosis is observed to decrease by approximately 20 percent. More importantly, it has moved from a value higher than that for gaussian to one less than for gaussian noise. Therefore the shear-stress distribution is becoming narrower at higher Reynolds numbers indicating a more

spiked time series for the shear. There is no significant change in the kurtosis values for the manipulated boundary layers.

The streamwise-velocity skewness and kurtosis distributions across the boundary layer for manipulated and regular boundary layers are shown in Figures 81 and 82. The skewness distribution in Figure 81 shows a maximum positive value between y+ of 1 and 7. This corresponds to most probably velocities less than the distribution mean, which would be associated with fluid moving away from the wall. Between y+ of 50 to 200, the skewness is approximately constant and near zero (gaussian). This corresponds to the constant stress region associated with the log-linear velocity profile. In the outer part of the boundary layer, $y+ > 200$, the skewness becomes largely negative. This indicates that the most probable velocities are greater than the mean. Similar statistics were presented by Gupta and Kaplan (1972).

Near the wall in the kurtosis distribution of Figure 82, we observe a peak kurtosis value in the sublayer between y+ of 1 and 7. In this region the kurtosis is greater than three indicating a probability distribution which is narrower than gaussian and a velocity time series which is more spiked in nature. This could be catagorized as indicating rapid parcels of low velocity (S greater than 0) fluid moving away from the wall. This

type of motion has been classified as the ejection phase of the bursting process.

In the buffer region between y+ of 20 to 50 we observe the minimum kurtosis values in the velocity distribution. The values correspond to a broader distribution than in a gaussian function. These statistics indicate that relatively large (less spiked signal) parcels of fluid are moving through this region. The near zero average skewness indicates that these parcels are an even distribution of locally low and high velocity regions.

Between y+ values of 50 to 200 we observe a nearly constant average kurtosis with a magnitude slightly less than for a gaussian signal. Again this corresponds to the region in the velocity distribution of constant stress. In the outer part of the boundary layer, the kurtosis distribution again attains values greater than that for a gaussian signal. This is associated with the spiked signal indicative of rapid, streamwise narrow regions of higher velocity fluid approaching from the outer regions of the boundary layer.

The greatest differences that occur in these statistics between the regular and manipulated layers is in the regions below y+ of 50 and above y+ of 200. In other words, statistic similarities in the streamwise velocity fluctuations are only unaltered in the

log-linear region of the velocity profile.

The vertical distribution of the integral length scales in the manipulated boundary layer at different downstream stations is shown in Figures 83 and 84 for both Reynolds number ranges. These results can be compared to the integral length scale distribution for the regular boundary layer shown in Figures 48 and 49. Comparing the figures reveals a growth in the streamwise scales near the wall in the manipulated layers. The same characteristic lengthening of the streamwise scales with increasing Reynolds number is exemplified in the manipulated layers in the lower half of the boundary layer. At the first two measurement stations in the outer part of the manipulated boundary layer, the lower integral scales are indicative of the vortex street emanating from the device.

The distribution of the integral length scales with Reynolds number is shown in Figure 85 for the manipulated boundary layer. This is comparable to the results for the regular boundary layer in Figure 50. Near the wall, below $y+ = 30$, the streamwise scale is observed to remain nearly constant with Reynolds number. In the regular boundary layer, the non-dimensional length scale decreased by a factor of two. In the log-linear region of the manipulated boundary layer in Figure 85, the non-dimensional streamwise scale is observed to increase with Reynolds number. In the regular boundary layer in

Figure 50, the streamwise scales demonstrated almost no growth in the log-linear part of the velocity profile. At $y+ = 400$, the non-dimensional integral length scale is increasing approximately 30 percent faster in the manipulated layer than in the regular case. In both cases, the non-dimensional streamwise scale at $y+ = 800$ increases at a slower rate with increasing Reynolds number, than those at $y+ = 400$. In the manipulated boundary layer, the growth rate of the scale at that non-dimensional height is approximately twice that in the regular boundary layer.

CHAPTER IX

UNSTEADY CHARACTERISTICS OF WALL LAYER

The results presented in this chapter correspond to the analysis of the "burst" conditioned velocity measurements obtained from the rake of hot-wires and the simultaneous digitized smoke-wire images of the flow. The techniques used for the acquisition and processing of these data are detailed in Chapters III, IV and V. The rake of wires, including a surface mounted shear wire, was located at measurement station 9 or the equivalent station 8 in the regular or manipulated layer, respectively. The mean characteristics of the boundary layers at those stations have been documented by the results in Chapters VII and VIII. The mean characteristics of the boundary layers at this streamwise station are also summarized in Table 2 of this chapter. The results will include one-dimensional (time) analysis and "burst" detection, two-dimensinal (space/time) reconstruction of the rake outputs and analysis of the digital images. In all cases, the results from the regular and manipulated boundary layers will be compared to draw light on the physical processes occurring in the near wall region of these turbulent boundary layers.

Table 2. Mean Boundary Layer Characteristics at Rake Location

BL	U_∞ (m/s)	$\delta_{1,2,3}$ (cm)	u_τ (m/s)	Re_{δ_2}	$C_f(\times 10^3)$	β	Π
R	6.7	1.231, .881, 1.548	.265	3819	3.026	.0628	.67
R	10.4	1.118, .811, 1.430	.378	5473	2.659	.0741	.91
M	6.7	1.117, .783, 1.371	.218	3364	2.136	.0628	.73
M	10.4	1.026, .732, 1.285	.316	4933	1.852	.0741	.79

One-Dimensional Analysis of Velocity: Time-series Data

The outputs from the 11 hot-wire sensors can be treated either as 11 individual time series or as a two-dimensional space-time array of velocity data. In this section we will first analyze the rake outputs in the former manner. The latter case of the results of a space-time analysis will be presented in the following section.

Figures 86-89 display a time-series record of the digitized outputs from the 11 hot-wire rake sensors for the low and high Reynolds number ranges of the regular and manipulated boundary layers. The time axes of these figures are non-dimensionalized by the outer variables U_∞ and δ. The spacing between sensors and their distance from the wall are denoted by their self similar coordinates based on inner-wall characteristic quantities

u_τ and ν. The time-series values are presented as the instantaneous fluctuating quantities normalized by the record average rms. This was equivalent to the long time average mean since the record lengths were chosen so that the mean statistics were ergodic. The central moments within a data record correspond to the long-time average moments, at least to the first four orders. Other than for the sensor at $y^+ = 0$, the quantity plotted in these figures is

$$(Q(y) - \bar{Q}(y))/Q(y)_{rms} \qquad Q = \begin{cases} U : y^+ > 0 \\ \tau : y^+ = 0 \end{cases}$$

For the remaining time series at the wall, the velocity in the above expression is replaced by the wall shear stress, τ_w. This method of non-dimensionalization is necessary for presenting these time series in this form because their mean values are increasing while the rms of their fluctuations are decreasing at greater non-dimensional distances from the wall. Also, since we are interested in focusing our attention on the coherent "structures" in the turbulence, this quantity represents a measure of the fluctuating intensities which stand out above the background turbulence fluctuations. In particular we were looking for the coherent "signatures" of these structures so as to obtain statistics about their distribution in the boundary layers.

The time series in Figures 86-89 correspond to the first 315 discrete data values in one record of continuous

data. As described in Chapter III, the data records in the low Reynolds number range were acquired simultaneously with the digitized images of the smoke-wire visualized flow. The instant in time at which the images were taken corresponds to point 50 of the 315 points displayed in Figures 85 and 88 and is denoted by an arrow on the time axis of these figures. The triggering was based on a locally high variance in the velocity signal for the wire at $y+ = 7$. Inspection of the time series at that non-dimensional distance from the wall in Figures 86 and 88 reveals a locally high excursion in the signal which would result in a high variance. Inspection of the time series at other distances from the wall at that instant in time reveals similar features on a time scale of approximately $2\text{-}3\delta/U_\infty$. These features appear coherent over an appreciable vertical extent of the boundary layer, including the time-distribution of the wall shear stress. As a first step in understanding the physical process depicted by these time series, analysis of the velocity distribution near the wall is first presented.

This phase of the experiment was designed to make comparisons between the regular and manipulated boundary layers over a range of Reynolds numbers. In particular we were interested in determining what effect, if any, the suppression of the large outer scale had on the wall "burst" process. As discussed in Chapter IV, the "burst"

events were also detected using a match filtering technique. In order to generate the velocity signature to be used as the impulse response filter function associated with the "burst" process, the VITA technique of Blackwelder and Kaplan (1976) was utilized. In keeping with the method presented in that paper, a threshold value of 1.2 and an averaging time of Tu_τ^2/ν approximately equal to 10 were used. The conditionally averaged time series were obtained from the data by summing up the velocity values about the detection point and dividing that total by the number of detections. Therefore the conditional average of the quantity Q is defined as

$$< Q(x_i,T) > y^+ = \frac{1}{N} \sum_{j=1}^{N} Q(x_i, t_j + T)$$

where x denotes the streamwise position at which the sampling was made and y+ denotes the vertical location of the detection wire. In the case of the rake, x was a fixed value. However, to investigate any Reynolds number effects on the results, the time series data taken from the traversable single wire probe, which was used to obtain one-dimensional velocity spectra, was analyzed for bursts. In this case, five streamwise positions at $y^+=15$ were used for the four boundary layer cases and two free-stream velocities. For the one-dimensional analysis, in all cases, the detection was made on the

signal from the hot-wire at y+ = 15. The quantities t_j in the relation are those points in the time series at which the detection occurred, and the quantity T is a positive or negative time delay used to determine the temporal behavior of Q before or after detection occurred. Because of the band limited nature of the data, events detected within less than half a wave length of the beginning or end of a record were not included in the ensemble. The variable N in the expression is the total number of detections included in the ensemble.

The ensemble average of the fluctuating velocity, non-dimensionalized by the local average rms at the 11 y+ locations, which were conditioned on a VITA detection with a threshold of 1.2 and time averaging $Tu_\tau^2/\nu = 10$, are presented in Figure 90 for the regular boundary layer with $Re_{\delta_2} = 3819$. The horizontal lines in the figure correspond to the record average mean value at each vertical height in the boundary layer. The spacing between these lines corresponds to 0.54 Q_{rms} where Q is the streamwise fluctuating wall shear, τ_w, for y+ = 0. For the other non-dimensional heights, Q is the streamwise velocity, u. Approximately 100 ensembles are included in the average distributions which were conditioned on the VITA detection in Figure 90.

If we compare this figure to the conditioned streamwise velocity distributions obtained by Blackwelder and Kaplan (1976) we observe the same velocity signature

which is associated with the "burst" process. If we focus on the normalized fluctuating velocity at y+ = 15, the detection height, we observe the characteristic local deceleration of the flow, very rapid acceleration and the subsequent slower deceleration. At this Reynolds number, the wavelength of the process is approximately $4\delta/U_\infty$ and the maximum peak-to-peak amplitude is approximately 2.2 u(rms). This compares extremely well to the characteristics of the velocity signature at the same non-dimensional height in the boundary layer of Blackwelder and Kaplan (1976) for a somewhat lower momentum thickness Reynolds number of 2550. At other distances from the wall we observe a characteristic pattern which extends as far as the sensor at y+ = 500, which is just at the lower edge of the wake region in the boundary layer. Blackwelder and Kaplan (1976) investigated the conditioned velocities out to y+ = 100. In the velocity signatures at y+ values from 200 to 500 we observe a characteristic higher velocity bulge which is upstream in time when conditioned on the wall events. This would indicate a structure which is inclined in the streamwise direction. This, of course, is not surprising since any flow structures in the boundary layers are subjected to a mean shear. Inclined coherent structures originating near the wall and extending out into the bulk of turbulent boundary layers was first proposed by Grant (1957) from space-time velocity correlation measurements.

At the wall, the normalized instantaneous shear stress is significantly changed during an event. The ensemble average of τ_w in this figure demonstrates a local decrease in the wall shear followed by a rapid increase which is associated with the rapidly accelerating fluid near the wall. The time scale for the event in the shear distribution appears to be slightly smaller than that in the scale of the coherent velocity fluctuations.

As was indicated in Chapter IV, reliable and objective "burst" frequencies cannot be obtained by the VITA technique. This was consistently demonstrated by Offen and Kline (1973) who, in addition to showing that the number of detections was non-linearly related to the threshold value for the VITA technique, also showed that the other commonly used methods exhibited the same problem. In addition to the dependence of the detection frequency on the threshold, the statistical distribution of events is non-linearly related to that threshold. This is demonstrated in Figure 91 in which the normalized probability distribution of burst events detected with two different thresholds are presented. As in the probability distributions presented in the results of Chapter VII for the instantaneous wall shear stress, the distributions in Figure 91 are plotted as number densities at rms increments away from their respective means. This type of normalizaiton should collapse related distributions. In the distributions of Figure 91

for only a ±10 percent deviation away from the 1.2 threshold used by Blackwelder and Kaplan (1976), we observe differences in the burst statistics which are related to the detection threshold value.

In spite of this criticism of the VITA technique for measuring the burst frequency, it is valid in the sense that it does generate the most coherent velocity signature that is associated with a large locally high rms in the streamwise velocity near the wall. Through such visualization studies as that of Offen and Kline (1973), who found a majority of VITA detections corresponded to the visual observance of a "burst" event, we can relate that average signature to that for an average "burst" cycle. Although Offen and Kline (1973) found, for a low Reynolds number boundary layer, that a VITA detection did detect bursts, they observed that the technique only detected 53 percent of those that were observed to visually occur in the region of the probe. A similar factor of two was observed in that study for the other techniques that they investigated. This same trend was also observed by Bogard and Tiederman (1981).

In light of these findings, the velocity signature obtained through the VITA technique was only used as a pattern in the match filter detection which was used to obtain the frequency statistics for the occurrence of wall events. In all the cases considered, we utilized a pattern that was generated from the data for that case.

As with the VITA detection, the patterns and match filter detection were generated from the velocity time series at $y+ = 15$.

In Figures 92 to 95 we have displayed typical cases of the raw data for velocity time series and the corresponding match filter correlation for regular and manipulated boundary layers at each of the respective Reynolds numbers. The top time series is the instantaneous velocity non-dimensionalized by the average rms. The bottom time series in these figures is the cross correlation between the pattern and the velocity series. The dashed lines correspond to zero level in both of the traces in these figures. As a reference, the time axis is presented non-dimensionalized with outer flow parameters.

The peaks in the correlation correspond to locations where a match occurred between the average burst signature and the time series. Inspection of points of positive correlatin peaks in these figures reveals that they correspond to the characteristic signature of the local deceleration of the flow followed by a rapid acceleration. These correlations are normalized by the output for a perfect correlation that corresponds to correlating the match filter function with itself. It is interesting to note that with this normalization it is possible to have cases where the correlation is greater than one. These cases are associated with detected

bursts that are spaced less than an average wave length apart where the positive correlations can sum up. The negative correlations that occur in these figures correspond to the cases pointed out by Nishioka et al. (1980), namely the deceleration of the same magnitude and time scale as that for a burst. Without any specification on the sign of the velocity change, the VITA technique, as it was proposed originally, would associate these occurrences with bursts.

The burst locations were taken as the locations of the significant positive correlation peaks in the match filter outputs. We chose a normalized correlation of 30 percent to be the minimum for a relevant match in the velocity series, i.e., minimum acceptable peak amplitude. This value corresponded to one end of a region of insensitivity of the detected bursts to the correlation level between 0.3 and 0.8.

Using the detection points obtained by the match filter, the ensemble averaged time series for the burst events at the 11 heights in the boundary layers were constructed and presented in Figures 96 - 99. The scale for the abscissa in these figures is the same as that for the ensembled time series obtained from the VITA detection in Figure 90. By comparing Figures 90 and 96 we observe that the main features of the ensemble averaged velocity signatures are basically the same. However, we observe that in the case of the match

detections, the velocity signature is coherent over a larger wave length than in the vita detection ensembles. This can be attributed to the inclusion of non-events in the VITA ensembles. This leads us to conclude that the VITA technique does not only miss some of the wall events but it also includes some non-events.

At the higher Reynolds number range in Figure 97, we observe a decrease in the peak-to-peak amplitude of the event signature below y+ = 100. Most of that decrease is a result of the much smaller level of deceleration in the beginning phase of the event at the higher Reynolds number. After the rapid acceleration in the instantaneous velocity, the velocity signatures exhibit a plateau which was not present at the lower Reynolds number. It is important to point out here that since the average signature at the higher Reynolds number exhibits an amplitude which is a smaller percentage of the turbulence fluctuating velocities, the threshold value in the VITA detection must be reduced in order to include all classes of the events. Inspection of the ensembles for the manipulated boundary layers in Figures 98 and 99 shows them to resemble the higher Reynolds number case in Figure 97. One most notable difference occurs in the shear stress signature. In the case of the manipulated layers we observe a much reduced decrease in the local shear which is associated with the decelerating fluid near the wall.

Another noticable feature at the plateau is a consistent pattern of regular oscillations. This may very well reflect the instability of the shear layer developed by the "burst" cycle and observed by visualization, i.e., by Kline et al. (1967) and during the largest stages of transition, i.e., by Nishioka et al. (1980).

The probability distributions of the period between burst events is shown in Figures 100 to 104. A comparison between the probability distributions for the events detected by the VITA and match detection is presented in Figure 100. As with the previously presented probability distributions, these are normalized by subtracting the mean period and dividing by the rms. Comparing the statistics in this figure shows that with the threshold value recommended by Blackwelder and Kaplan (1976), the match detection makes approximately twice as many detections. This result is consistant with the results of Offen and Kline (1976) who found that the VITA technique, as well as other methods which employ a threshold, detected only half of the events that were observed to occur with visualization. Comparing the statistical distribution of events as reflected in the skewness and kurtosis yields further results. The match detected events are skewed approximately twice as much as those of the VITA technique. This indicates that the VITA technique with the given threshold is not detecting

the events occurring with longer periods between them. This would indicate that these events were less intense than those occurring nearer to the mean period. The kurtosis of the distribution for the VITA method indicates a distribution which is narrower than gaussian. In contrast, the kurtosis for the match detection is approximately three times greater, indicating a much broader distribution of events.

Blackwelder and Kaplan (1976), using the VITA technique, estimated that the burst events occurred approximately 25 percent of the time in the life of the boundary layer. The statistics presented here for the match detection indicate that these events are occurring over a much greater percentage of time. The two-dimensional reconstruction of the velocity from the hot-wire rake, to be presented later in this chapter, will give more insight into this aspect. However, it is clear from this figure that a technique which relies on detection of events through locally large statistical quantities may be accepting only part of the total distribution of these events. In particular, setting a local threshold only includes events of a particular class that are sufficiently energetic or otherwise pass some biased criterion. Other events of the same class may exist but are being ignored because they do not fall within a narrow sampling criteria. This is not said to criticize this method of signal detection, but rather to

point out that results based on such an approach must be qualified in a manner which is appropriate with the selection parameters.

The distributions are compared for the regular and manipulated boundary layers at both ranges of Reynolds numbers in Figures 101 and 102. These results indicate that the distributions become less skewed and less broad with increasing Reynolds number. This trend is consistantly demonstrated in the manipulated layers which appear to emulate higher Reynolds number boundary layers. A direct comparison of the regular and manipulated boundary layers at the same free-stream velocity is presented in Figures 103 and 104. These are the same distributions as in the previous two figures but replotted to allow a direct comparison. In all cases, the peak in the distribution occurs at approximately one rms period less than the mean. The addition of the manipulator, which we observed earlier to result in lower friction at the wall and a thicker sublayer, leads to an increased absolute period. at both free-stream speeds.

Two-dimensional Analysis of Velocity: Space/Time Data

As described in Chapter III, space-time analysis of the output of the rake of 11 hot-wires was done by performing reconstructive two-dimensional low-pass filtering. The one-dimensional filter function was shown in Figure 19 and the generated two-dimensional filter

function was shown in Figure 20. Typical records of two-dimensional reconstructed velocities are presented in Figures 105 and 106 for all four boundary layer cases. The velocity data are presented as contours of constant normalized velocity, $U(y) - \bar{U}(y)/u(y)_{rms}$. The dashed line contours correspond to "structures" having negative normalized velocities, or velocities less than the mean. The solid line contours correspond to structures containing velocities greater than the mean.

Structures corresponding to the wall bursts are designated by their one-dimensional signature to be the deceleration of the fluid near the wall followed by the rapid acceleration. By this definition, the burst cycle will correspond to a dashed line structure followed by a solid-lined structure for the notation of Figures 105 and 106. In the contours of Figure 105, the acquisition was initiated by the detection of a burst event which is visible as the dashed-solid pair centered about TU_∞/ν approximately equal to 1 in the time sequences in that figure. The high velocity data were not acquired based on a "burst" detection and the same comparison cannot be made at the non-dimensionalized time of 1. Inspection of Figures 105 and 106 strongly suggests that the velocity field near the wall is in a constant state of acceleration and deceleration. In fact it almost looks like an bistable mode. This is reminiscent of the behavior of the wall layer proposed by Black (1966),

Einstein and Li (1956) and Hanratty (1956) which modeled the flow to be in a constant state of dissipation and regeneration. Another way to interpret the quasi-periodic low and high velocity structures near the wall would be in terms of a bulk instability of the wall layer. This aspect will be explored more, later in this chapter.

These two-dimensional velocity reconstructions also bring out another startling result. In the bottom part of Figures 105 and 106, there appears to be some coherent eddy structure reminiscent of the vortex street emanating from the manipulator plates. The presence of these is clearly missing in the one-dimensional velocity spectra taken at this height in the boundary layer. However, the two-dimensional data indicate that the eddies are sparsely coherent, thereby resulting in a broad band distribution of their one-dimensional spectral energy.

The ensemble averaged reconstructed velocity profiles conditioned at the time-instant when the digital images were acquired are shown in Figures 107 and 108 for the regular and manipulated boundary layers, respectively. These indicate that most of the digital images were triggered on a burst event, although the detection is observed to be more sensitive to the high velocity sweep of fluid near the wall. This information will be used in the interpretation of the ensembled digital images.

The ensemble averaged reconstructed velocity profiles conditioned at the match filter detected time of an event are presented in Figures 109 - 112 for the regular and manipulated boundary layers at the two free-stream velocities. The range of contour levels in these figures is the same as that for the previous two figures. The features depicted by the contours about the detection point, $TU_\infty/\delta = 0$, correspond to the average "burst" structure. If we compare the average structure between Figures 109 and 110 we observe a streamwise extension with increasing Reynolds number. In the manipulated layers in Figures 111 and 112 we observe that the structure has a longer streamwise extent compared to the regular boundary layer. This is consistant with the idea of the manipulated layers emulating higher Reynolds number boundary layers. The fact that some coherence is evident away from the detection point is indicating of the quasi-periodic nature of the process.

In order to better understand the mechanisms of the wall layer events, the average structure associated with burst periods greater than 3σ away from the mean period was investigated. This was done so as to pinpoint what differences, if any, existed in these structures for which the nearest event occurred 3σ time scales before. These are presented in Figures 113 and 114 for the regular boundary layer at the low and high free-stream speeds, respectively. The non-matching of

some contours is a result of having to form the ensembles in separate 64 point segments so as to maximize the number of realizations in the ensemble average for these doubly restrictive conditions in the band-limited time sequences. The 3σ burst time scale corresponds to approximately one-third of the continuous sampling time and as seen in Figure 99, only approximately one percent of the total events occur at periods greater than 3σ away from the mean. As a result of these limitations, the ensembles in Figures 113 and 114 contain only approximately six realizations. However, certain conclusions can be drawn from the results. In particular these figures indicate that when an event has not happened for a previously "long" time, the wall structure remains at a low velocity state, compared to the mean flow, which is observed to extend well up into the constant stress layer. A high velocity shear layer is observed to form above the low velocity structure prior to the formation of the high velocity wall structure. This is evident in the ensemble averages shown in both of the figures.

In order to look at the wave-number distribution of the structures near the wall, two-dimensional spectra were computed of the two-dimensional reconstructed velocity distributions of the type shown in Figures 105 and 106. The two-dimensional spectra are presented in Figures 115 - 118 for the regular and manipulated

boundary layers at the two free-stream speeds. The spectra are normalized by the volume under their distributions which corresponds to the two-dimensional variance and plotted as contours of constant spectral levels. In addition, the two-dimensional spectra are plotted as all four quadrants of positive and negative wave numbers.

At the low free-stream speed for the regular boundary layer in Figure 115, we observe narrow band peaks at $f\delta/U_\infty$ equal to approximately 2 and 0.5, along a spatial frequency ky/δ equal to approximately 0.005. The higher frequency corresponds to a non-dimensional period of 0.5, which is evident as the smaller scales observed at the lower Reynolds number in the top part of Figure 105. The other peak corresponds to an approximate non-dimensional period of 2 U_∞/δ, which is the approximate mean burst period determined from the one-dimensional match filter analysis. The peak in the spatial frequency coordinate corresponds to a vertical scale of approximately 0.2δ which is the approximate scale of the structures with velocities greater than the mean in Figure 105. The other spatial peak corresponds to a vertical scale of 0.09δ which is the approximate scale of the wall structures having velocities less than the mean.

At the higher Reynolds number, the two-dimensional spectrum in Figure 116 does not show a peak at $f\delta/U_\infty = 2$

and the other peaks are observed at lower wavenumbers. The peak at approximately $f\delta/U_\infty = 0.25$ corresponds to a structure period of approximately 0.028 seconds which is approximately the burst period for the regular boundary layer at the higher free-stream speed. These structures have a spatial wave number of approximately $ky/\delta=0.004$ which corresponds to vertical scales of approximately 0.16δ. Thus the wall structures are observed to increase their streamwise extent and decrease their vertical extent with increasing Reynolds number.

The two-dimensional spectral distributions for the manipulated boundary layers exhibit the same trends as brought out by the match filter analysis, in that we see an increase in the streamwise extent of the wall structures with the addition of the manipulator. In addition, the spectra also indicate that the vertical scale of the wall structures is increasing. This is consistent with the observed growth of the sublayer in the manipulated boundary layers.

Two-dimensional Image Analysis

The rake of hot-wires provided information about the spatial features of the boundary layer in a region primarily below the mid-point of the boundary layer thickness. In order to view the coherent structures across the whole bulk of the boundary layer, the digitized images of the smoke-wire visualized flowfield

were analyzed. Grey-level representations of typical digitized images are shown in the top half of Figures 119 and 120 for the regular and manipulated boundary layers. These are photographs taken from the color television monitor as output from the MDP display processor with a black and white color table which gives an increasing grey intensity corresponding to the digitized luminance levels in the smoke image. In these representations, black corresponds to the lowest intensity and white corresponds to the maximum intensity value. The images in these figures correspond to the zoomed-in view of the flow in the near vicinity (approximately 2_δ) of the hot-wire rake, which is visible in the left bottom corner of the photograph.

In order to distinguish the coherent features in the visualized flow, the images were match filtered utilizing the same two-dimensional filter used in the velocity reconstructions presented in the previous figures. This was appropriate since the physical scalings were identical in both of the processes. The details of the match filtering for the digitized images were presented in Chapter V. The results of that process yields enhanced images consisting of features whose spatial variations in luminance correlated well with the spatial characteristics of the two-dimensional filter response. We therefore are searching for particular scales of features in these images which are consistent with those

brought out in the velocity distributions of the two-dimensional reconstructions.

The bottom photographs in Figure 119 and 120 are the corresponding match filter reconstructions of the respective digitized images in those figures. In these cases, the black/white color table was loaded with a step function so as to distinguish distinct levels and form contours of constant match correlation. Black corresponds to a negative correlation and white corresponds to a maximum positive match. Comparing the digital images and their corresponding match-filter representations points out the features that this processing highlights. The hot-wire rake, which yields a strong correlation, was left in the processed images to aid as a reference to the photographs.

Comparison of the images for the regular and manipulated layers in Figures 119 and 120 reveals some differences. It is important to remember that the acquisition of these images was initiated by the detection of a "burst" event. This was indicated by a large local variance in the velocity signal at $y^+ = 7$ in the boundary layer. At that instant in the regular boundary layer, the match-filter enhancement in Figure 119 reveals some coherent features near the wall and in the outer part of the flow that extend toward the wall. In the manipulated layer in Figure 120, we observe a larger feature near the wall and what appears to be a

regular eddy pattern in the outer part of the flow. These, however, correspond to one realization only of the "burst" event. In Figure 121, the ensemble-averaged enhanced-images of these events are presented. As was indicated earlier in this chapter, the detection of wall events based on a locally high variance is not always reliable. Therefore, the image realizations included in the ensemble were those which corresponded to a match-filter detection at that instant in the velocity signal, which was acquired simultaneously. The acceptance rate in this case was approximately one out of three.

The ensemble average of the images without any enhancement tended to smear the details, but conditionally averaged match filtered images which are presented in Figure 121 revealed some features. If we focus on the result for the regular boundary layer, in the top of the figure, we observe what looks to be a relatively large slender feature which is inclined in the flow direction. This shape is reminiscent of the Townsend (1970) inclined eddies or the Brown and Thomas (1977) description of the outer inclined structures they associated with the wall "bursting". The local maximum at the outer tip of the feature indicates that the smoke was rolled-up in that region suggesting a possible eddy structure. This may very well be a visual ensemble of the hairpin-like vortices.

In the ensemble averaged images for the manipulated boundary layer in the bottom half of Figure 121, we see a similar feature. However we find it residing in a region below approximately 60 percent of the boundary layer thickness. Above that we observe the alternating light and dark regions that are indicative of the eddy pattern in a vortex street, most likely emanating from the manipulator plates. If we compare these images to the ensemble-averaged reconstructed velocity distributions in Figures 107 and 108 we see some similarities. The velocity distributions were normalized so as to bring out features that stood out against the background non-coherent turbulence. For the regular boundary layer the normalized velocity contours in Figure 107 reveal a lifted structure which is inclined at an angle similar to that of the feature in the image. In the manipulated layer, the structure implied from the velocity contours in Figure 108 is observed to exhibit less of a vertical extent than in the regular layer. This was also evident in the ensemble image for the manipulated layers.

In order to view a greater streamwise portion of the boundary layer, the images viewing approximately 10δ in the flow were analyzed. These are shown in Figures 122 and 123 for the regular and manipulated boundary layers. Again the match filter enhanced images were generated for these realizations which also were acquired upon the detection of a wall event. These are comparable,

C-3

although not the exact same realizations, to the two-dimensional reconstructed velocity time series in Figure 105. There are clear and identifiable differences in the enhanced images for the two cases. The regular boundary layer exhibits long coherent features that extend across the bulk of the boundary layer and which are inclined along the mean shear. In the manipulated boundary layer these features are not evident. Rather, the outer part of the boundary layer flow appears to be dominated by a stream of alternating vortex patterns. This feature was pointed out in the discussion of the features for the two-dimensional reconstructions of earlier in this chapter.

Considerably more analysis is needed to interpret these images. However, they do bring out coherent features which are linked with the burst events and which are consistent with the picture we obtained from the simultaneous velocity surveys. We hope that they will also provide us with the time sequence of events from an objective and quantitative assessment of flow visualization records.

CHAPTER X

DISCUSSION

In the previous two chapters, the consequences of suppressing the large-scale intermittent outer structures in turbulent boundary layers were presented. In this chapter these results will be tied together so as to pinpoint the physical mechanisms involved in these manipulated boundary layers. In doing this, emphasis will be placed on the role of the intermittent outer corrugations on the boundary layer growth as well as on the production and distribution of the turbulence scales of motion. Next, the outer flow processes in the boundary layer will be tied to the mechanism for turbulence generation in the wall layer through their interaction with the coherent motions near the wall. This analysis will attempt to lead to a unified phenomenological representation for the mutual interaction of inner and outer fluid layers in boundary layer flows. Whenever possible, the results of other investigators will be drawn upon for comparison and to reinforce the conclusions arrived at in this investigation.

Mechanisms Governing Operation of Parallel-Plate Manipulators

The manipulated boundary layers were observed to have marked differences in their mean and unsteady characteristics when compared to the regular turbulent

boundary layers over a comparable Reynolds number range. The major differences occurring in the manipulated boundary layers are characterized by the following:

1) a visual evidence of the suppression of large outer turbulent scales that leads to a lack of intermittent excursions of high speed potential fluid into the boundary layer,

2) a decrease in the streamwise growth of the boundary layer thickness and integral thicknesses δ_1, δ_2, and δ_3,

3) a disproportionately larger shape factor H_{12},

4) a 30 percent decrease in the local skin-friction coefficient over the regular boundary layer at comparable Reynolds numbers,

5) a growth in the sublayer by approximately 17 percent which is refleced in an upward translation of the log-linear velocity distribution,

6) a 17 percent decrease in the von Karman constant reflected in a more sloped log-linear velocity distribution for the manipulated layers,

7) a decrease in the entrainment velocity which is

also observed to decrease with increasing Reynolds numbers,

8) a reduction in the wake strength coefficient, Π, in the manipulated boundary layers at comparable Reynolds numbers,

9) a lower level of u'/U_∞ in the manipulated boundary layers below $y^+ = 100$ and an increase in u'/u_τ in the wall layer up through the constant stress layer,

10) growth of the constant stress layer and an increase in the rate of growth of the streamwise length scale of turbulent eddies, and

11) a reduction in the absolute frequency of occurrence of the so-called "burst" events in the manipulated boundary layers.

We look to these documented changes in the manipulated boundary layers in order to ascertain the mechanisms governing the operation of the parallel plate manipulators in a turbulent boundary layer. It should be kept in mind that these cited effects appear to persist for appreciable distances (at least 70 boundary layer thicknesses) downstream of the manipulator.

If we consider the results of the parametric study of this class of devices in Chapter VI, we note that an

optimum exists for the different parameters in the different manipulator plate configurations. The table in Figure 22, for which the optimum parameters are scaled with the characteristic boundary layer lengths, indicates that the maximum reduction in the outer intermittent scales is produced by devices which have dimensions and are placed at heights that are comparable to the average size of the eddies which are to be suppressed. The fact that two-plate parallel and series manipulators worked as well as the four plate manipulator suggests that the lower plates in M-1 had little effect on the large scale turbulence. What is extremely interesting in the parametric study is that the optimum spacing between the streamwise oriented plates of M-4 is 6 to 8 boundary layer thicknesses which correspond to the average life of a large scale eddy estimated from the velocity correlation measurements of Blackwelder and Kovasznay (1972).

There appears to be four key mechanisms for the observed suppression of the outer scales in the turbulent boundary layer. Any one or all of these mechanisms may be acting at once although some are most likely more dominant than others. The first explanation for the effectiveness of these simple devices is that the manipulator plates restrict the vertical velocity components associated with the large scale motions (Kovasznay, 197 in very much the same way as a

honeycomb supresses the lateral velocity components of grid turbulence within eight mesh lengths (Loehrke and Nagib, 1976). The fact that these scales dissipate so rapidly may be an indication that they are relatively inactive motions.

The unsteady circulation generated by the flat plate in the fluctuating turbulent flow leads to the second mechanism. A flat plate at zero incidence in an unsteady shear flow similar to the boundary layer will generate circulation in the same and opposite sense to that of the large scale structures. The exercise carried out with a one-plate manipulator at various positive and negative angles of attack in Chapter VI was aimed at demonstrating this mechanism. In those experiments we observed both suppression as well as augmentation of the large scales depending on the angle of attack being negative (or zero) or positive, respectively. The augmentation of the large scale motions is an appealing idea for improved heat transfer applications.

The third mechanism is based on generation of new scales in the outer part of the turbulent boundary layer as a result of the vortices being formed in the wakes of the plates. Although the one-dimensional velocity spectra taken at the height of the manipulator plates at downstream stations indicate that these vortices rapidly lose their identity through the turbulence velocity fluctuations, the two-dimensional velocity

reconstructions and image processing records indicate that some coherent remnants may exist in intermittent packs far downstream of the device. These eddies, which are of a smaller scale than the larger outer bulges in the boundary layer may act to redistribute small scale turbulence. Through visualization of the outer flow of a turbulent boundary layer, Taneda (1981) and Taneda et al. (1981) have demonstrated that a most amplified mode may exist for the passage of large outer flow structures. The generation of a vortex street with passage frequencies away from the most amplified case may disrupt this process.

The last mechanism, which may have a role in suppressing the large outer scales and in redistributing the fine scale turbulence through a greater part of the boundary layer, results from having a wake profile embedded in the mild mean velocity shear in the outer part of the boundary layer. The turbulent energy equation for a two-dimensional incompressible mean flow, outside the viscous sublayer (Townsend, 1956) takes the following form

$$\frac{1}{\rho}\left(U\frac{\partial \bar{q}^2}{\partial x} + V\frac{\partial q^2}{\partial y}\right) - \rho\overline{uv}\frac{\partial U}{\partial y} + \frac{\partial}{\partial y}\left(\overline{Pv} + \frac{1}{2}\rho\overline{q^2 v}\right) + \rho\varepsilon = 0$$

advection production diffusion dissipation

Normally in the outer wake part of the boundary layer, $\frac{\partial U}{\partial y}$ is small, as well as the uv correlation, thereby

resulting in a near zero turbulence production. In the wake of the manipulator plates, we have a locally large dU/dy. This is evident just downstream of the device as shown in Figure 52. On the wall side of the manipulator plate we might expect that dU/dy would be negative but because of the mean shear the U(y) distribution directly below the plate is nearly constant as shown in Figure 52. On the potential flow side of the manipulator plate, we observe a substantially larger positive velocity gradient. As a result of the unsteady vorticity generated by the manipulator plates, we also might expect that the $\overline{uv}$ correlation would increase. Therefore, the wake of the plates is a likely site for turbulence production in the manipulated boundary layers. Additional evidence and discussion of this is presented in Appendix B.

The last mechanism may explain why the manipulated boundary layers are filled with fine-scale turbulence as depicted in the photographs in Figure 51. Furthermore this would explain why the u'/u_τ distributions in the manipulated layers in Figures 54 and 55 have higher values than their regular boundary layer counterparts. In the regular case, the streamwise velocity stress was found to be related at all heights in the boundary layer to the wall shear velocity, u_τ, as was shown in Figures 31 and 32. This was not the case in the manipulated boundary layers. However, since u_τ is a measure of the

turbulence production at the wall, it would not account for other sources which contribute to the turbulent stresses away from the wall. With the added turbulence production in the wake of the manipulator plate, we would expect a thickening of the constant stress layer which indeed was observed in the one-dimensional velocity spectra.

Although this concept is very appealing for explaining one of the turbulence control mechanisms, the mean velocity distributions indicate a fairly rapid decay of the wake of the plates. Therefore, the turbulence production must be localized to the near wake of these plates. However, once the fine scale turbulence is generated, it might be convected for long streamwise distances.

Each of these mechanisms that may govern the effectiveness of these large scale turbulence manipulators in the boundary layer have justifying aspects. Most likely, all of them are acting to suppress the large-scale outer structures and to redistribute turbulence throughout the boundary layer. The fact that an optimum exists for this process indicates that these devices are acting on some fundamental properties of the turbulence in the boundary layer.

Drag Reduction and Reynolds Number Effects on Boundary Layer Large Scales

In Chapter IX we documented a 30 percent reduction in the local skin friction in the manipulated boundary layers. Accounting for the drag of the device, this resulted a net reduction in the friction ccefficient of 21 percent by the last streamwise station at the end of the tunnel test section, i.e., about 55 boundary layer thicknesses downstream of the manipulator. This part of the chapter will address the physics behind this behavior and make some judgments as to how long this effect may persist.

In the photographs of Figure 51, along with those in Figures 24 and 25 from the parametric study, we observed a lack of the intermittent excursions of high speed potential fluid into the recesses in the boundary layer with the manipulator. As a result of this we measured a decrease in the streamwise growth of the boundary layer and all of its integral thicknesses as evidenced by Figures 56 and 57. By impeding the high speed fluid from reaching close to the wall we would expect to reduce the high local instantaneous wall shear stresses and thereby the time averaged value. The reduction in the growth of the boundary layer and reduction in the local average wall shear stress are a result of the lower rates of

entrained potential fluid into the boundary layer. This was demonstrated in Figure 69 which presented the mean rate of propagation of turbulent fluid into the free-stream or the entrainment velocity, V_p, as a function of Reynolds number in the regular and manipulated boundary layers. In this figure we observe an approximately 40 percent reduction in the entrainment velocity with the large scale manipulators. Bradshaw (1967) found that the quantity V_p/U_∞ was very nearly proportional to $\tau/\rho U^2$ in equilibrium and non-equilibrium boundary layers. Furthermore that ratio of the large-eddy velocity fluctuations to the small-scale velocity fluctuations in the central part of the boundary layer is proportional to $(\tau/\rho U^2)^{\frac{1}{2}}$. Moreover, the ratio of advection or diffusion to production in the outer part of the layer is proportional to C_f.

Figure 69 demonstrates that the Reynolds number distribution of friction coefficient is related, within a proportionality constant, to the ratio of the entrainment velocity to free-stream velocity. Therefore, removing the large outer scales leads to a reduction in the entrainment rate in the manipulateld boundary layers which then results in a subsequent reduction in the local friction coefficient.

Considering the regular boundary layer case in this figure we find that the entrainment velocity is

decreasing with increasing Reynolds number in a manner proportional to $C_f(Re_{\delta_2})$. This indicates that the large outer scales, defined by the regions of intermittency in the turbulent boundary layer, are becoming less coherent. In a similar fashion the ratio of diffusion to production in the outer part of the layer is decreasing like $2C_f(x)$. This is a result of the decrease in the ratio of the large-eddy velocity fluctuations to the small-scale velocity fluctuations proportional to $(2C_f)^{\frac{1}{2}}$. Thus the outer part of the boundary layer is filling with smaller scale turbulence like $(Re_{\delta_2})^{-\frac{1}{2}}$. The process has been observed through visualization records of turbulent boundary layers over a range of Reynolds numbers including transitional values by Naqib et al. (1978).

In the manipulated boundary layers we are hastening this process by removing the intermittent outer scales and thereby "aging" the boundary layer in a Reynolds number sense. These manipulated boundary layers therefore emulate higher Reynolds number flows. By this same argument, however, we are implying that the large outer scales are associated with "young" boundary layers. Extending this argument one step further leads to the hypothesis that these large outer scales are the remnants of the turbulence transition process. This reasoning is reinforced by the fact that we have not observed a recurrence of these large outer bulges in the manipulated boundary layers within the 70 bounday layer thickness

available to us downstream of the device.

Given the relationship between the entrainment and friction coefficients, we examined the Reynolds number dependence of C_f for the regular and manipulated boundary layers in Figure 124. This figure demonstrates that a power law relation exists between the friction coefficient and Reynolds number. In particular, the C_f values for the regular boundary layer are observed to decrease like the -1/4 power of Re_{δ_2}. This is predicted by the Ludwig-Tillmann relation for a constant shape factor H_{12}. In the manipulated boundary layers, the C_f dependence on Reynolds number falls on a higher slope of -3/7. The fact that the $C_f(Re_{\delta_2})$ distribution is not only shifted but also diverging from the regular case indicates that the boundary layer is not only "aged" by the manipulator, but that it is "aging" faster with increasing Reynolds numbers.

We can estimate the equivalent Reynolds number corresponding to the manipulated boundary layers by translating the C_f distribution in Figure 124 so that the values fall on the -1/4 distribution of the regular layer. This is equivalent to multiplying those values by a coefficient which corresponds to a translation on the log axis. The coefficient value, however, increases with increasing Reynolds numbers in the manipulated boundary layer to account for the greater slope. This process yields a range of equivalent Reynolds numbers for the

manipulated boundary layers from 7,000 to 22,000.

Based on the above arguments and, in particular, the hypothesis that the large scales are remnants of the transition process, one may expect that the effects of the manipulator on the wall friction would persist for very long distances. Only if the large scales would be regenerated by a truly turbulent boundary layer, one may expect a return toward the regular boundary layer correlation. Additional evidence on this matter is presented in the next section. However, if the return of the large scales is not likely or is very slow, the manipulators investigated here may present a very attractive tool for reducing drag over bodies with turbulent boundary layers.

Wall Layer Instability

The one- and two-dimensional analysis of the coherent features in the wall region in turbulent boundary layers indicated that the so-called wall "bursts" which were determined by other investigators to occur approximately 25 percent of the time (Blackwelder and Kaplan, 1976) actually occur in a continuous quasi-periodic process. The random nature associated with these events is a result of their extremely broad distribution of wavelengths. It is this behavior which has prompted us to associate these events with a bulk instability mechanism in the wall layer. In this section

of the chapter we will address this issue and relate the frequency of occurrence of these events to the boundary layer parameters so as to identify the physical process governing these important features in the wall layer.

In the results in Chapter IX, we demonstrated that the one-dimensional match filter detection of the wall events gave the same results as those obtained from two-dimensional spectral analysis of the reconstructed velocity distributions. Given the consistency of both approaches, the results from the traversing single wire probe and stationary rake of wires were used to establish the Reynolds number dependence for the frequency of the wall events. In line with an instability approach we formed a Strouhal number based on a wall layer velocity, U_ℓ, and length, ℓ, to non-dimensionalize the wall event frequency. That Strouhal number is

$$St^+ = \frac{f\,\ell}{U_\ell}$$

This can be put in terms of quantities characteristic of the sublayer, where we take an arbitrary value for y+ which is near the edge of the sublayer to obtain

$$St^+ = \frac{fy^+\nu/u_\tau}{y^+u_\tau} = \frac{f\nu}{u_\tau^2}$$

This yields the traditional inner variable non-dimensionalization of the burst period or

$$\frac{T_B\,U_\tau^2}{\nu} = \frac{1}{St^+}$$

The quantity $1/St^+$ is plotted versus Reynolds number in Figure 125 for the regular and manipulated boundary layers. In this form the event frequencies show some very interesting trends. If we concentrate on the frequencies obtained from the rake of wires, shown as half filled symbols, for which the change in Re_{δ_2} was obtained by changing U_∞, we find the trend denoted by the dashed line in the figure. The slope of this line, both for the regular and manipulated boundary layers, is 1.5. If, however, we measure the burst frequency at one free-stream velocity and increase Re_{δ_2} by increasing the downstream x location, we obtain a different trend as denoted by the solid lines in Figure 125. In the regular boundary layer for both free-stream velocities, the slope of the line is -3/8. The manipulated boundary layers show a slightly steeper slope, however. This is a result of the differences in the C_f distributions, which were shown in Figure 124, and will be accounted for in the next figure. It is clear that both trends must intersect at the x station for the hot-wire rake. The two data values at that station are an indication of the repeatability, albeit from two different probes and two different experimental runs.

The results in Figure 125 clearly indicate that in order to collapse the nondimensionalized burst period we need to introduce two parameters, namely, Re_{δ_2} and Re_x. Without introducing this second parameter we cannot

collapse the data which occur over an overlapping range of momentum thickness Reynolds numbers. Given this insight as to this two parameter system, we can reexamine the data taken by other investigators and look for similar trends.

Figure 126 presents the data from this experiment along with the "burst" frequency data of other investigators who employed a number of detection techniques. The solid symbols, corresponding to the manipulated boundary layers, have been shifted out to their equivalent higher Reynolds number values in this figure (see last section for more details). The scatter of values in this figure is typical of what has been observed in the past. However, if we focus on the data taken with flow visualization by Kim et al. (1971) corresponding to the flagged circles and by Schraub and Kline (1965) corresponding to the flagged squares, in the lower left corner of the figure, we observe consistent trends. The cited data of Kim et al. (1971)was taken with increasing free-stream velocities at a constant x station and it demonstrates the expected upward trend. The data of Schraub and Kline (1965) was obtained at a constant free-stream speed and increasing x locations and it demonstrates the expected downward trend. The consistent trend is observed in the visually detected burst frequency results of Corino and Brodkey (1969) in a turbulent pipe flow. There they obtained an approximate

1.5 power dependence on Reynolds number with increasing velocity. They, however, could not explain the opposite trend exhibited by Schraub and Kline (1965). It is clear from this that early investigators were compounding the problem by indiscriminately changing both of these parameters so as to obtain a range in one of them.

Based on these results, we used our data to obtain the dependence on Re_x required to collapse the curves for the regular boundary layer. That dependence is plotted in the log-log distribution in Figure 127 versus Re_{δ_2}. In collapsing the data for the regular boundary layer we have also succeeded in collapsing all of the data values in the previous figure on the same line with a slope of 5. From this we conclude that

$$St^+ \left(\frac{x}{\delta_2}\right)^5 = \text{CONSTANT}$$

The implications of this result are that in a boundary layer flow which is self-similar by all parametric definitions, the wall layer bulk instability is dependent not only on the characteristics of the layer (δ_2) but also on how you reached these characteristics (x). The relatively large power (5) on these parameters is a result of the near parallel nature of their growth in the boundary layer. In that regard it may be thought of as a non-parallel flow correction to the instability process. The fact that this correlates the results taken over a

range of Reynolds numbers where the boundary layer is fully turbulent and down to Re_{δ_2} = 600, where the flow is transitional, indicates that the mechanisms are the same in both of these flow regimes.

It is only simple to conclude at this point that the large scale structures, which have been studied in great detail over the last 20 to 30 years in laboratory boundary layers, are remnants of the transition process. The turbulent spots observed and documented again in detail during the transition of boundary layer and channel flows must persist well into the turbulent regime. The hairpin-like vortices observed within them must be the same ones that have been captured recently by various techniques in laboratory turbulent boundary layers. However, there is no strong reason to expect these spots to be regenerated in a turbulent boundary layer if they are suppressed by a manipulator.

In presence of these spots or large scales, the wall layer reacts to them by undergoing some violent wall events or "bursts". However, this reaction to the "external" forcing is only part of the sensitivity of the viscous sublayer. The instability of the same viscous sublayer appears to be a continually ongoing process which scales with the inner variables and is dependent on Re_x as well as Re_{δ_2}. The Re_x dependence is not surprising when one considers the instability of this layer dominated by viscous effects from the wall.

The manipulators may then be viewed as a way of "aging" the boundary layer past its post-transition state. This of course leads to the attractive lower C_f values of high Reynolds number boundary layers. If the wall layer instability would lead to large scales like those of the "spots", the return to the original behavior may be forthcoming. Even so, this return may be very slow and net gain for technological devices may be feasible. If the wall generated scales would not lead to such large scales, better performance may be even available to us.

CHAPTER XI

CONCLUSION

The conclusions address two separate but interrelated subjects that were experimentally investigated. First, the main results dealing with the management of turbulent boundary layers with the objective of reducing their drag are summarized. In the second part, the main conclusions describing the new view of turbulent boundary layers which emerged from the detailed measurements are put forth. An extensive discussion of the findings of the experiments is available to the reader in Chapter X and the details of facilities, techniques, flowfields and results are contained in earlier chapters.

The following section will address the various conclusions in detail. However, the major findings can be summarized by the three statements: (i) Turbulent boundary layers can be manipulated by suppressing their large scales and net drag reduction can be achieved, (ii) These large scales, which have been the subject of many recent laboratory investigations, turn out to be remnants of the transition process, i.e., slowly decaying turbulent spots that are imbedded in the boundary layer, and (iii) The wall layer events leading to the production near the surface, which have been termed "bursts", appear to be a result of an instability of the viscous sublayer.

It was then not surprising to find that they are correlated by the two combined parameters Re_{δ_2} and Re_x, rather than by the first one alone, as has been assumed for many years.

Conclusions

The experiment verified that large-scale outer structures defined by the intermittent excursions of high-speed potential fluid into the boundary layer can be suppressed by simple parallel-plate "manipulators". A parametric investigation of the different types of parallel plate devices verified that optimum designs existed for the different configurations of stacked and tandem plate arrangements. A final design consisting of two single plates residing at a height of 0.8δ and spaced 8δ apart in the streamwise direction was chosen for the final set of measurements. This manipulator was selected because it provided the minimum device drag among the arrangements considered and because the plates were well away from the wall layer. The latter criterion was important so that the effect of suppressing the large outer scales on the wall layer events can be examined without the added influence of the plate wakes. Several mechanisms have been identified to explain the operation of these manipulators and are discussed in Chapter X.

As a result of suppressing the outer scales in the turbulent boundary layer with the manipulator, over the

range of Re_{δ_2} from 2000 to 5800, we obtained a decrease in the streamwise growth of the layer and its integral thicknesses. The entrainment velocity was decreased by approximatlely 40 percent in the manipulated boundary layers. Consistent with the reduction in the entrainment was a 30 percent decrease in the local friction coefficient.. After accounting for the drag on the manipulator plates, the net drag reduction in the manipulated boundary layers reached a value of approximately 20 percent within 55 boundary layer thicknesses downstream of the device. Further net drag reduction is likely at farther downstream distances since we see no evidence for recurrence of the large scale at the farthest downstream distance in the test section.

In the absence of the intermittent outer scales, the manipulated layers exhibit a 17 percent thickening of the wall sublayer. Consistent with the this was a vertical translation of the log-linear distribution which has also been observed in boundary layers with drag reducing additives. In addition, the frequency of bursts at the same x location is reduced by a comparable amount. The manipulated layers consistently exhibit a 19% lower u'/U_∞ turbulence intensity in the region below y+ = 100 although they display a higher u'/u_τ distribution over a bulk of the layer, primarily because of their low skin friction.

Various features of the manipulated layers are

consistent with the idea that they emulate higher Reynolds number boundary layers. The wall friction distribution for the manipulated layers is equivalent to that for regular boundary layers in the Reynolds number range from 7000 to 22000 based on the momentum thickness. This concept suggests that by removing the large-scale turbulence, we hasten the "aging" of the flow in a Reynolds number sense and that at higher Reynolds numbers, the large intermittent outer scales are diminished.

With the aid of the manipulators we were able to isolate and focus on boundary layers with comparable outer characteristics and a lower wall friction, i.e., smaller wall variables. This led to a better insight into the mechanisms of the wall layer. Introducing new techniques for objective detection and description of the two-dimensional velocity field near the wall, these mechanisms were documented. These techniques included match filtering, two-dimensional velocity reconstruction as well as digital image processing and pattern recognition.

Correlation of the results established that the frequency of occurrence of coherent wall structures is simultaneously dependent on two parameters, namely on Re_{τ} and Re_x. By forming a Strouhal number, St^+, based on a sublayer thickness and velocity we obtained the familiar inner scaling nondimensionalization of the event

frequency. A correlation between this Strouhal number and the two parameters was formed and used to collapse the results of this investigation for both regular and manipulated boundary layers. For the first time, results of other investigators, over a range of momentum thickness Reynolds numbers from 600 to 38000, are correlated by the resulting relation, i.e.,

$$St^{+}\left(\frac{x}{\theta_2}\right)^{5} = \text{constant}$$

The ratio multiplying the Strouhal number can be thought of as a non-parallel flow correction for the wall layer bulk instability frequency. It further points out that the mechanism governing the coherent motions near the wall must include information about the history or initial conditions of the boundary layer. The fact that this relation correlates the data over the Reynolds number range for fully turbulent flow, and down to transition Reynolds numbers below 1000, confirms that the physical processes near the wall are similar for both of these flow regimes.

Based on the above conclusions, there is little reason to expect these spot-like large scale structures to be regenerated from a turbulent boundary layer after they are suppressed by a manipulator. As pointed out earlier during the discussion, one may view the manipulator as means of "aging" the boundary layer past

its post-transition state. If the wall-layer instabilities would lead to large scales like these "spots", a return to the original trends, including the skin friction coefficient, may be forthcoming. Even so, this return is likely to be very slow and net gain for technological devices may be within our reach. Better performance may materialize if wall generated scales in an "aged" turbulent boundary layer would not lead to such large structures. While in free shear layers, wakes and jets, the mean velocity profiles may provide continuously unstable modes, the outer boundary layer velocity profile is most likely not to do the same. It is conjectured that the main source of instability leading to exponential growth and rapid production of turbulence would continue to be the wall layer, i.e., smaller scales.

Recommendations

The recommendations for further work must include surveys with multiple sensor rakes oriented in the transverse direction and placed close to the wall in order to study the so called "streaky" structure in regular and manipulated boundary layers. Two-dimensional velocity reconstructions and pattern recognition would give an altogether new view of these flow structures and yield quantitative statistics of their spacing with changing wall layer parameters. In particular we can

determine if they scale in accordance with the results for the wall events.

The experiment should also be extended to higher Reynolds numbers and greater distances downstream of the manipulator. Preferably, the Reynolds numbers should fall in the range or exceed the proposed equivalent Reynolds numbers of the manipulated layer so that direct comparisons can be made. In this work, additional velocity surveys farther out in the boundary layer should be conducted in order to calculate the intermittency distribution and determine its Reynolds number dependence. In the present investigation, that data was not available. Pattern recognition may be quite useful in detecting the turbulent/non-turbulent interface at the edge of the boundary layer. It may also be very interesting to subject the manipulated boundary layer flows to strongly adverse pressure gradients in order to see if the large scales reemerge.

In terms of the image processing, a great deal more analysis can be done on the present images. This includes two-dimensional pattern recognition of bursts from the long-view images. In future measurements, however, images more analagous to the Eulerian velocity acquisition of the hot-wire rake can be obtained through the illumination of the smoke along a line by a laser beam and scanning the image across the digital camera with a rotating mirror. This would give the needed time

aspect to the digital images and should yield some very interesting results after digital enhancement and frequency analysis.

APPENDIX A

INSTRUMENTATION DESIGN CONFIGURATION

As indicated in Chapter II, a rake of 11 hot-wires was used to spatially sample the velocity field in the turbulent boundary layers. It was cost and space prohibitive to utilize commercially available constant temperature anemometers, to operate the hot-wires or amplifiers and low-pass filters, to pre-condition the analog signals before digitization and acquisition. We therefore designed and built constant temperature anemometers and analog signal conditioners which were low in cost and compact in size. The latter criterion was important because we wanted to place the anemometer circuitry relatively close to the sensors in order to minimize electronic noise and provide frequency compensation for the cables which connected the anemometers.

The circuit diagram for the CTA was shown in Figure 5. The etch pattern for that circuit is shown on the top of Figure 128. This was designed for single-sided, copper-clad printed circuit board. The photo negatives of this pattern were placed together, in line, in groups of three so that the parallel lines formed a continuous connection. These lines carried the ±15 volt supply to the individual circuits. This arrangement was used as the pattern on a 6 x 22 cm photo-negative printed circuit board from which the copper was etched to leave the

conducting lines indicated by the black regions in this figure. Two of these boards, containing six anemometers, were stacked in an 8 x 8 x 28 cm component box which contained the required BNC connectors and switches. A total of 3 complete sets, corresponding to 18 channels, were built during this experiment.

Included with each group of six anemometers was a square wave generator based on a 7405, Hex-inverter. The etch pattern for that simple circuit is shown in the middle of Figure 128. This was sucessively connected to each anemometer bridge through a rotary switch, which also connected the anemometer output to a common BNC for monitoring the response during feedback adjustments to the anemometer bridge. The square wave generator was turned off after adjustments were completed.

The pre-conditioning of the analog outputs from the anemometers was done by the bias/gain/filter circuit shown in Figure 7. The etch pattern for each channel of that circuit is shown on the bottom of Figure 128. In this case, six channels were compactly fit into a 15x8x25 cm. component box. Each channel utilized external connectors to allow for different feedback resistors to set the gain of each amplifier stage. Also, each channel incorporated a single rotary switch which simultaneously connected two sets of matched precision resistors to change the cut-off frequency of the low-pass filter. The phase and frequency characteristics of all of the filters

designed in this experiment were adjusted to give the identical response to that shown in Figure 7. External connectors were also available on the component box to allow for the use of different resistor combinations for different frequency cut-offs.

In all three circuits, special attention was placed on keeping electronic noise to a minimum. In this regard, all power inputs to the generator amplifiers were DC coupled with .01 μf capacitors. Also, all external leads were properly shielded so as not to be sources of power line noise.

APPENDIX B

SUMMARY OF RESULTS FROM A PARALLEL EXPERIMENT

A parallel experiment on the control of the large-scale intermittency in a turbulent boundary layer was performed by H. Nagib, in collaboration with R. Westphall, during the period from December 1980 to February 1981, while on sabbatical leave at the HTTM Laboratory of the Mechanical Engineering Department of Stanford University. In that work, a turbulent boundary layer was developed on one wall of a 2.4 m long wind-tunnel test section which had been adjusted to give a near zero streamwise pressure gradient. The cross-sectional dimensions of the tunnel were 0.2 m by 0.3 m with the measurements being performed on the longer dimensioned side. The point of transition to turbulent flow was fixed at the entrance by sandpaper in a manner similar to that used in this investigation. The turbulent manipulator consisted of two 0.25 mm thick plates which were suspended in the tunnel in an arrangement of the M-4 type,i.e., very similar configuration as that of the final results of the present investigation. The streamwise chord of the plates was approximately equal to the boundary layer thickness, δ, as their distance from the wall was approximately 0.5δ. The streamwise spacing between the plates corresponded to δ as in the present investigation. Therefore, the main difference in the design of the manipulator in the two

investigations is the elevation of the two tandem plates from the wall. Here we used 0.8δ while Nagib used 0.5δ.

The manipulator was placed in the boundary layer at the streamwise location x = 1.3 m where the Reynolds number based on the momentum thickness was approximately 1700. The free-stream velocity was 10.6 m/s and the turbulence intensity at that speed was approximately 0.5 percent. The free-stream velocity fluctuations were mainly a result of low frequency contributions.

The measurements consisted of mean velocity and turbulence intensity profiles which were analyzed to provide the mean properties of the flow including the integral thicknesses, shape factors, and friction coefficients. These were obtained for 9 stations along the streamwise centerline as well as 2 off center stations. In addition to the mean profiles, pulsed-wire probe measurements were made near the wall at each of these locations to evaluate the mean wall-friction coefficients, their rms and probability density functions. The hot-wire and pulsed-wire data were acquired digitally and stored on floppy disks. The data presented here are based only on the hot-wire data and were processed at IIT using the same routines developed for this investigation. Various problems were encountered with the acquisition and interpretation of the pulsed-wire data and, therefore, they are not summarized here.

Smoke-wire visualization was also employed to give visual evidence of the performance of the turbulence manipulator and to aid in optimizing the device. The results to follow are intended to summarize the work of that study. Additional details may be published later on this parallel effort. In particular, the evidence from the smoke wire visualization in the form of photographs is very similar to that presented here.

Figure 129 documents the mean velocity and turbulence intensity profiles just upstream of the streamwise location of the device. The dashed and solid lines in the figures correspond to the distributions with and without the manipulator in place, respectively. In all these figures, the mean and rms velocities are non-dimensionalized with the local free-stream velocity. This independence of the initial conditions from the presence of the manipulator is amply verified by this figure.

The distributions just downstream of the device ($x/h=2.3$) are shown in Figure 130. These clearly show the wake of the manipulator plates. Also evident is the lower u'/U_∞ values in the manipulated boundary layers, which was also observed by Corke et al. (1980) for the four-plate manipulator. The velocity defect in the manipulator wakes was larger in this work by Nagib because of the somewhat thicker plates and larger chord lengths. As will be seen, this will result in a somewhat

smaller net drag reduction in this investigation for a distance from the device comparable to that for the present work. This added drag is also evident in the larger increase in Re_{δ_2} for the manipulated boundary layer at the same free-stream speed, i.e., larger increase in momentum thickness due to the device.

Farther downstream of the device in Figures 131 and 132, the wake of the device be dissipated by the turbulence in the boundary layer. By 21 device heights downstream of the manipulator in Figure 131, the momentum thickness in the manipulated layer is still somewhat larger than in the regular case but it clearly is not growing as quickly. By the last station, 90 device heights downstream, the mean velocity profile demonstrates the same characteristic differences as shown in Figures 25 and 26 of the present work. The lower turbulence intensity in the outer part of the boundary layer indicates a reduction in the velocity fluctuations associated with the large scale excursions of turbulent fluid away from the wall. By this station, the momentum thickness is less than that exhibited at the same x-location in the regular layer; i.e., without the device.

The Reynolds number distribution of the local wall-friction coefficients is shown in Figure 133 for the regular and manipulated boundary layers. The results of Nagib are plotted along with the C_f distributions

obtained from the present investigation. The values for C_f for Nagib's data were obtained from the same momentum balance software written for the present investigation and summarized in Chapter IV. The values for the regular boundary layer fall in close agreement with average values obtained for the present results. The error bars for those data points correspond to the range of values obtained from the momentum balance, the Clauser log-fit and the Ludwieg-Tillmann correlation.

The results in the manipulated boundary layer demonstrate a comparable reduction in the local friction coefficient to the results of the present work. The error bars in these data points are a result of uncertainty in measuring dP/dx along the test section. In one limit, the C_f distribution was calculated utilizing the momentum balance with the streamwise pressure difference of zero set to an accuracy of 0.03 mm of water by Nagib over the entire length of test section. The other limit of the error bars was obtained for the dU/dx distribution which was returned from the analysis and is based on the hot-wire readings in the free stream. Both values show approximately 30 percent reduction in the local friction coefficient. If we include the added drag of the device, based on its momentum defect, the results of Nagib indicate a net drag reduction of approximately 15 percent with a fetch of less than 60 boundary layer thicknesses.

The results of this experiment by Nagib demonstrate, in a separate facility, the effectiveness of the series type manipulator in reducing the drag in turbulent boundary layers. They further substantiate the findings of the present work and document the effects of altering the intermittent scales in a turbulent boundary layer. Finally, they clearly identify one of the mechanisms of this type. The reduction in turbulence level beneath and in the lower part of the plate wake, depicted in Figure 130, is very important to the operation of these devices. Here we can see that the transfer of energy to the mean flow in that part of the wake is partly balanced by a transfer back into the turbulence from the mean flow above the plate elevation. The change in the sign of across the perturbation introduced to the equilibrium boundary layer flow in the form of the wake is a very important ingredient to this two-way transfer. While the reduction of turbulence near the wall is the important ingredient, this two-way transfer may make its implementation very efficient.

APPENDIX C

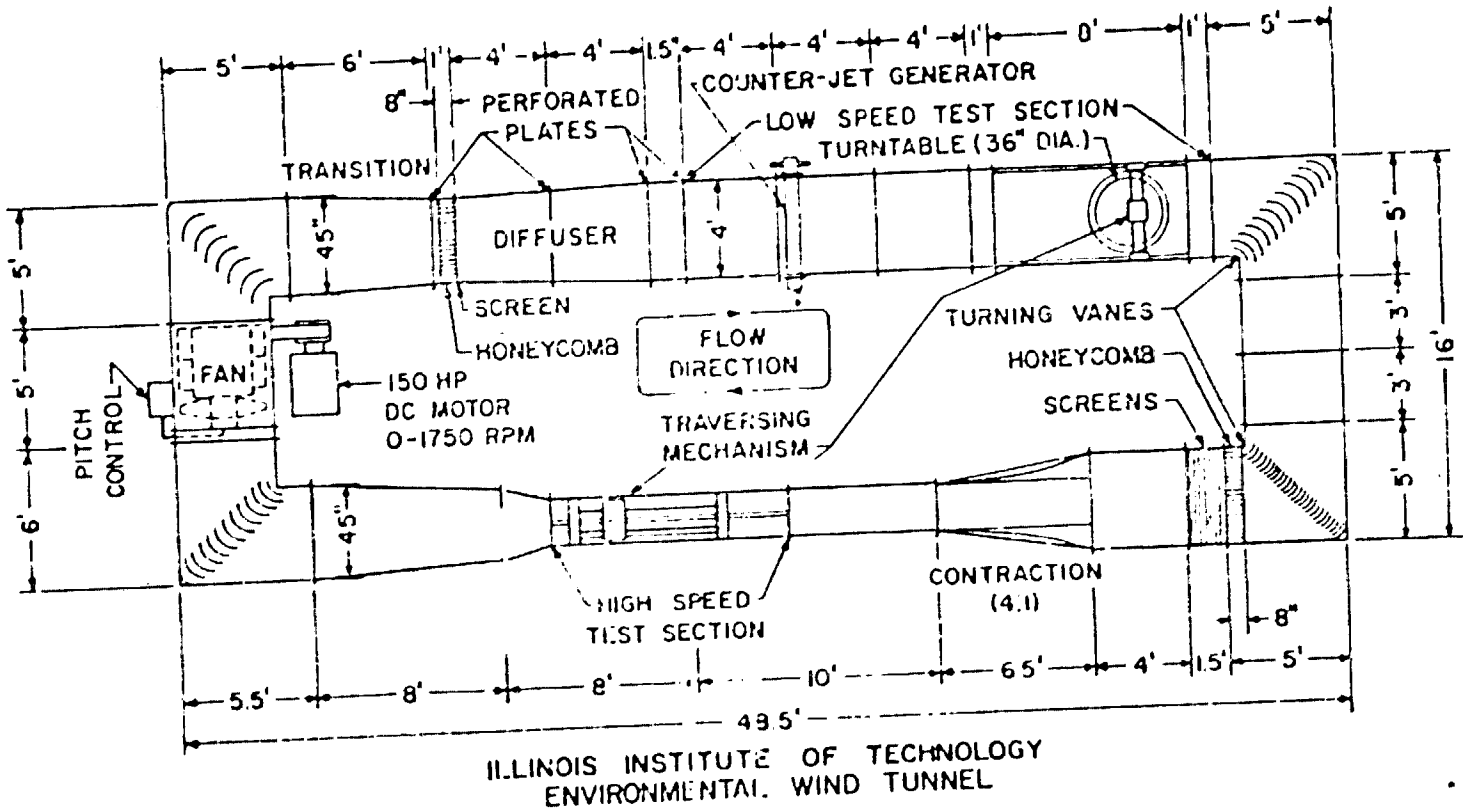

Figure 1. Plan-View Schematic of IIT Environmental Wind Tunnel Showing Newly Lengthened High-Speed Test Section.

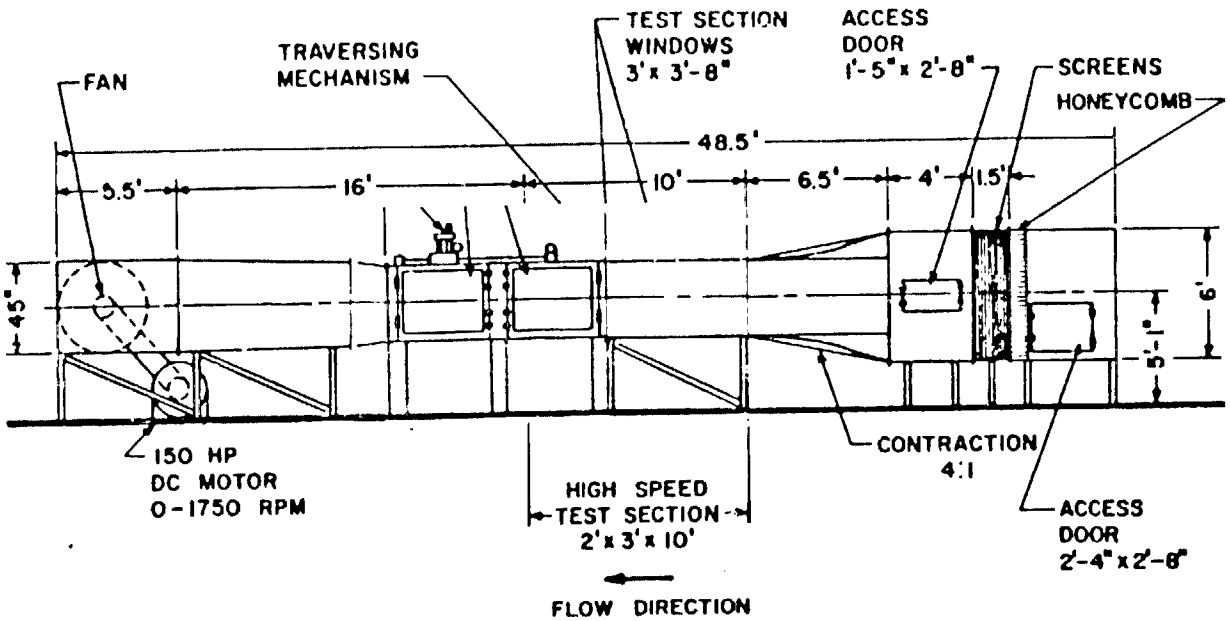

Figure 2. Side-View Schematic of High-Speed Test Section

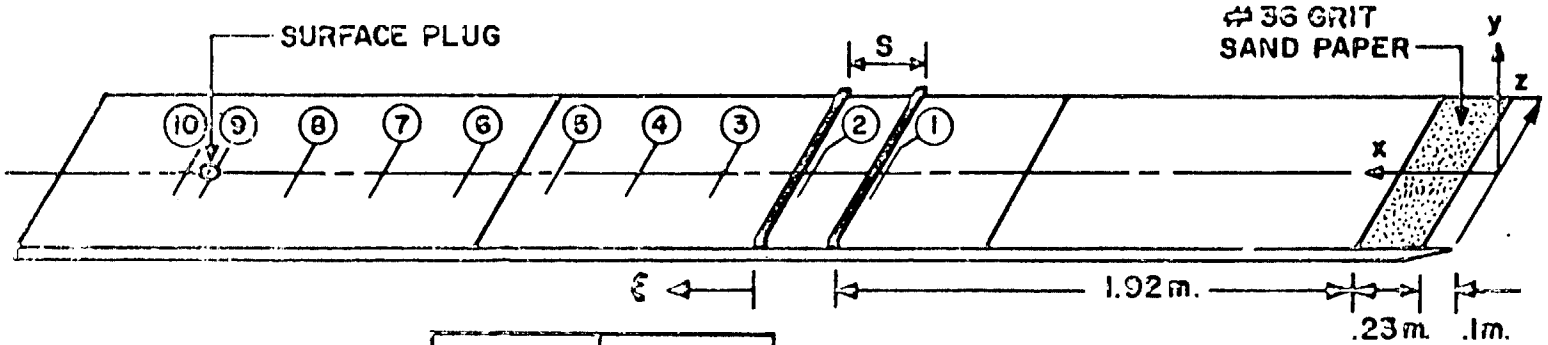

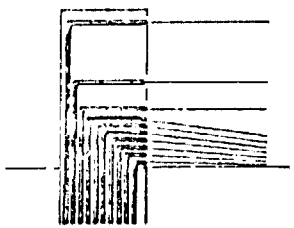

STATION #	X (m)
1	2.25
2	2.46
3	2.76
4	3.07
5	3.37
6	3.68
7	3.98
8	4.09
9	4.59
10	4.68

M-4

$h_1 = h_2 = 0.8(3 \text{ all}) = 3.2$ cm.

$\ell_1 = \ell_2 = 3.2$ cm.

$S = 8h_1 = 25.4$ cm.

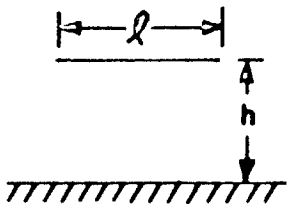

Figure 3. Schematic of Boundary-Layer Plate Showing Measurement Stations and Two Tandem Manipulator Plates

ORIGINAL PAGE
BLACK AND WHITE PHOTOGRAPH

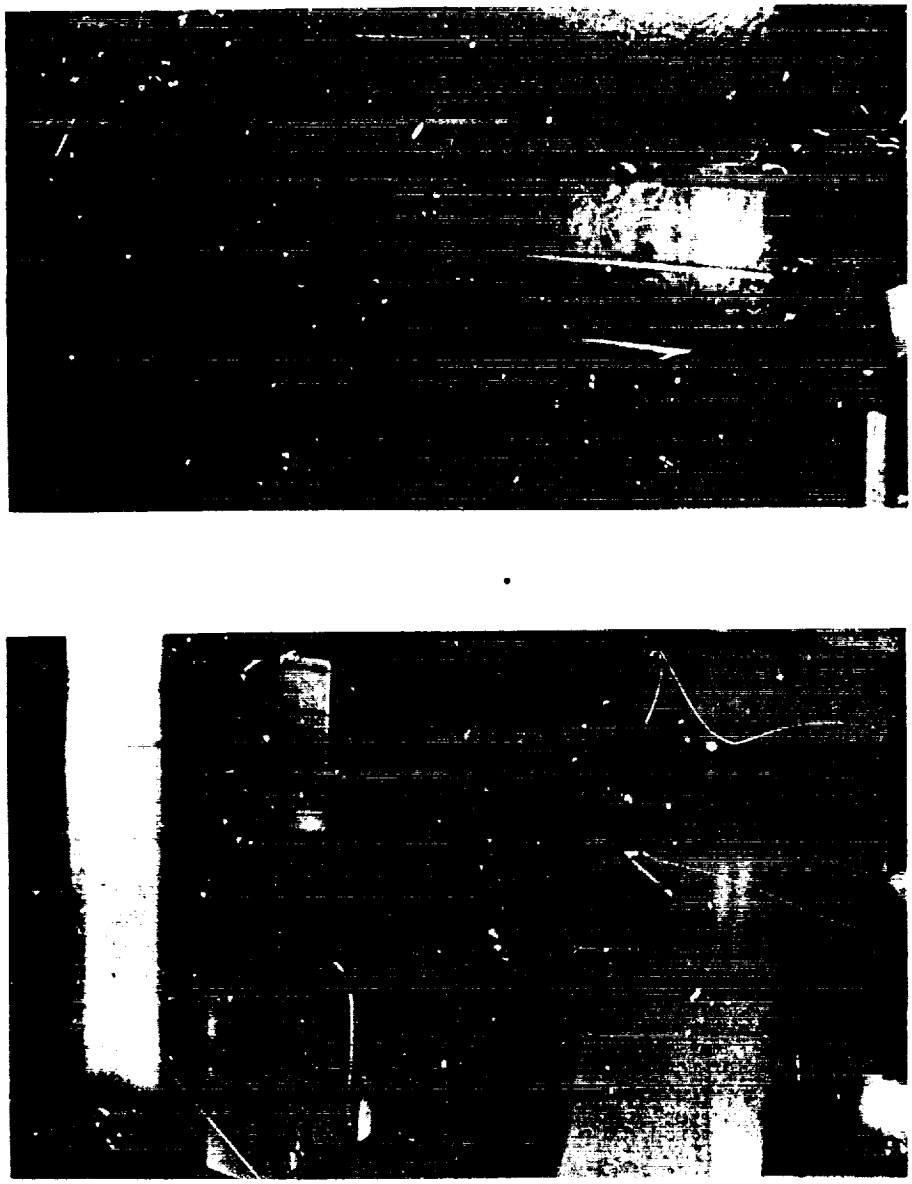

Figure 4. Photographs of Series Manipulator (top) Suspended Above Boundary Layer Plate in Wind Tunnel, and of Surface Plug with Rake of Hot-wires and Shear-Wire

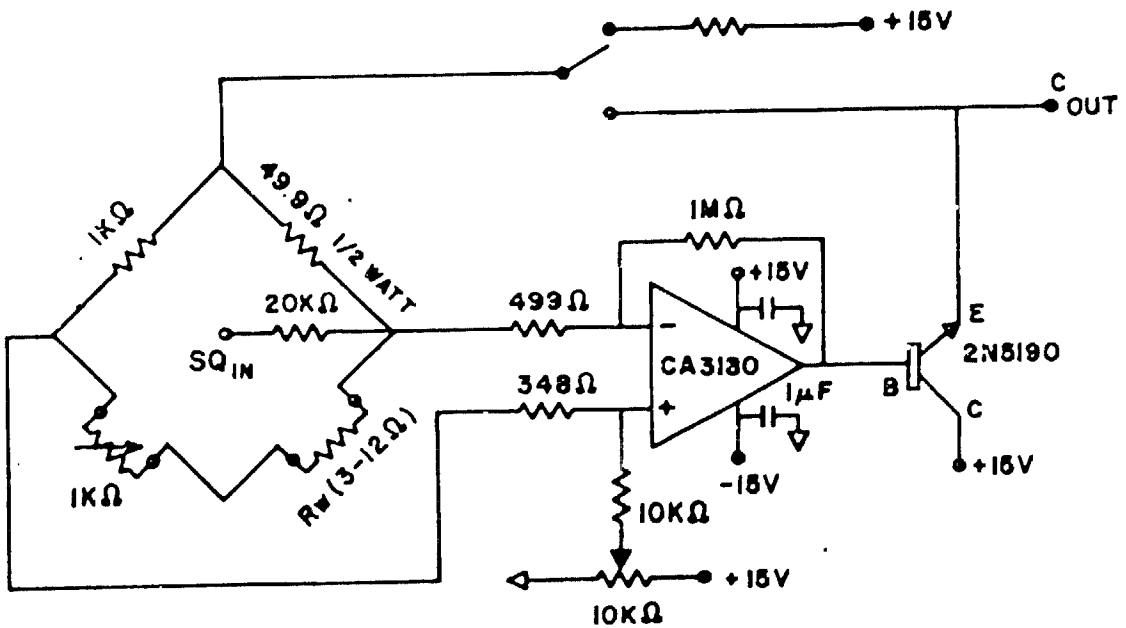

Figure 5. Circuit Diagram of Constant Temperature Anemometers Used in 12-Channel System

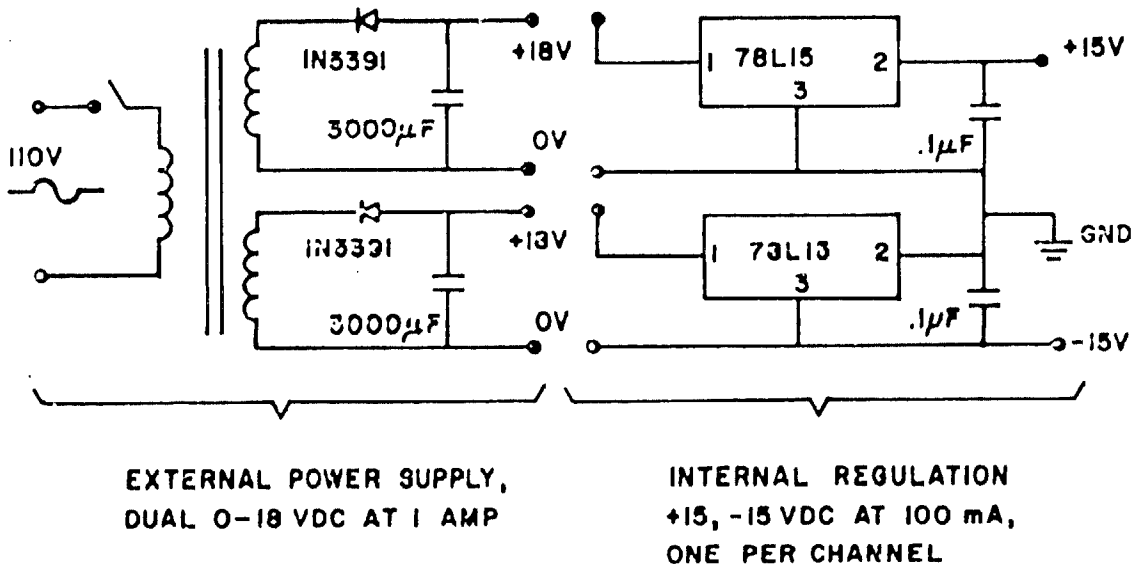

Figure 6. Circuit Diagram of DC Power Supply Used for 12-Channel C.T.A.

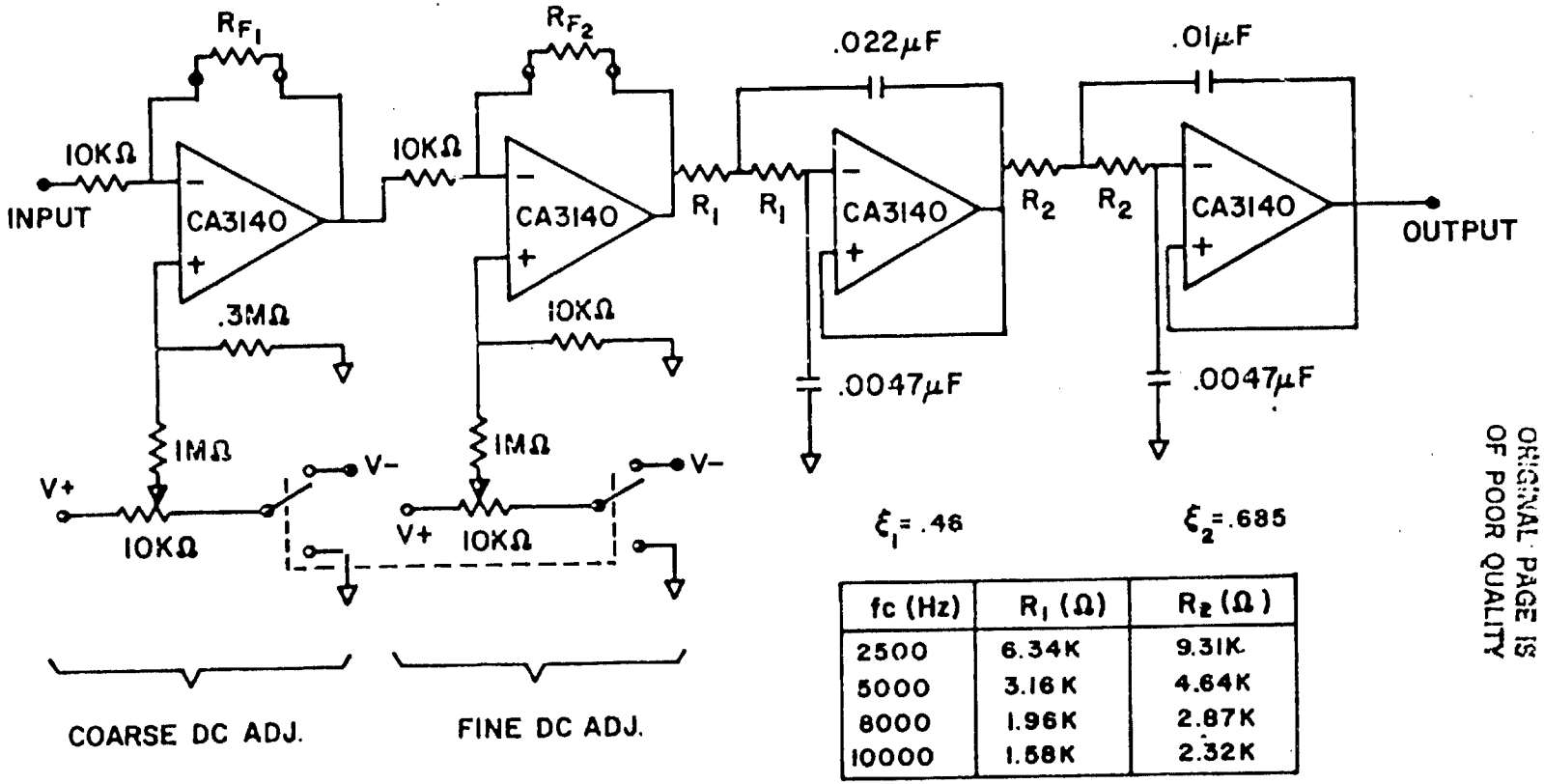

fc (Hz)	R_1 (Ω)	R_2 (Ω)
2500	6.34K	9.31K
5000	3.16K	4.64K
8000	1.96K	2.87K
10000	1.58K	2.32K

Figure 7. Circuit Diagram of Variable DC Bias Amplifiers and Low-Pass Filters Used to Preprocess Analog Signals Before Digitization

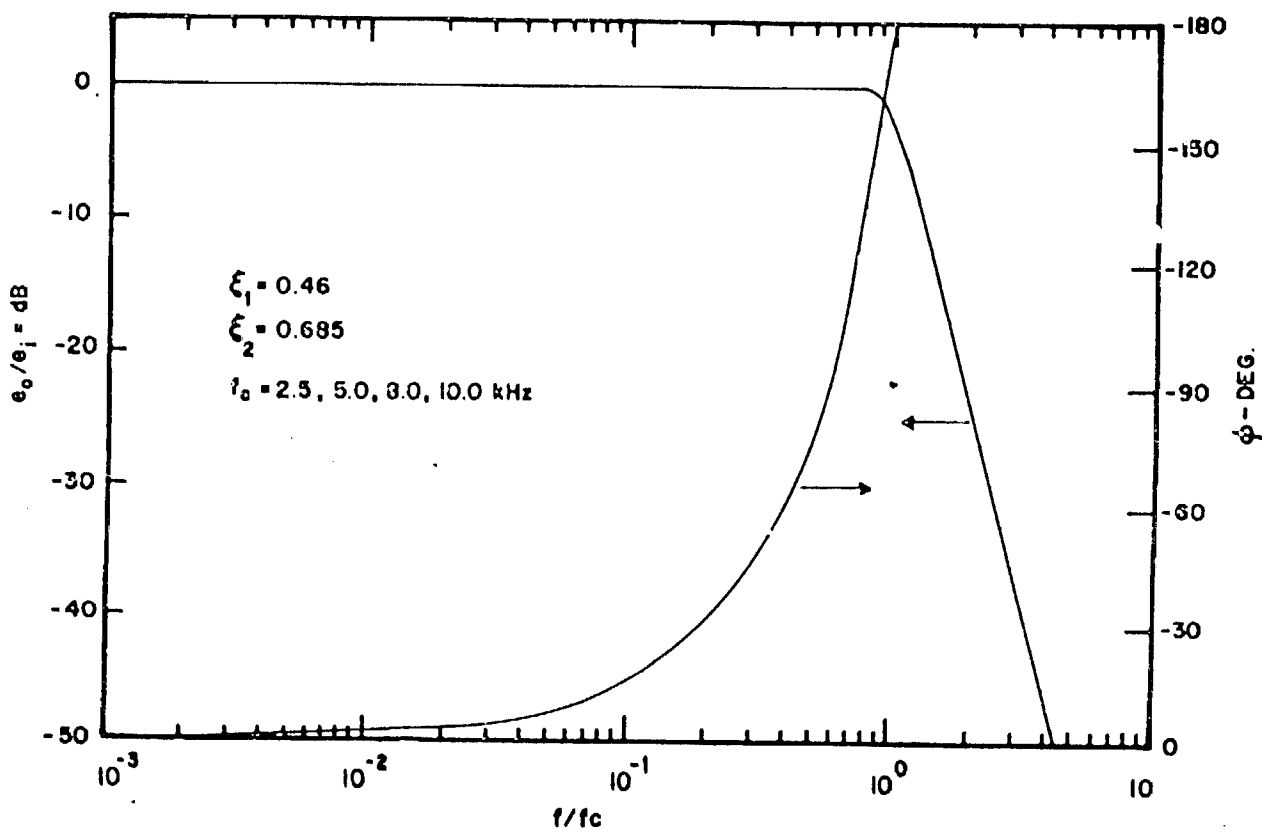

Figure 8. Frequency Response Curves for Second-Order Butterworth Low-Pass Filters Shown in Figure 7

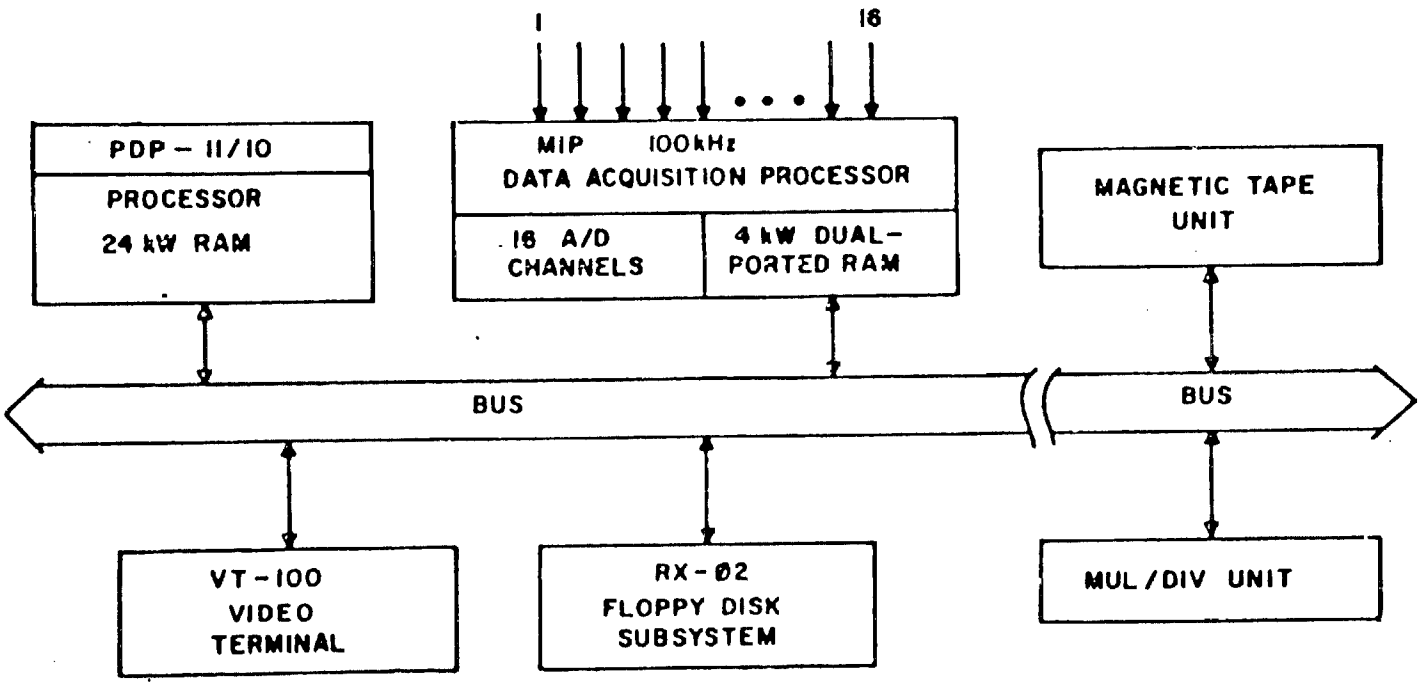

DAPS FAST ACQUISITION SYSTEM (FAS)

Figure 9. Schematic of PDP-11 Based Fast Acquisition System

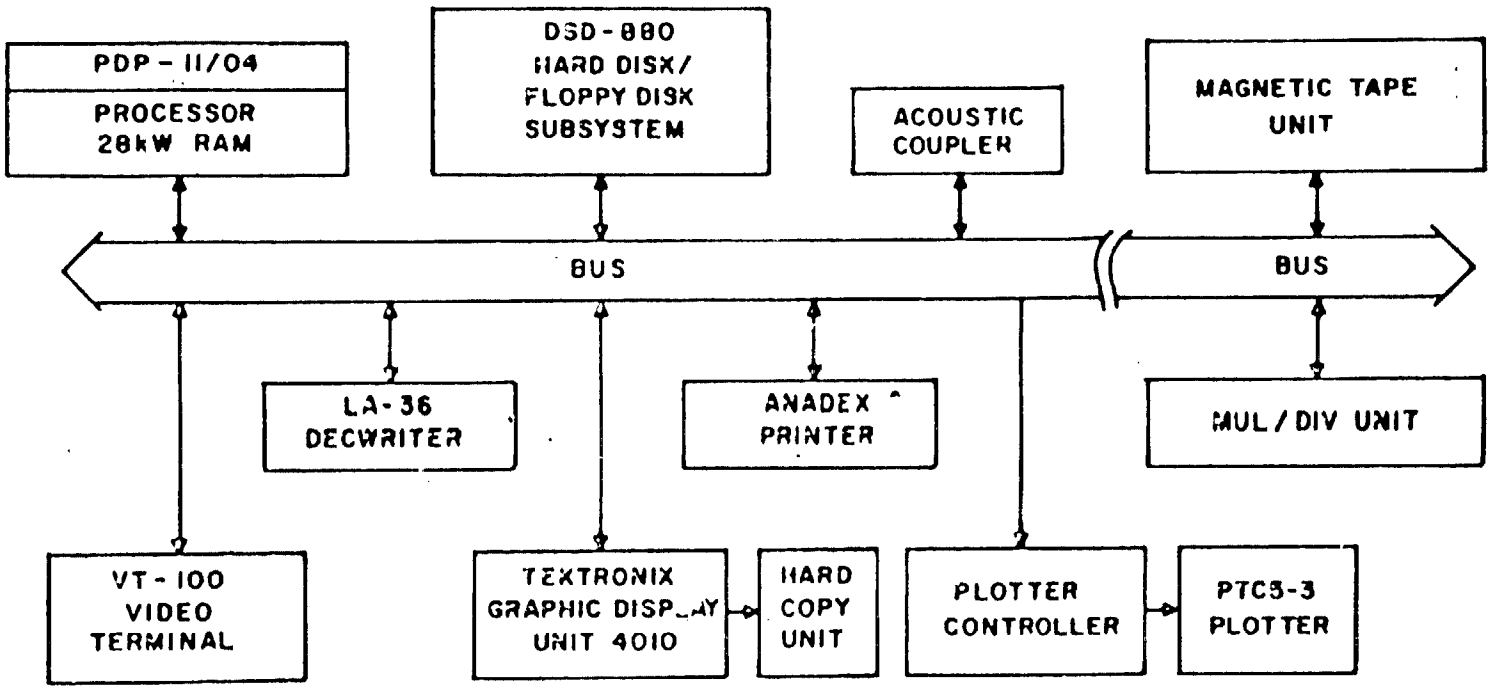

Figure 10. Schematic of PDP-11 Based Software Development and Data Processing System

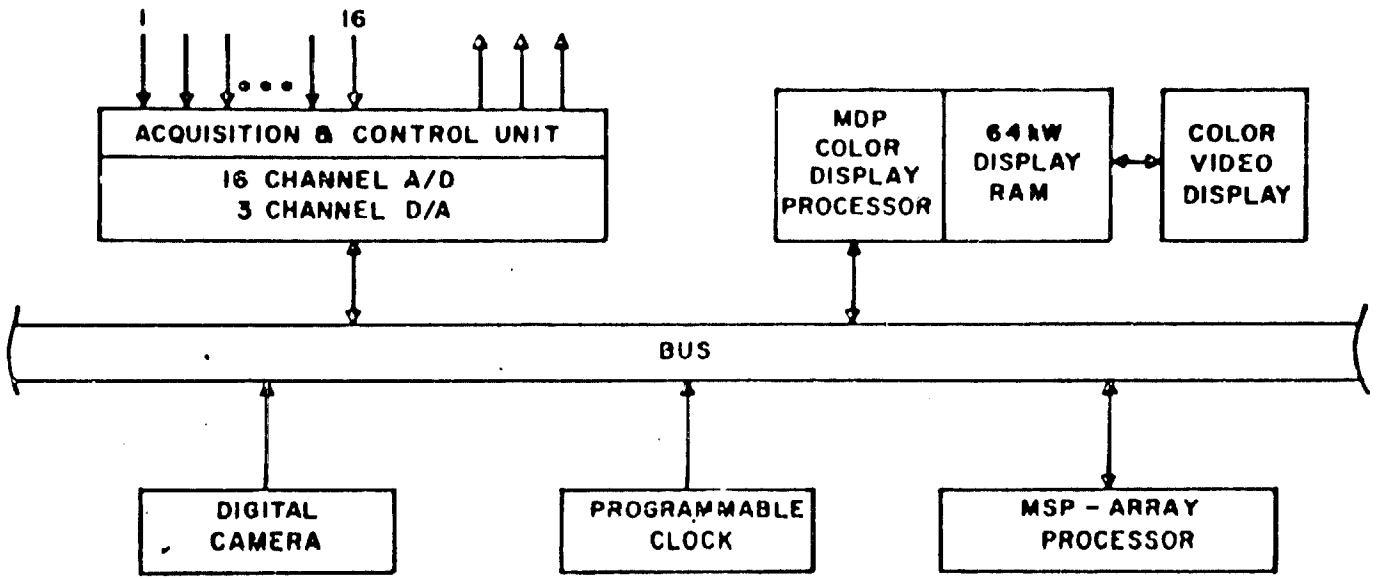

DAPS SPECIAL PURPOSE MODULE (SPM)

Figure 11. Schematic of Special Purpose Module Containing Microprocessor-Controlled Array and Display Processors

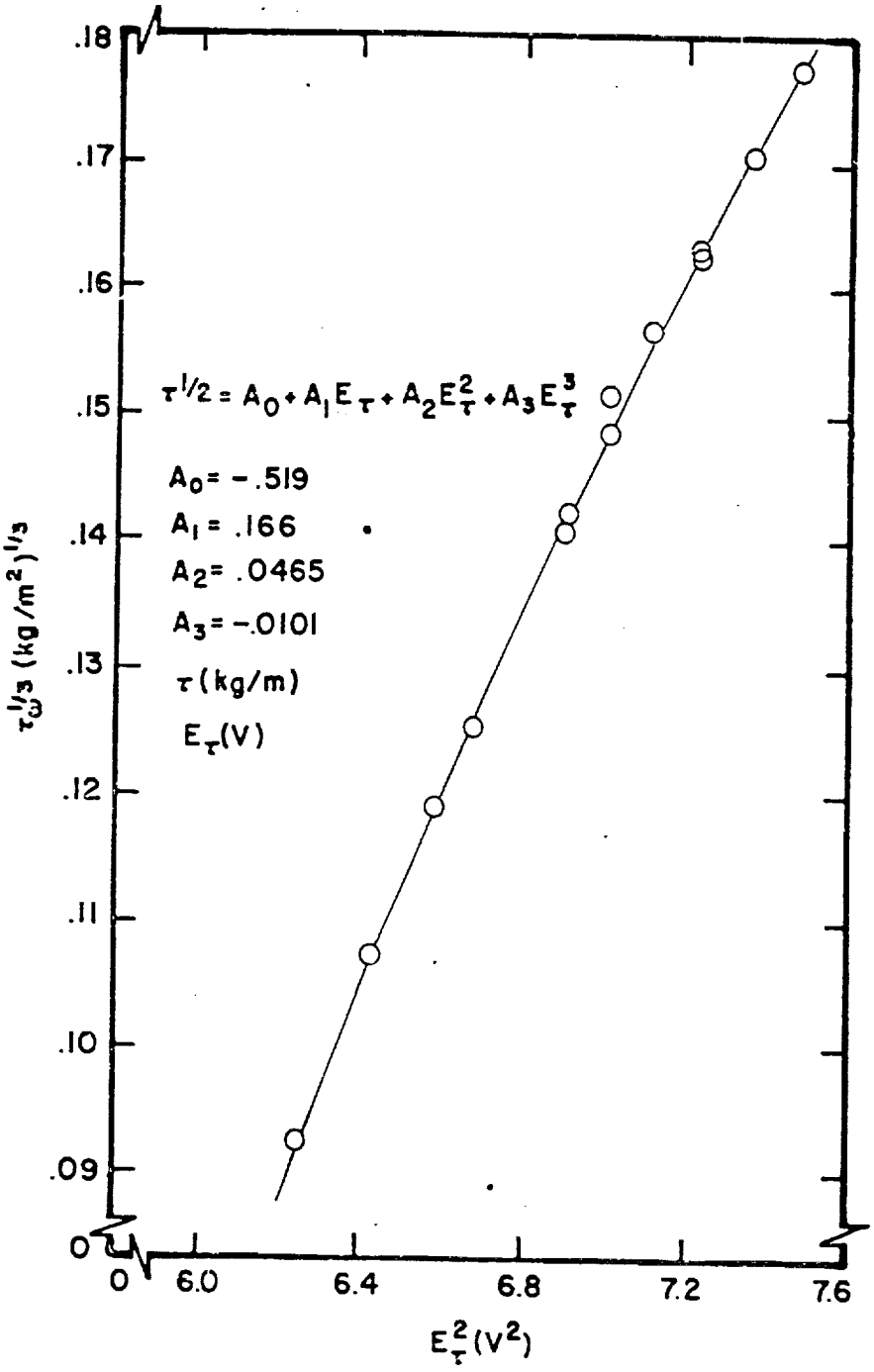

Figure 12. Calibration Curve for Surface Mounted Hot-wire Shear Stress Sensor

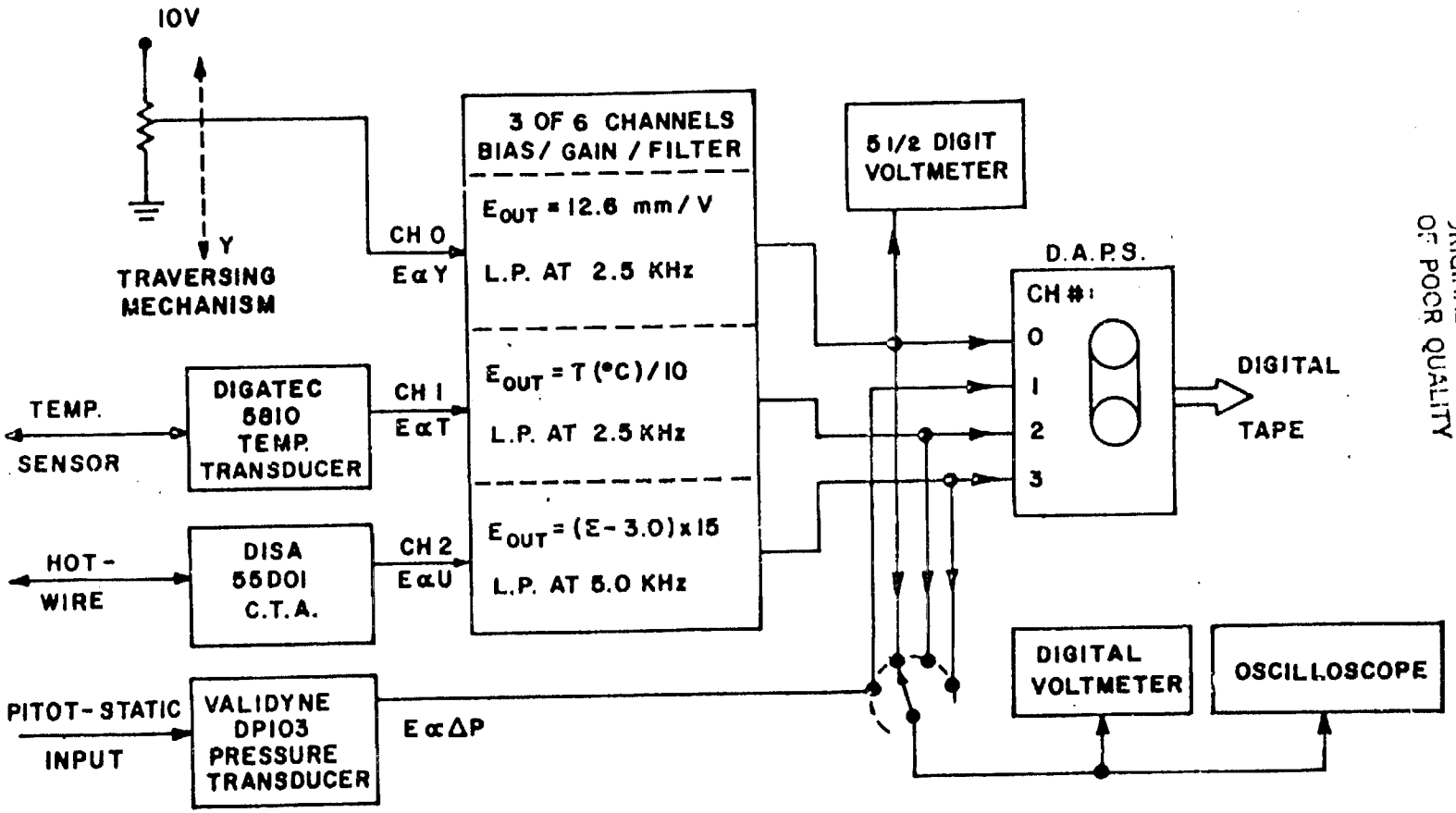

Figure 13. Schematic of Instrumentation Used in Mean Profile Measurements

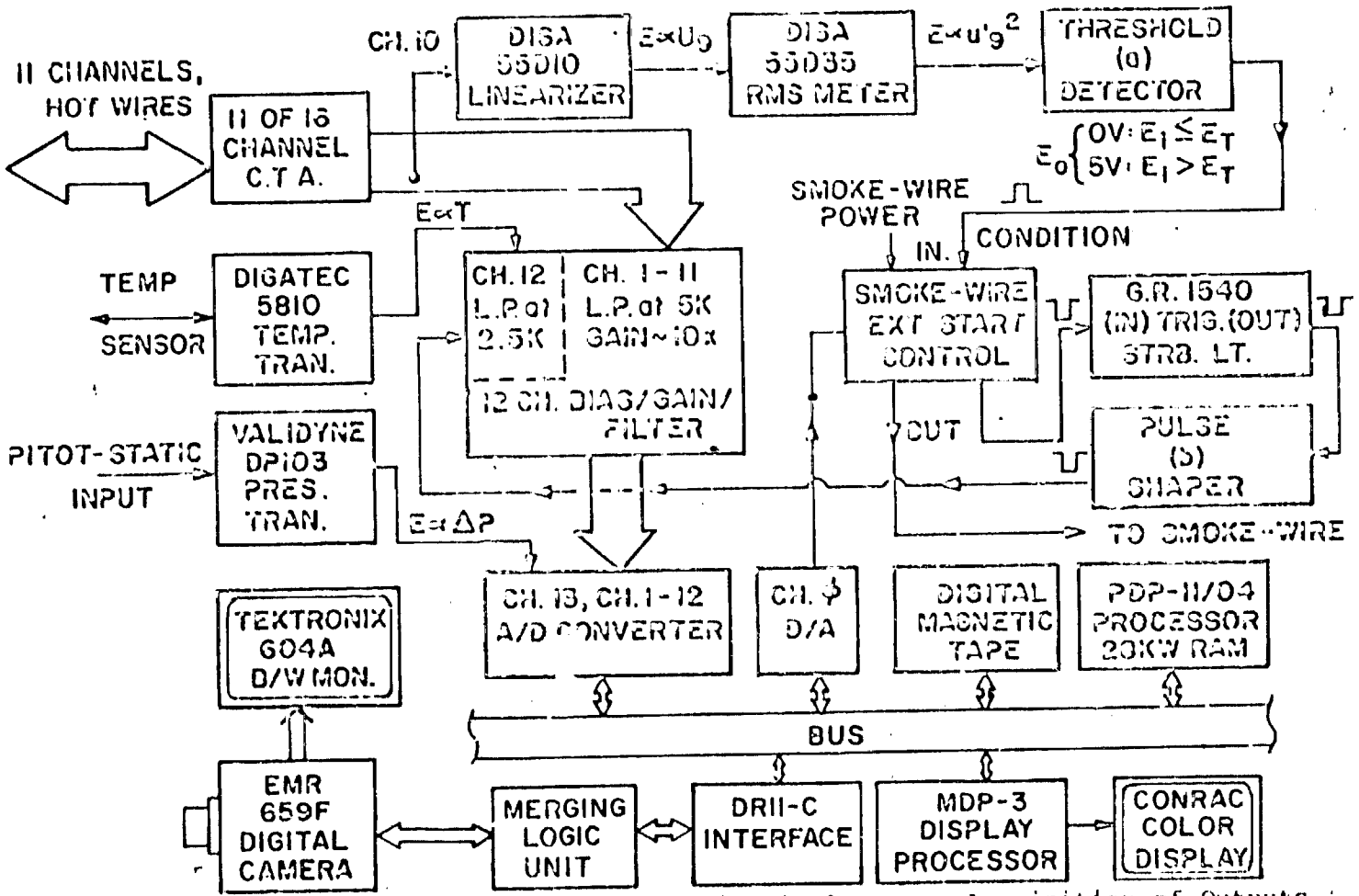

Figure 14. Schematic of Instrumentation Used in Simultaneous Acquisition of Outputs from Hot-Wire Rake and Digital Camera

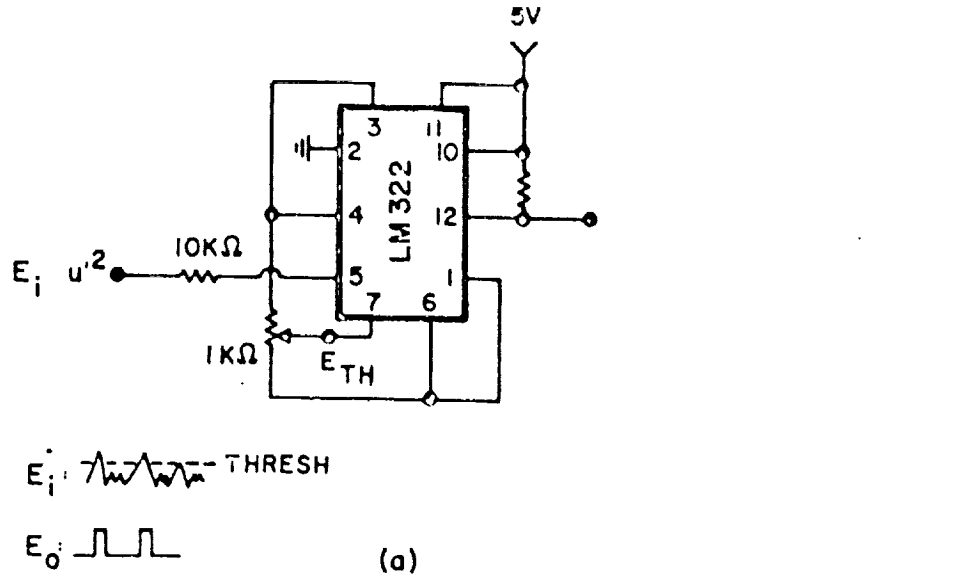

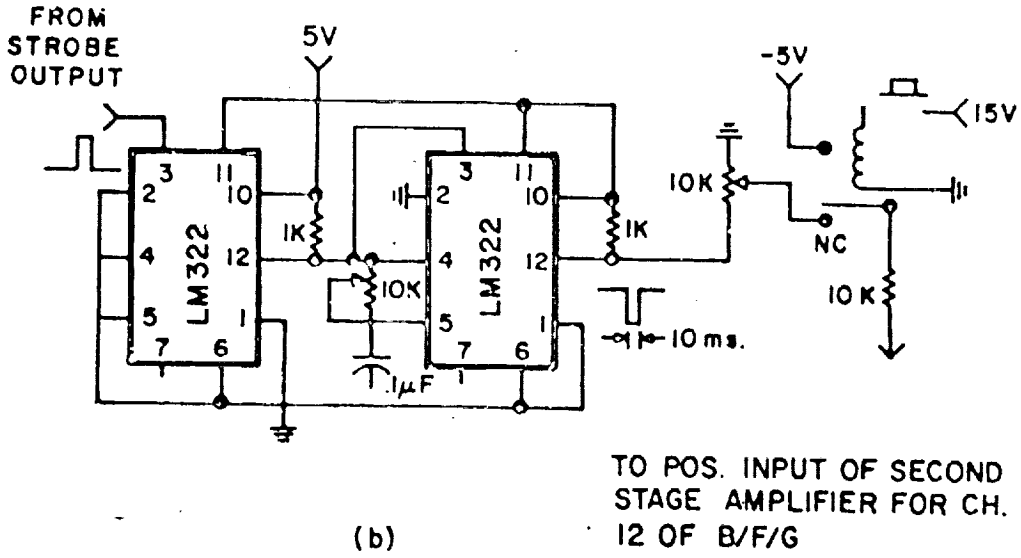

Figure 15. Circuit Diagrams of Threshold Detector (a) and Strobe Output Signal Conditions (b) for Instrumentation Schematic of Figure 14

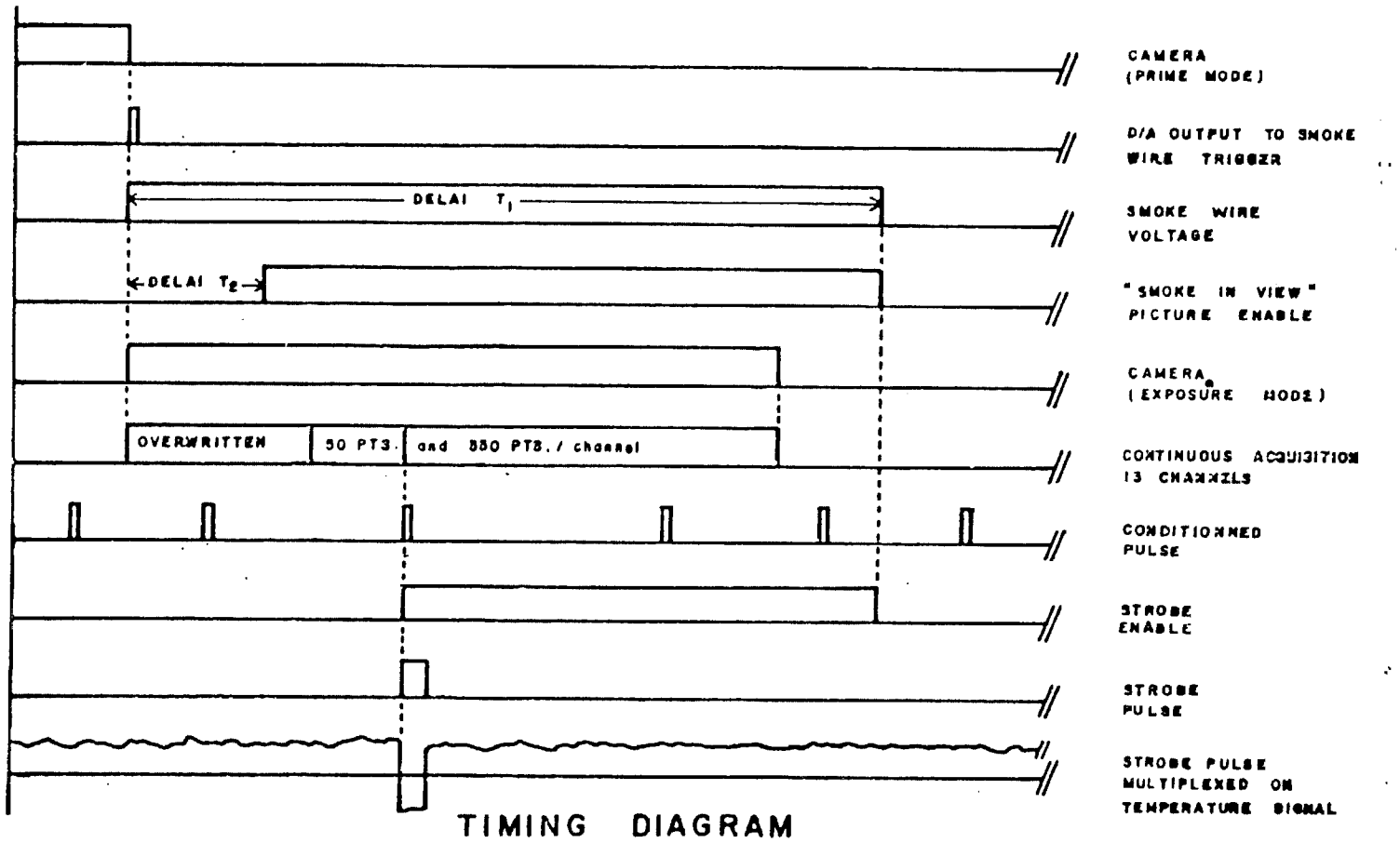

Figure 16. Timing Diagram for Conditioned Acquisition Sequence of Outputs from Hot-Wire Rake and Digital Camera

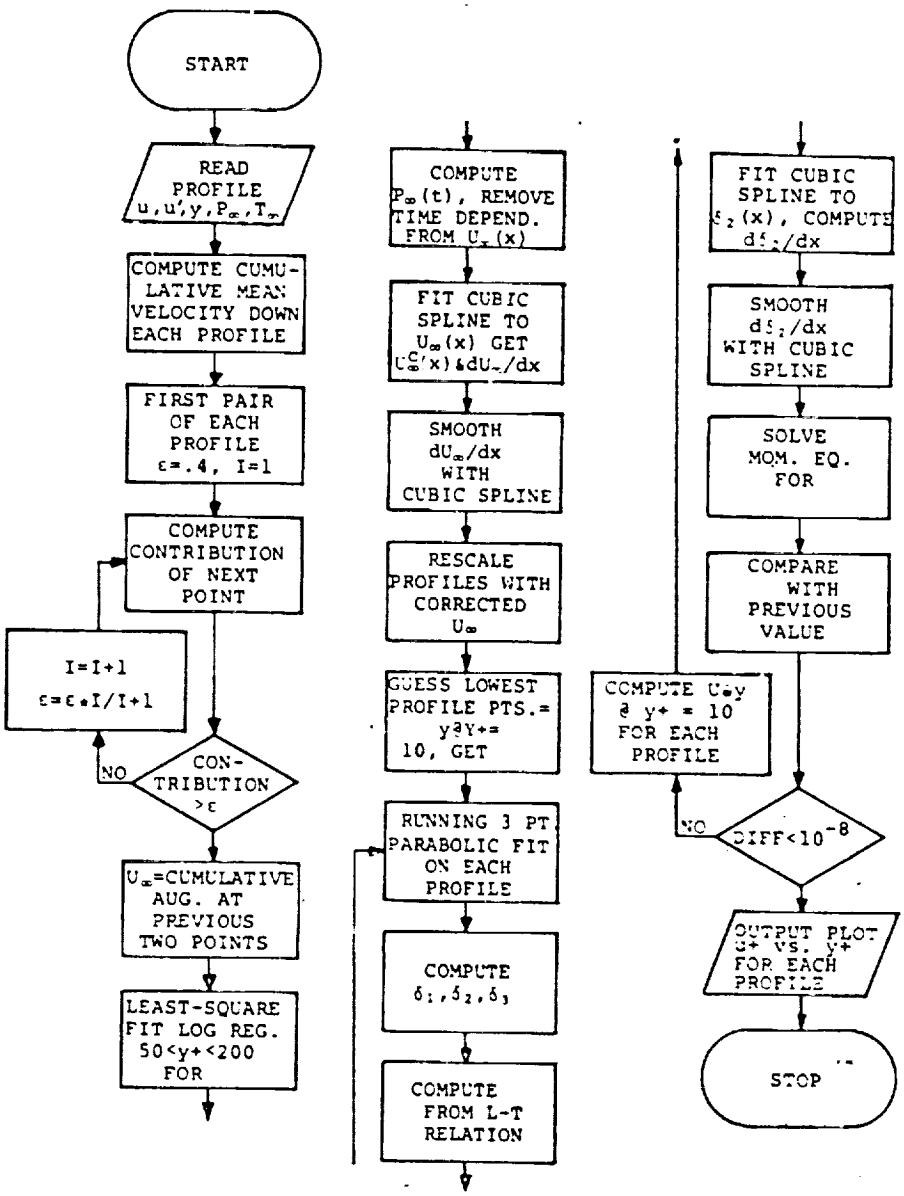

Figure 17. Flow Chart Representation of Computational Method Used to Determine the Wall Shear from Momentum Balance

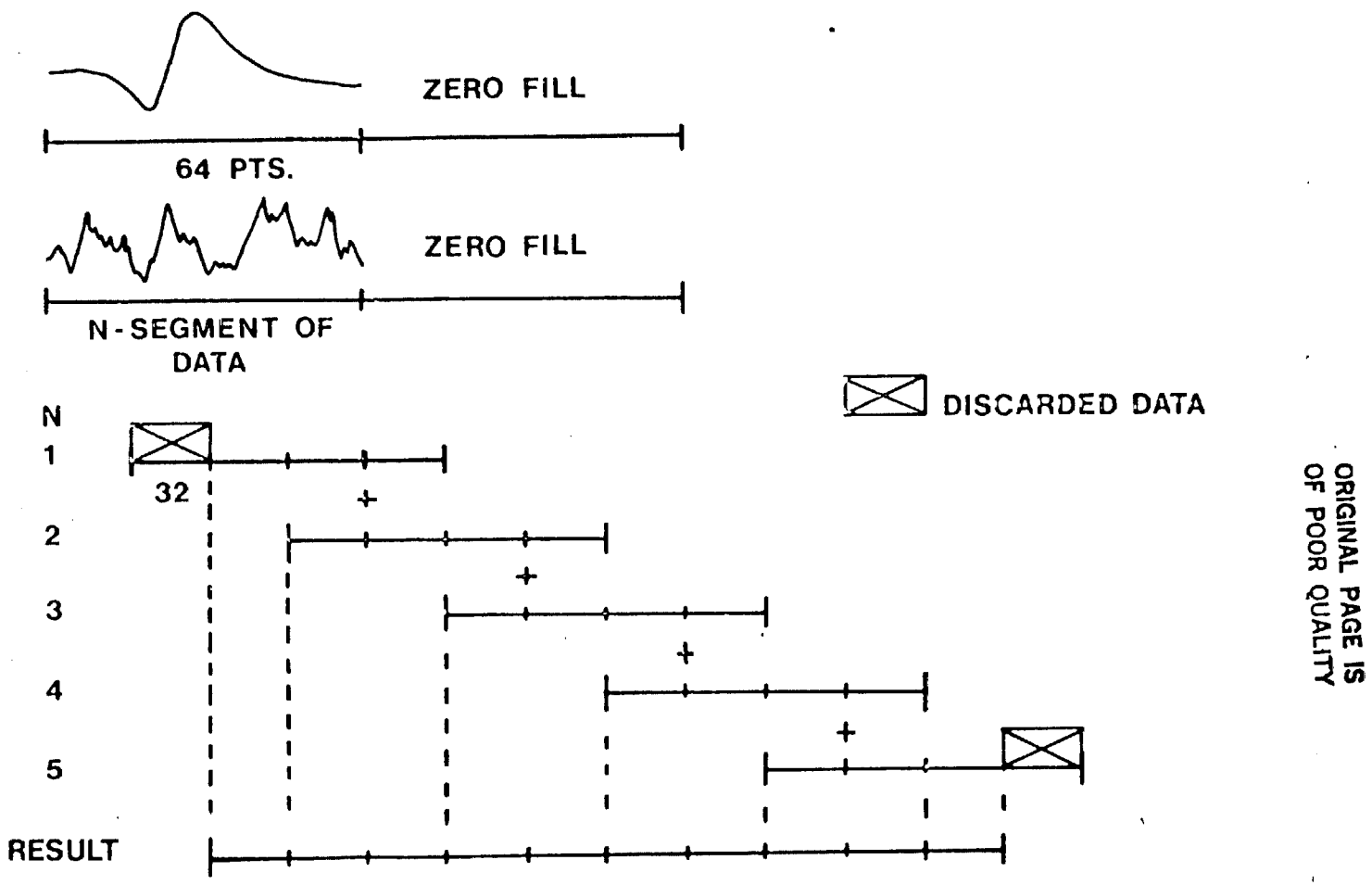

Figure 18. Schematic of Data Handling of One-Dimensional Match Filtering Method for Detection of Wall Events

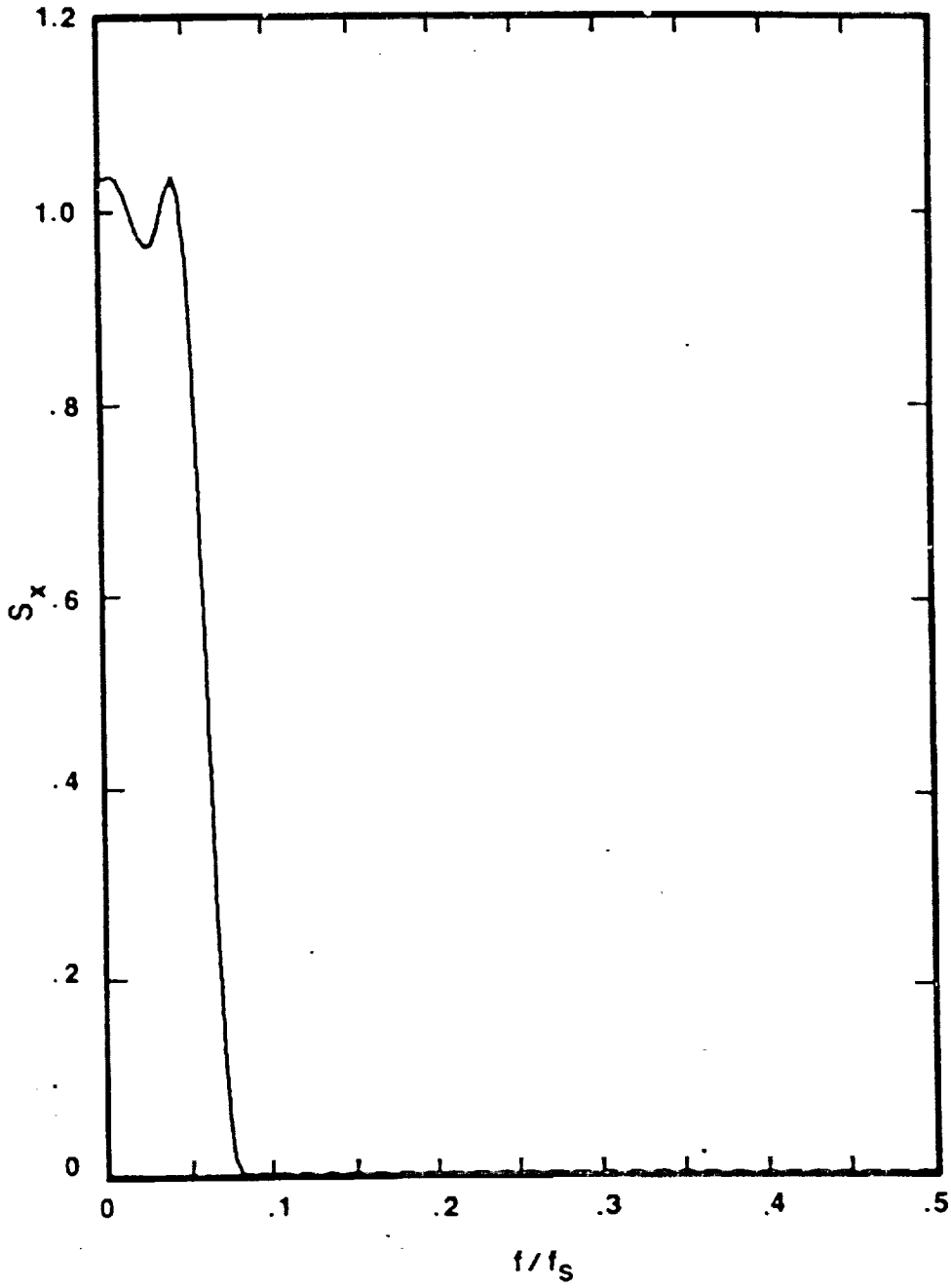

Figure 19. Spectrum of One-Dimensional Low-Pass Digital Filter Function

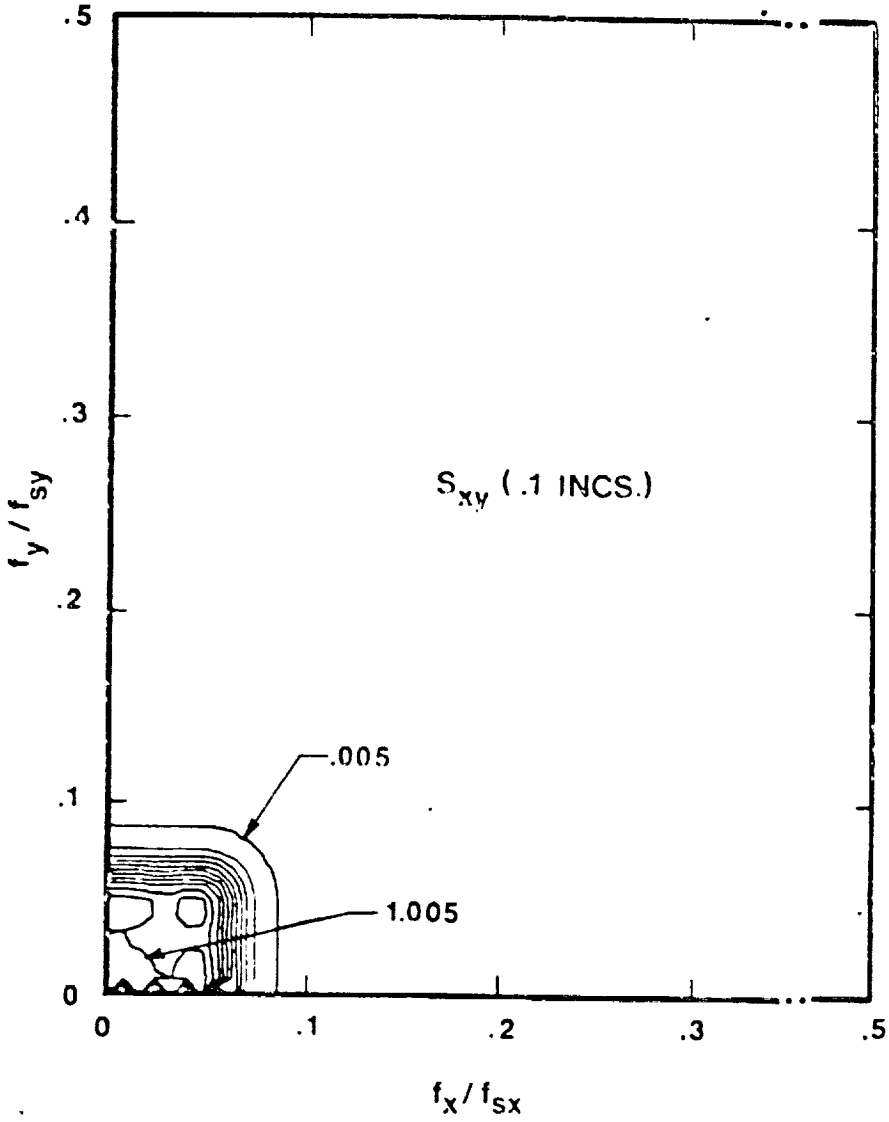

Figure 20. Spectrum of Two-Dimensional Low-Pass Digital Filter Function Generated from One-Dimensional Filter of Figure 19

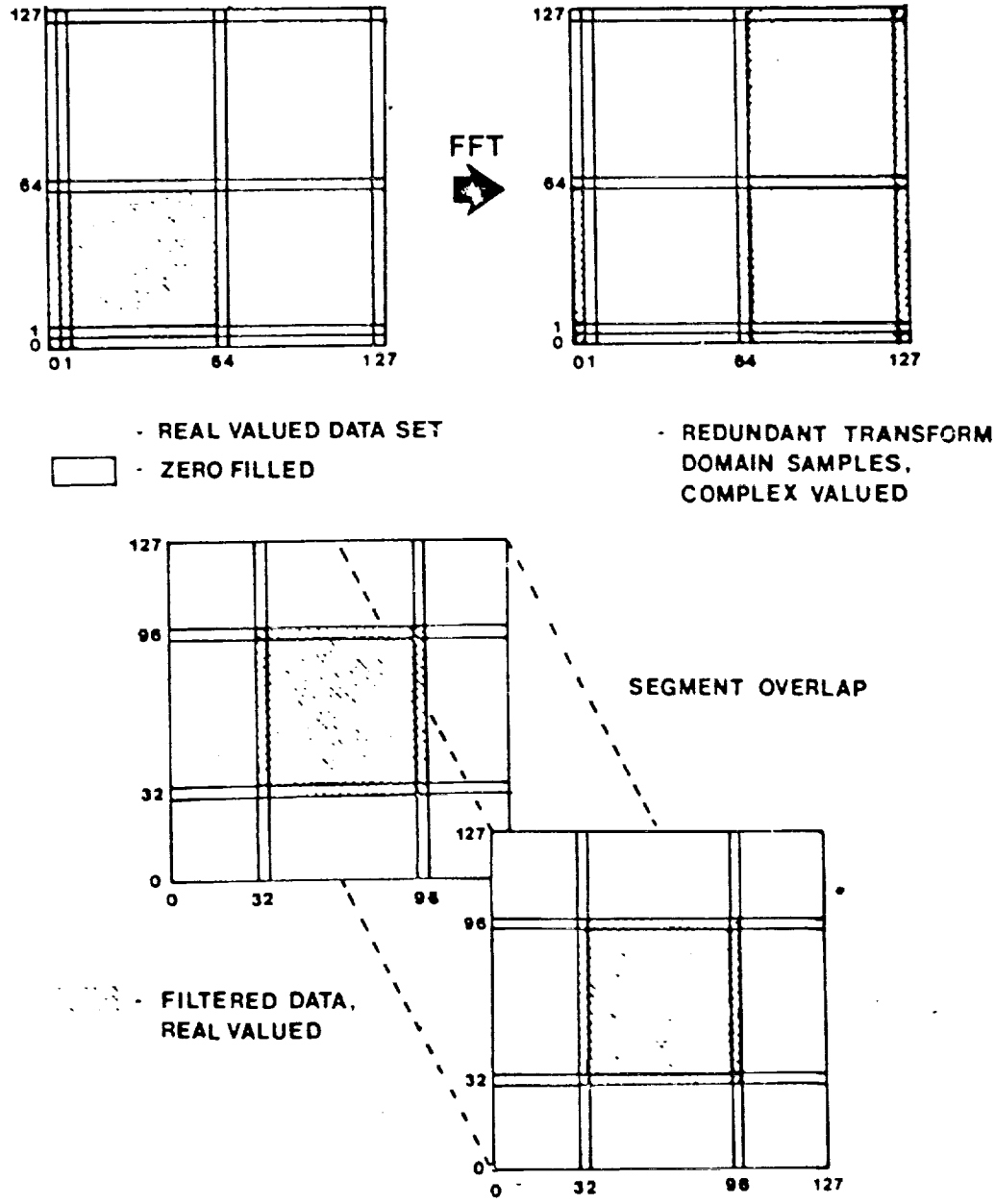

Figure 21. Schematic of Data Handling for Two-Dimensional Processing of Hot-wire and Image Data

DEVICE	$\frac{U_\infty \delta x_0}{\nu}$	$l/\delta x_0$	$h_n/\delta x_0$	$S/\delta x_0$	α
M-1	4×10^4	.95	.8 - .4 .2 - .1		
M-1	3×10^4	.80	.7 - .4 .2 - .1		
M-2	3×10^4	.80	.6		$0°, \pm 10°$
M-3	3×10^4	.80	.6 .2		
M-3	1.2×10^4	1.2	1.0 .5		
M-4	3×10^4	.80	.6 - .8	6 - 8	

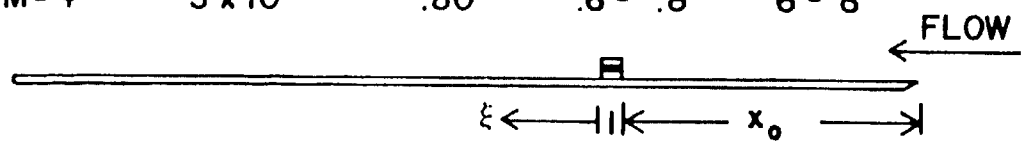

Figure 22. Parameter Values for Optimized Manipulator Configurations

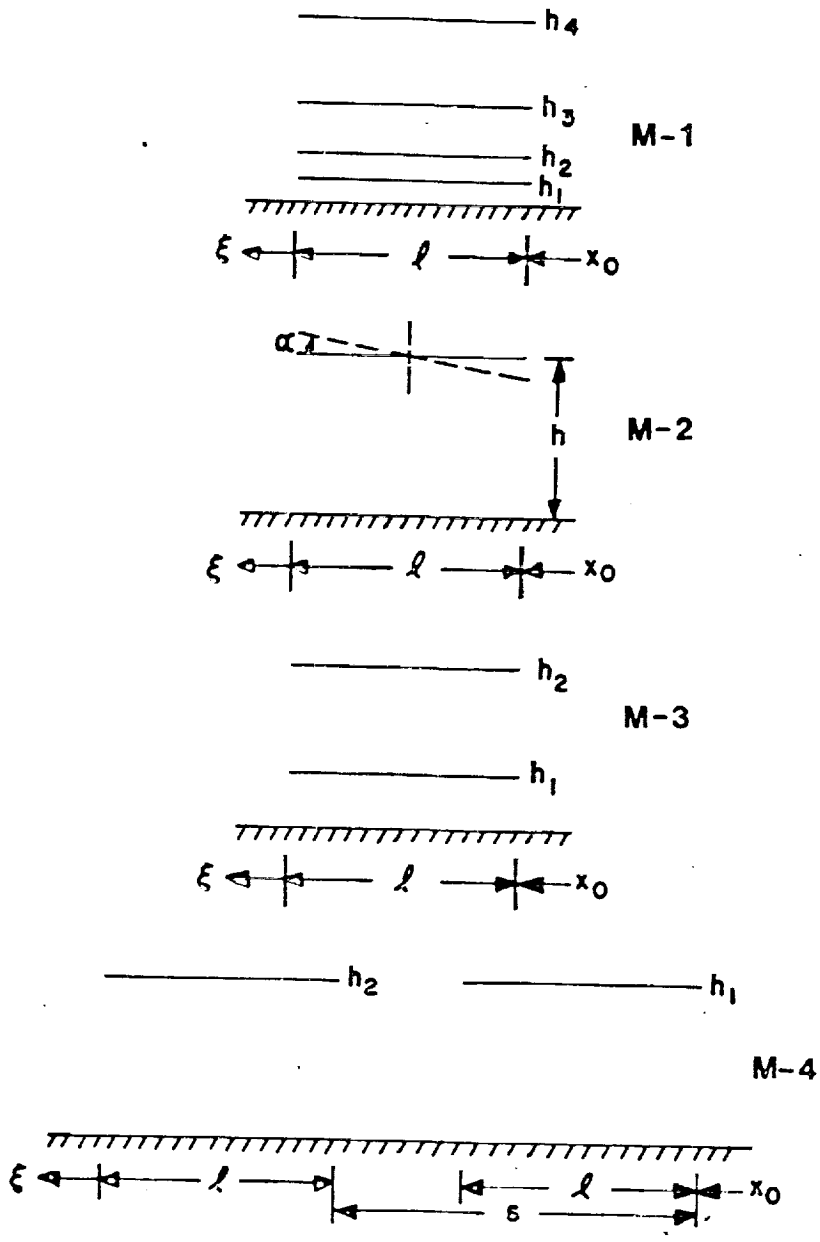

Figure 23. Plate Configurations for Boundary Layer Manipulators

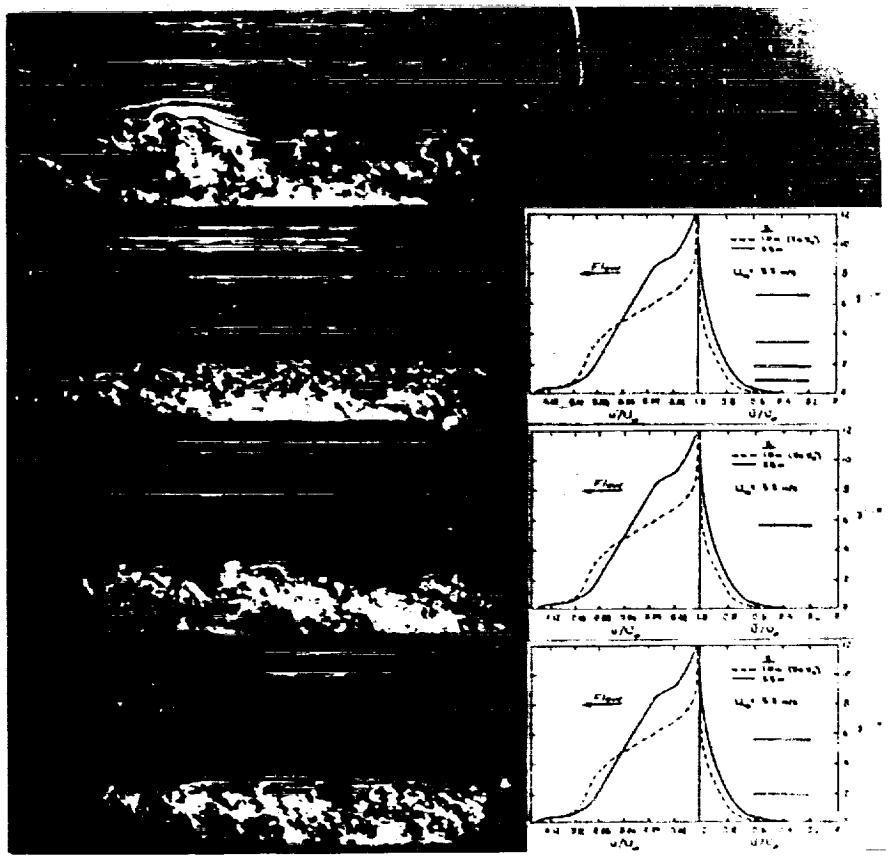

Figure 24. Effect of Varying Number of Plates on Reduction of Large-Scale Turbulence for Optimized Manipulators

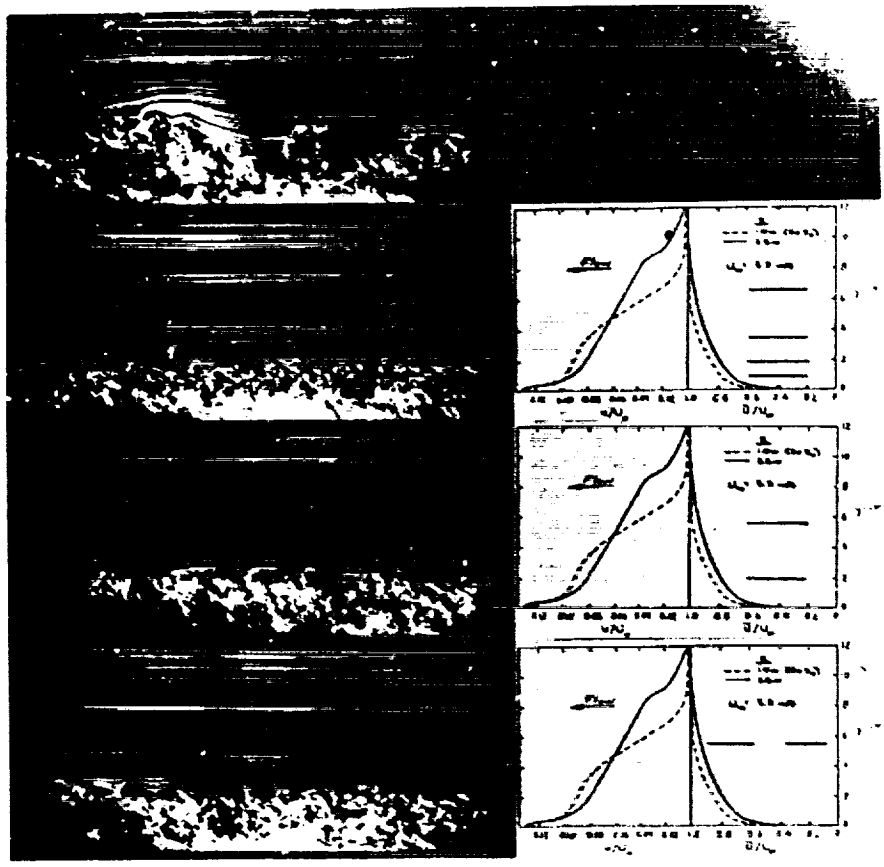

Figure 25. Comparison Between Optimized Parallel and Tandem Plate Arrangements for Reducing Large-Scale Turbulence

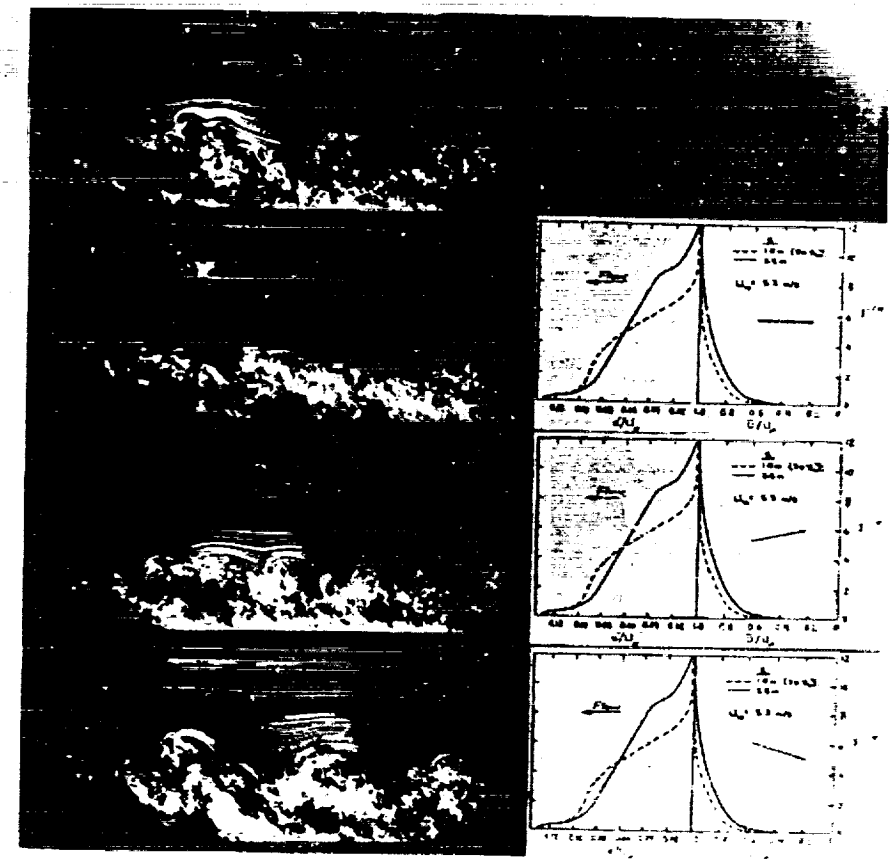

Figure 26. Effect of Single-Plate Angle of Attack on Large-Scale Turbulence

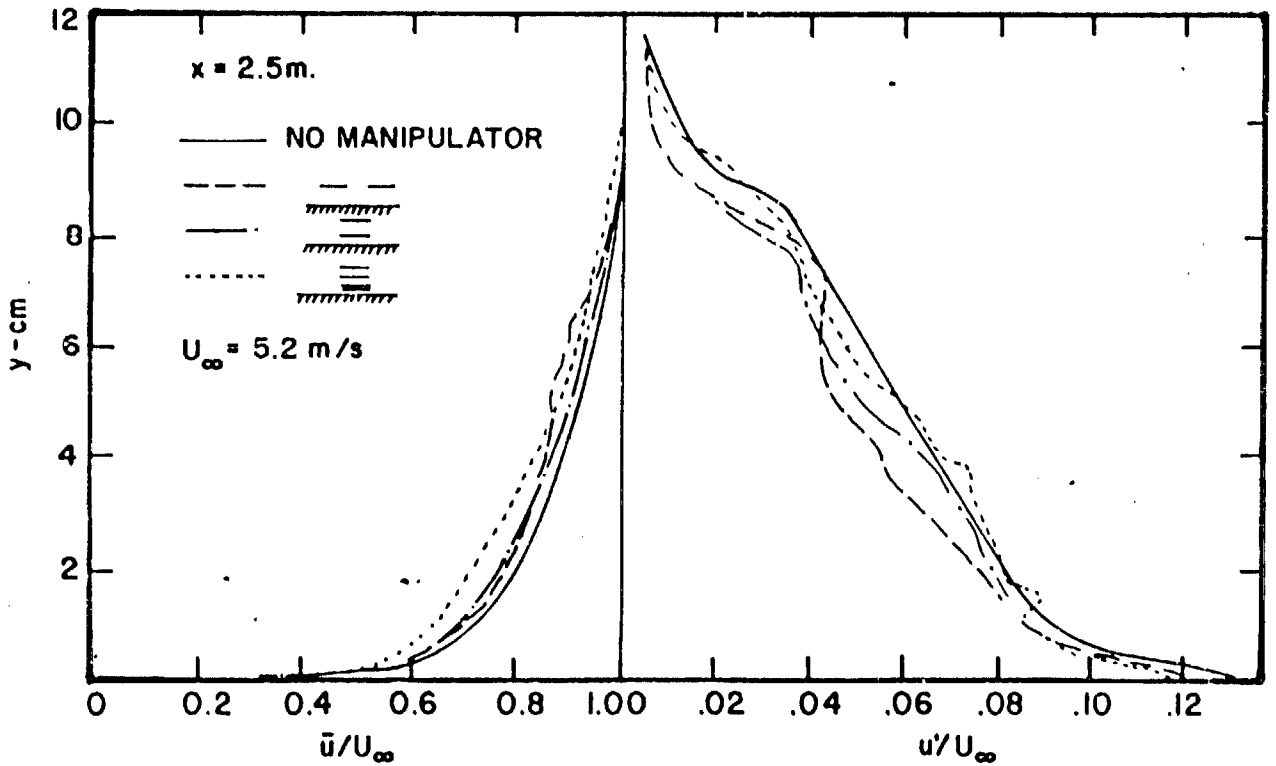

Figure 27. Comparison of Mean Velocity and Turbulence Intensity Profiles for Boundary Layer Alone and with Optimized Manipulators

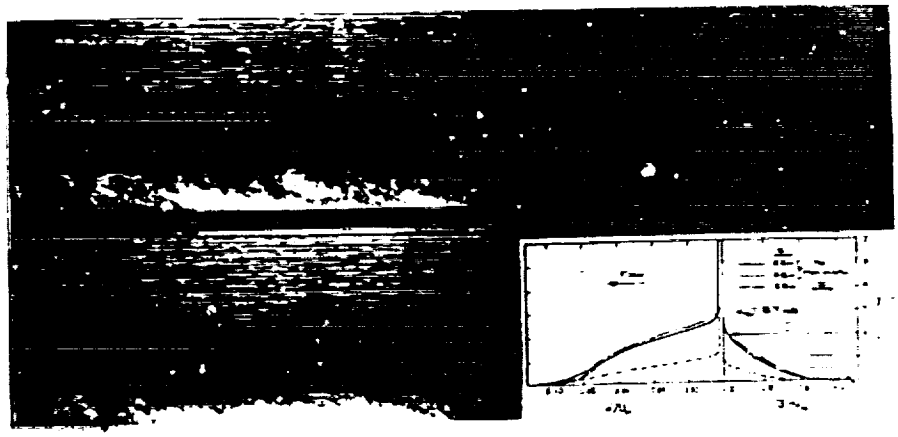

Figure 28. Visualized Flow Without and With the Addition of Two-Plate Manipulator, Showing Streamwise Extent (7.06) of Large-Scale Turbulence Suppression

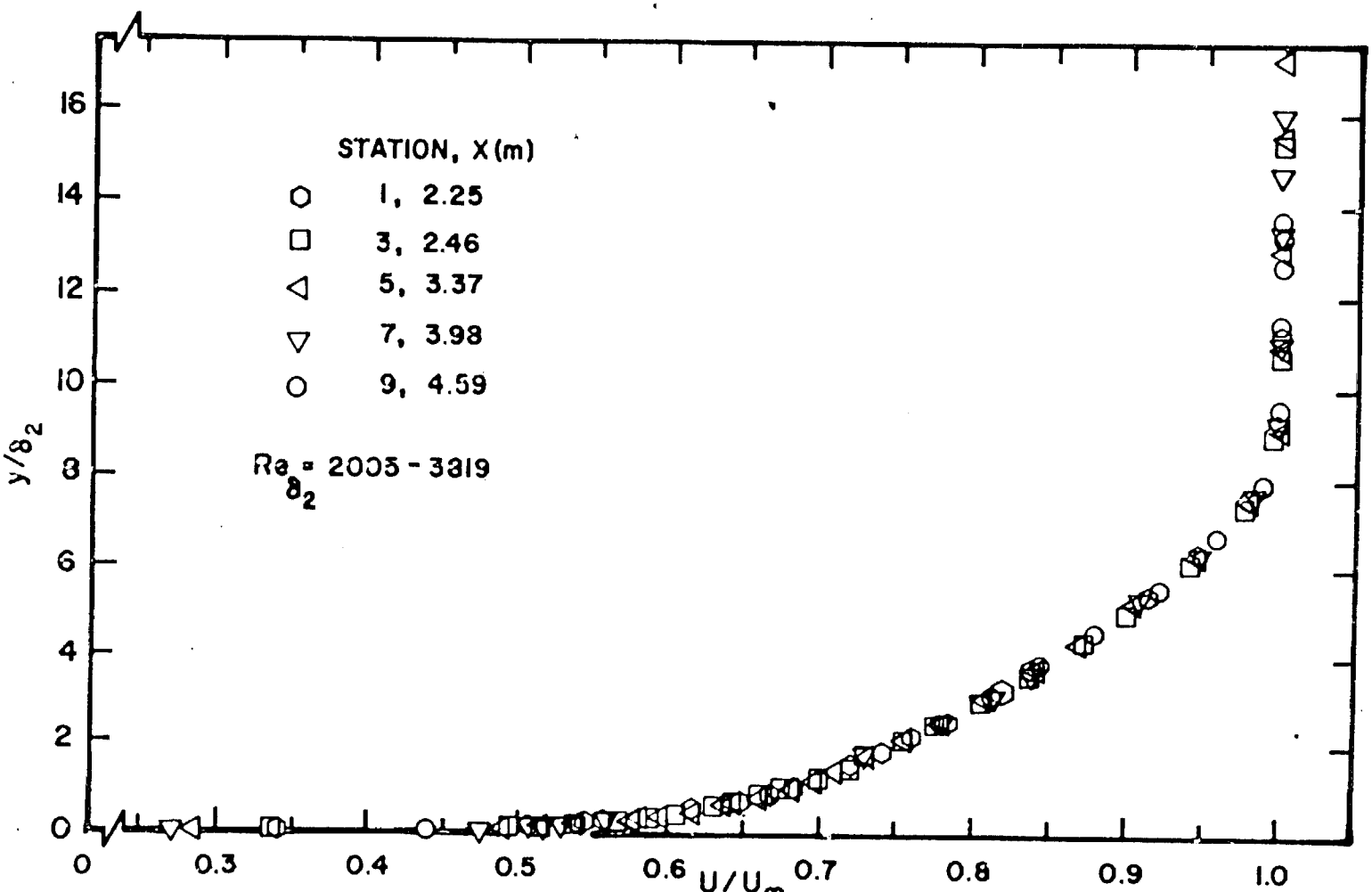

Figure 29. Non-dimensional Mean Velocity Profiles at Various Streamwise Stations in Regular Boundary Layer for Low Reynolds Number Range

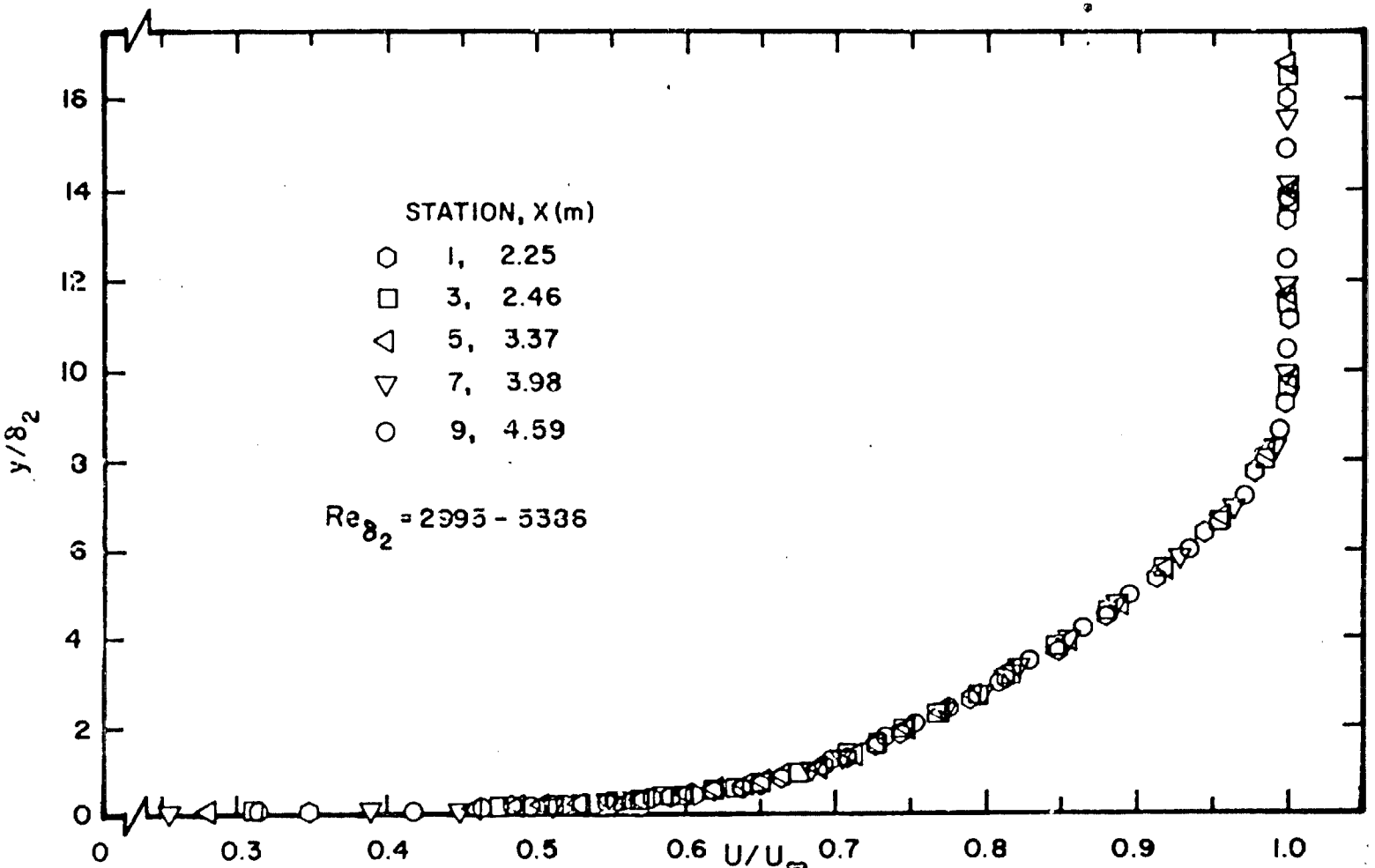

Figure 30. Non-dimensional Mean Velocity Profiles at Various Streamwise Stations in Regular Boundary Layer for High Reynolds Number Range

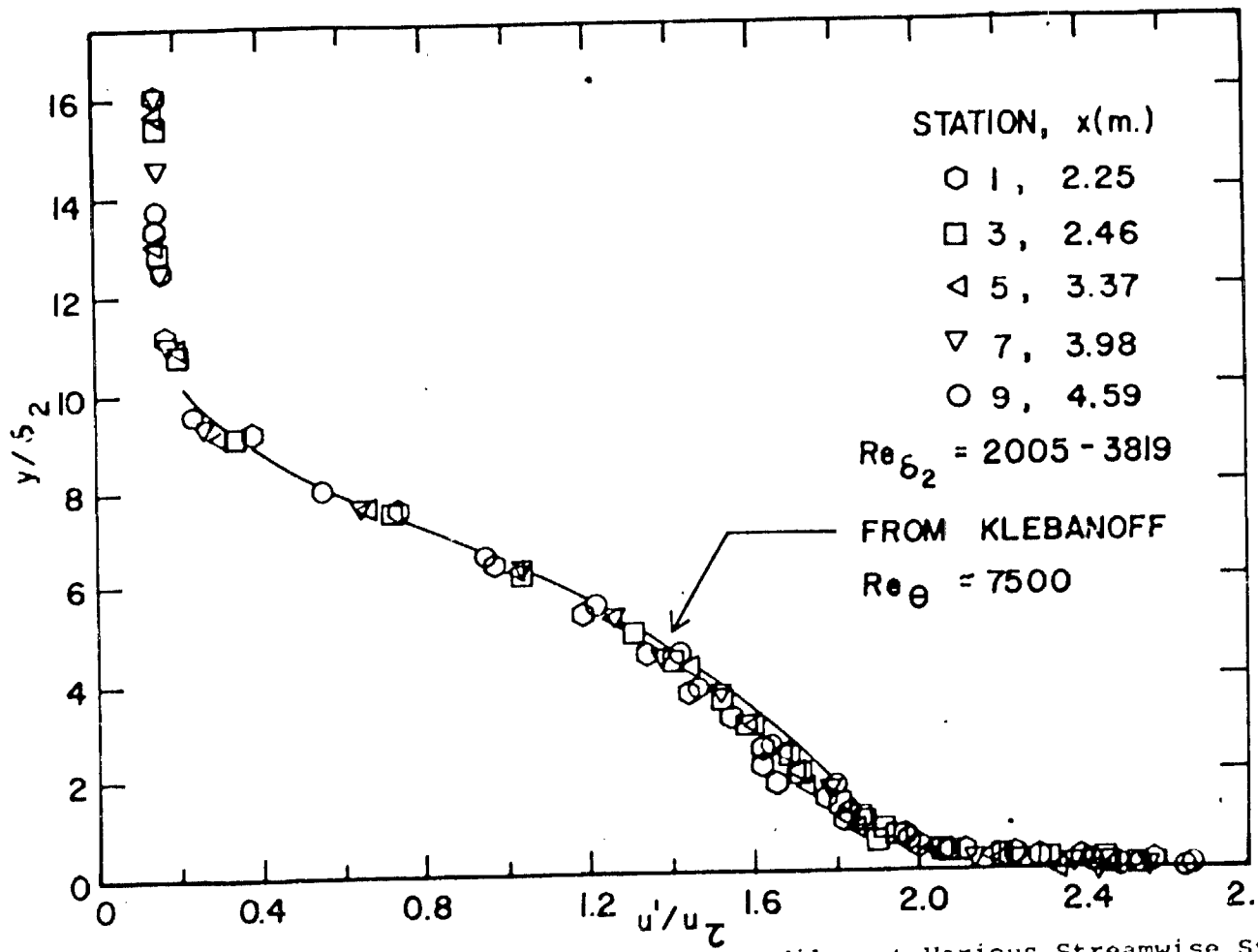

Figure 31. Non-dimensional Fluctuating Velocity Profiles at Various Streamwise Stations in Regular Boundary Layer for Low Reynolds Number Range

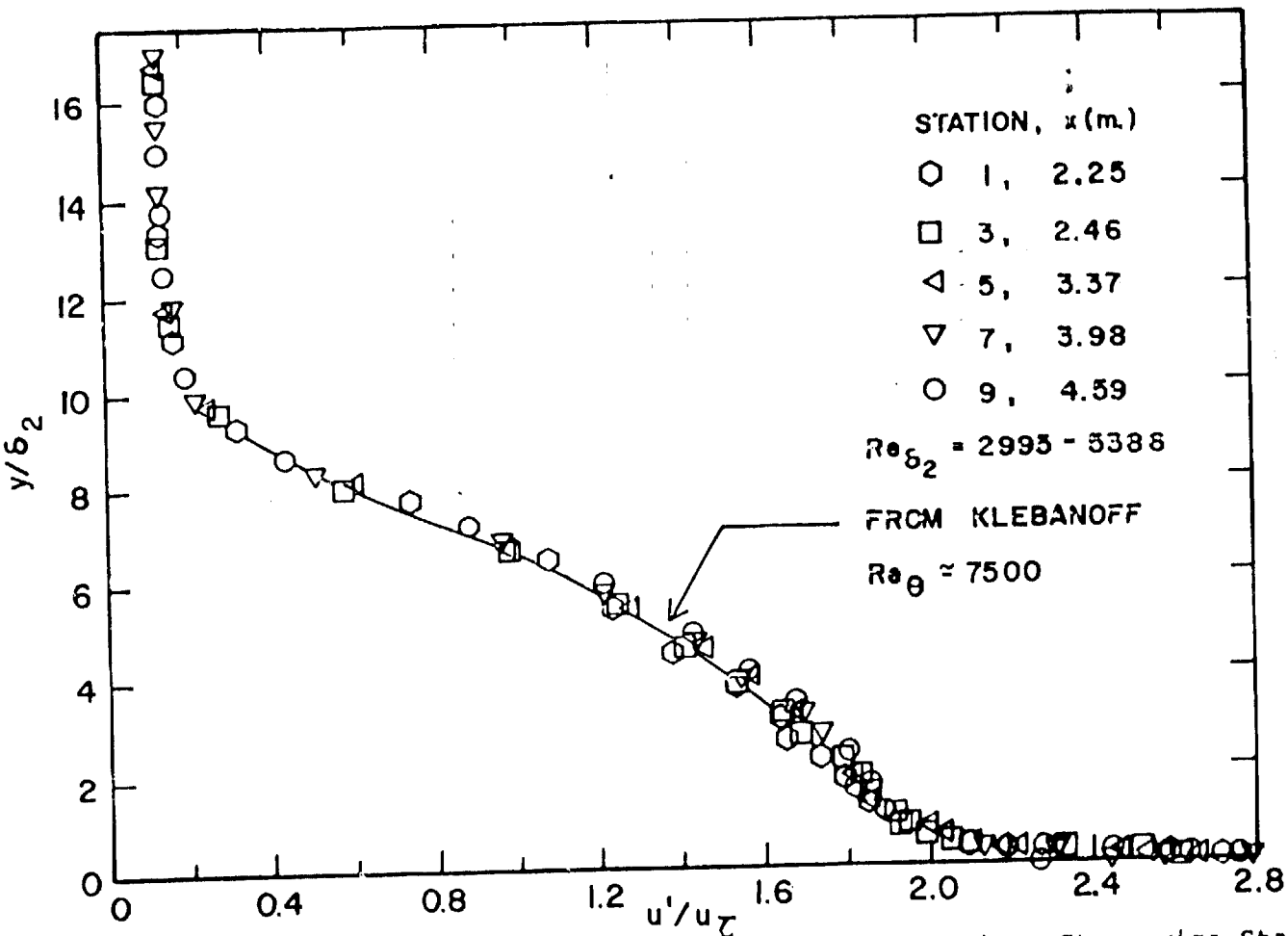

Figure 32. Non-dimensional Fluctuating Velocity Profiles at Various Streamwise Stations in Regular Boundary Layer for High Reynolds Number Range

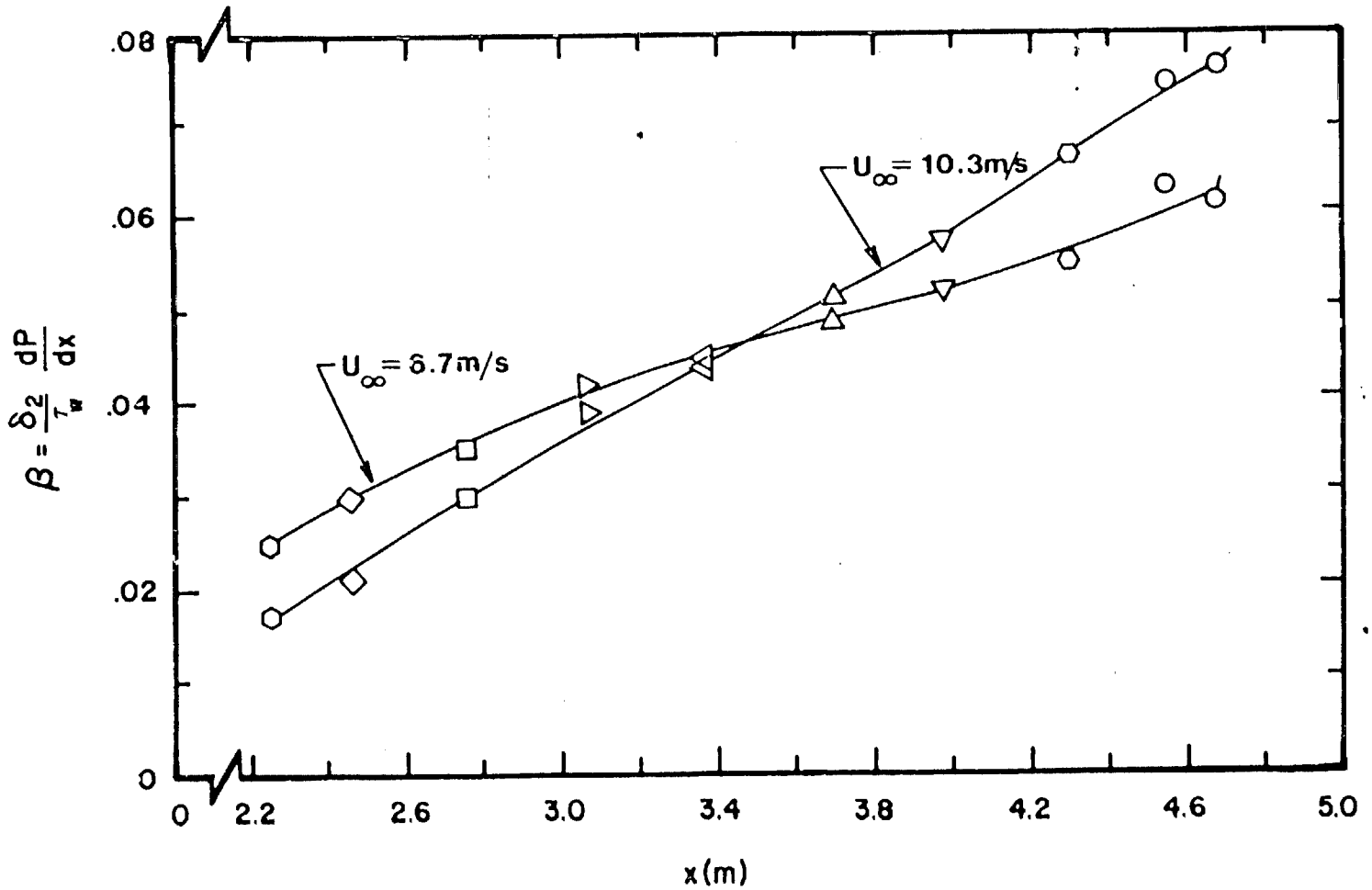

Figure 33. Streamwise Development of Non-dimensional Free-Stream Pressure Difference

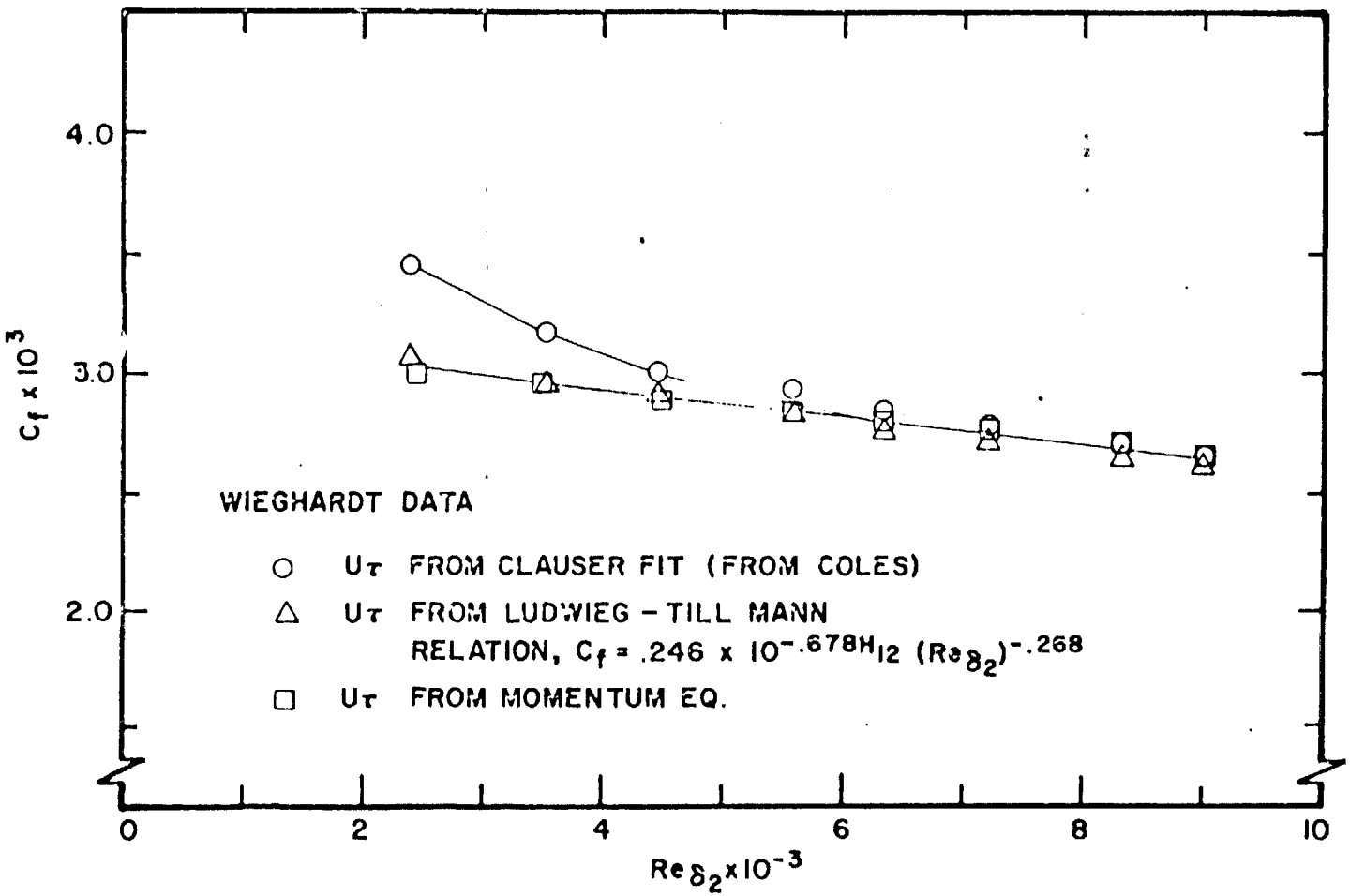

Figure 14. Comparison of Wall-Friction Coefficient Values Obtained by Three Methods for Data of Wieghardt

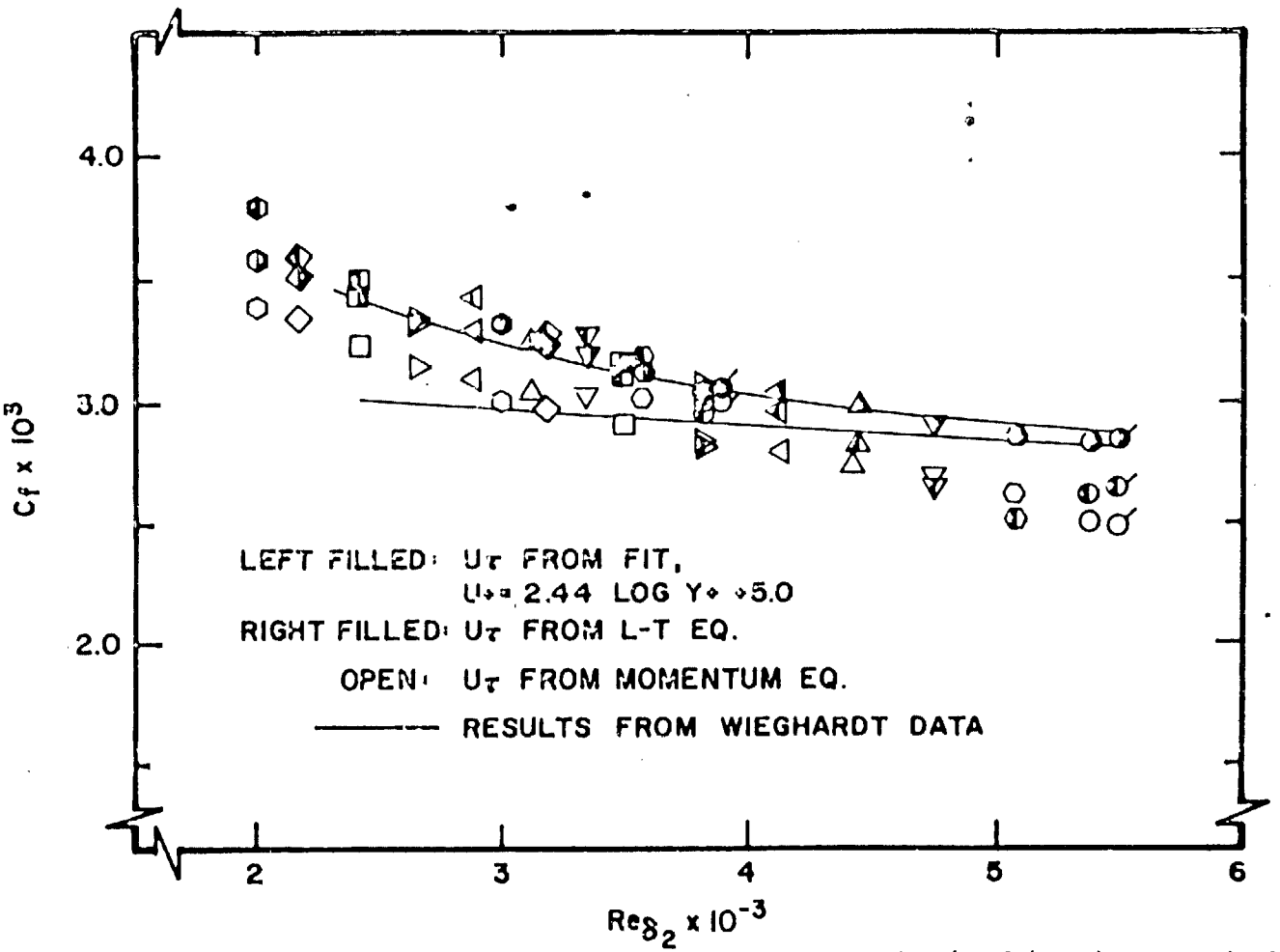

Figure 35. Comparison of Wall-Friction Coefficient Values Obtained by Three Methods for Regular Boundary Layer

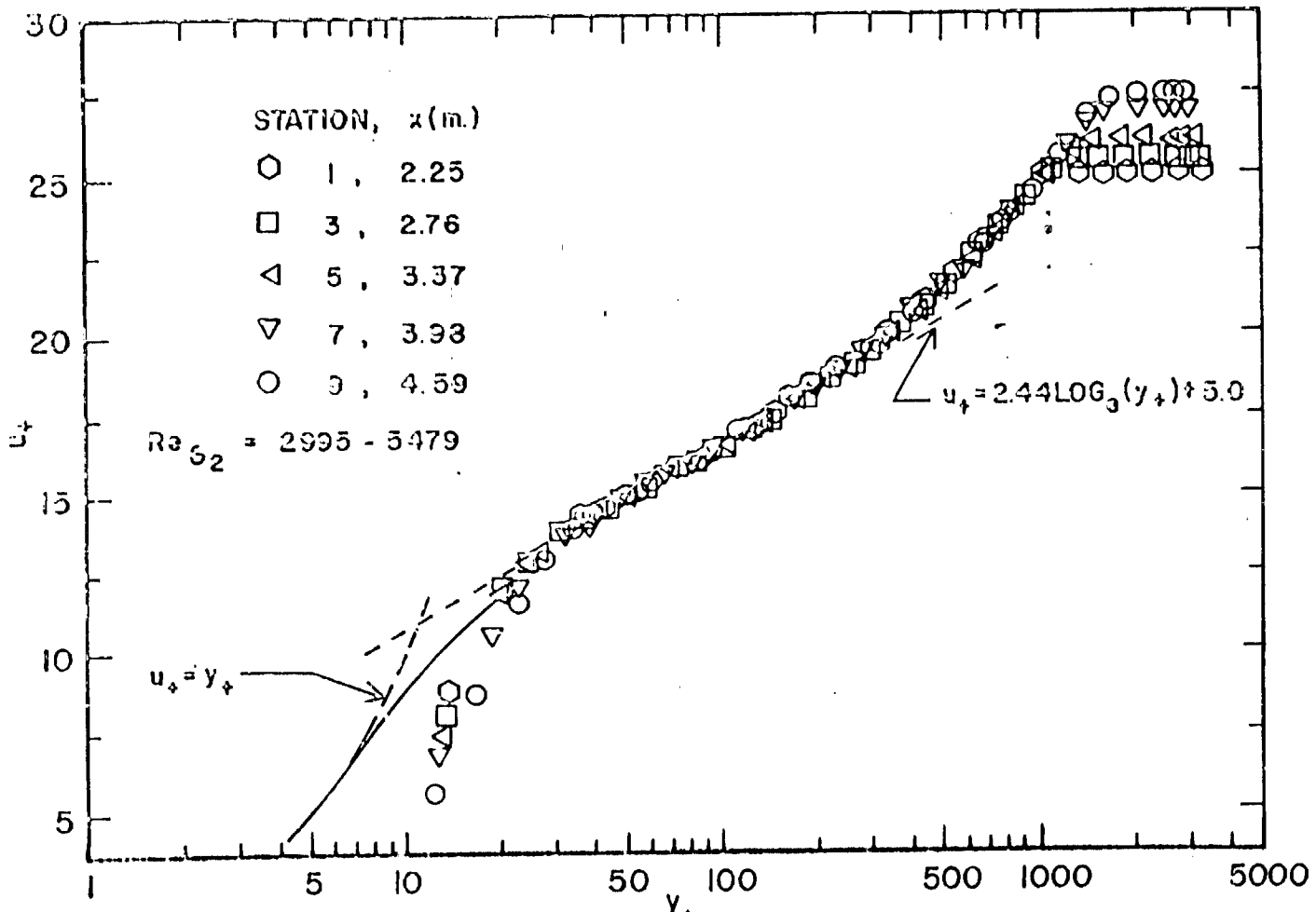

Figure 36. Wall-Unit Non-dimensionalized Mean Velocity Profiles at Various Streamwise Stations in Regular Boundary Layer for Low Reynolds Number Range

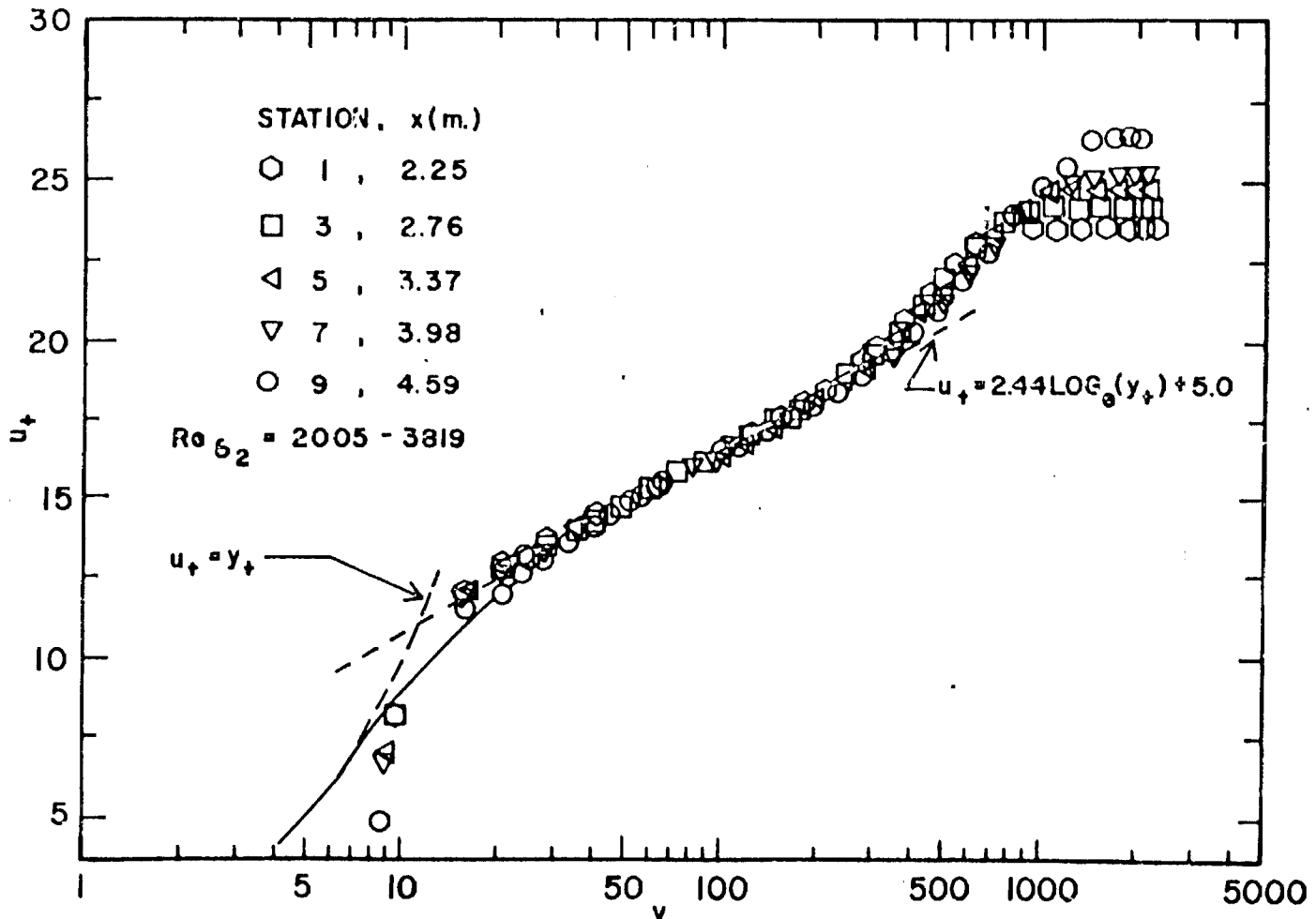

Figure 37. Wall-Unit Non-dimensionalized Mean Velocity Profiles at Various Streamwise Stations in Regular Boundary Layer for High Reynolds Number Range

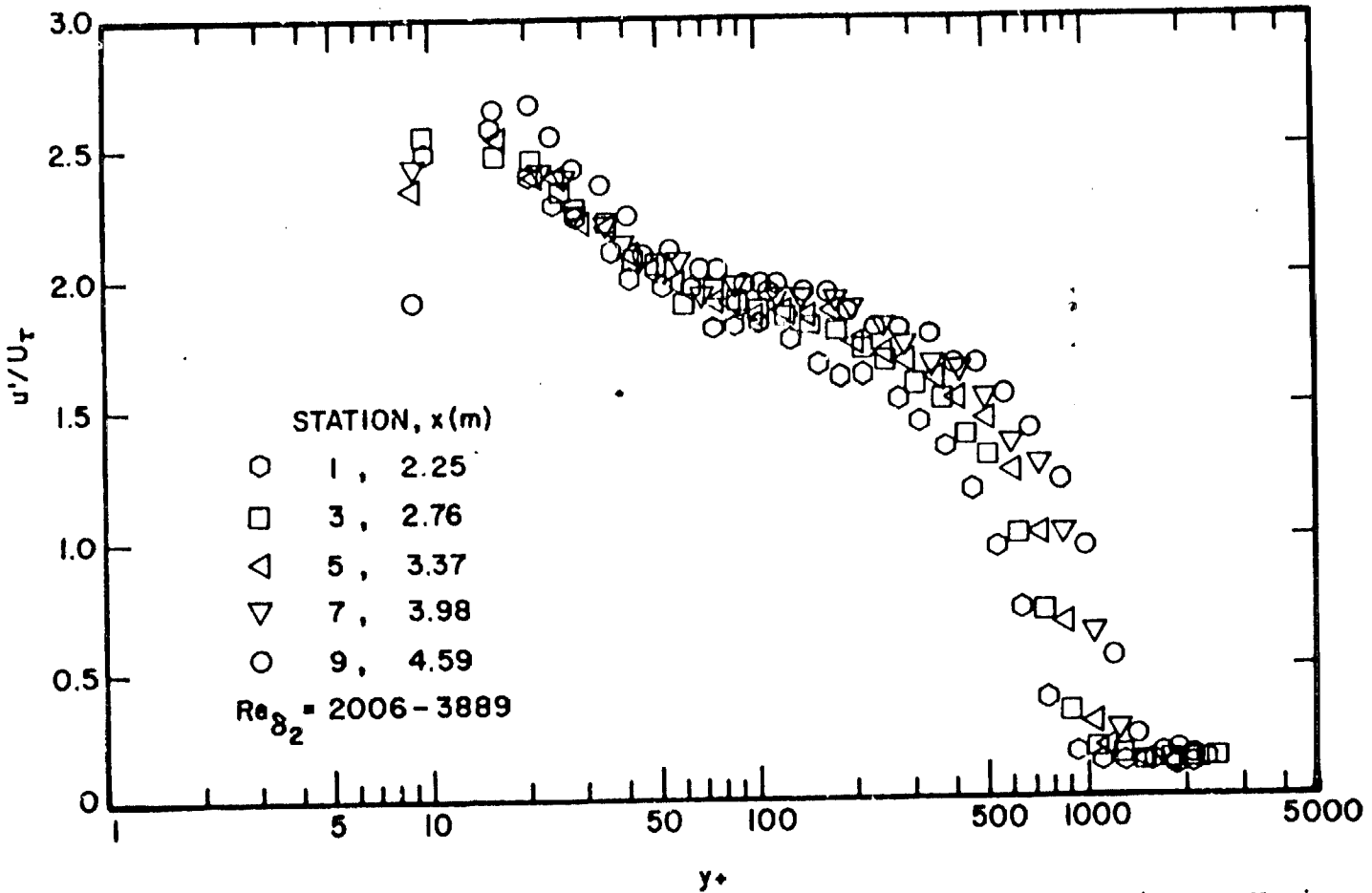

Figure 38. Wall-Unit Non-dimensionalized Fluctuating Velocity Distribution at Various Streamwise Stations in Regular Boundary Layer for Low Reynolds Number Range

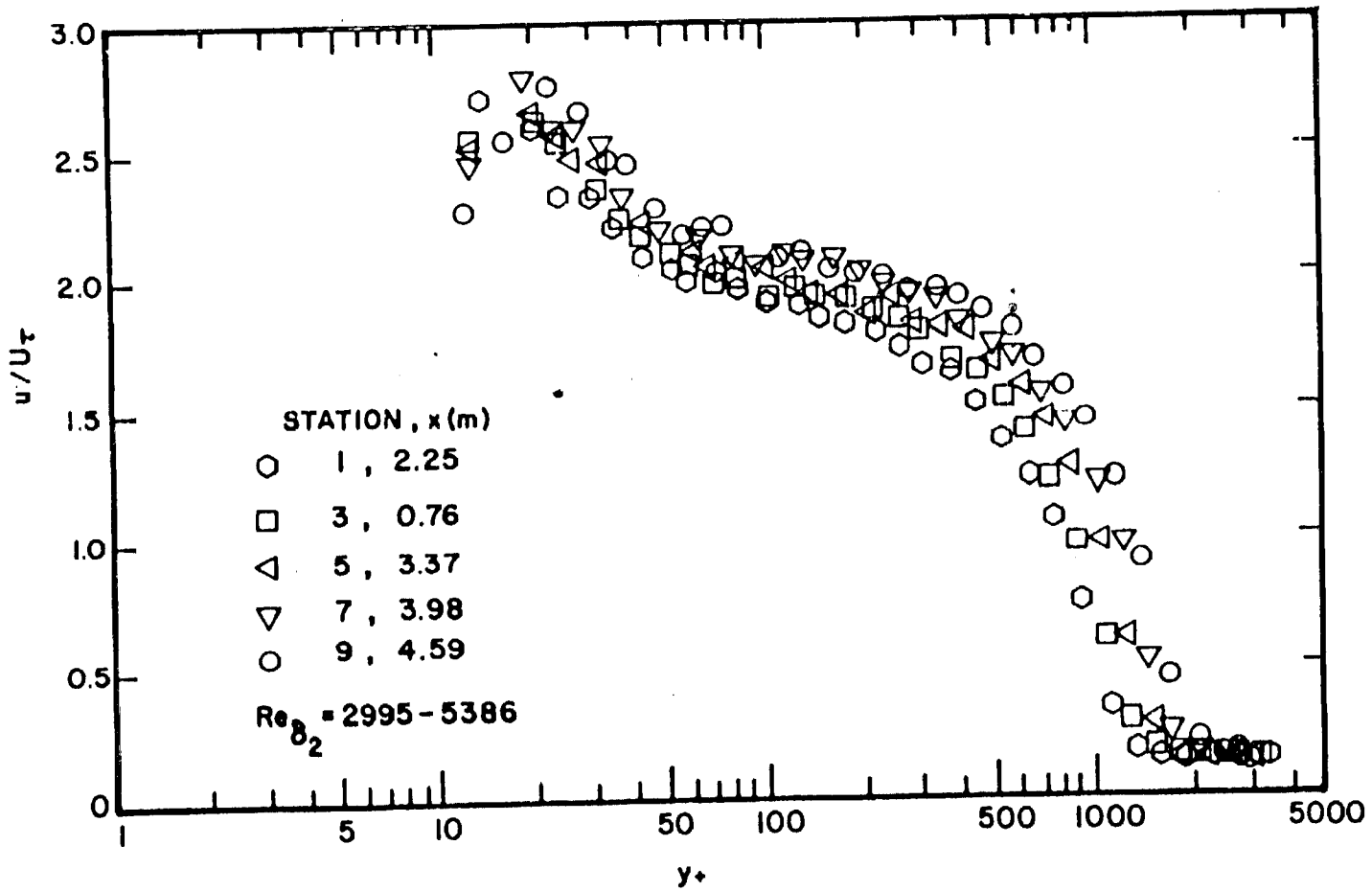

Figure 39. Wall-Unit Non-dimensionalized Fluctuating Velocity Distribution at Various Streamwise Stations in Regular Boundary Layer for High Reynolds Number Range

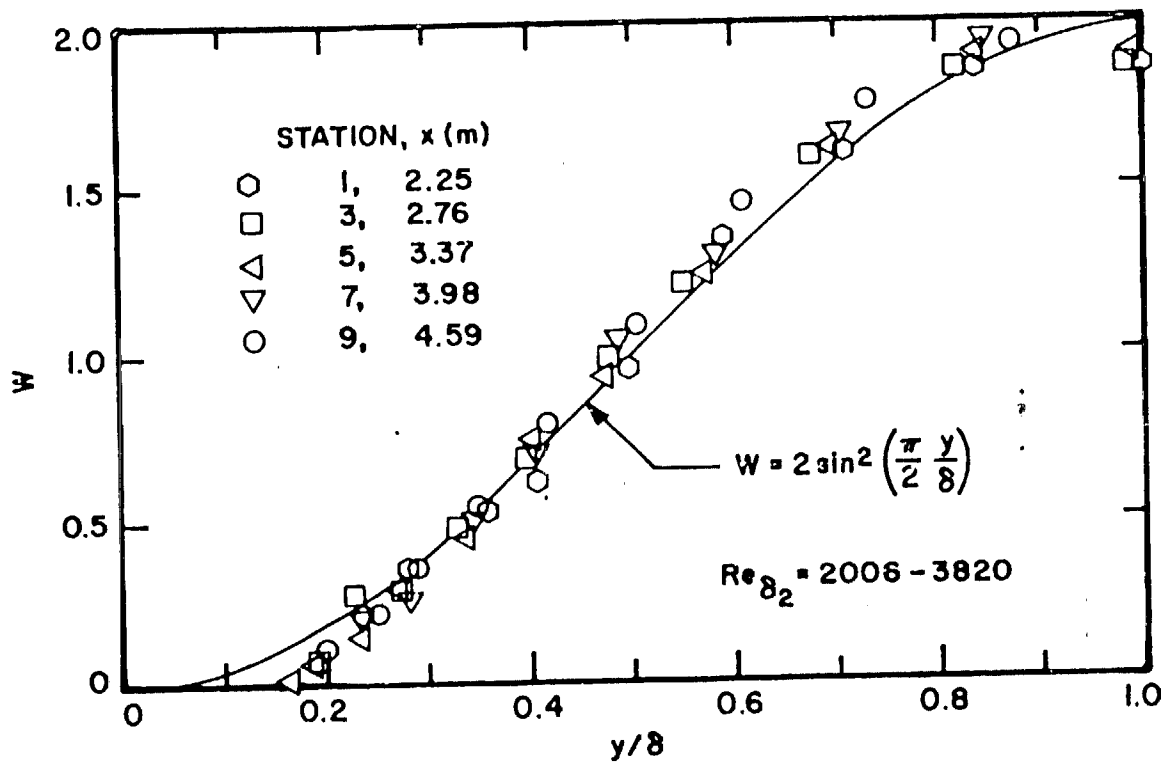

Figure 40. Wake Function Distribution at Various Streamwise Stations in Regular Boundary Layer for Low Reynolds Number Range

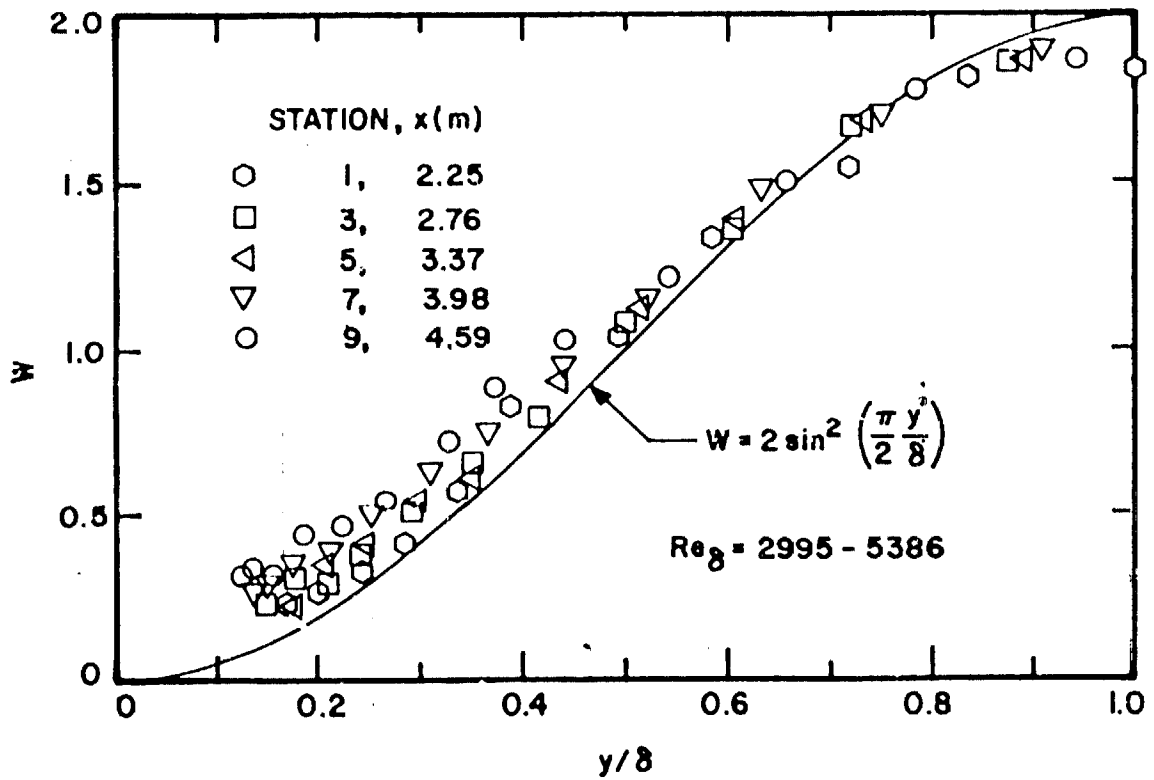

Figure 41. Wake Function Distribution at Various Streamwise Stations in Regular Boundary Layer for High Reynolds Number Range

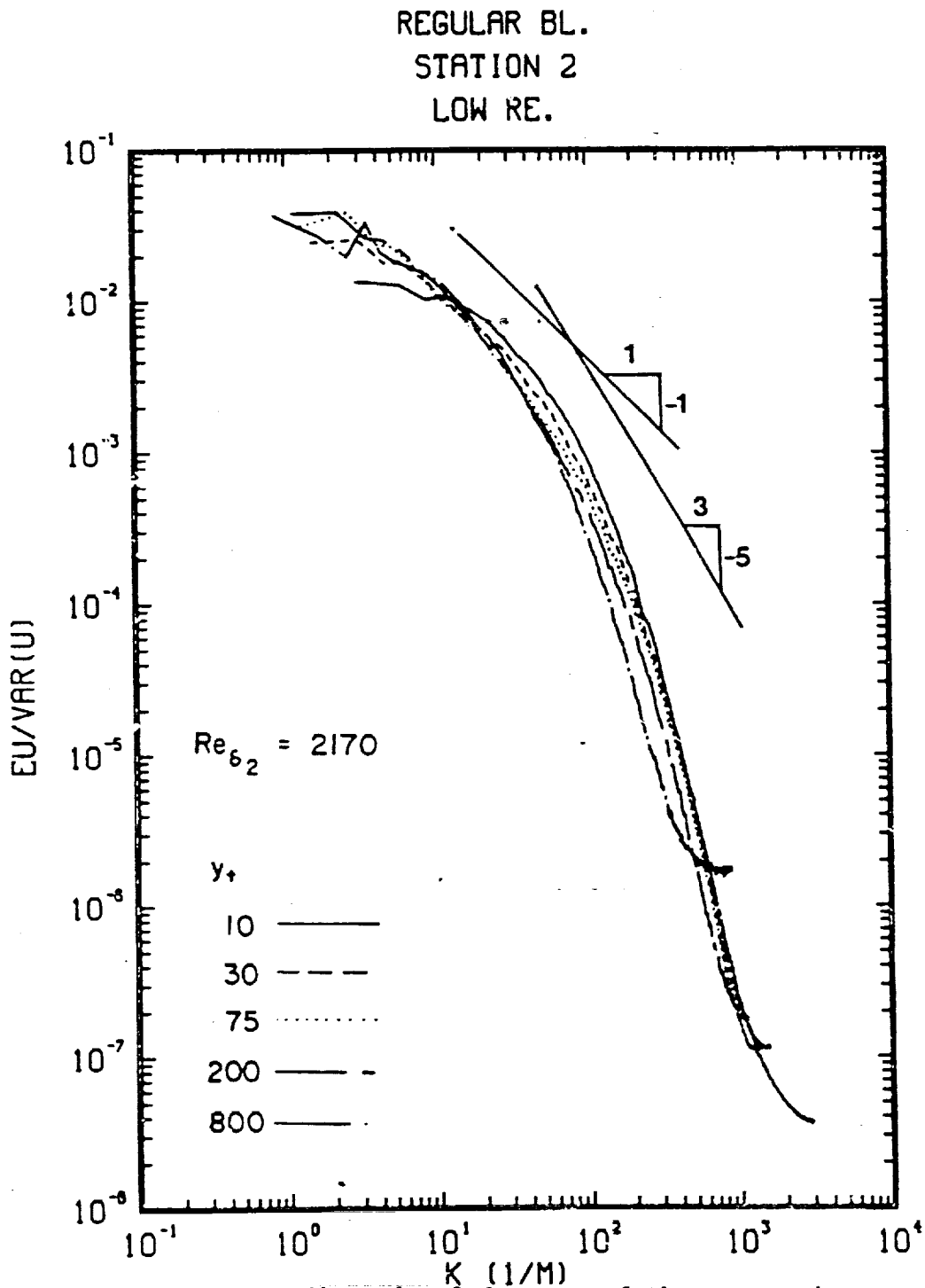

Figure 42. One-dimensional Spectra of the Streamwise Velocity Component at Different Self-Similar Heights at Station 2 in the Regular Boundary Layer for Low Reynolds Number Range

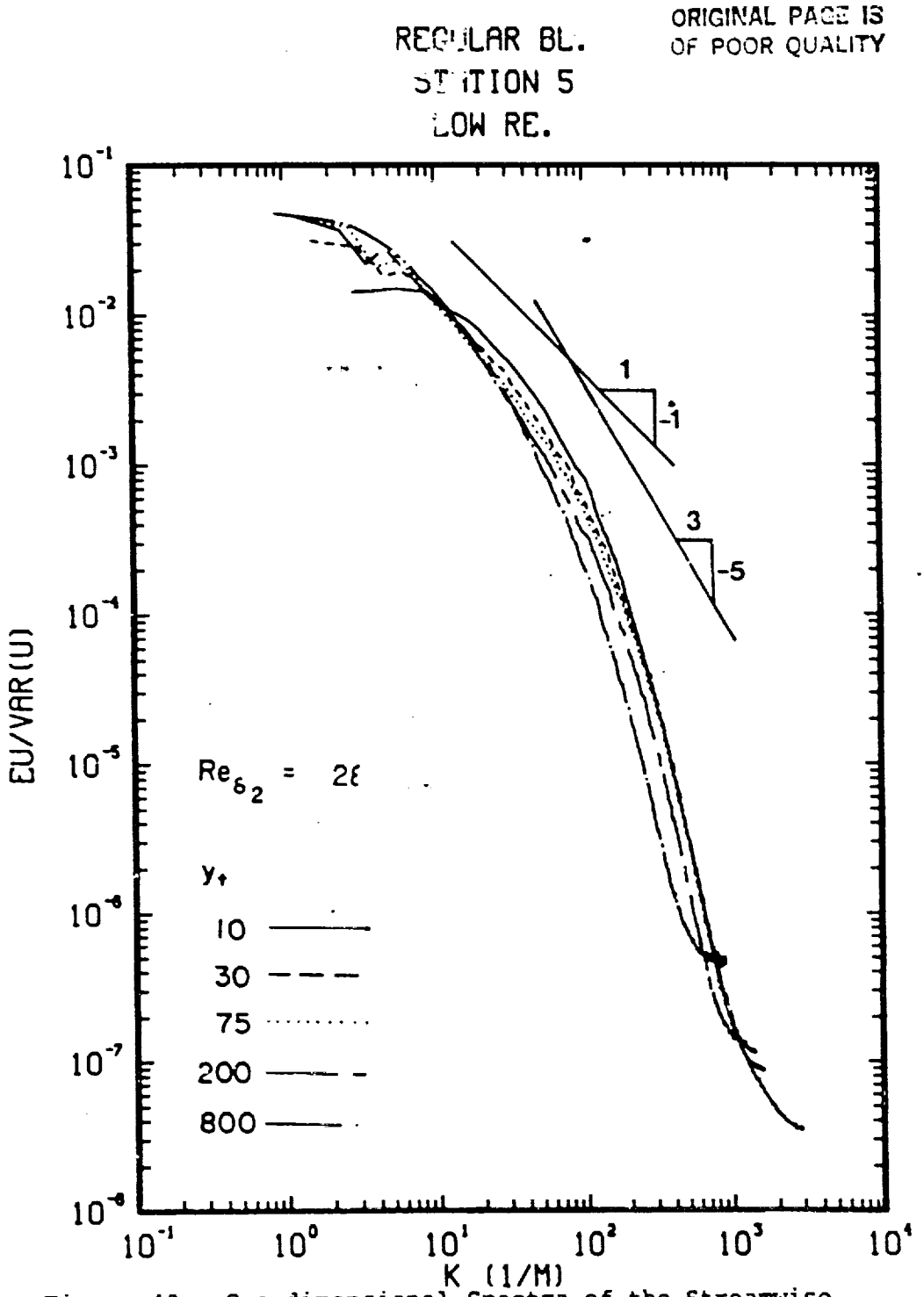

Figure 43. One-dimensional Spectra of the Streamwise Velocity Component at Different Self-Similar Heights at Station 5 in the Regular Boundary Layer for Low Reynolds Number Range

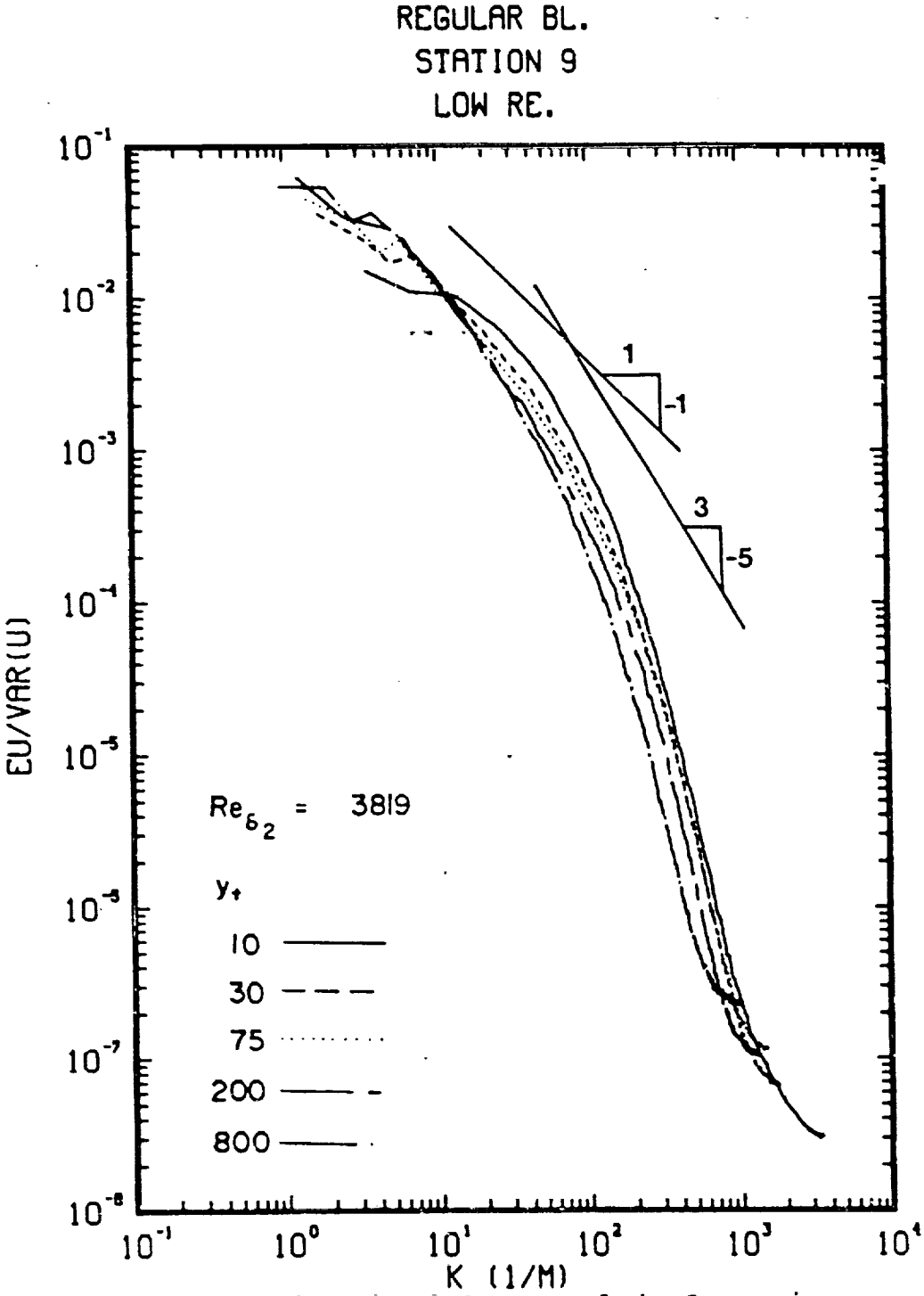

Figure 44. One-dimensional Spectra of the Streamwise Velocity Component at Different Self-Similar Heights at Station 9 in the Regular Boundary Layer for Low Reynolds Number Range

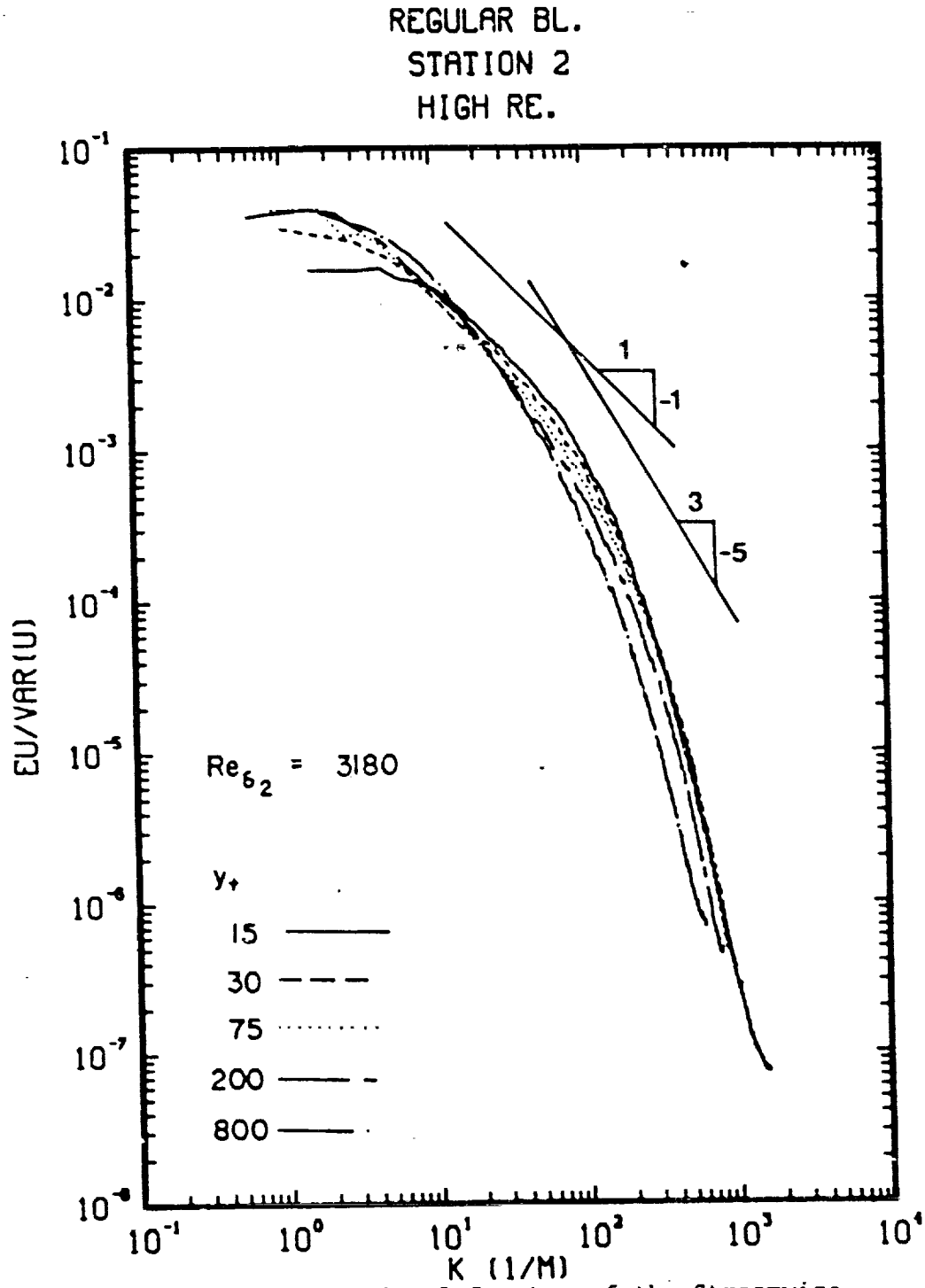

Figure 45. One-dimensional Spectra of the Streamwise Velocity Component at Different Self-Similar Heights at Station 2 in the Regular Boundary Layer for High Reynolds Number Range

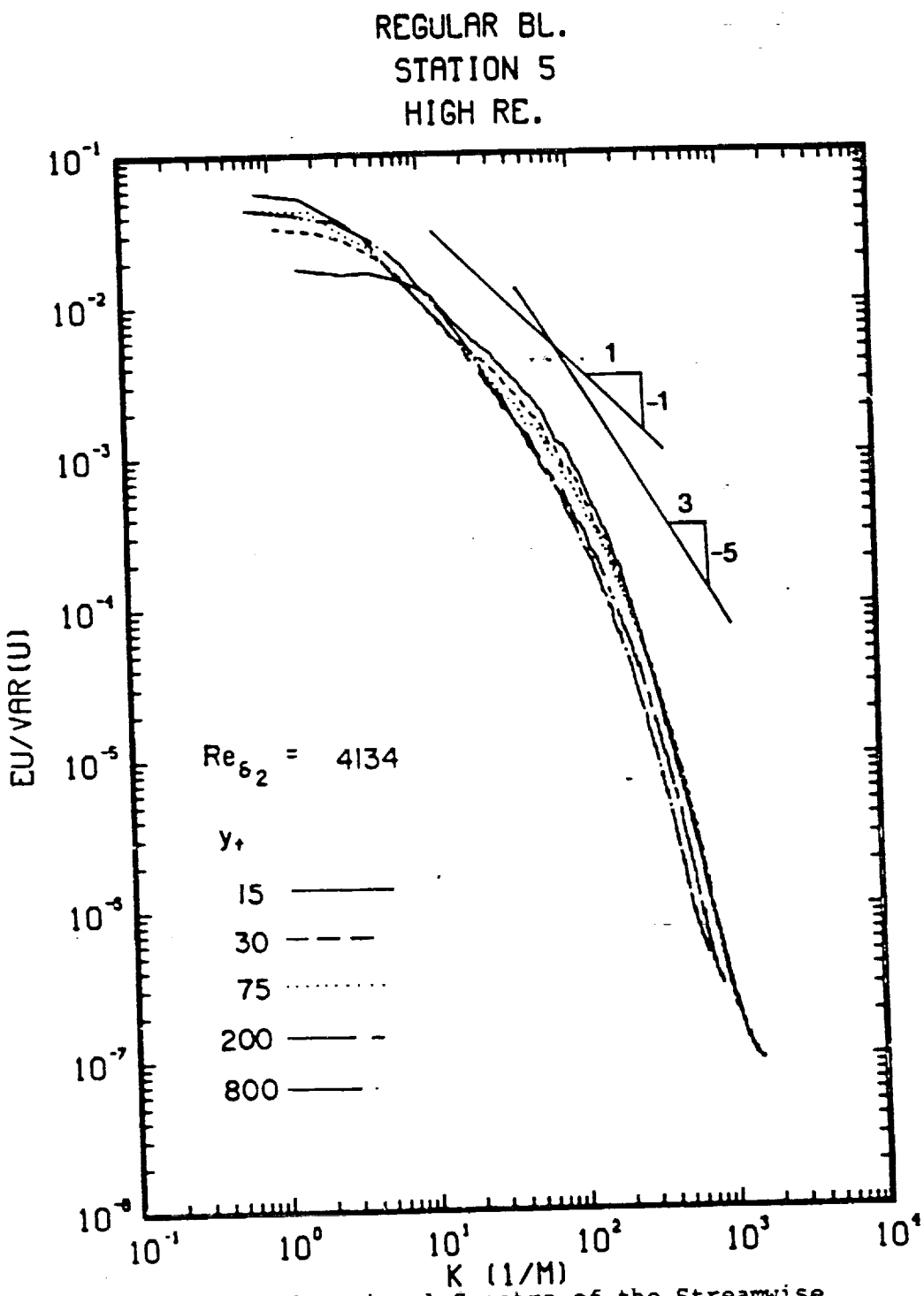

Figure 46. One-dimensional Spectra of the Streamwise Velocity Component at Different Self-Similar Heights at Station 5 in the Regular Boundary Layer for High Reynolds Number Range

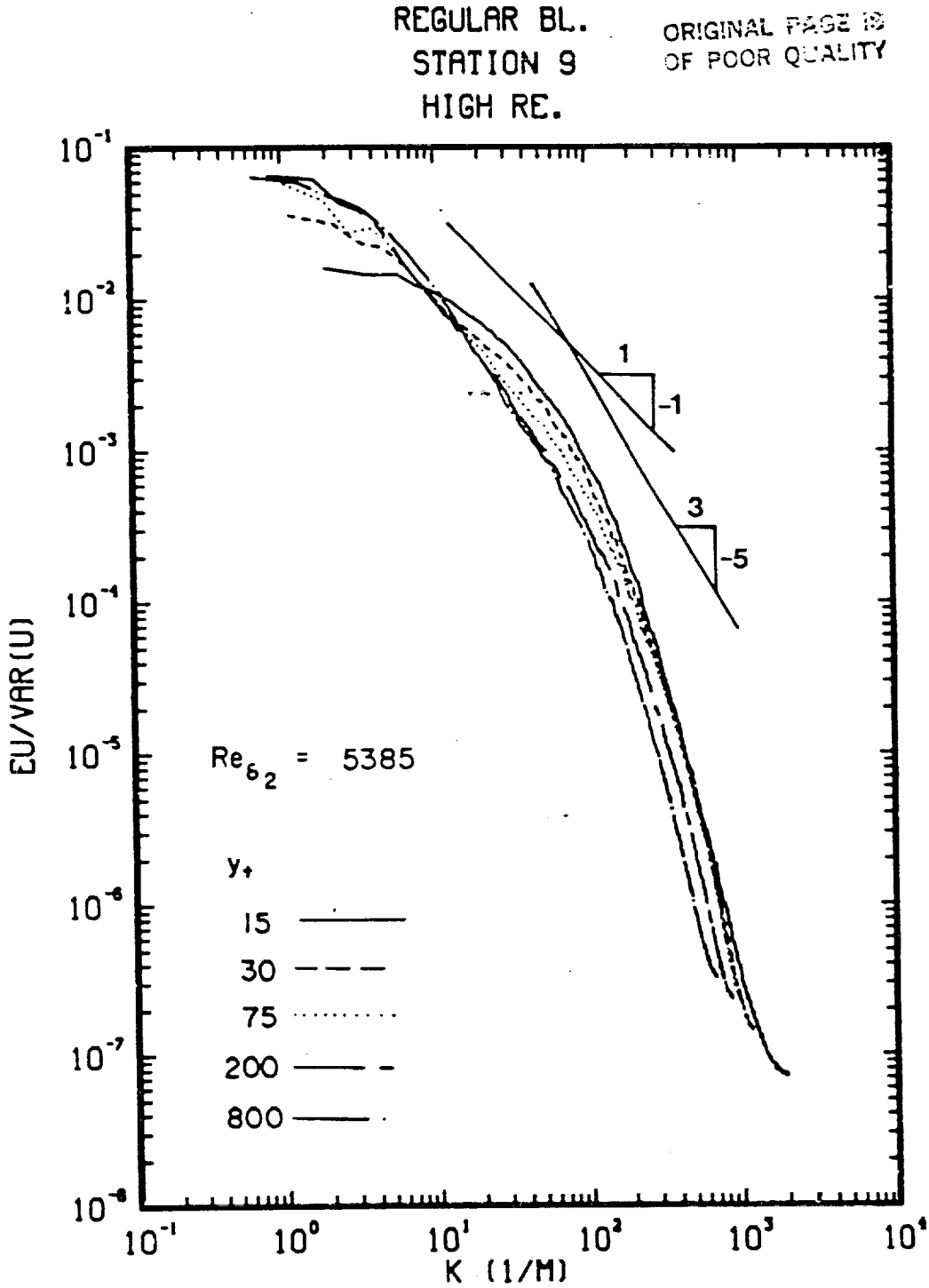

Figure 47. One-dimensional Spectra of the Streamwise Velocity Component at Different Self-Similar Heights at Station 9 in the Regular Boundary Layer for High Reynolds Number Range

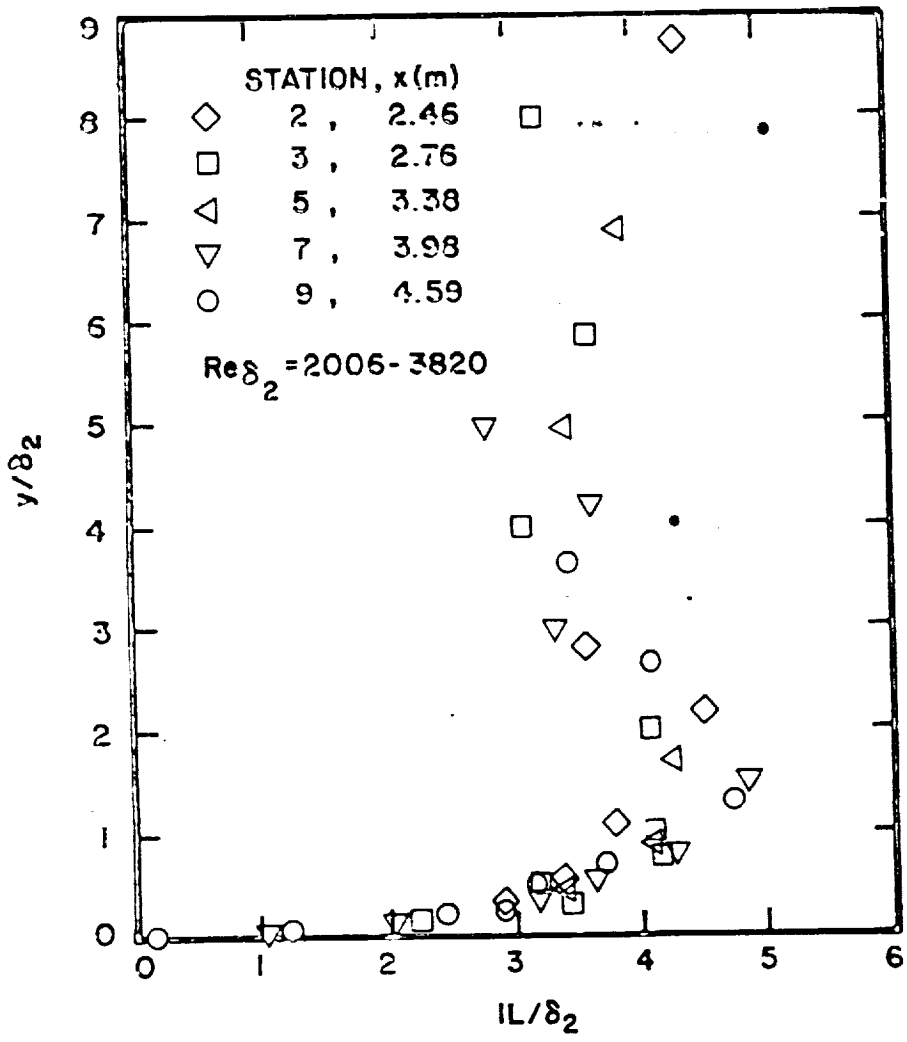

Figure 48. Vertical Distribution of Non-dimensional Streamwise Integral Length Scale at Various Downstream Stations in Regular Boundary Layer for Low Reynolds Number Range

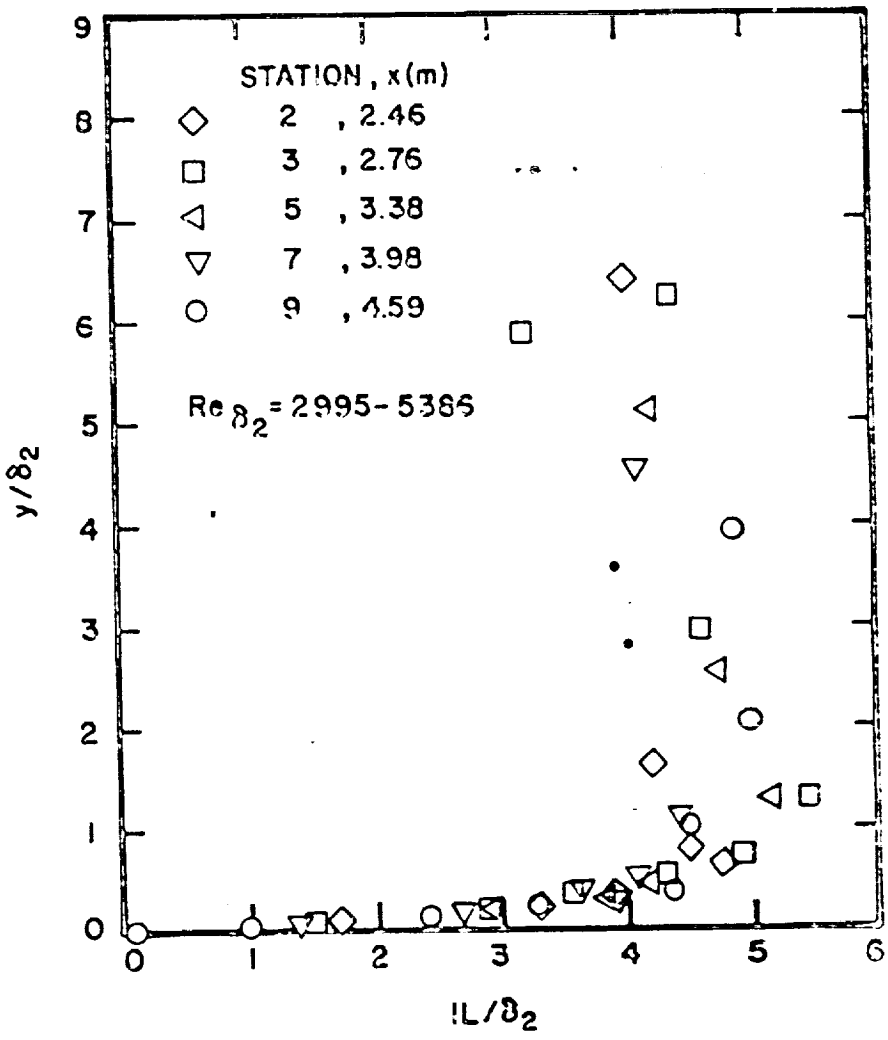

Figure 49. Vertical Distribution of Non-dimensional Streamwise Integral Length Scale at Various Downstream Stations in Regular Boundary Layer for High Reynolds Number Range

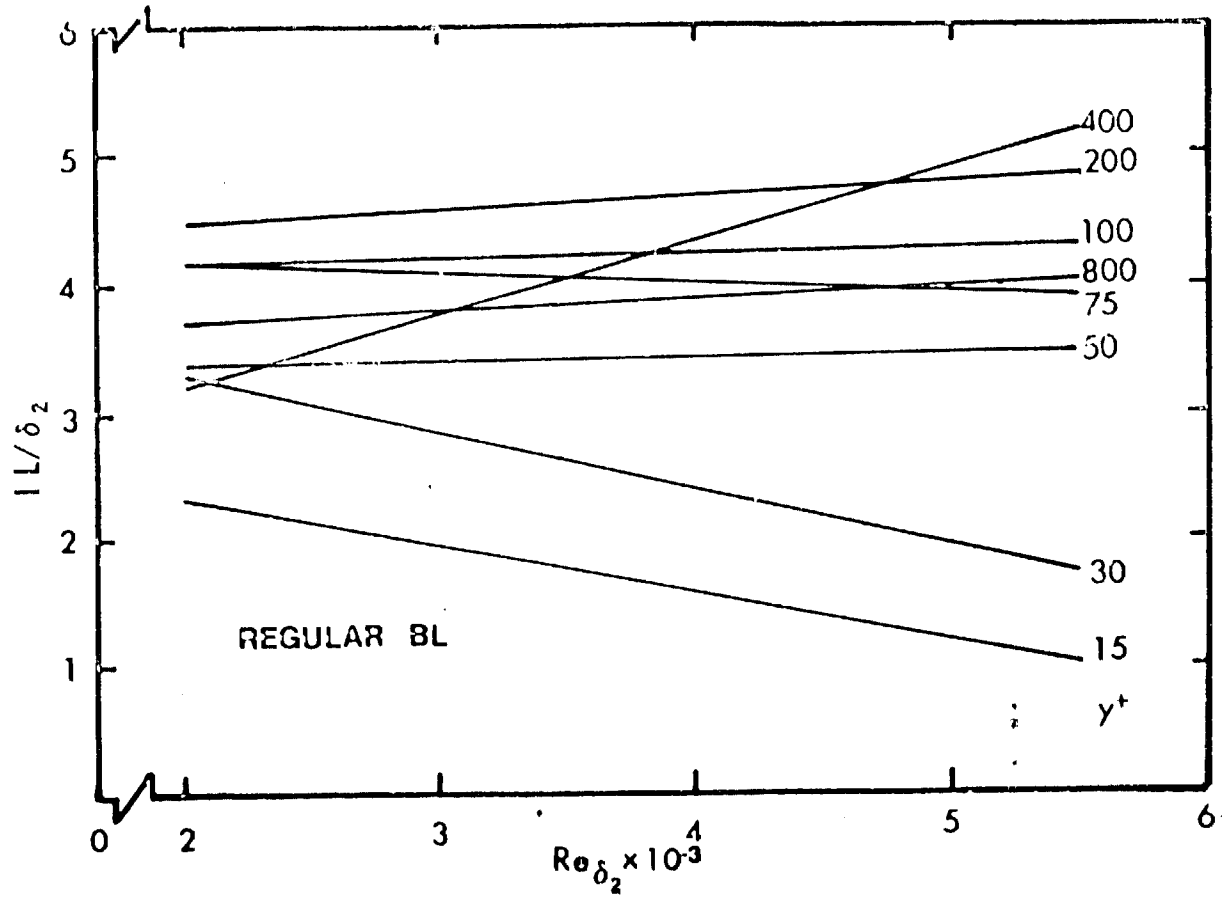

Figure 50. Reynolds Number Dependence of Non-dimensional Streamwise Integral Length Scale at Different Self-Similar Heights in the Regular Boundary Layer

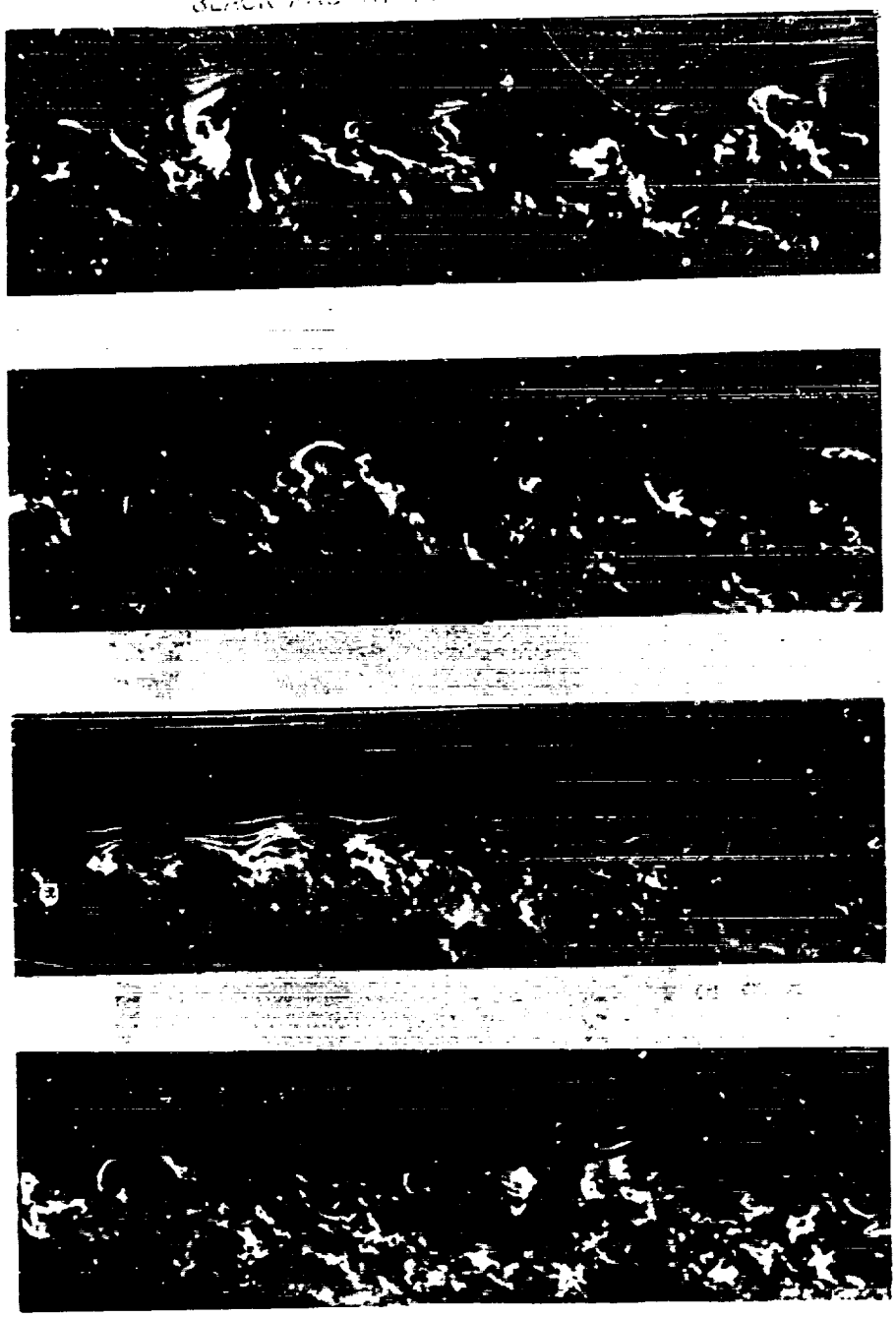

Figure 51. Two Realizations of Smoke-wire Visualization Photographs of Flowfield in Regular Boundary Layer (Top) and Manipulated Boundary Layer (Bottom) Representative of Final Data Runs

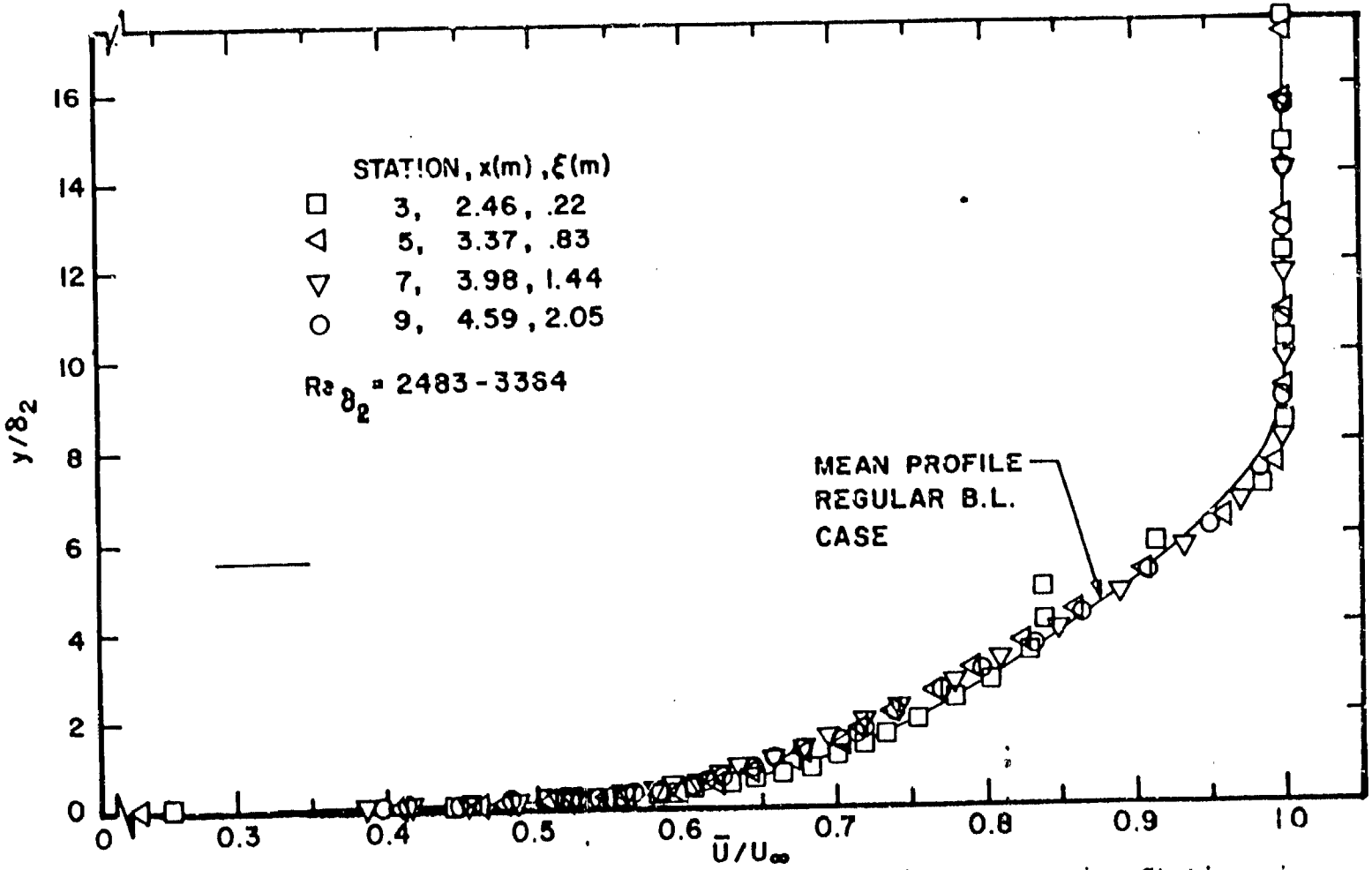

Figure 52. Non-dimensional Mean Velocity Profiles at Various Streamwise Stations in Manipulated Boundary Layer for Low Reynolds Number Range

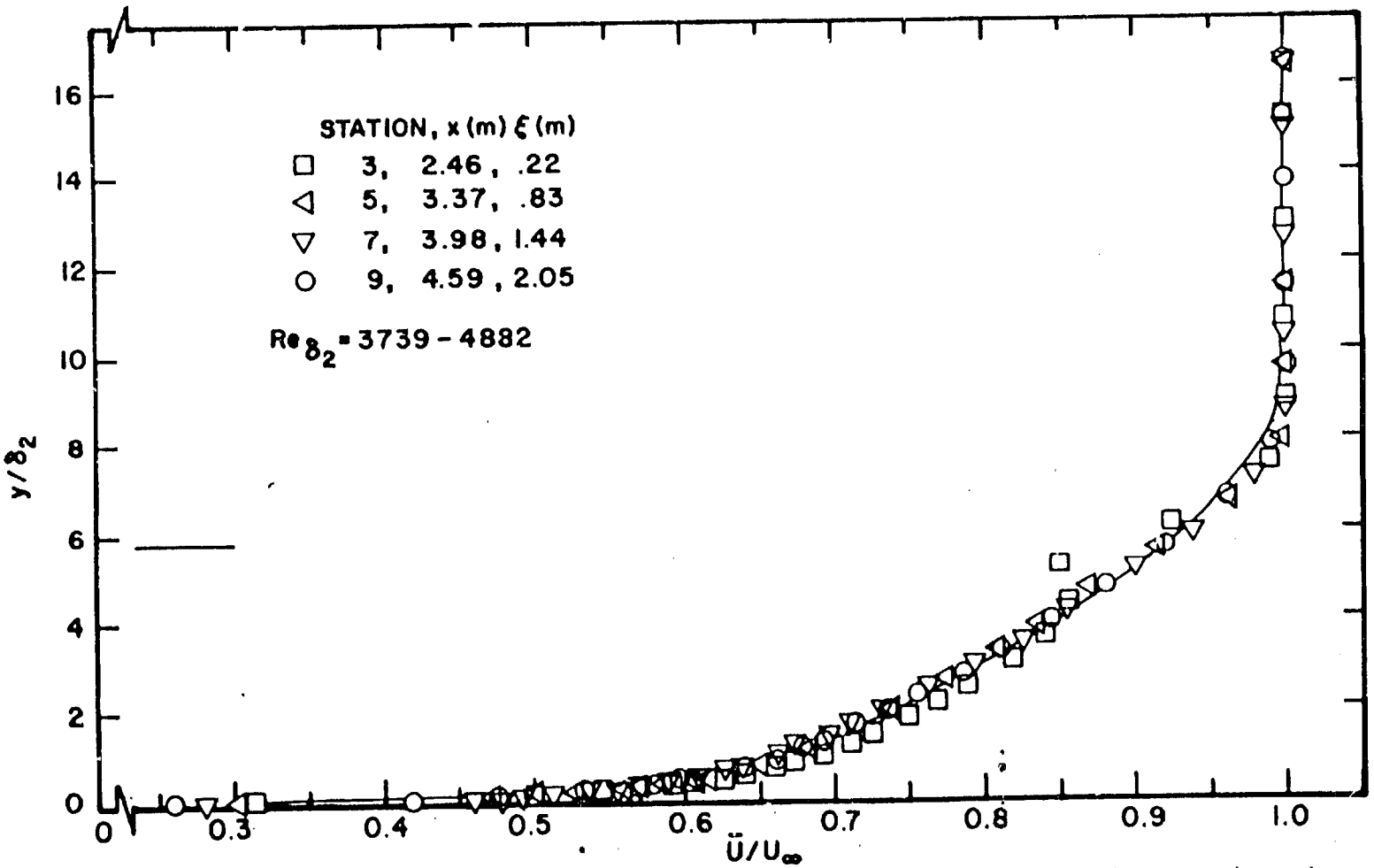

Figure 53. Non-dimensional Mean Velocity Profiles at Various Streamwise Stations in Manipulated Boundary Layer for High Reynolds Number Range

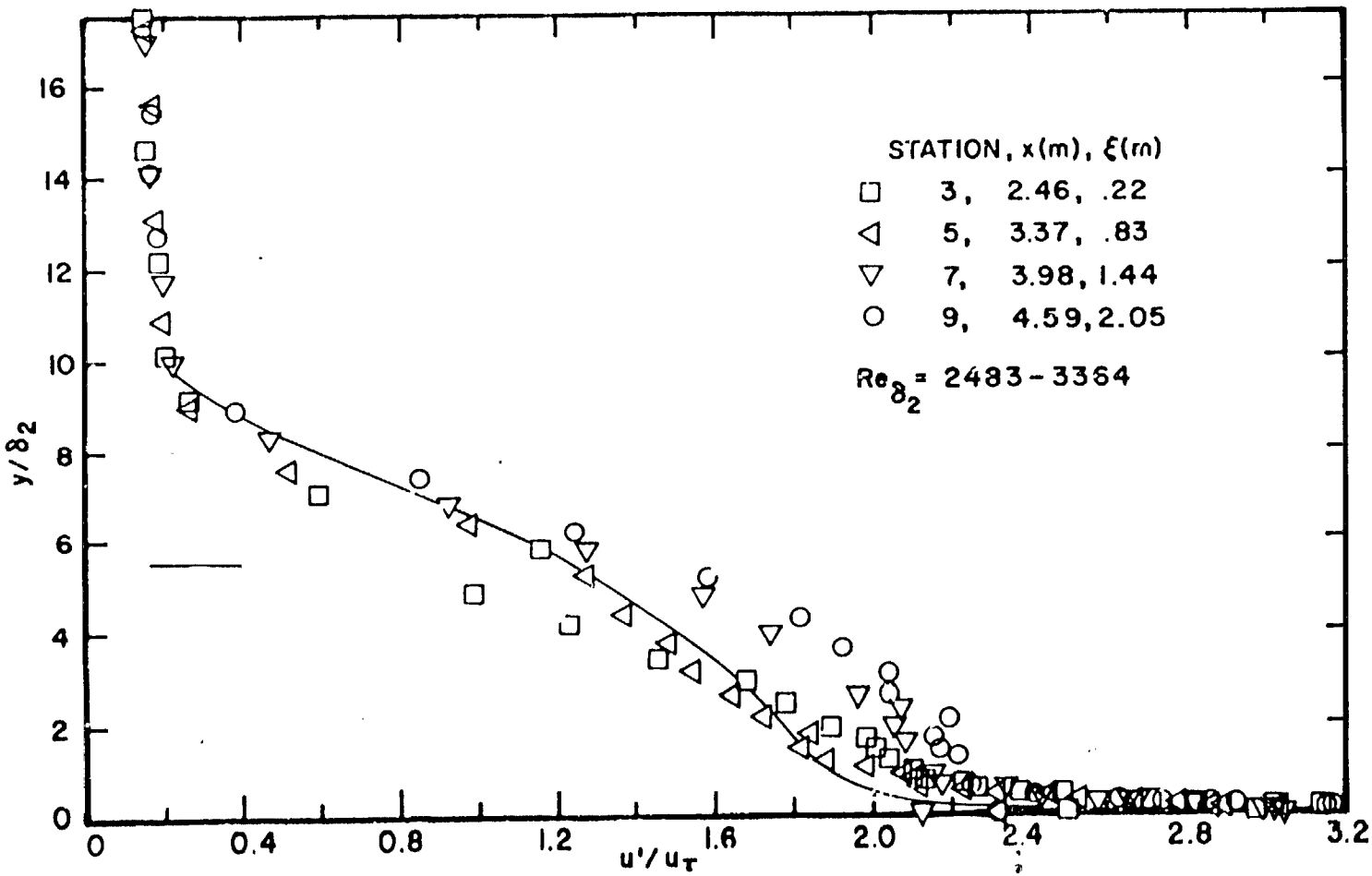

Figure 54. Non-dimensional Fluctuating Velocity Profiles at Various Streamwise Stations in Manipulated Boundary Layer [illegible] Reynolds Number Range

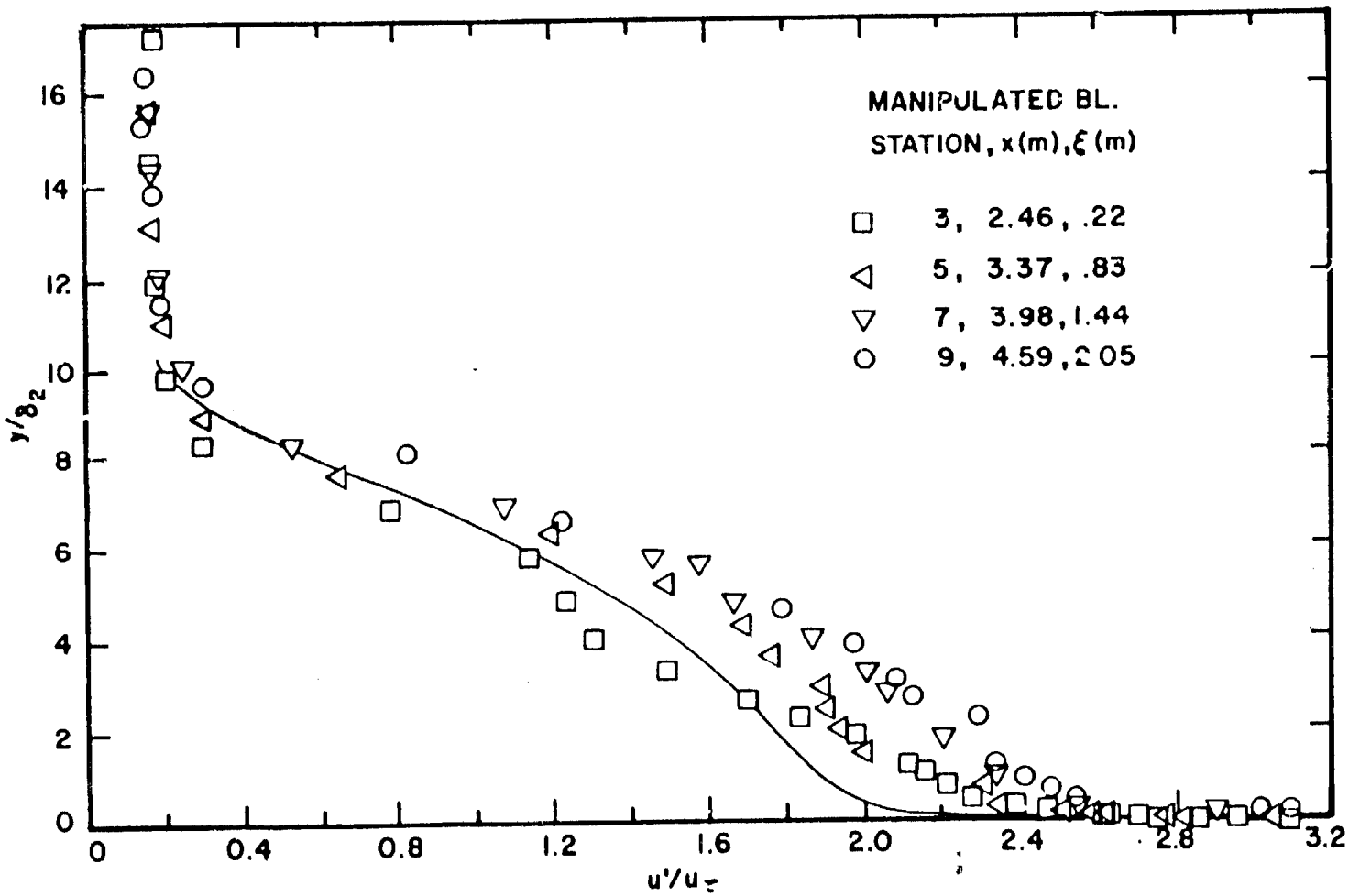

Figure 55. Non-dimensional Fluctuating Velocity Profiles at Various Streamwise Stations in Manipulated Boundary Layer for High Reynolds Number Range

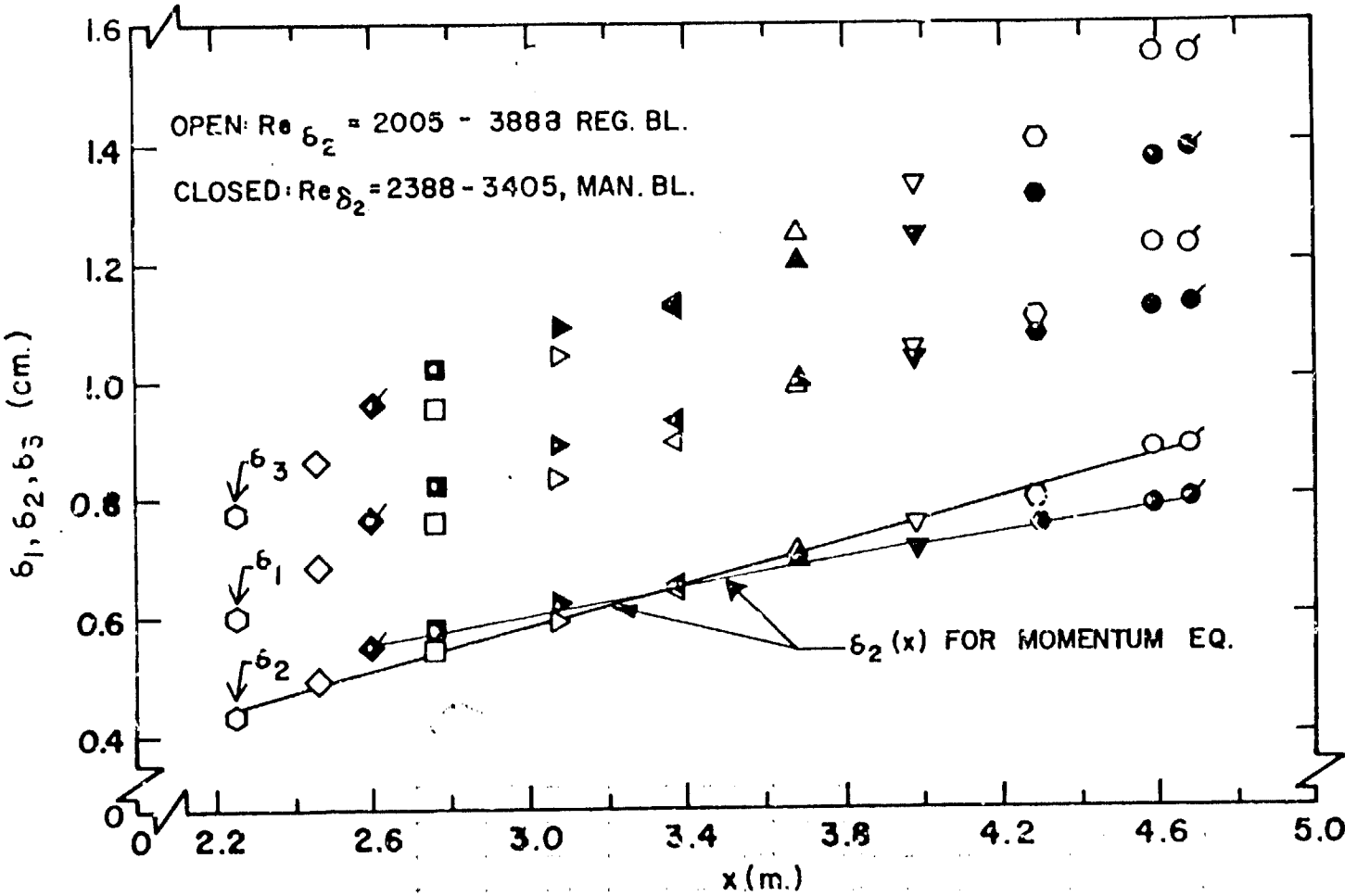

Figure 56. Comparison Between Streamwise Distribution of Integral Thicknesses in Regular and Manipulated Boundary Layers for Low Reynolds Number Range

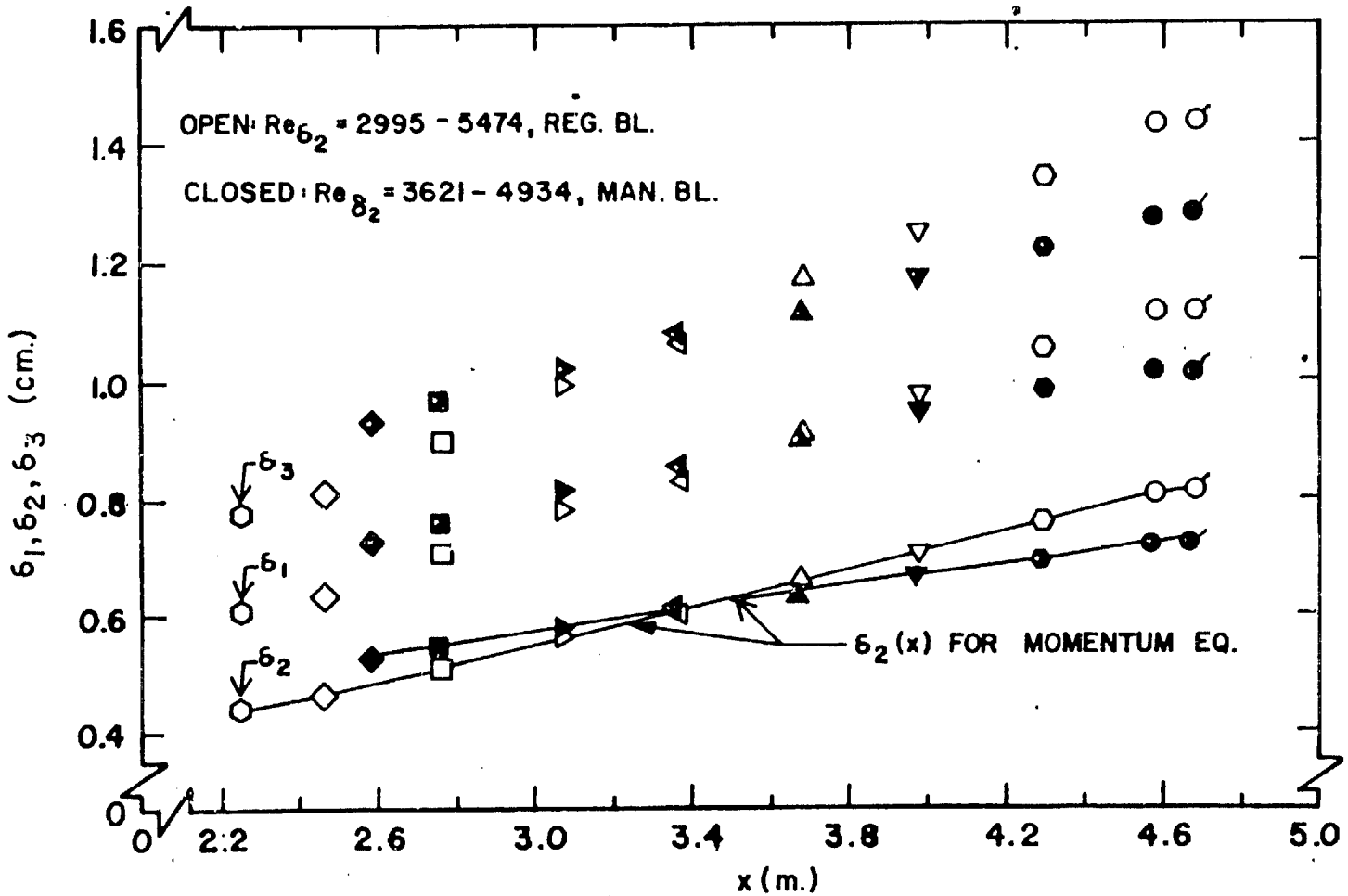

Figure 57. Comparison Between Streamwise Distribution of Integral Thicknesses in Regular and Manipulated Boundary Layers for High Reynolds Number Range

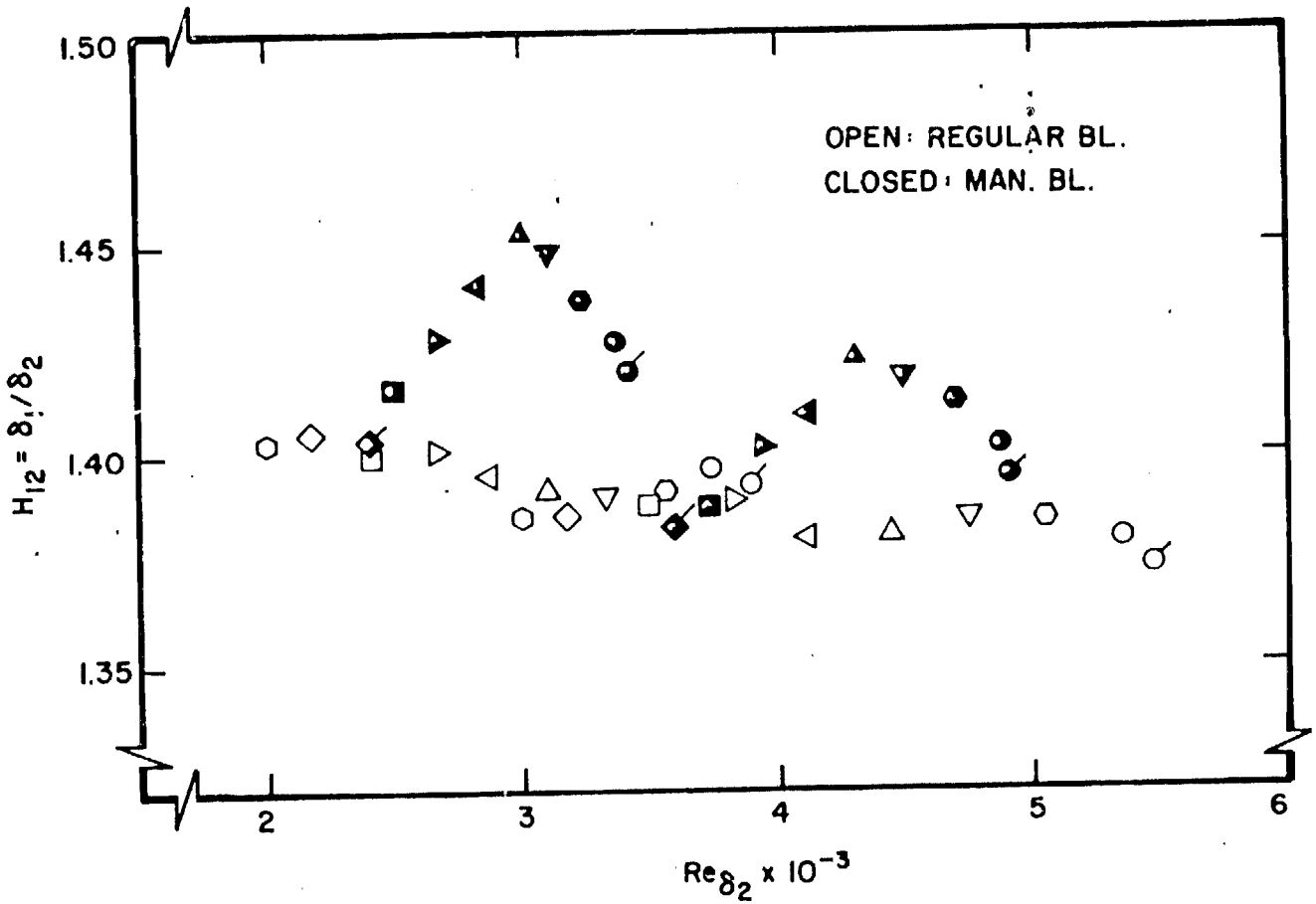

Figure 58. Reynolds Number Dependence of Shape Factor for Regular and Manipulated Boundary Layers

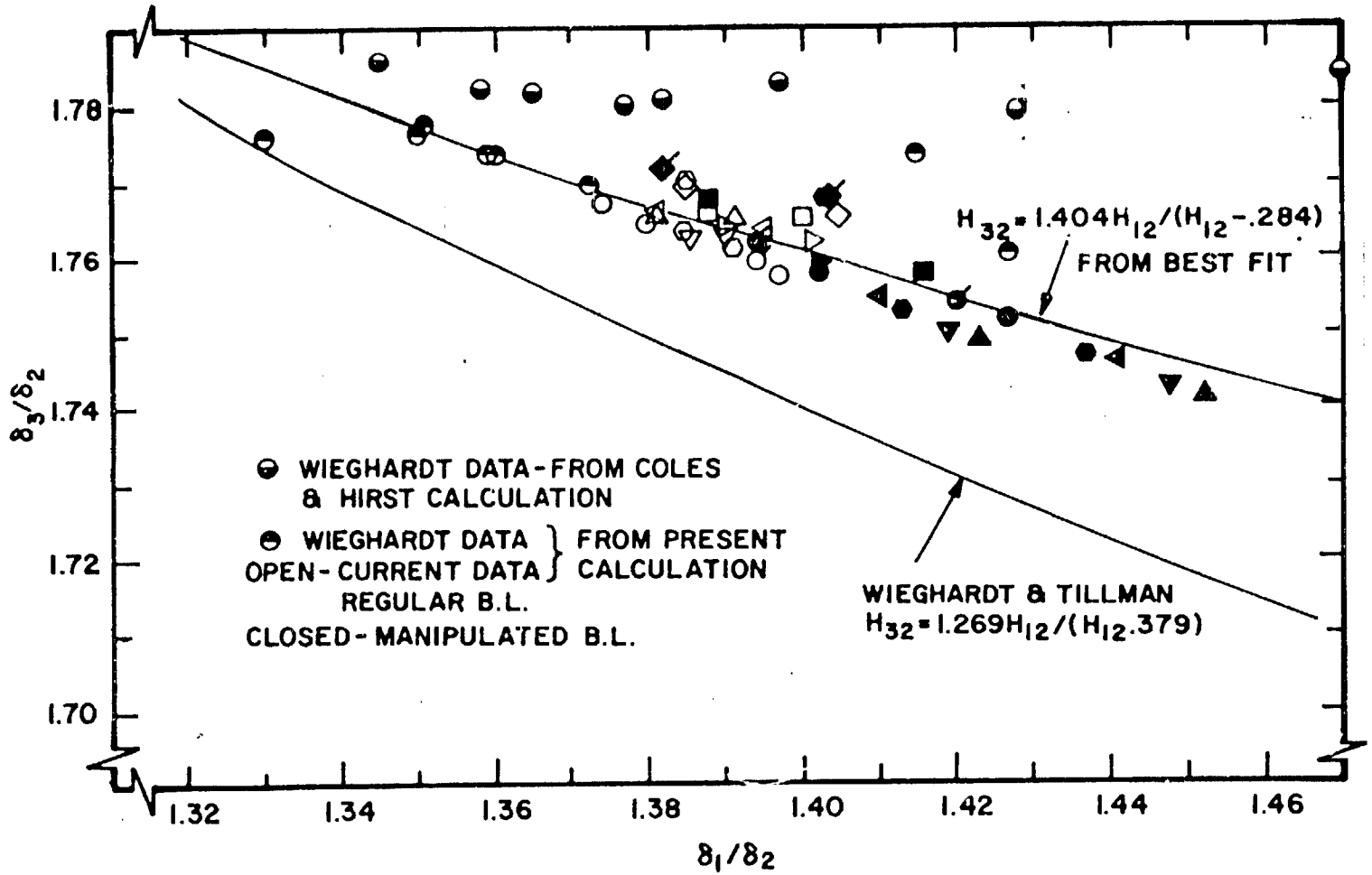

Figure 59. Correlation of Energy to Momentum Thickness Ratio with Shape Factor for Regular and Manipulated Boundary Layers

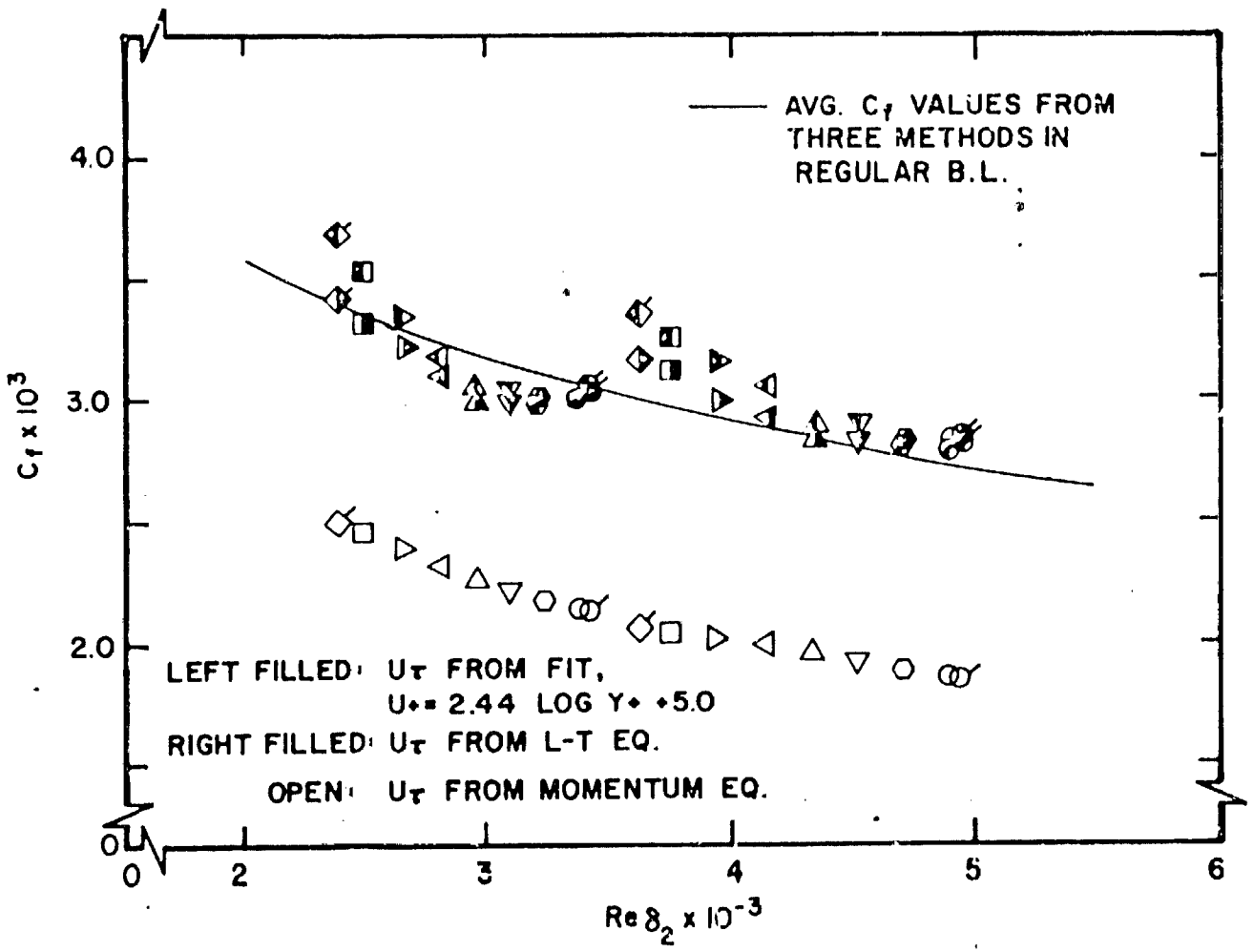

Figure 60. Comparison of Wall-Friction Coefficient Values Obtained by Three Methods in Manipulated Boundary Layer and Average Distribution in Regular Boundary Layer

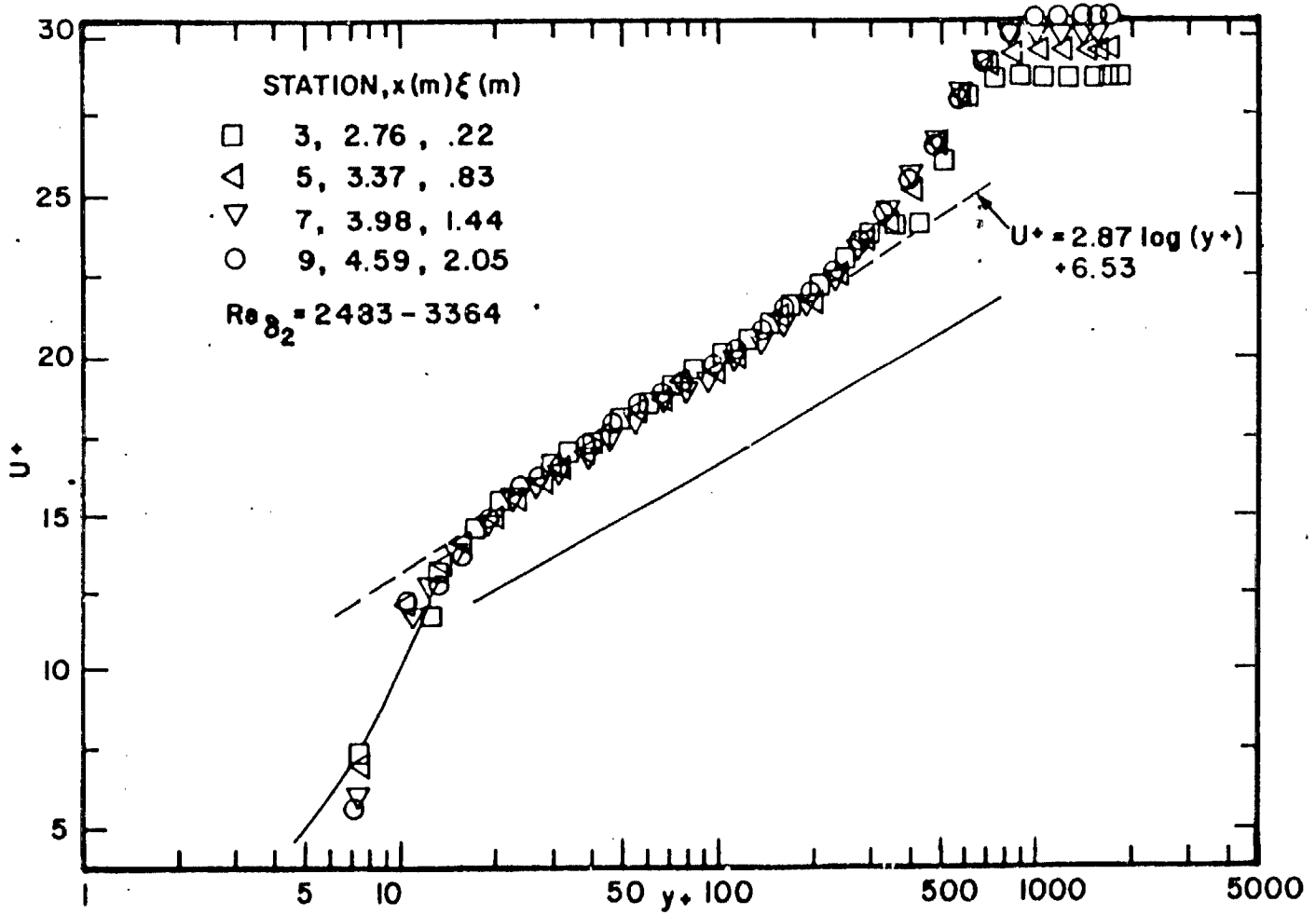

Figure 61. Wall-Unit Non-dimensionalized Mean Velocity Profiles at Various Streamwise Stations in Manipulated Boundary Layer for Low Reynolds Number Range

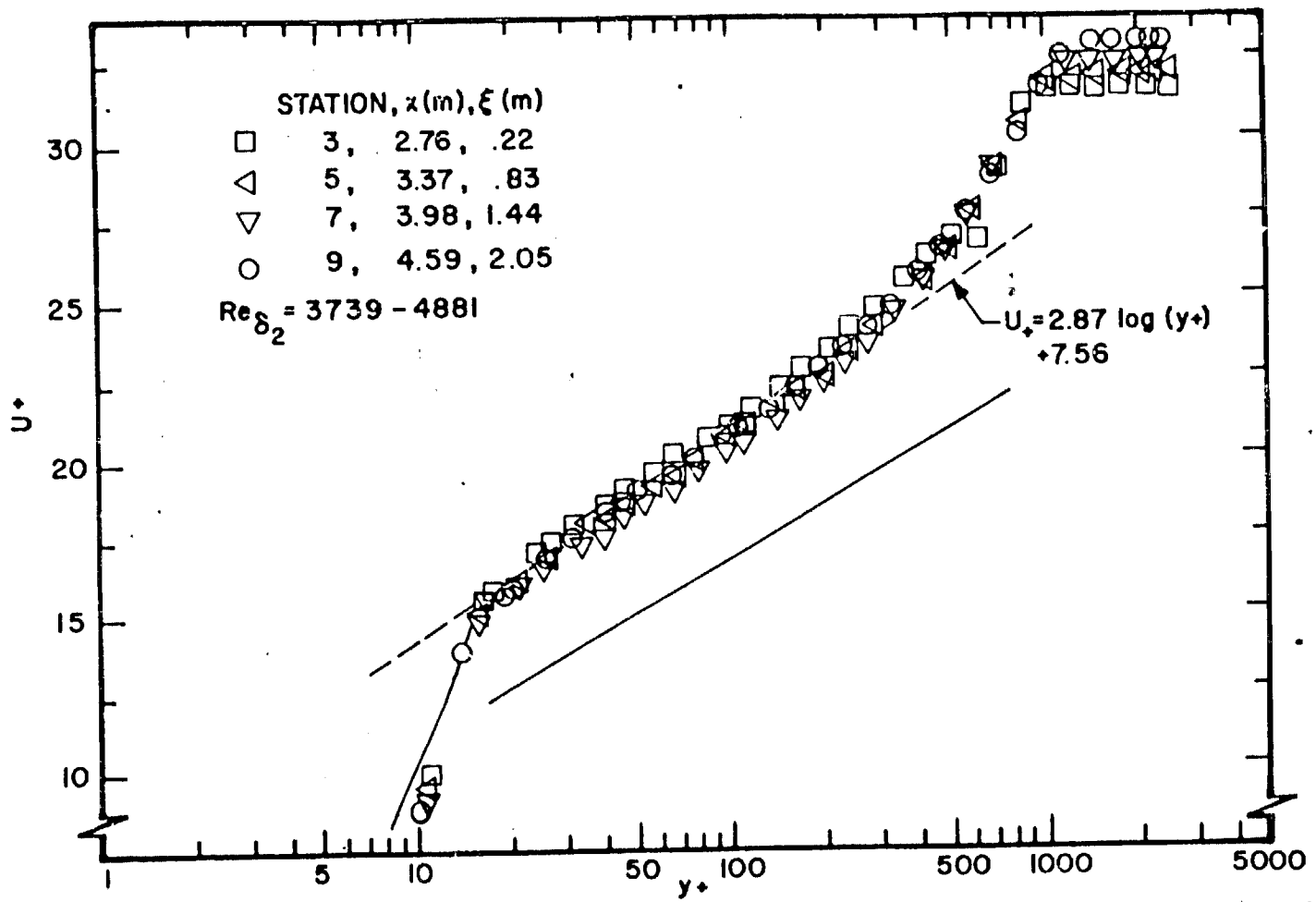

Figure 62. Wall-Unit Non-dimensionalized Mean Velocity Profiles at Various Streamwise Stations in Manipulated Boundary Layer for High Reynolds Number Range

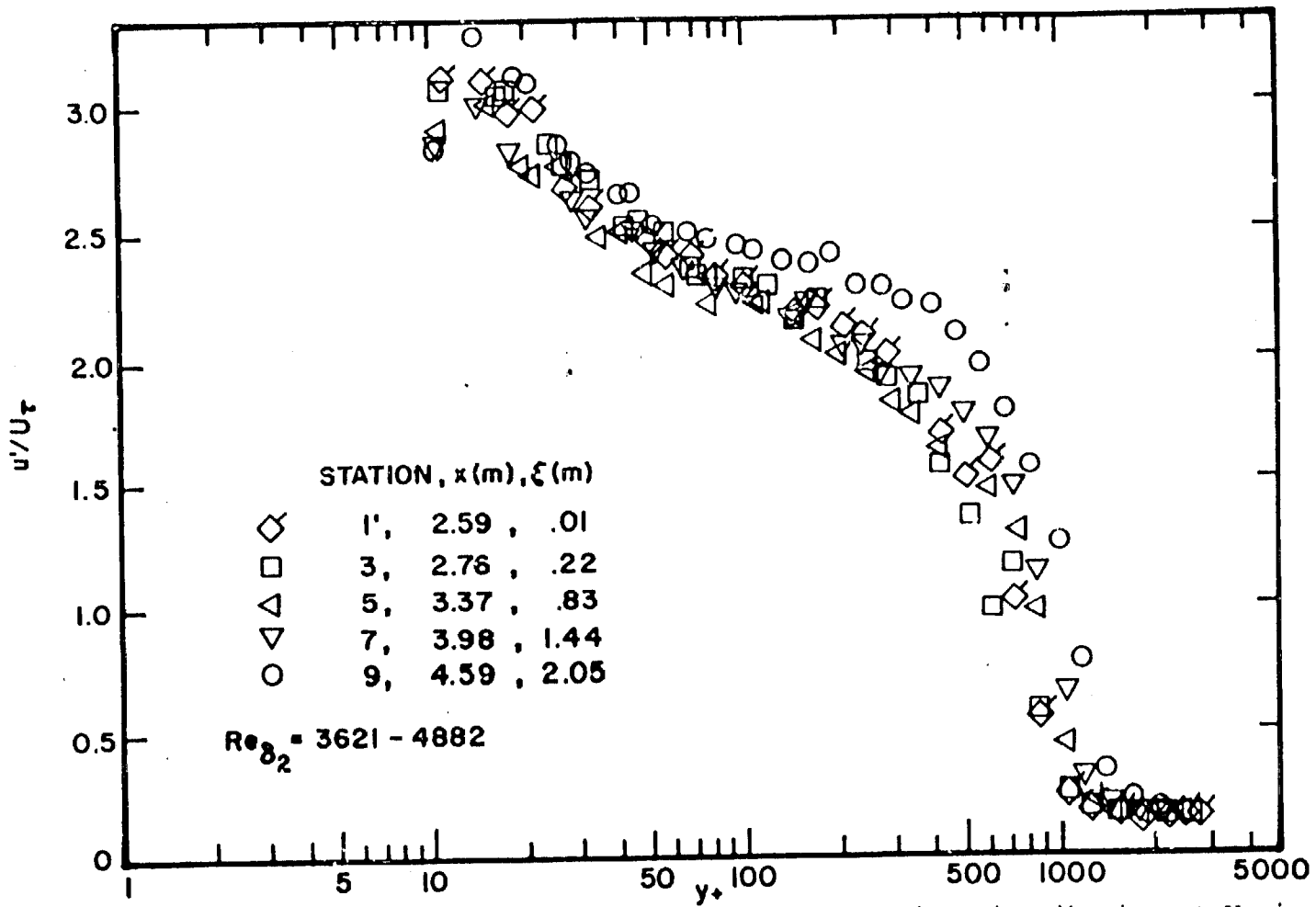

Figure 63. Wall-Unit Non-dimensionalized Fluctuating Velocity Distribution at Various Streamwise Stations in Manipulated Boundary Layer for Low Reynolds Number Range

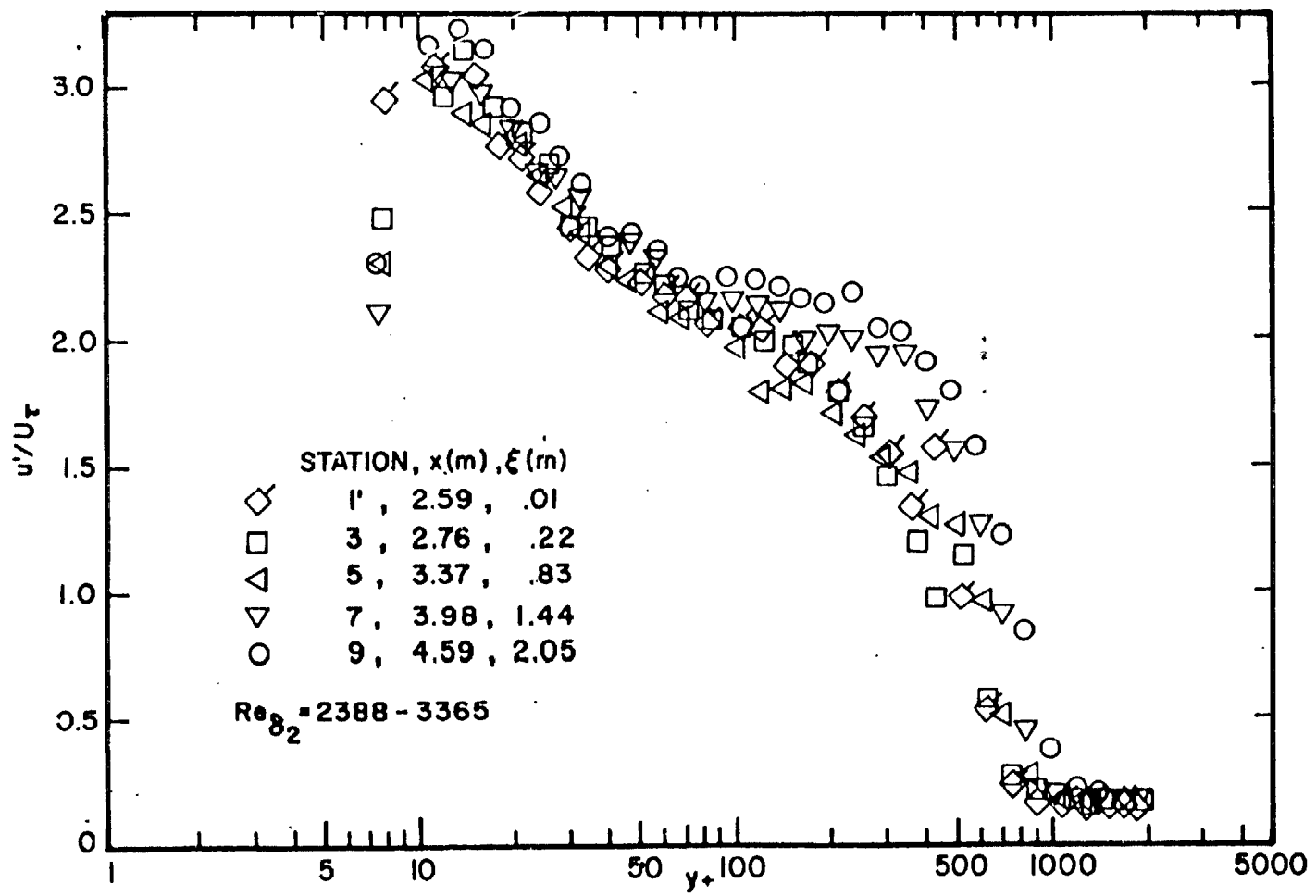

Figure 64. Wall-Unit Non-dimensionalized Fluctuating Velocity Distribution at Various Streamwise Stations in Manipulated Boundary Layer for High Reynolds Number Range

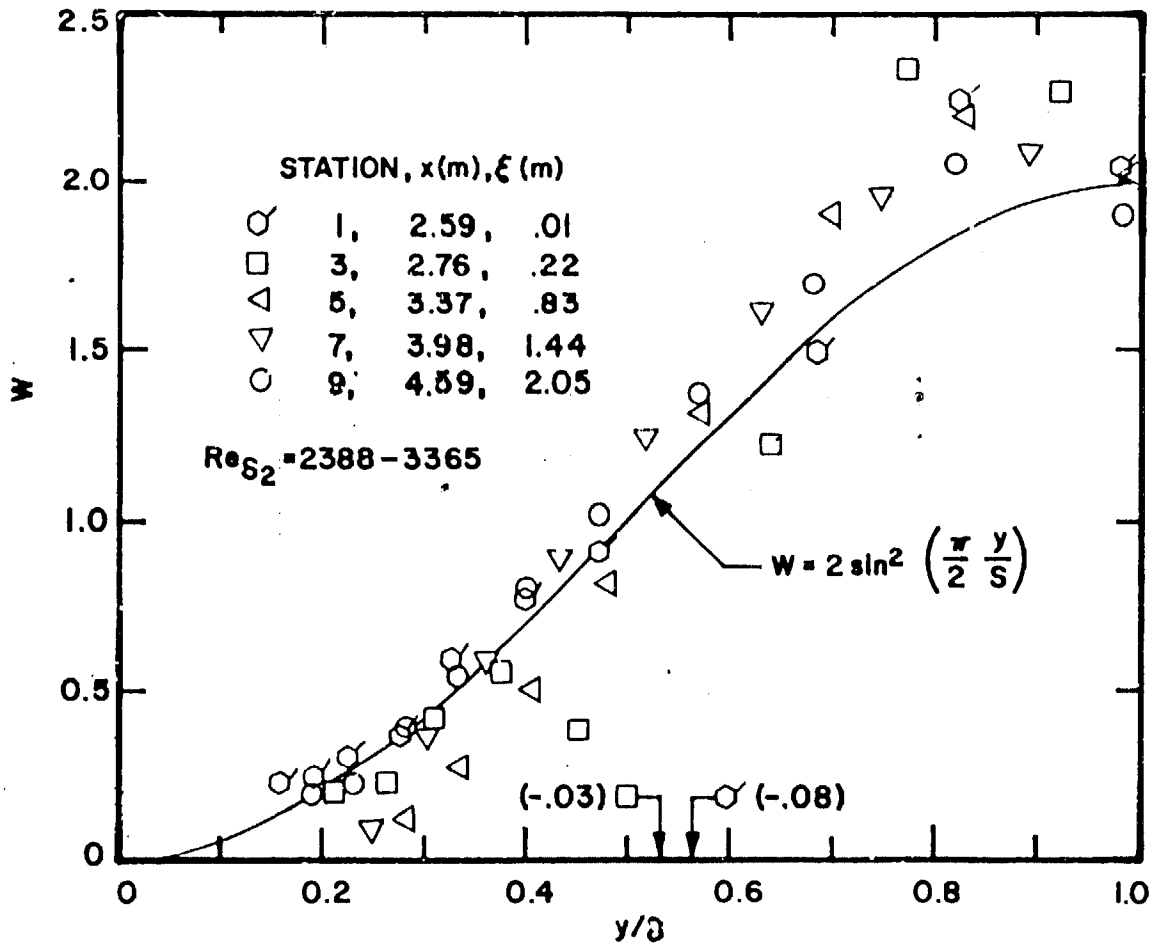

Figure 65. Wake Function Distribution at Various Streamwise Stations in Manipulated Boundary Layer for Low Reynolds Number Range

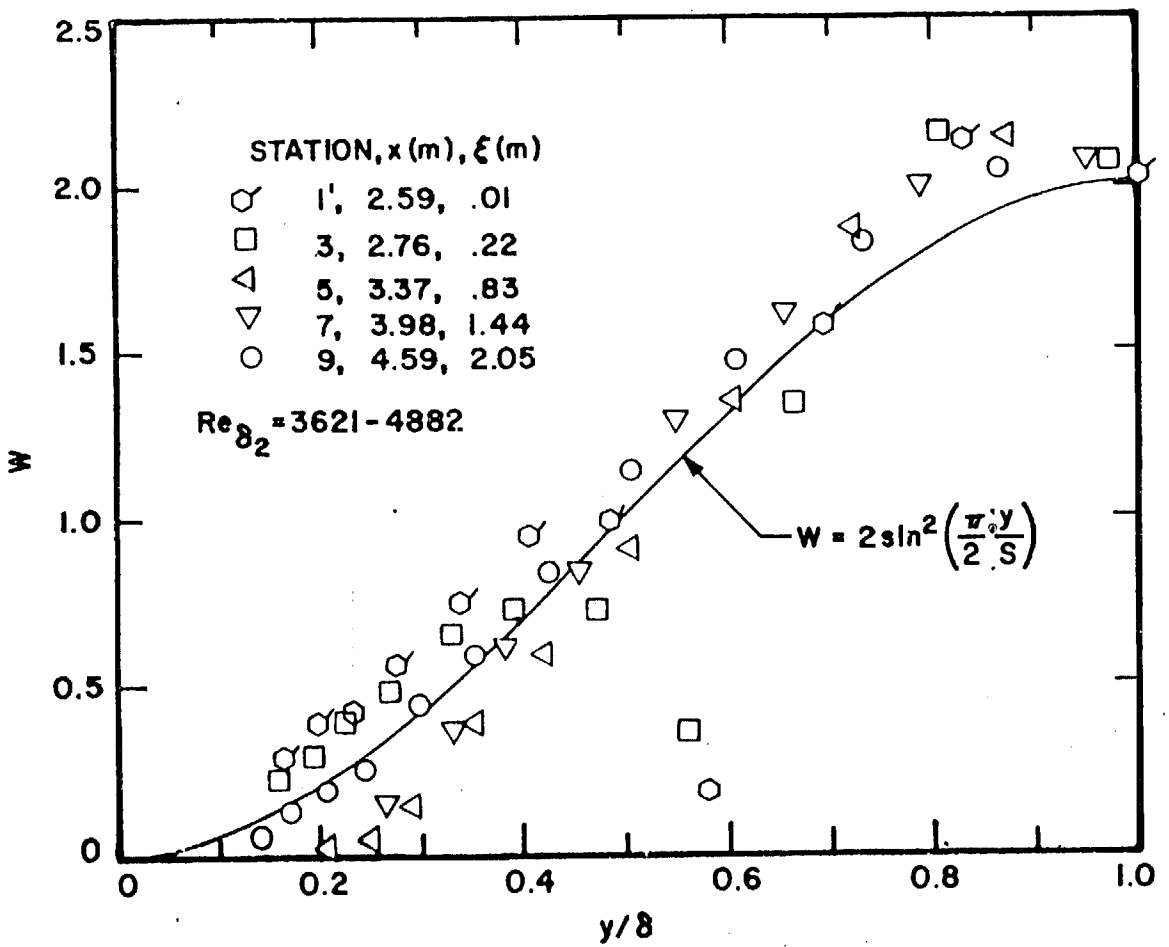

Figure 66. Wake Function Distribution at Various Streamwise Stations in Manipulated Boundary Layer for High Reynolds Number Range

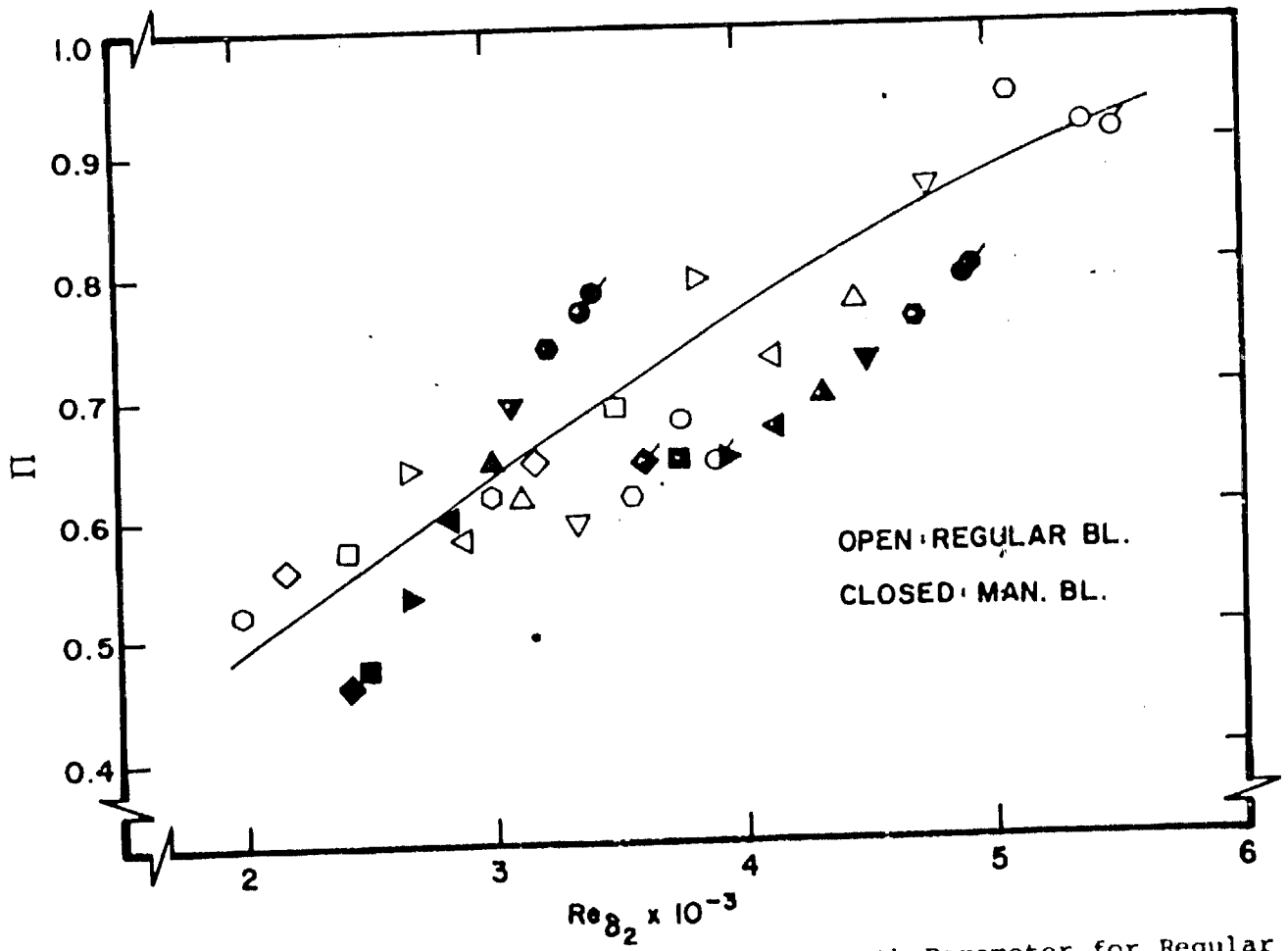

Figure 67. Reynolds Number Dependence of Wake Strength Parameter for Regular and Manipulated Boundary Layers

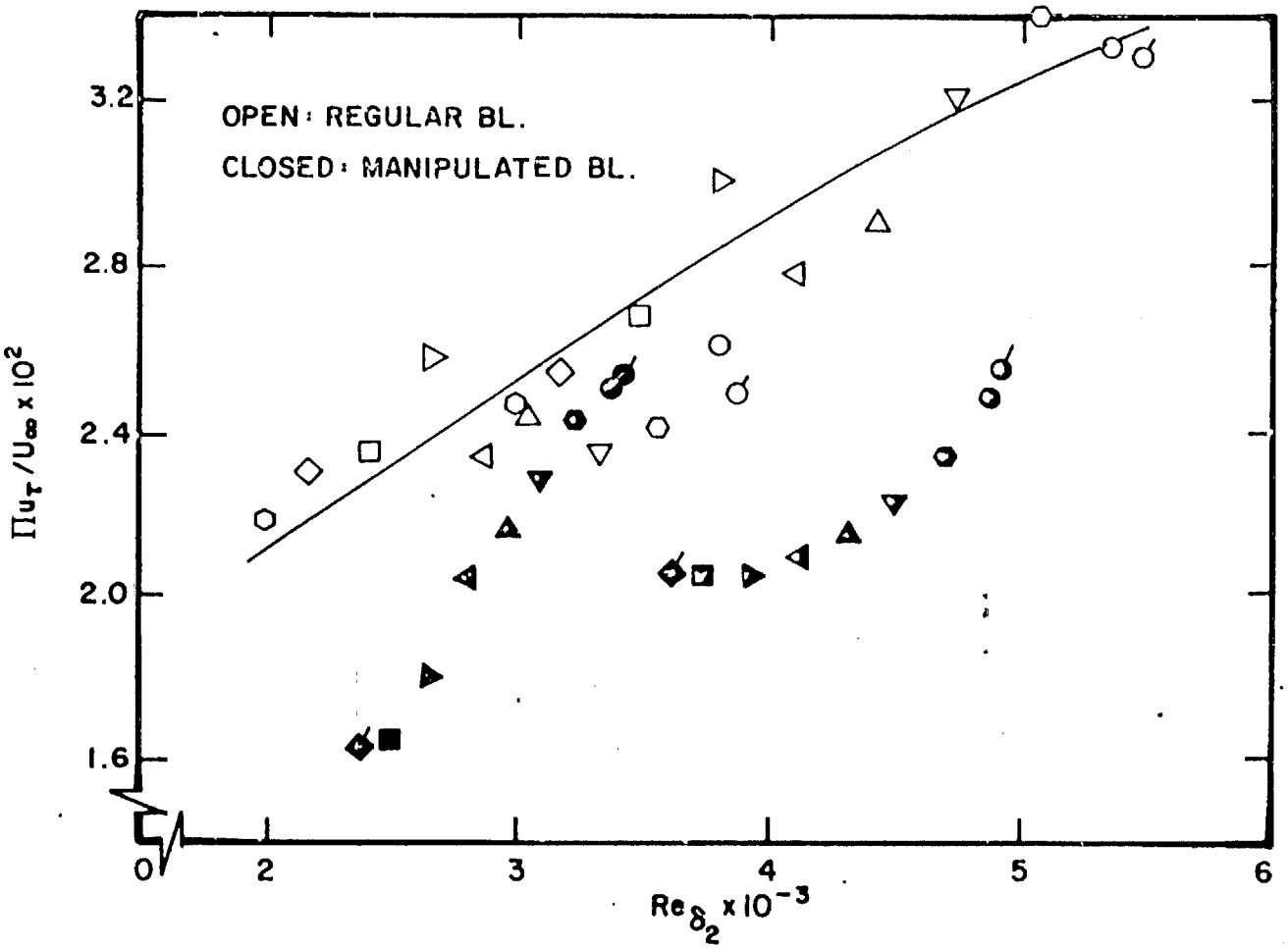

Figure 68. Reynolds Number Dependence of Normalized Wake Strength Parameter for Regular and Manipulated Boundary Layers

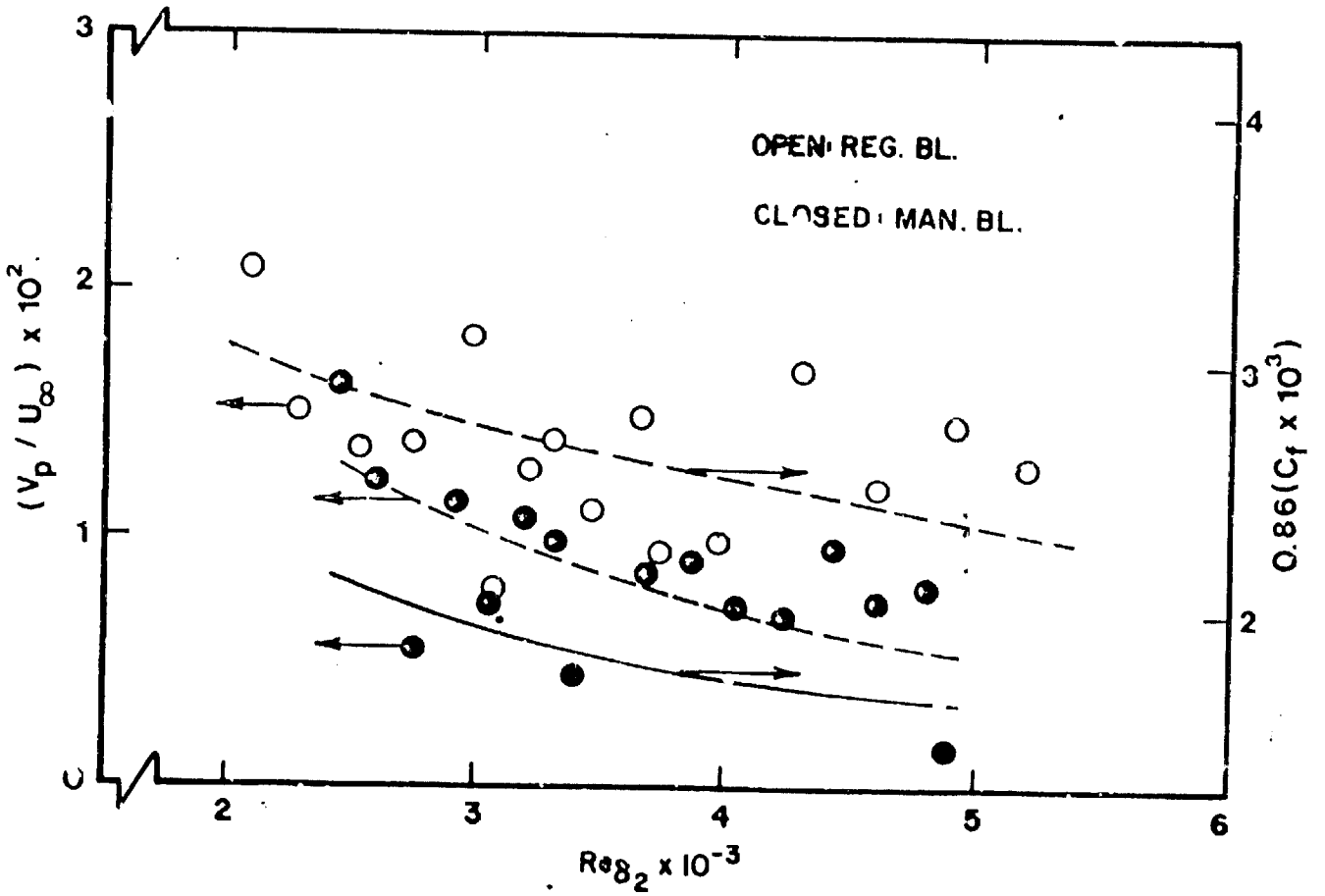

Figure 69. Reynolds Number Dependence of Non-dimensional Entrainment Velocity and its Correlation to Wall-Friction Coefficient

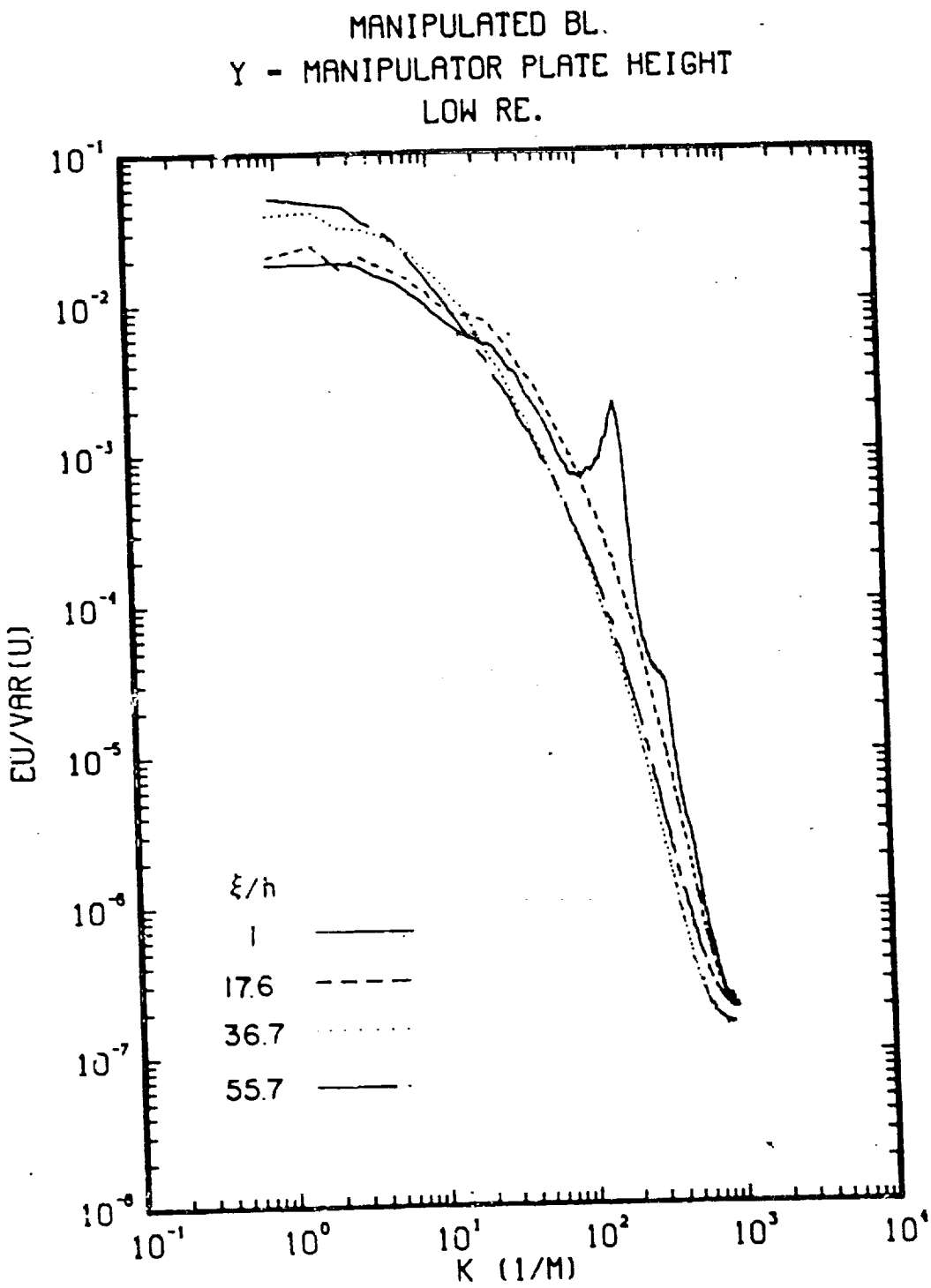

Figure 70. One-dimensional Spectra of Streamwise Velocity Component at Various Stations Behind Manipulator Plate for Low Reynolds Number Range

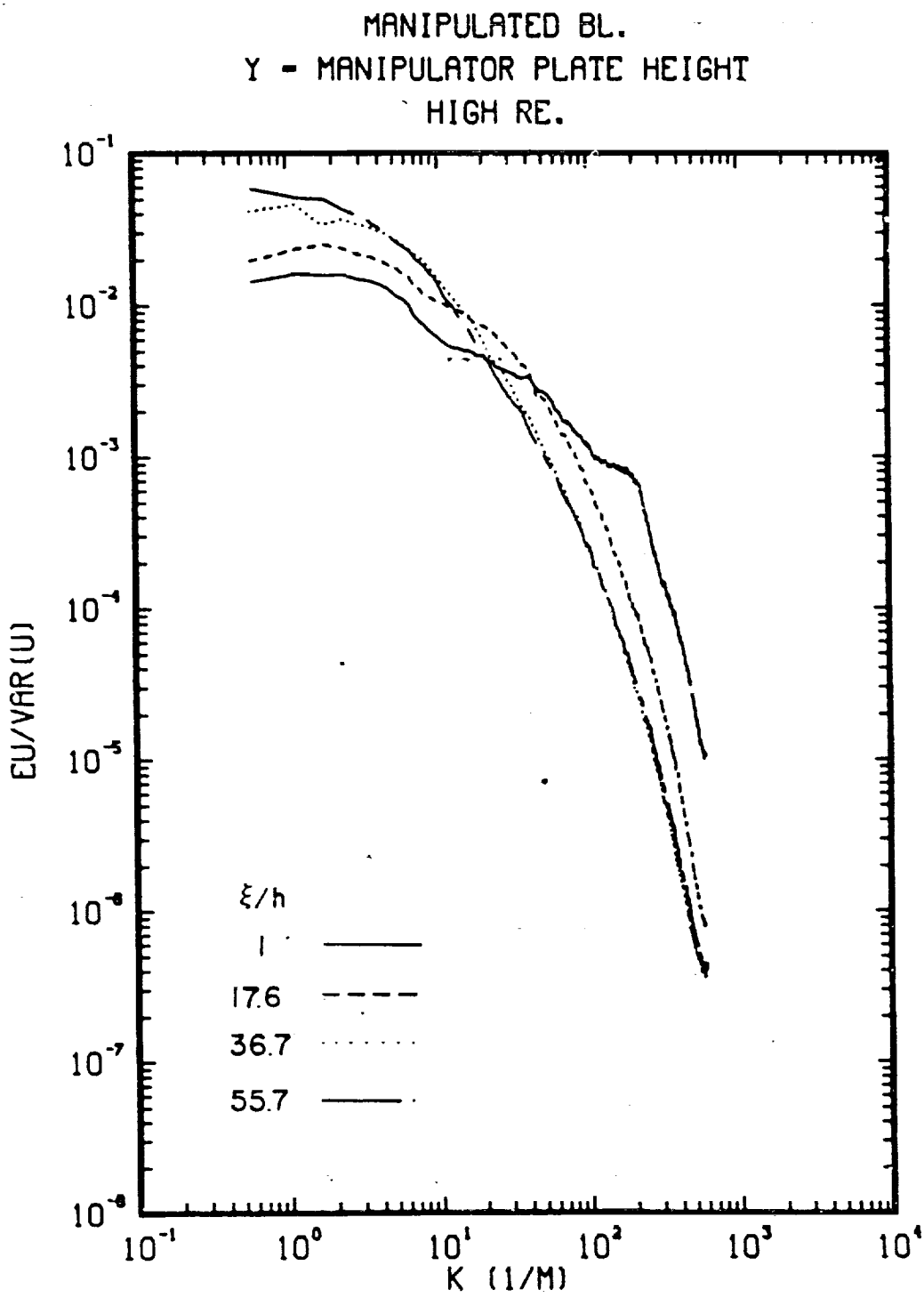

Figure 71. One-dimensional Spectra of Streamwise Velocity Component at Various Stations Behind Manipulator Plate for High Reynolds Number Range

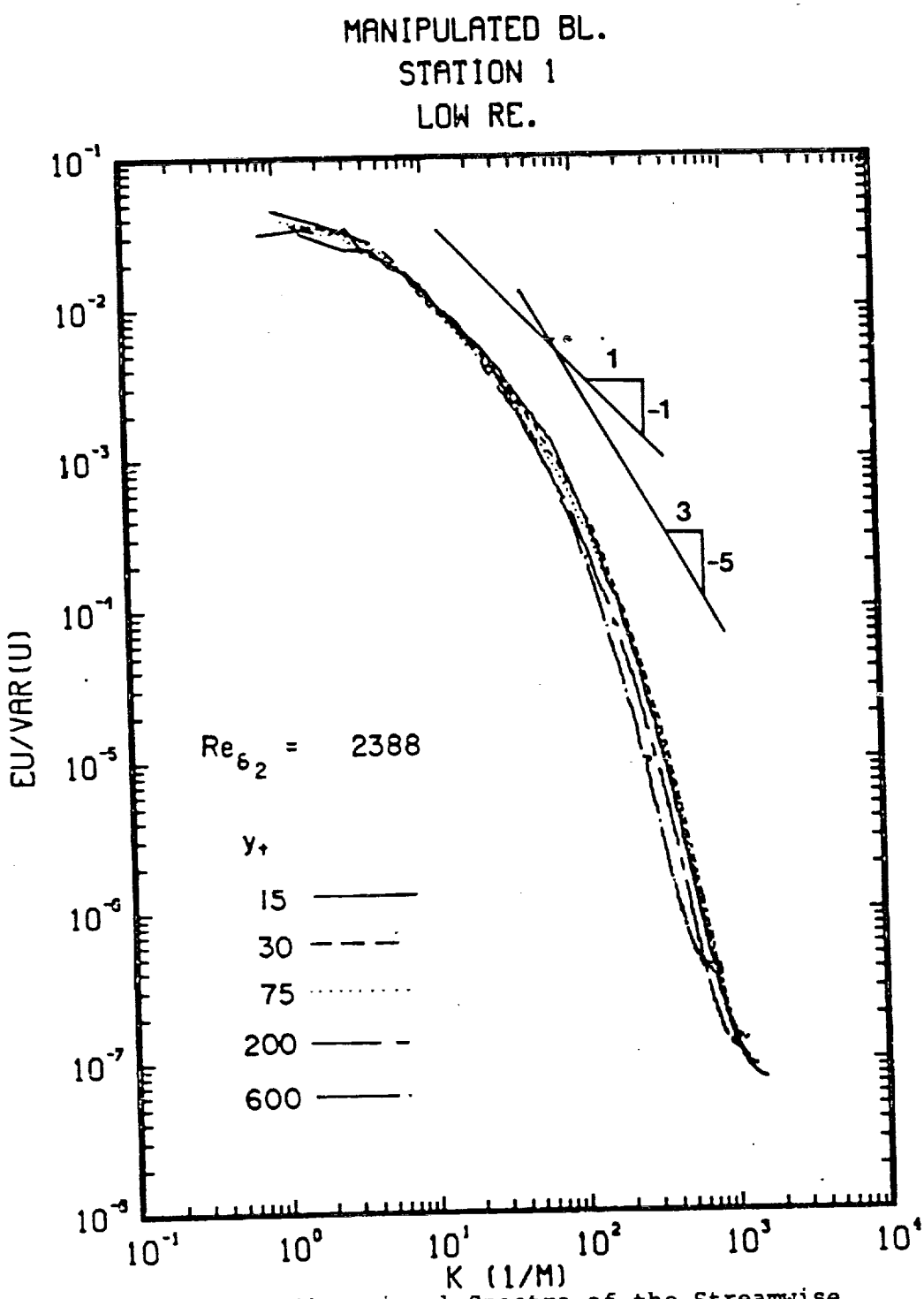

Figure 72. One-dimensional Spectra of the Streamwise Velocity Component at Different Self-Similar Heights at Station 1 in the Manipulated Boundary Layer for Low Reynolds Number Range

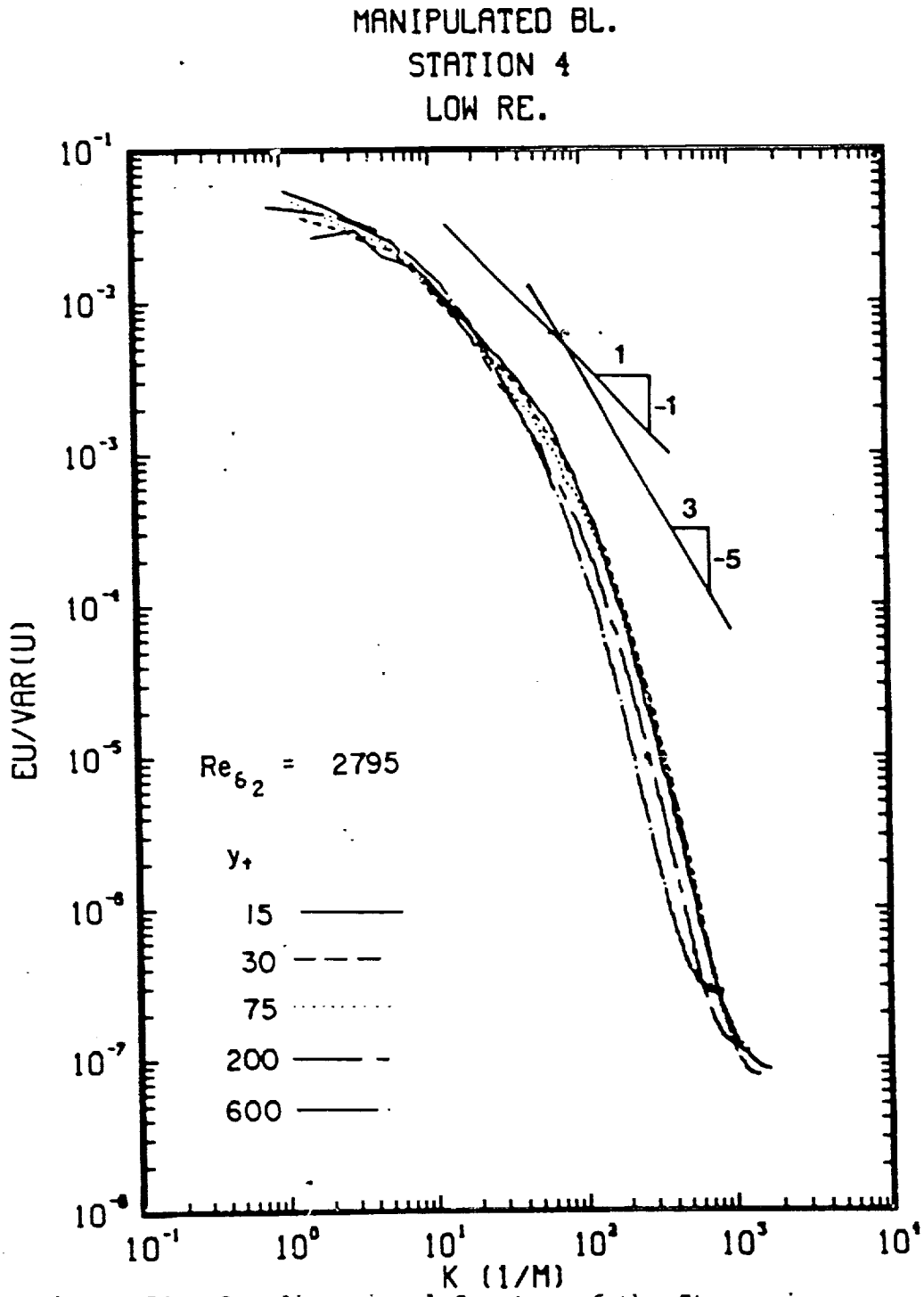

Figure 73. One-dimensional Spectra of the Streamwise Velocity Component at Different Self-Similar Heights at Station 4 in the Manipulated Boundary Layer for Low Reynolds Number Range

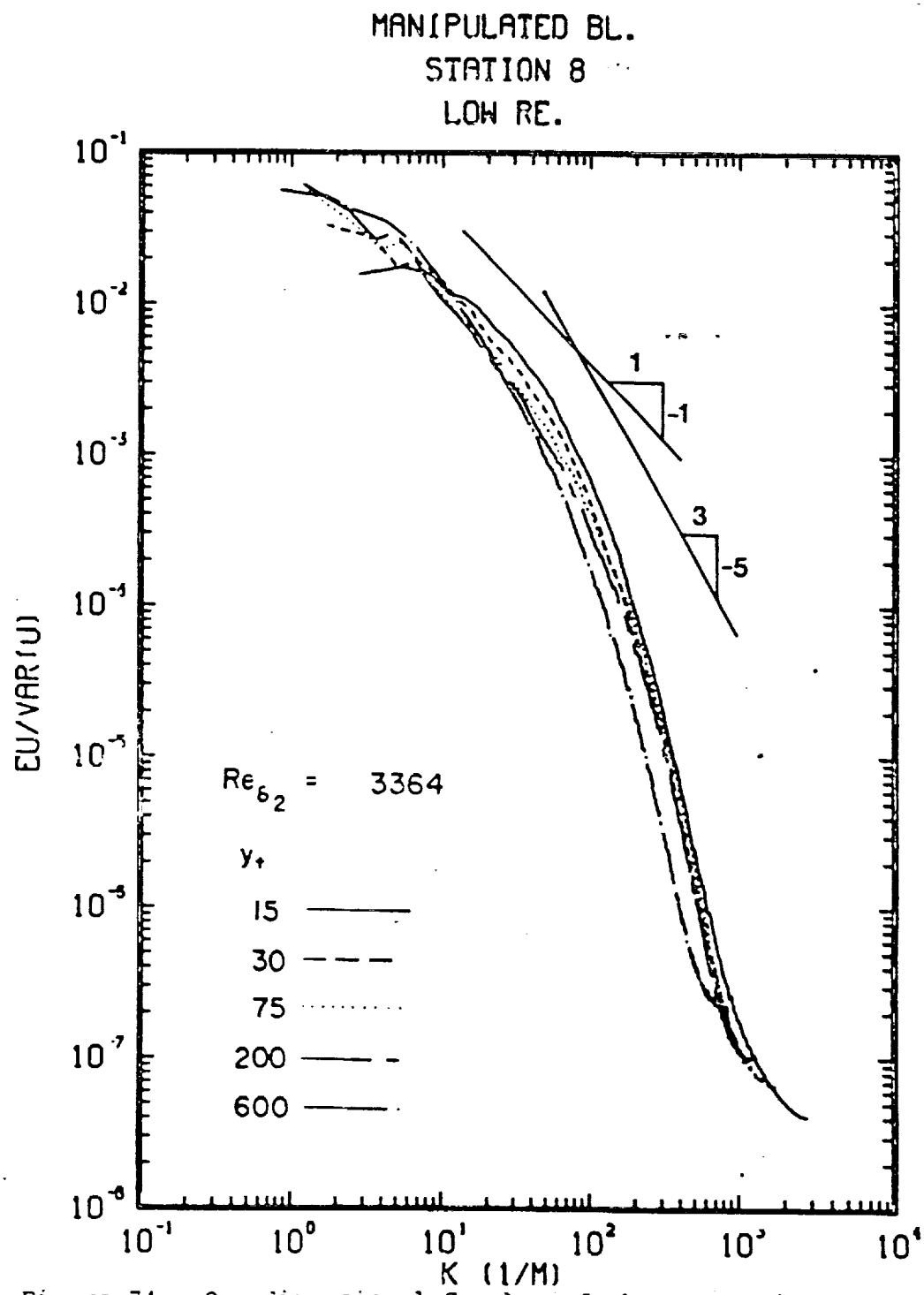

Figure 74. One-dimensional Spectra of the Streamwise Velocity Component at Different Self-Similar Heights at Station 8 in the Manipulated Boundary Layer for Low Reynolds Number Range

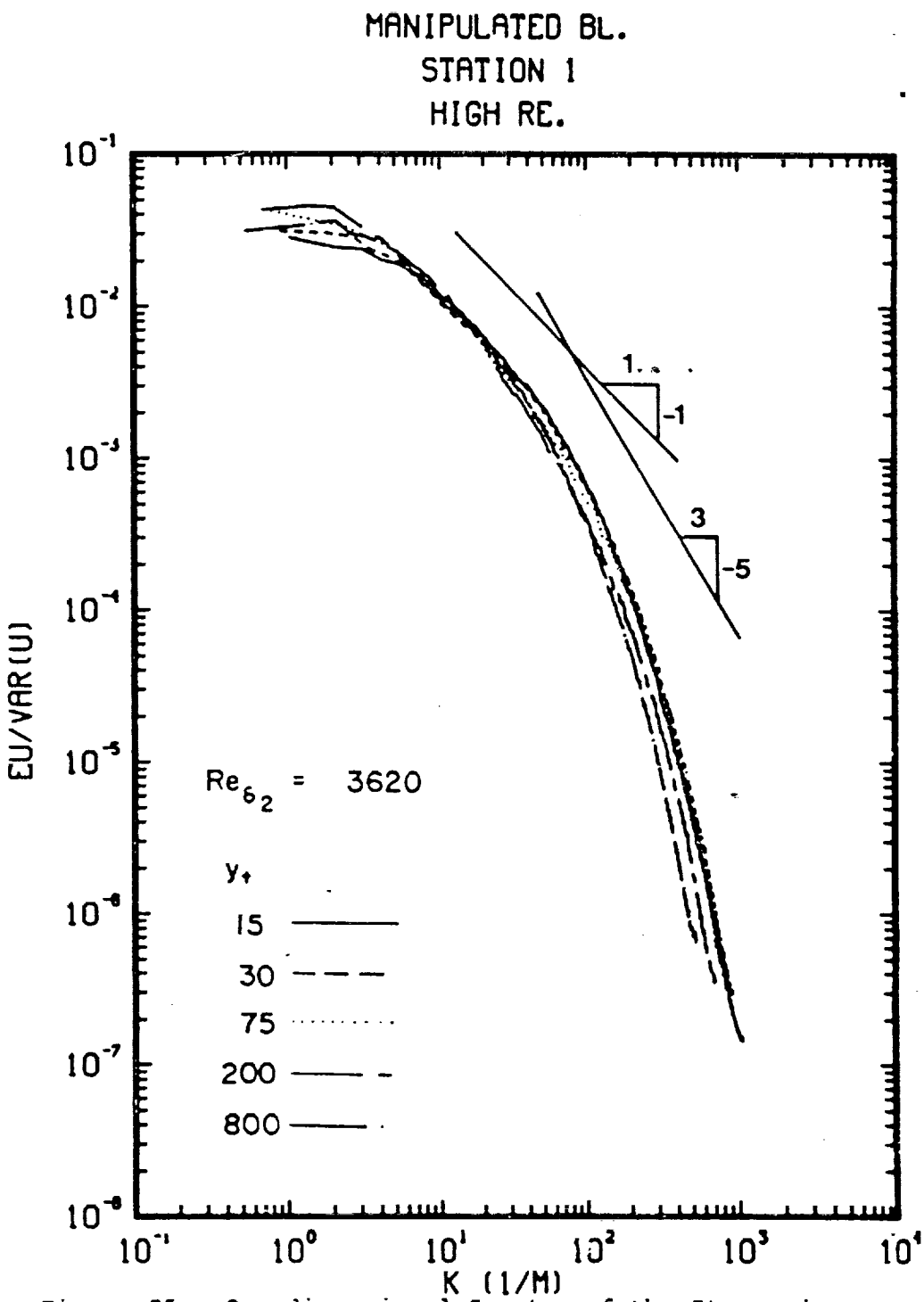

Figure 75. One-dimensional Spectra of the Streamwise Velocity Component at Different Self-Similar Heights at Station 1 in the Manipulated Boundary Layer for High Reynolds Number Range

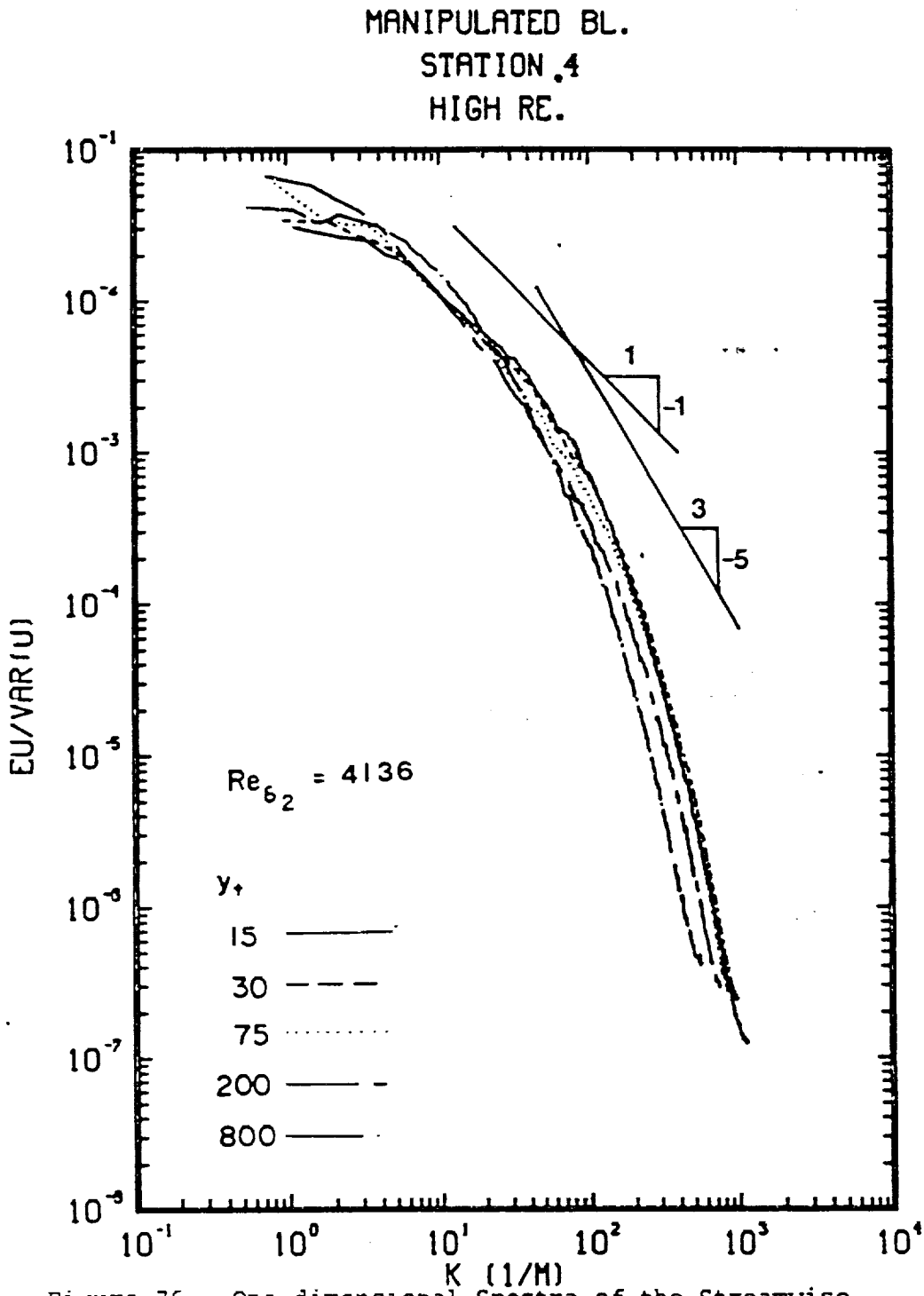

Figure 76. One-dimensional Spectra of the Streamwise Velocity Component at Different Self-Similar Heights at Station 4 in the Manipulated Boundary Layer for High Reynolds Number Range

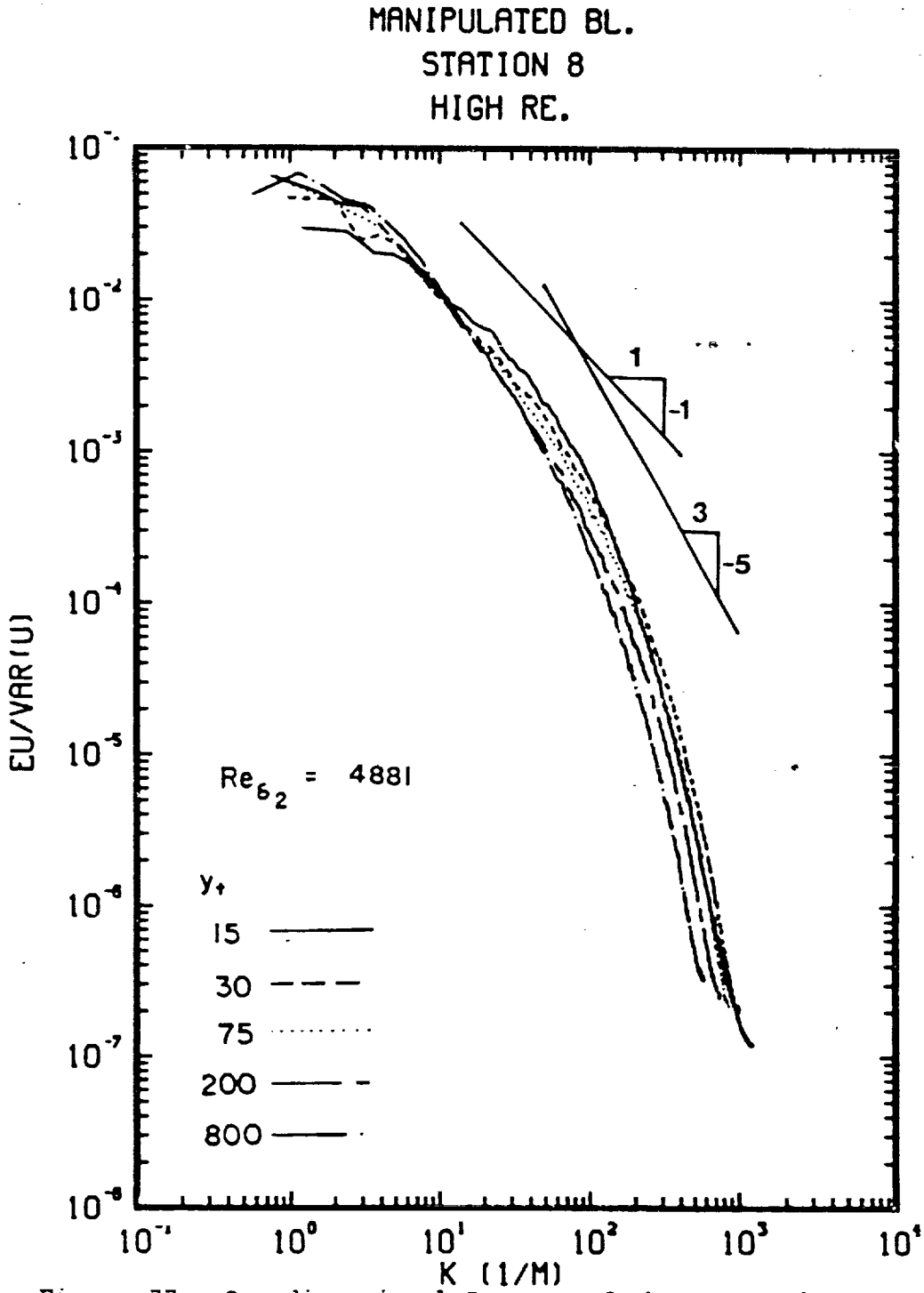

Figure 77. One-dimensional Spectra of the Streamwise Velocity Component at Different Self-Similar Heights at Station 8 in the Manipulated Boundary Layer for High Reynolds Number Range

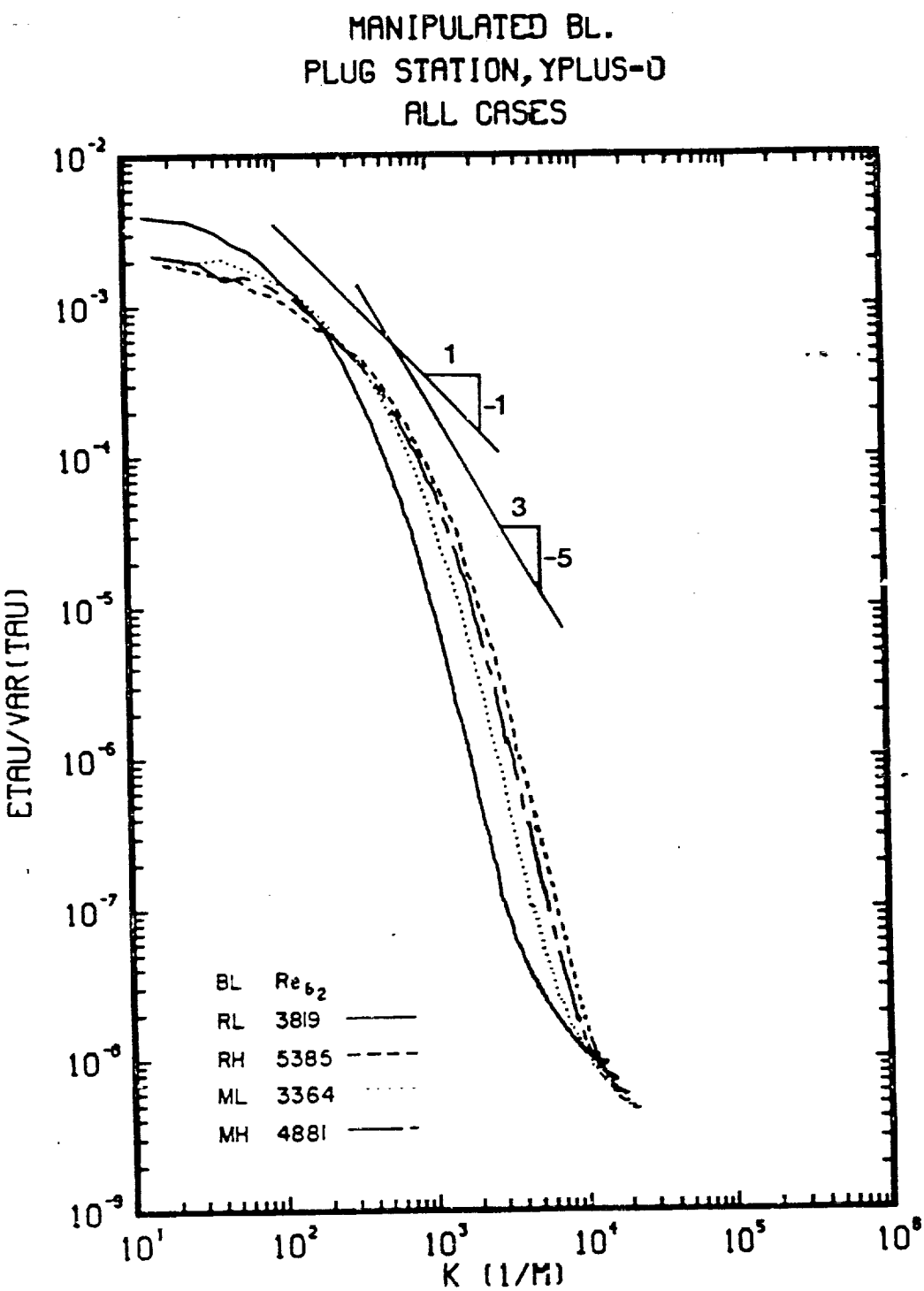

Figure 78. One-dimensional Spectra of Wall-Shear Stress for Regular and Manipulated Boundary Layers at Both Free-Stream Speeds

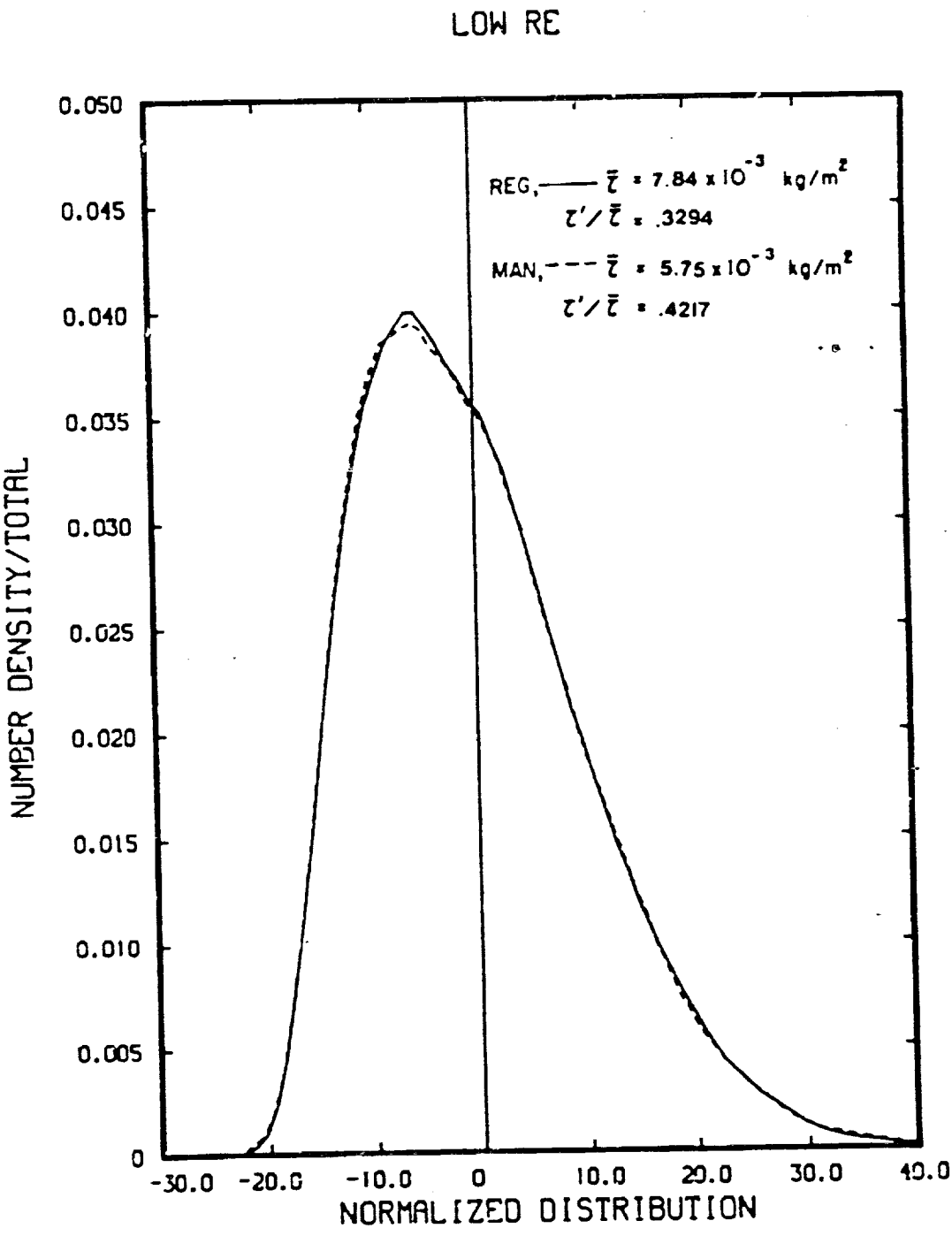

Figure 79. Normalized Probability Distribution of Wall-Shear Fluctuations for Regular and Manipulated Boundary Layers at Low Free-Stream Speed

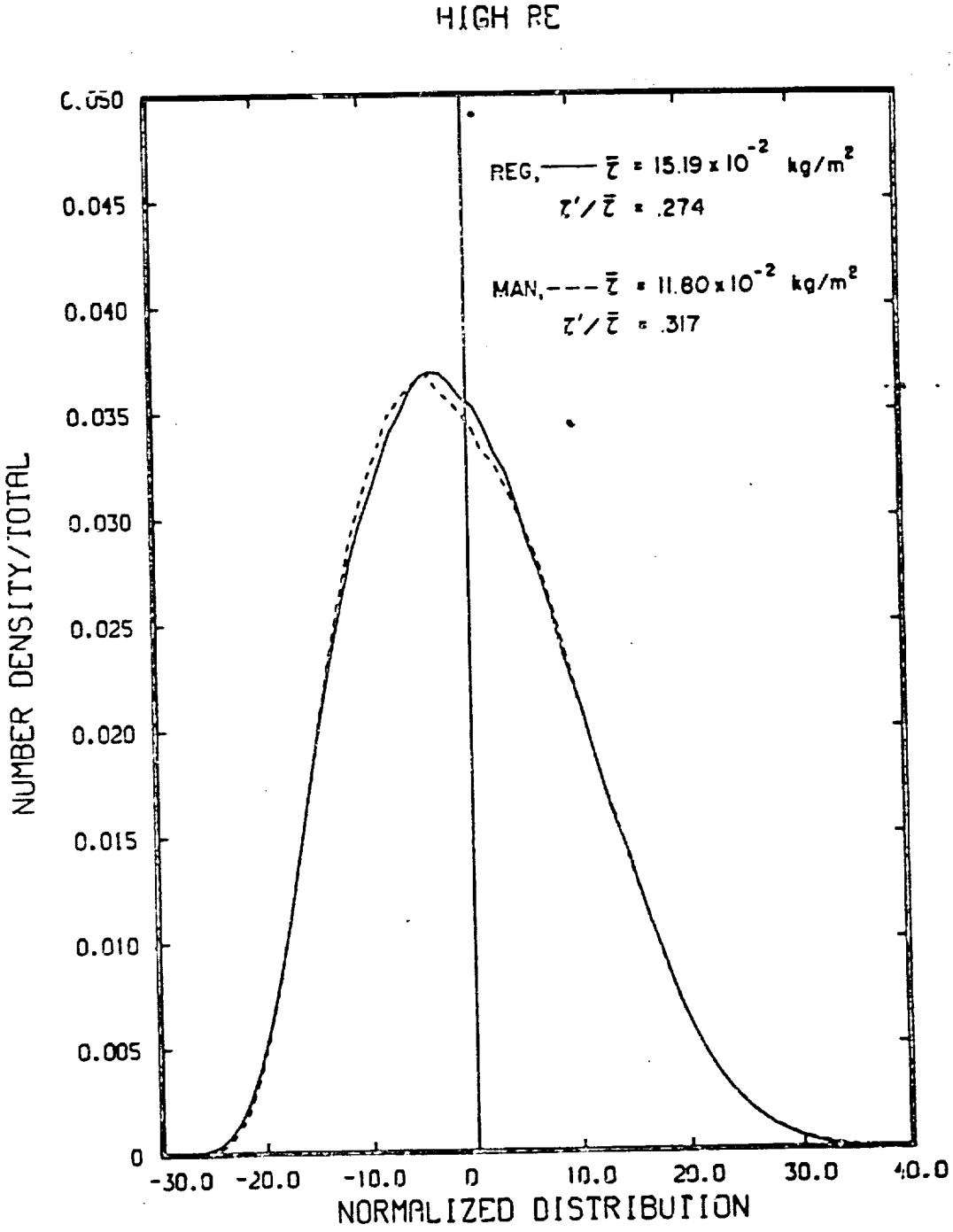

Figure 80. Normalized Probability Distribution of Wall-Shear Fluctuations for Regular and Manipulated Boundary Layers at High Free-Stream Speed

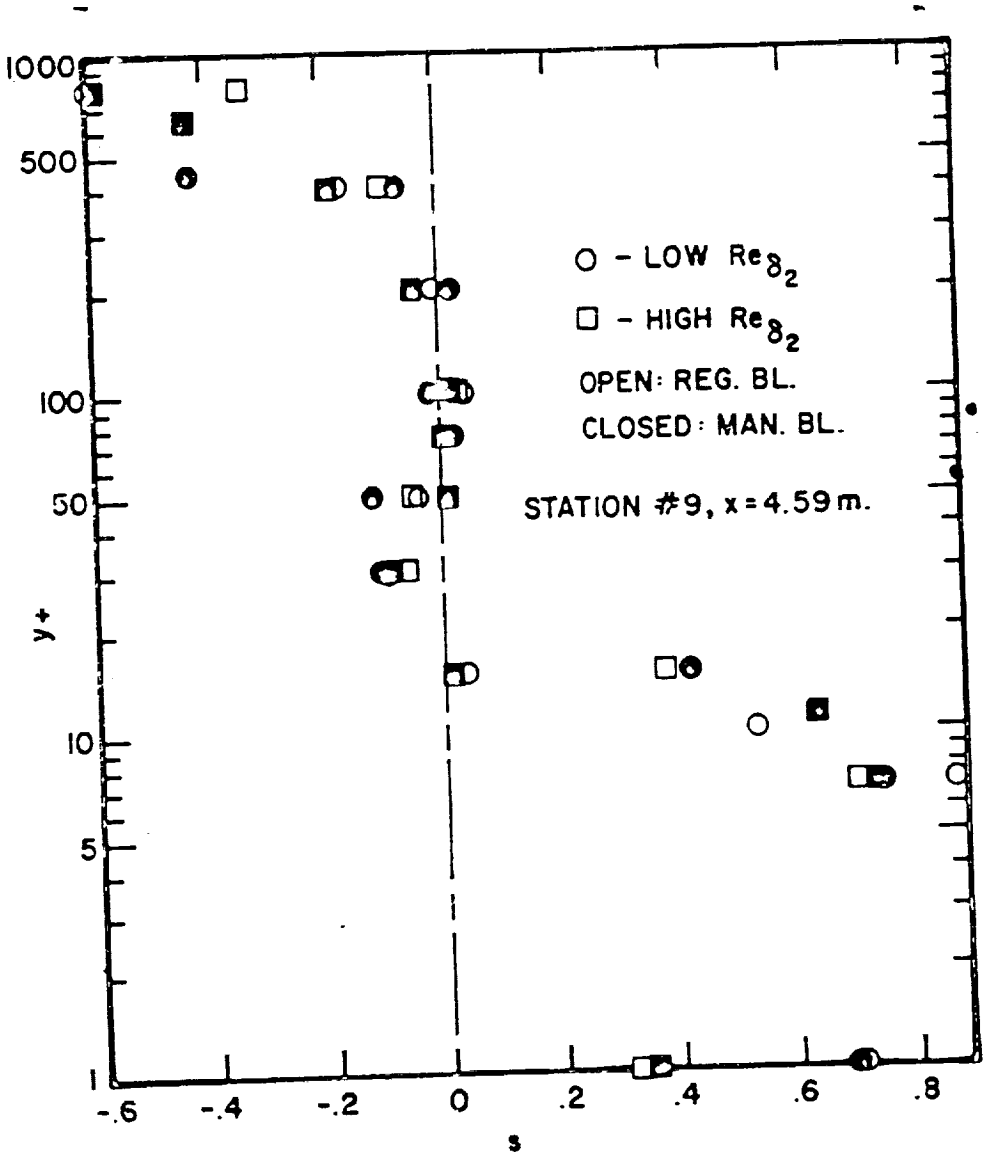

Figure 81. Vertical Distribution of Skewness of Streamwise Velocity in Regular and Manipulated Boundary Layers

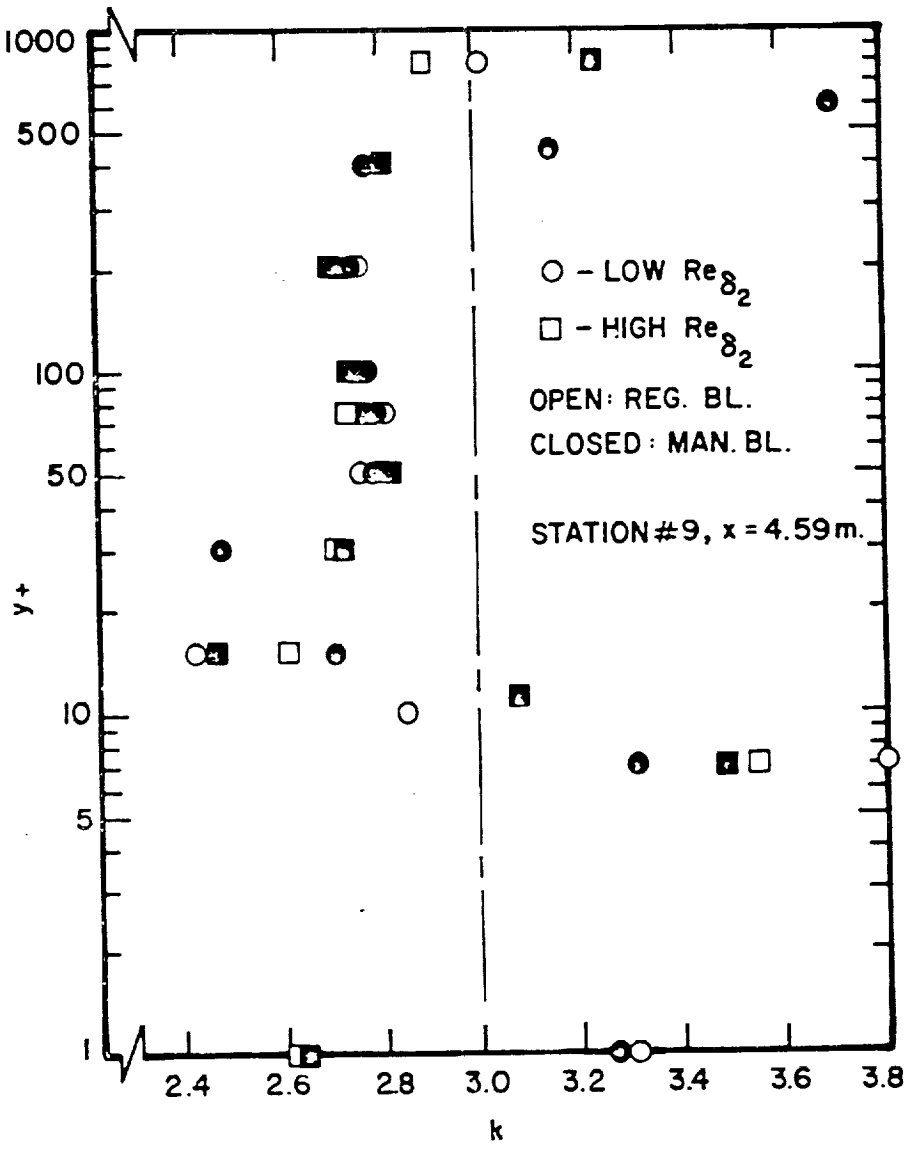

Figure 82. Vertical Distribution of Kurtosis of Streamwise Velocity in Regular and Manipulated Boundary Layers

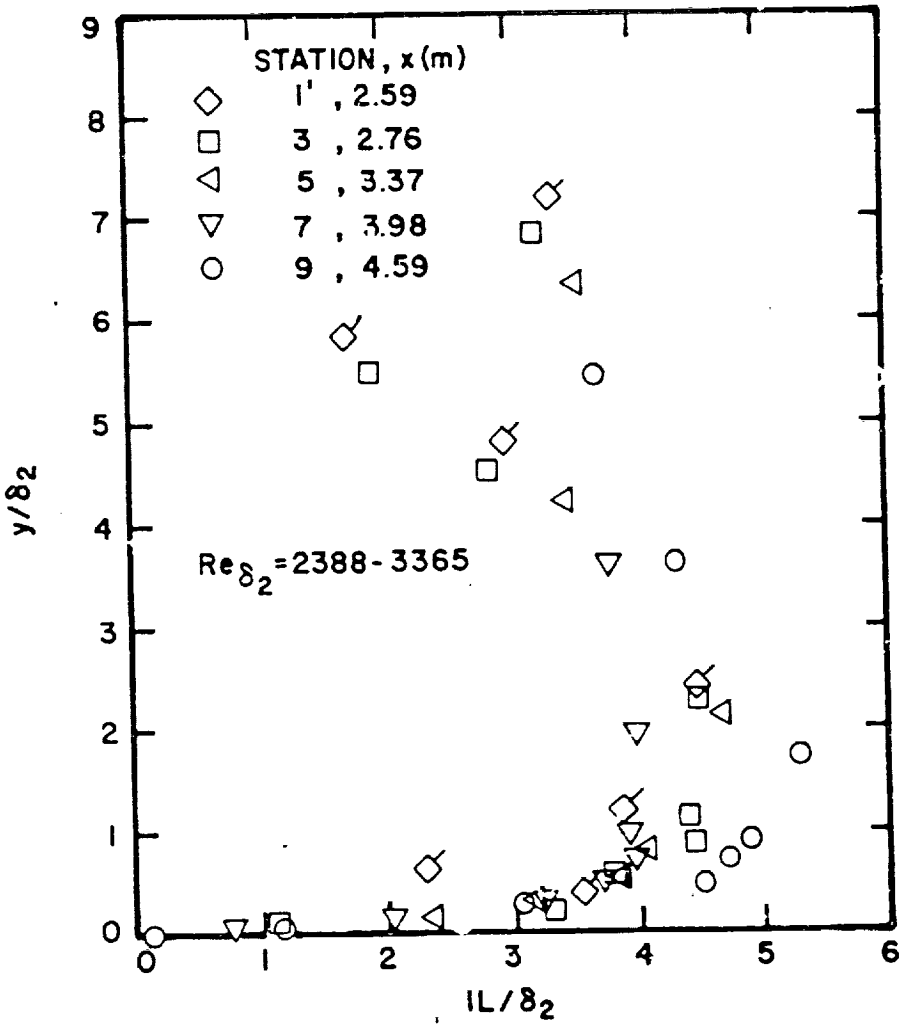

Figure 83. Vertical Distribution of Non-dimensional Streamwise Integral Length Scale at Various Downstream Stations in Manipulated Boundary Layer for Low Reynolds Number Range

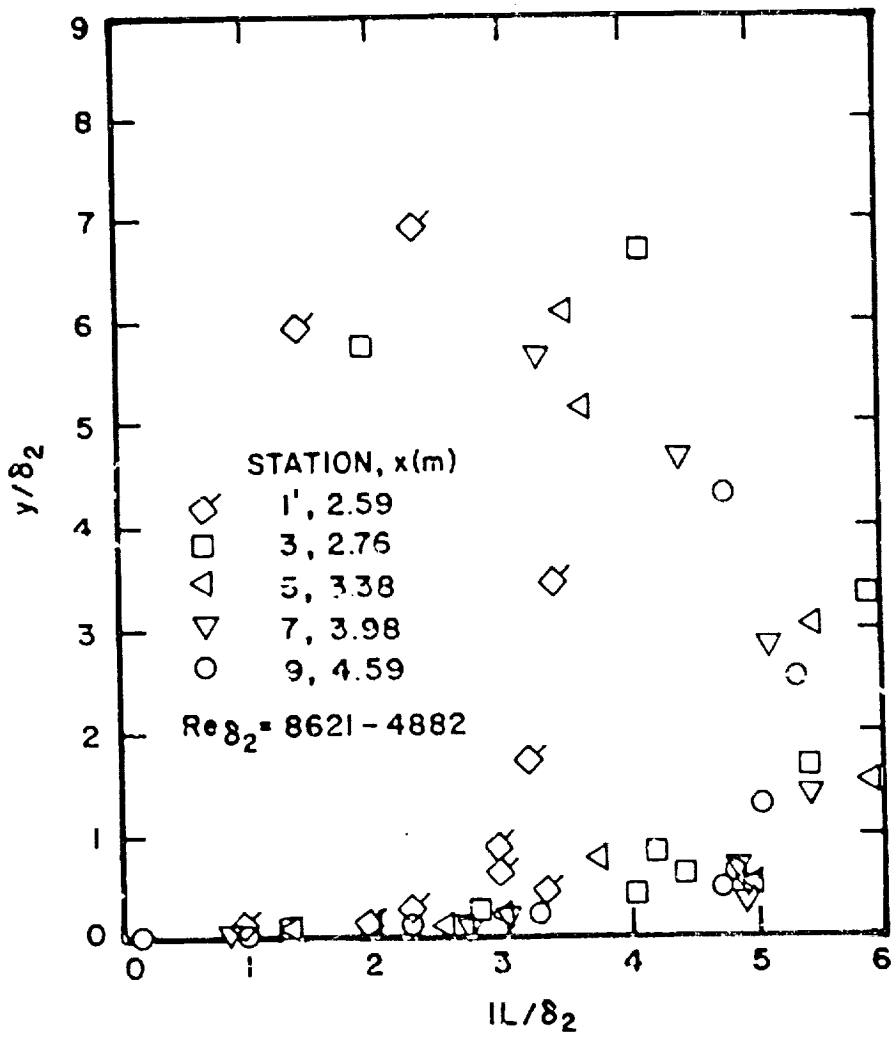

Figure 34. Vertical Distribution of Non-dimensional Streamwise Integral Length Scale at Various Downstream Stations in Manipulated Boundary Layer for High Reynolds Number Range

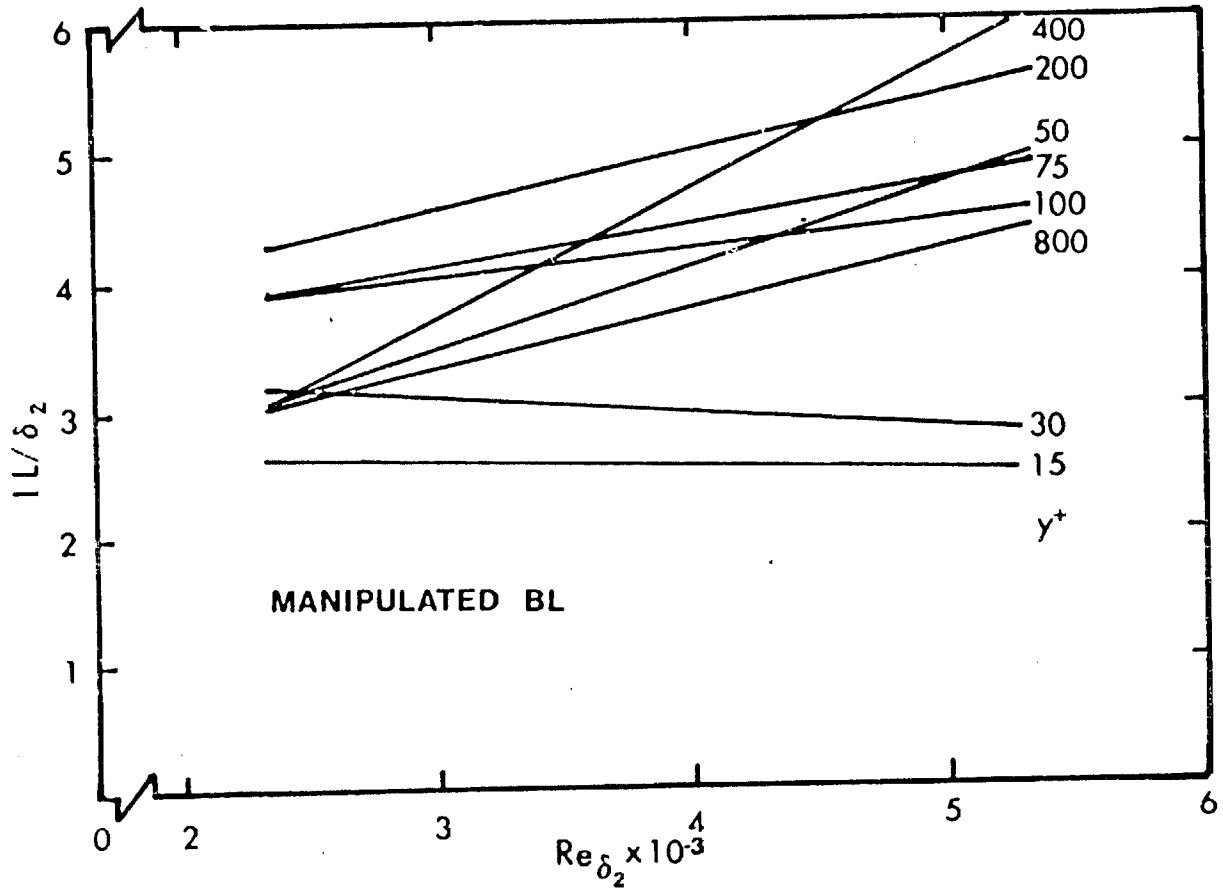

Figure 85. Reynolds Number Dependence of Non-dimensional Streamwise Integral Length Scale at Different Self-similar Heights in the Manipulated Boundary Layer

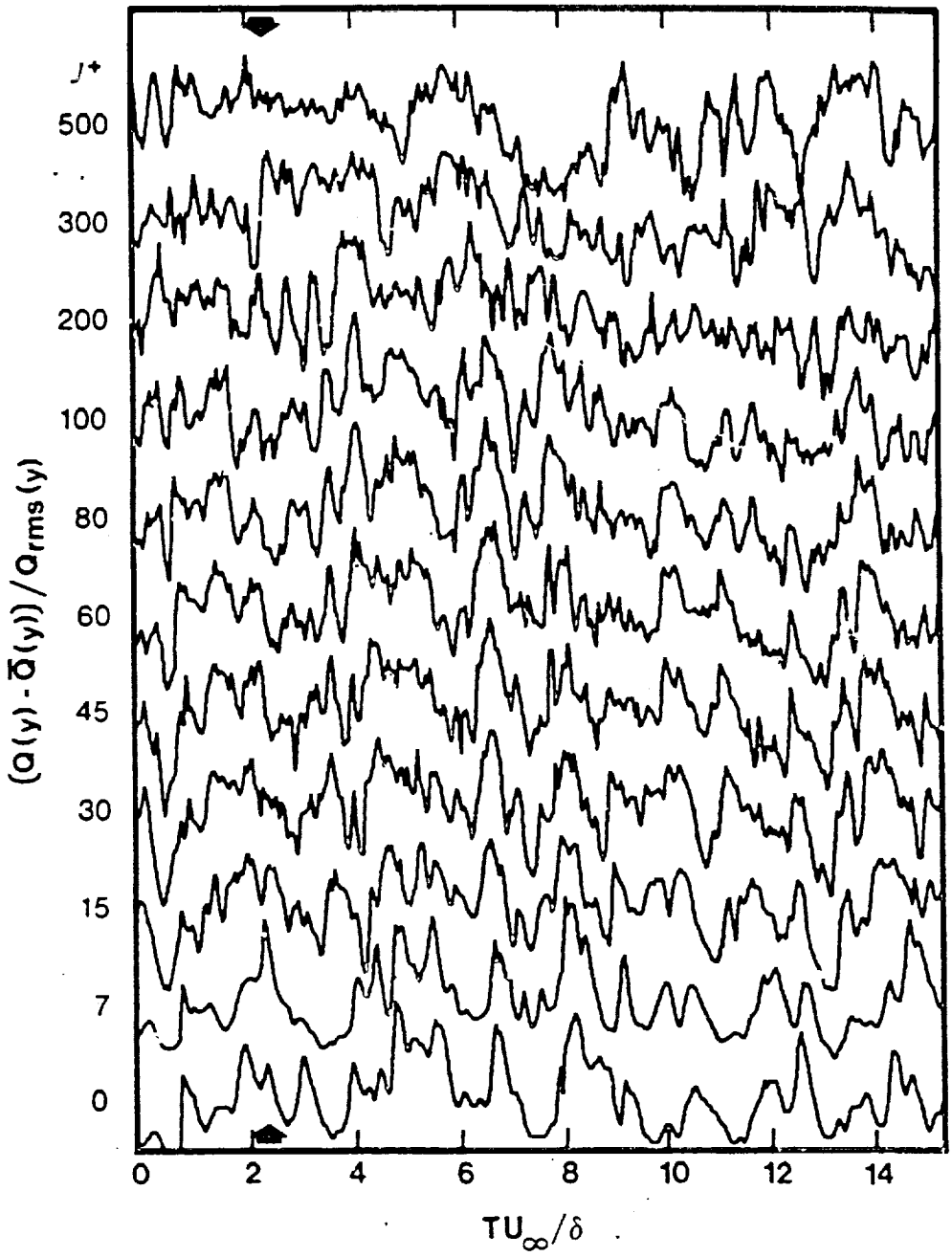

Figure 86. Normalized Time Series Outputs From Hot-wire Rake and Surface Mounted Shear Wire for Regular Boundary Layer at Low Reynolds Number

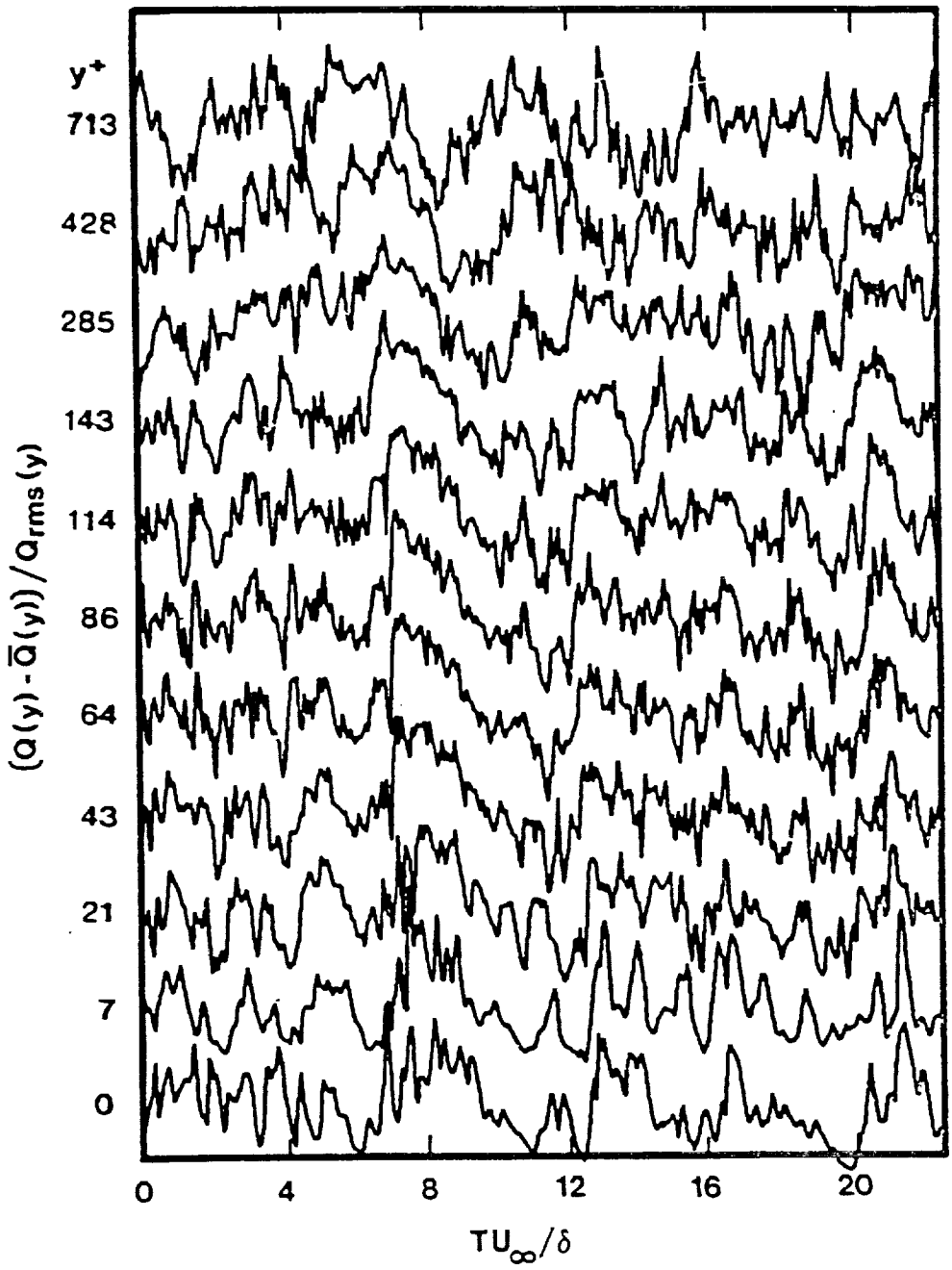

Figure 87. Normalized Time Series Outputs From Hot-wire Rake and Surface Mounted Shear Wire for Regular Boundary Layer at High Reynolds Number

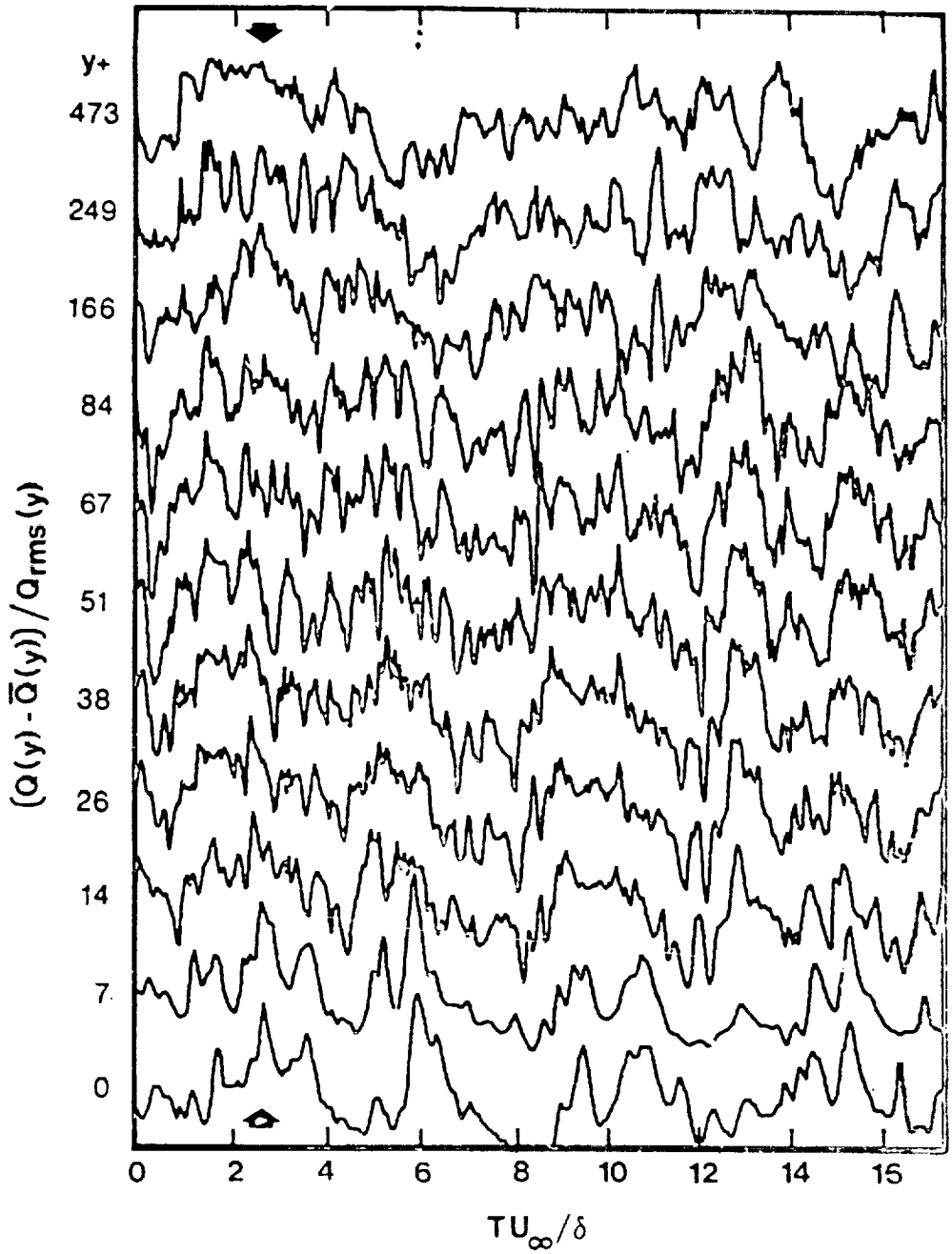

Figure 88. Normalized Time Series Outputs From Hot-Wire Rake and Surface Mounted Shear Wire for Manipulated Boundary Layer at Low Reynolds Number

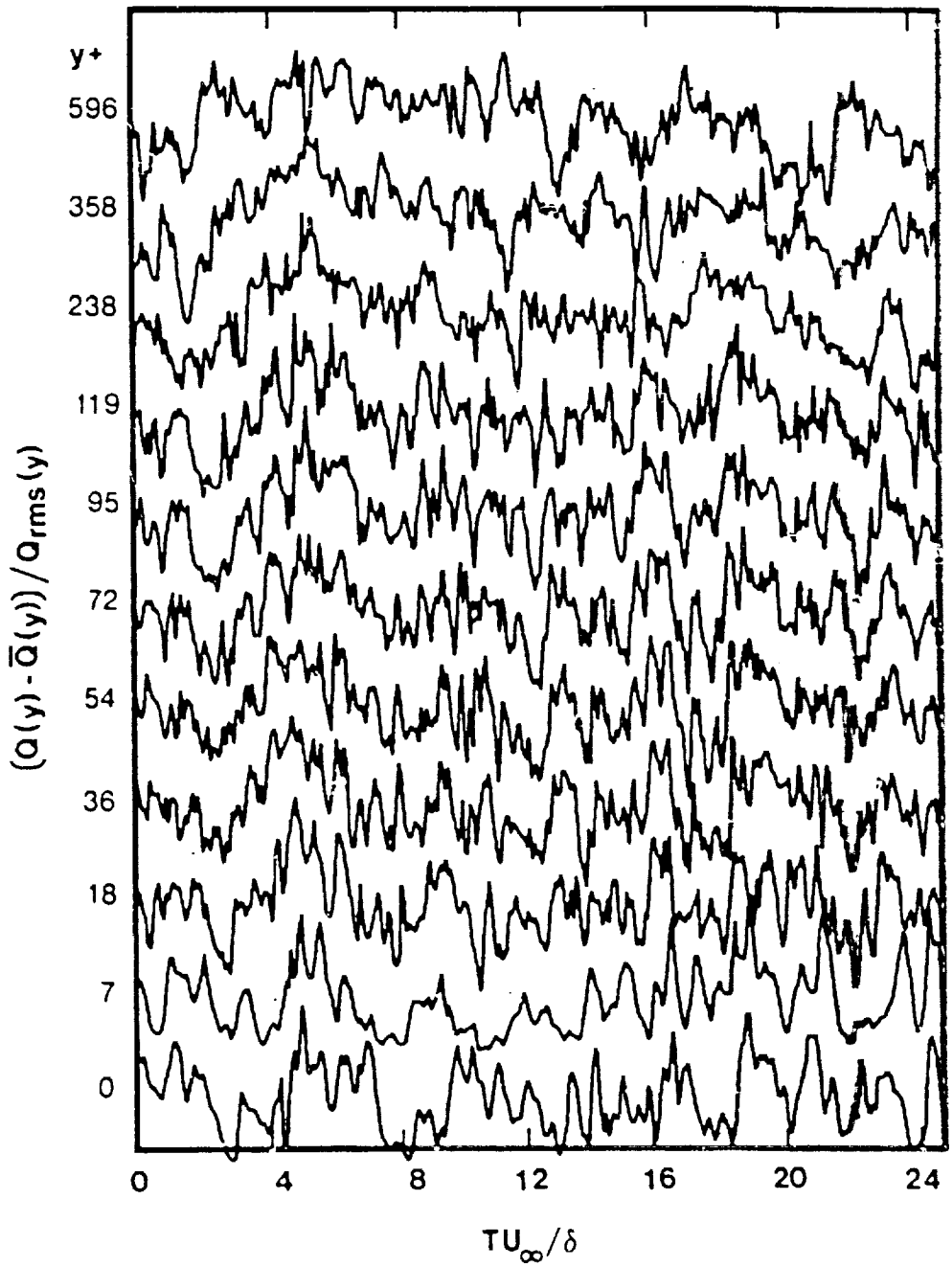

Figure 89. Normalized Time Series Outputs From Hot-wire Rake and Surface Mounted Shear Wire for Manipulated Boundary Layer at High Reynolds Number

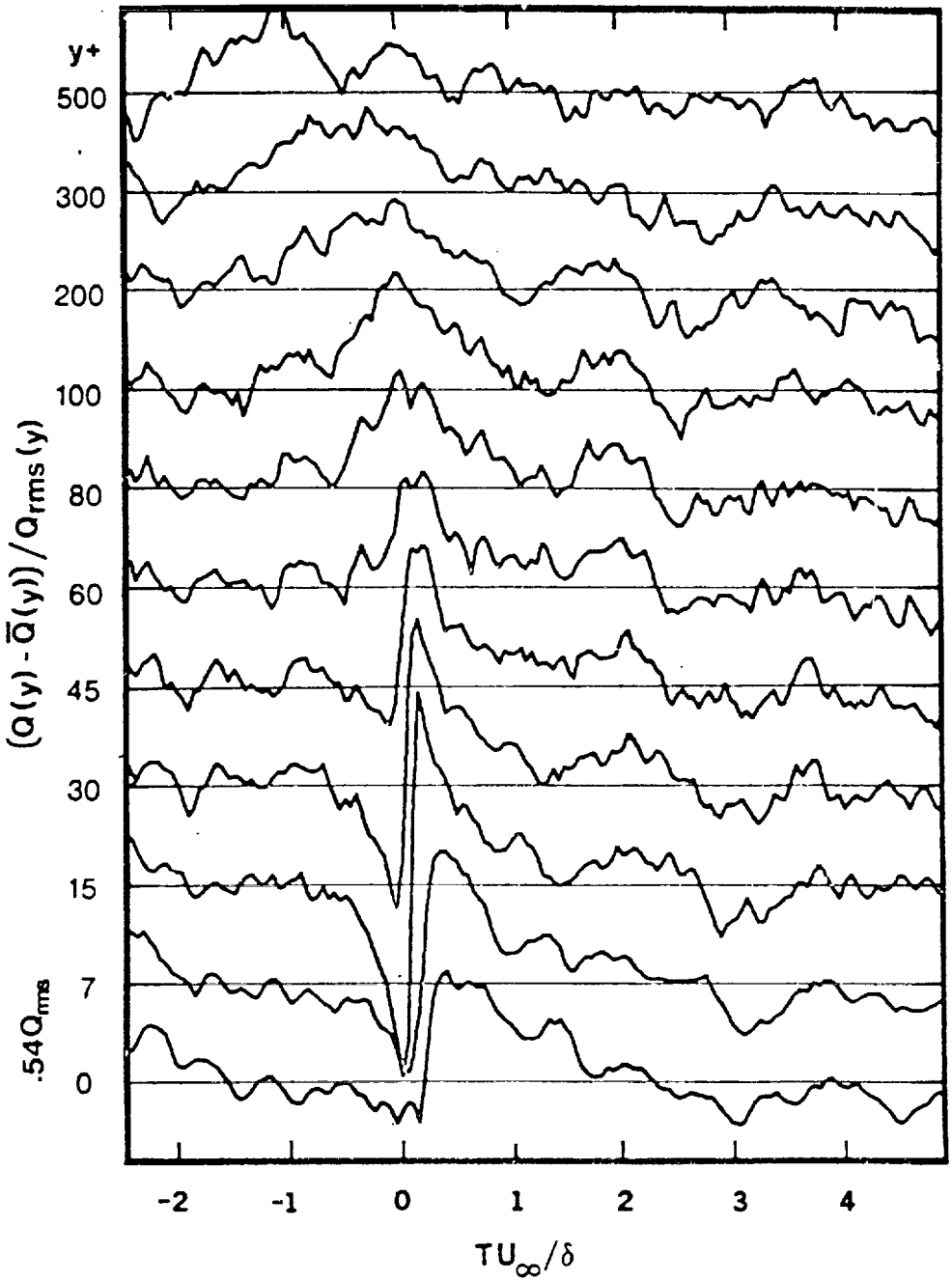

Figure 90. Normalized Burst-Conditioned Ensemble-Average Time Series Obtained from VITA Detection in Regular Boundary Layer at Low Reynolds Number

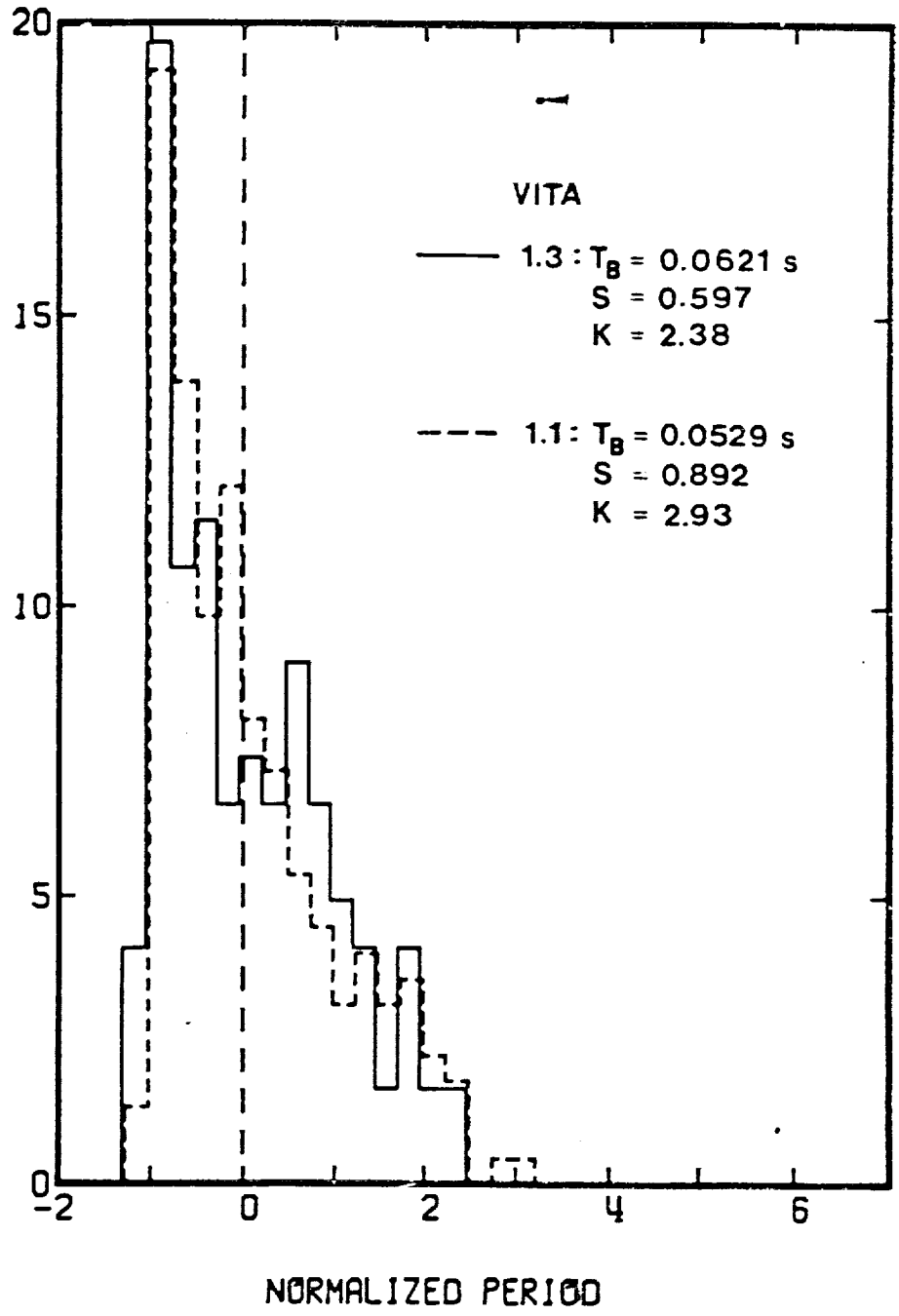

Figure 91. Normalized Probability Distributions of Burst Periods from VITA Detection with Different Thresholds in Regular Boundary Layer at Low Reynolds Number

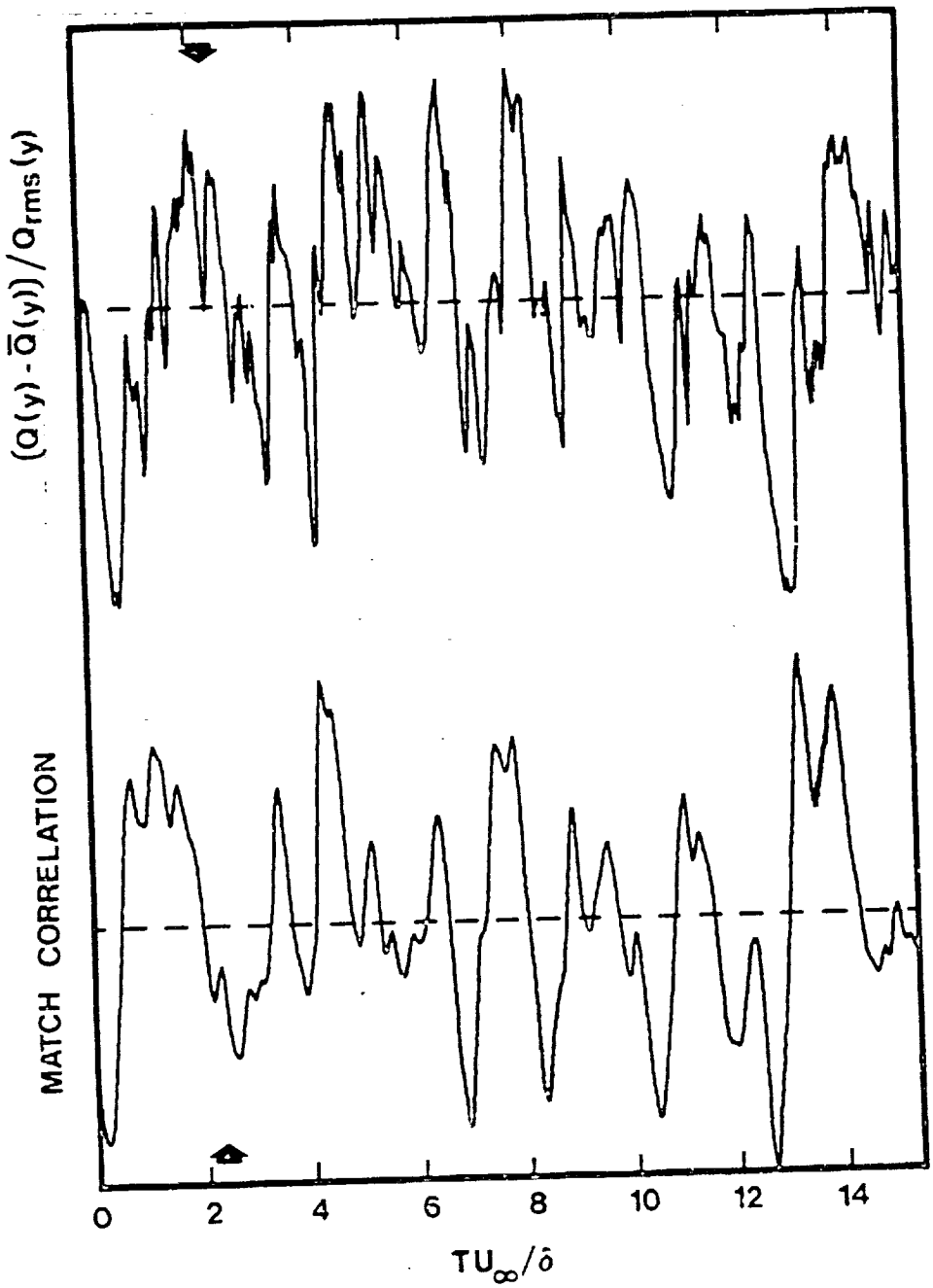

Figure 92. Normalized Velocity Time Series From Sensor at y+ = 15 and Corresponding Match Filter Output in Regular Boundary Layer for Low Reynolds Number

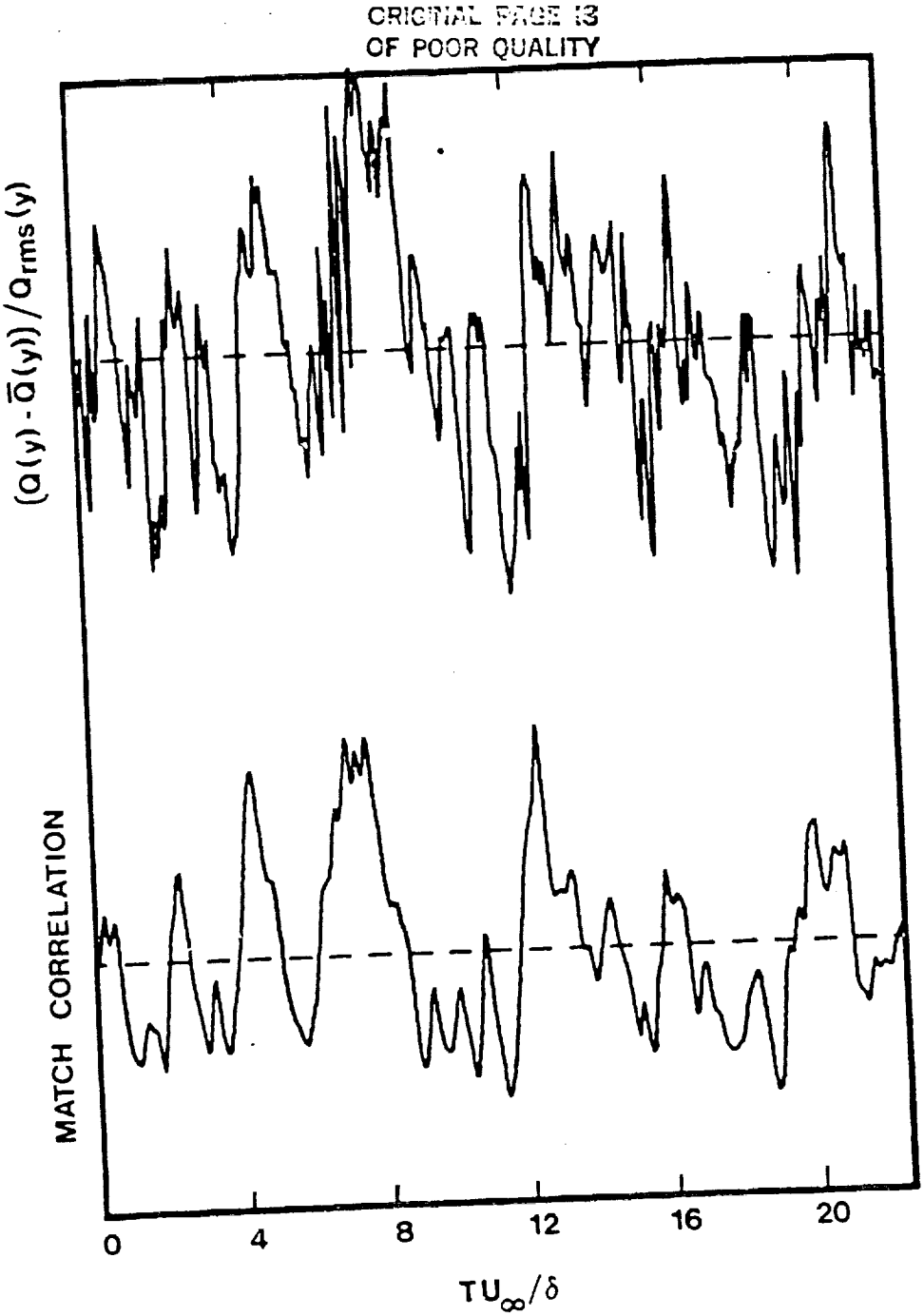

Figure 93. Normalized Velocity Time Series From Sensor at y+ = 15 and Corresponding Match Filter Output in Regular Boundary Layer for High Reynolds Number

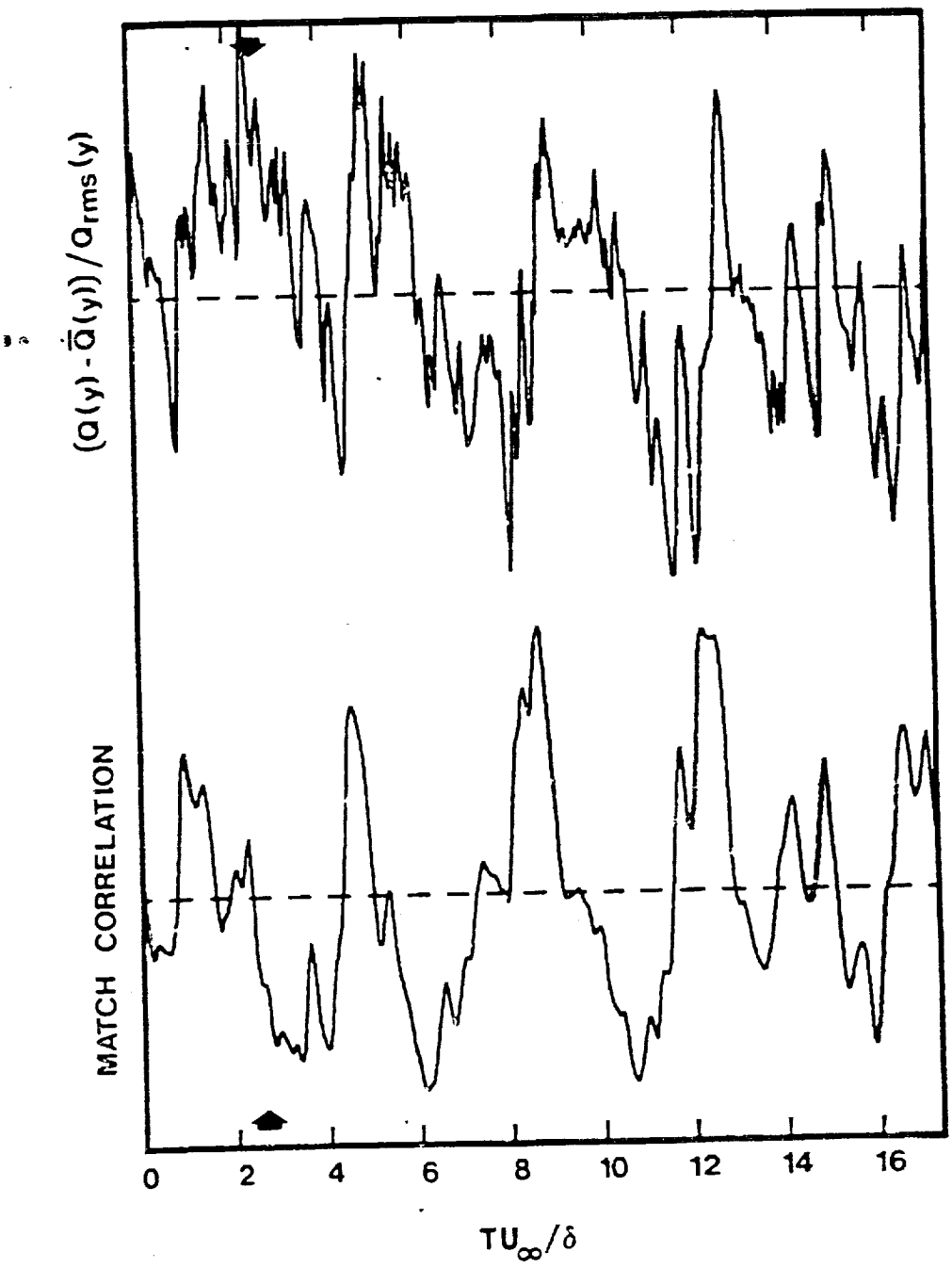

Figure 94. Normalized Velocity Time Series From Sensor at $y^+ = 15$ and Corresponding Match Filter Output in Manipulated Boundary Layer for Low Reynolds Number

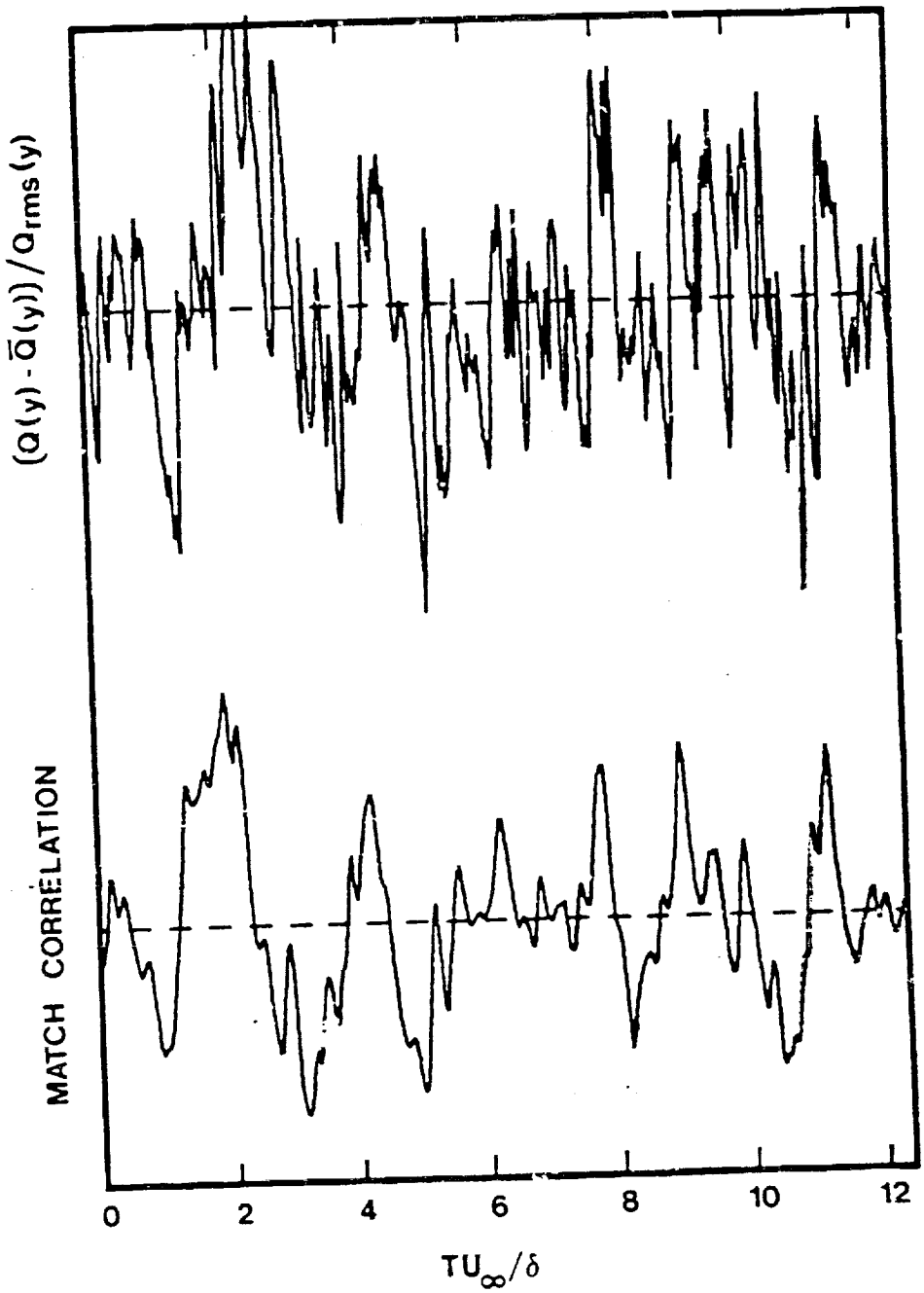

Figure 95. Normalized Velocity Time Series from Sensor at y+ = 15 and Corresponding Match Filter Output in Manipulated Boundary Layer for High Reynolds Number

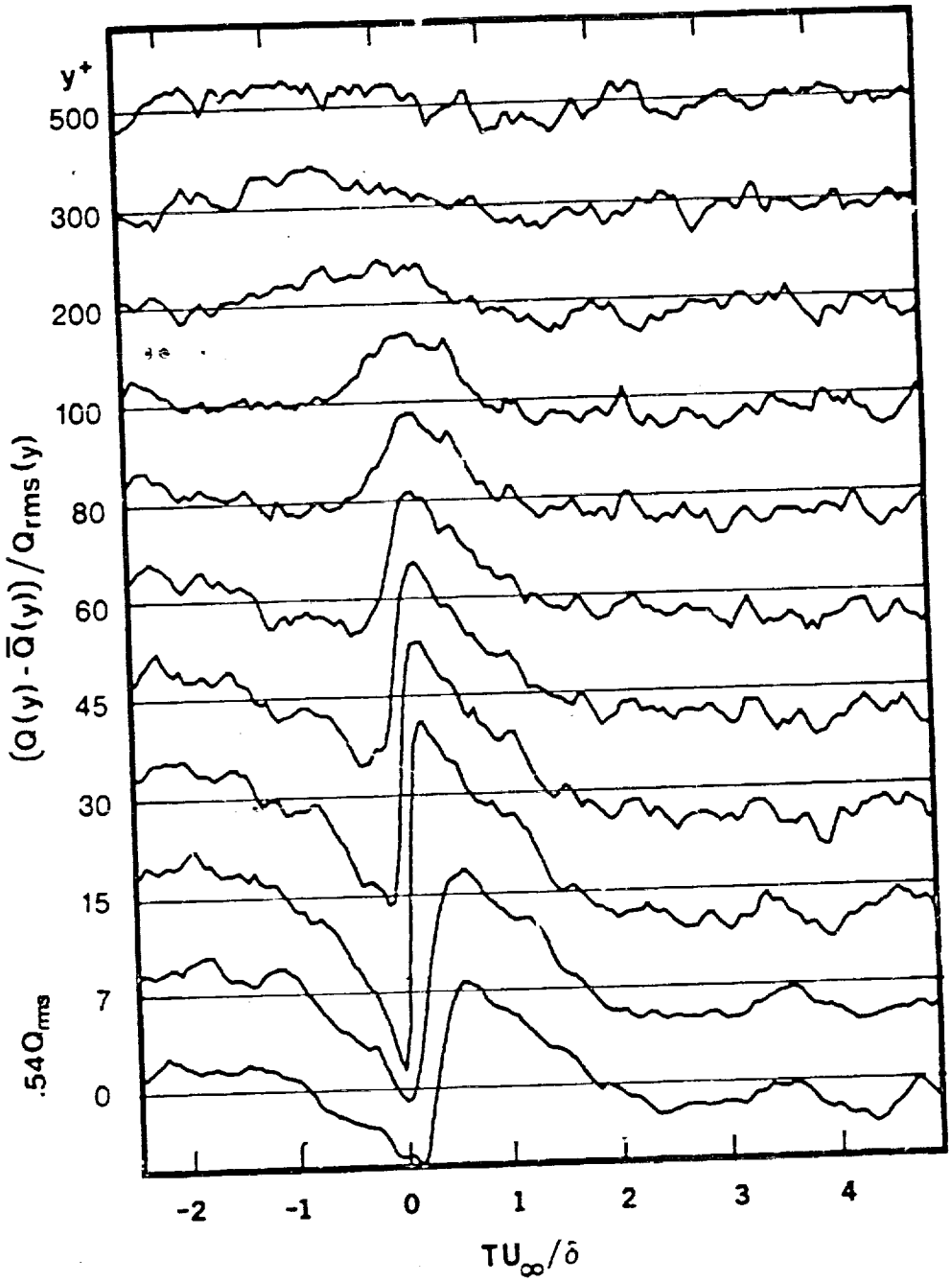

Figure 96. Normalized Burst-Conditioned Ensemble Average Time Series Obtained from Match Filter Detection in Regular Boundary Layer at Low Reynolds Number

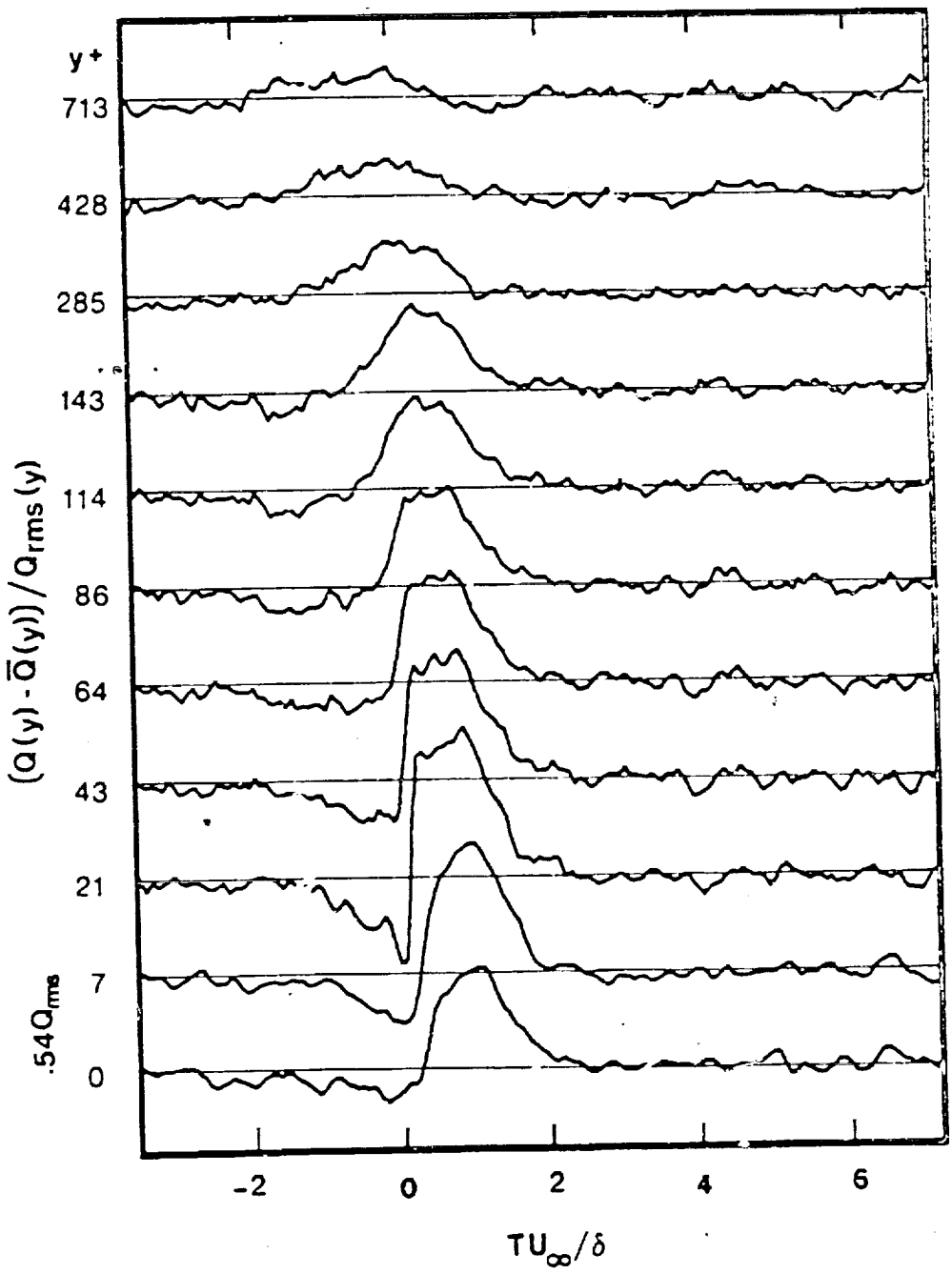

Figure 97. Normalized Burst-Conditioned Ensemble Average Time Series Obtained from Match Filter Detection in Regular Boundary Layer at High Reynolds Number

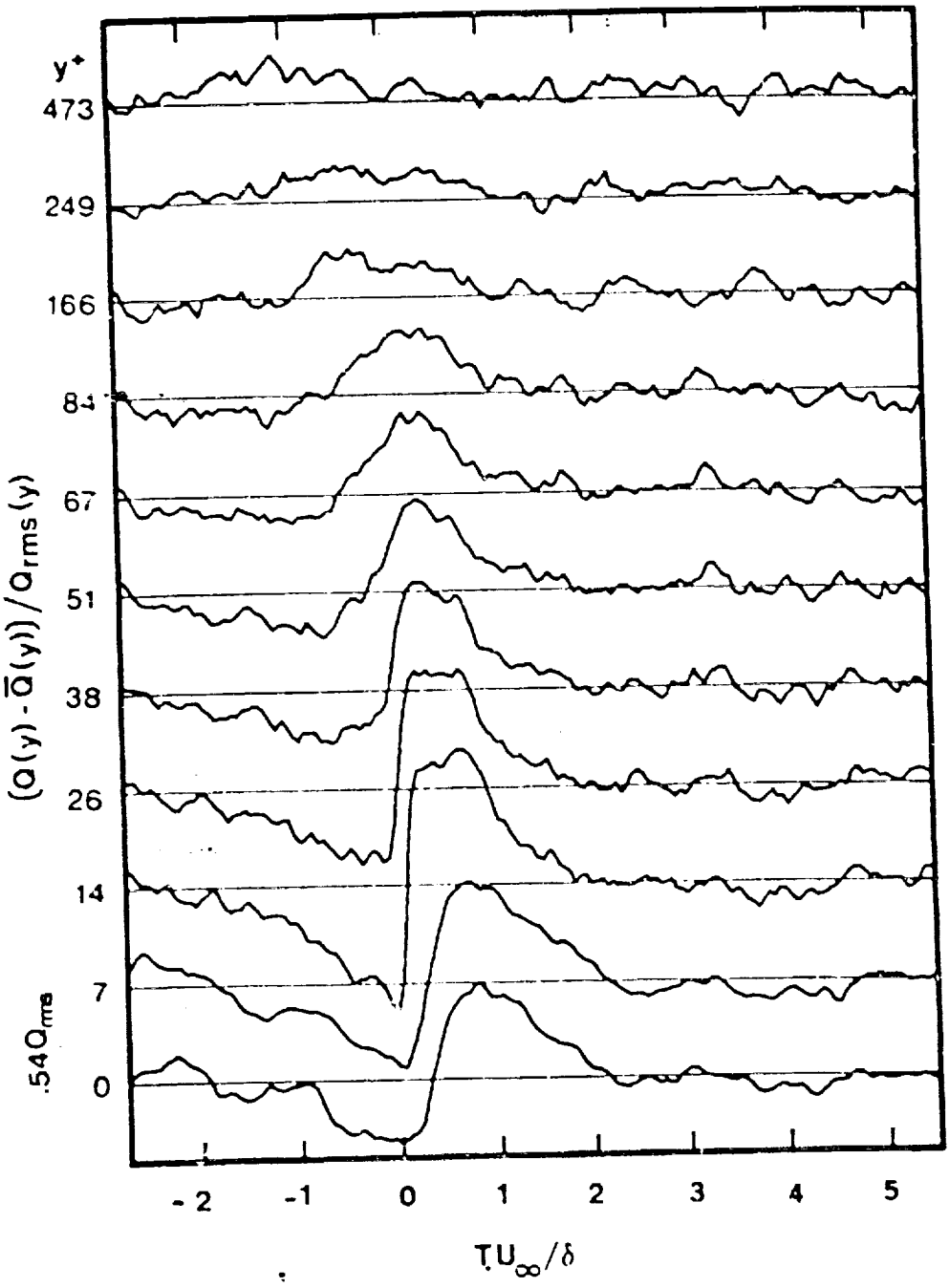

Figure 98. Normalized Burst-Conditioned Ensemble Average Time Series Obtained from Match Filter Detection in Manipulated Boundary Layer at Low Reynolds Number

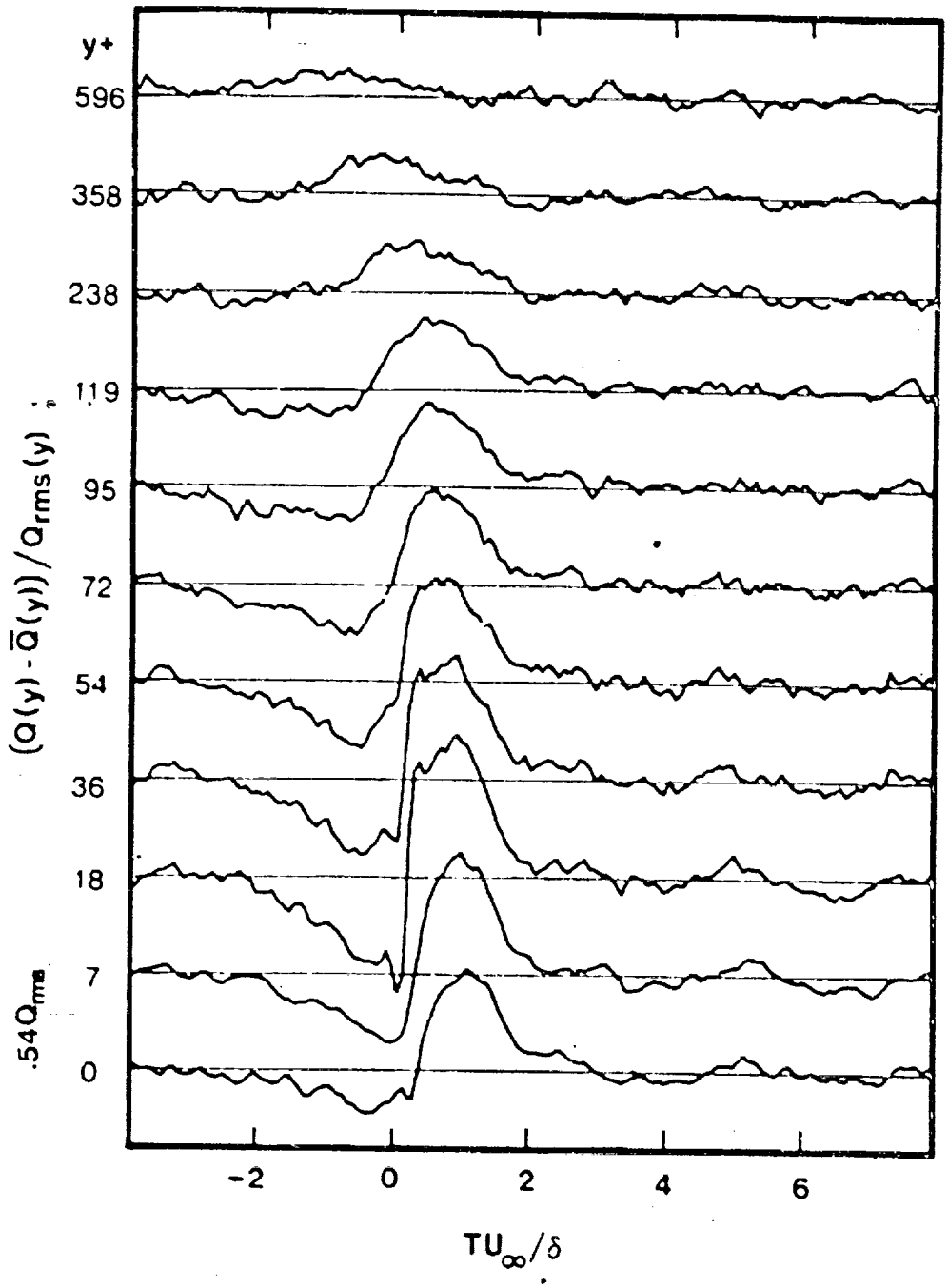

Figure 99. Normalized Burst-Conditioned Ensemble Average Time Series Obtained from Match Filter Detection in Manipulated Boundary Layer at High Reynolds Number

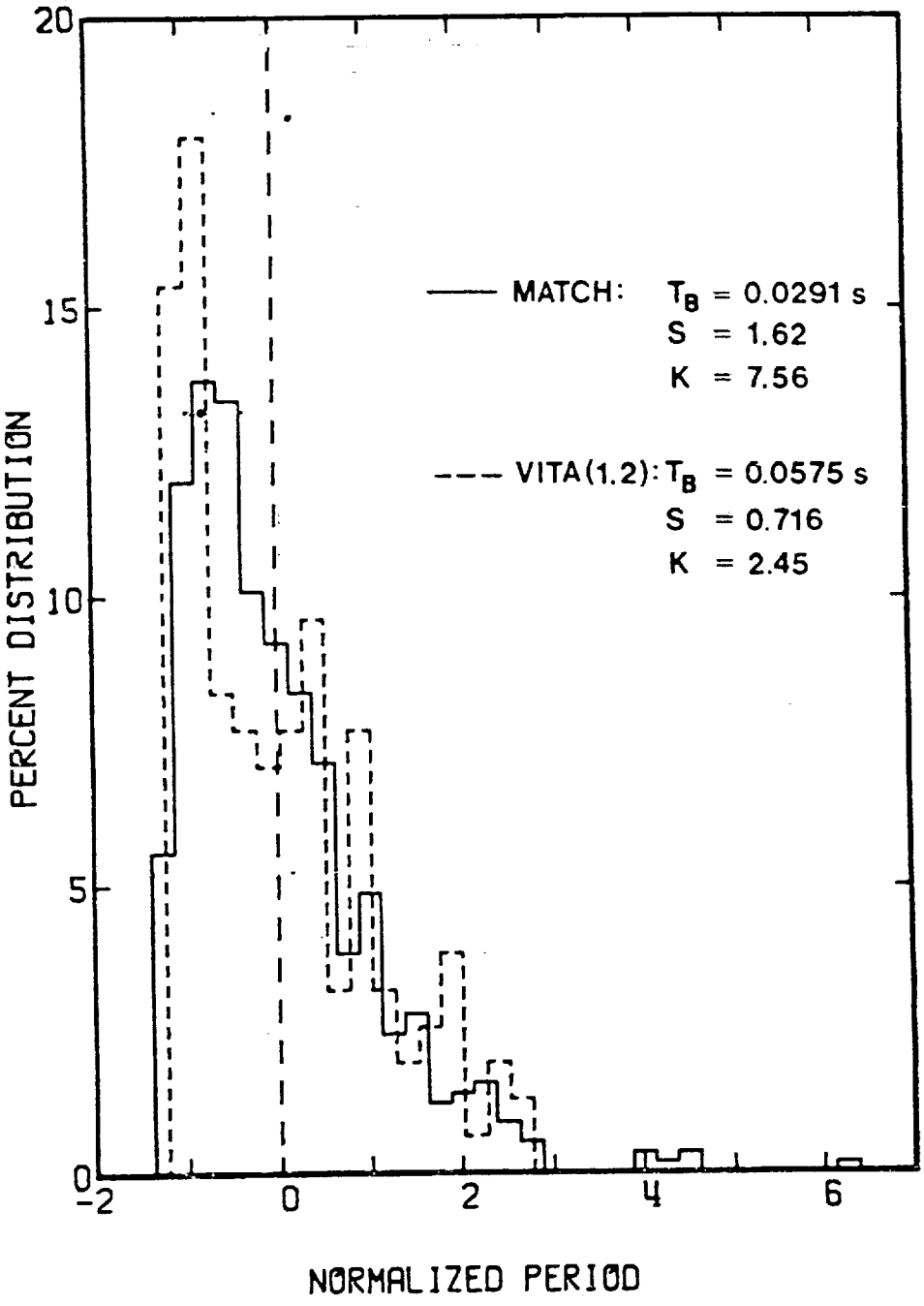

Figure 100. Normalized Probability Distributions of Burst Periods for VITA(1.2) and Match Filter Detections in Regular Boundary Layer at Low Reynolds Number

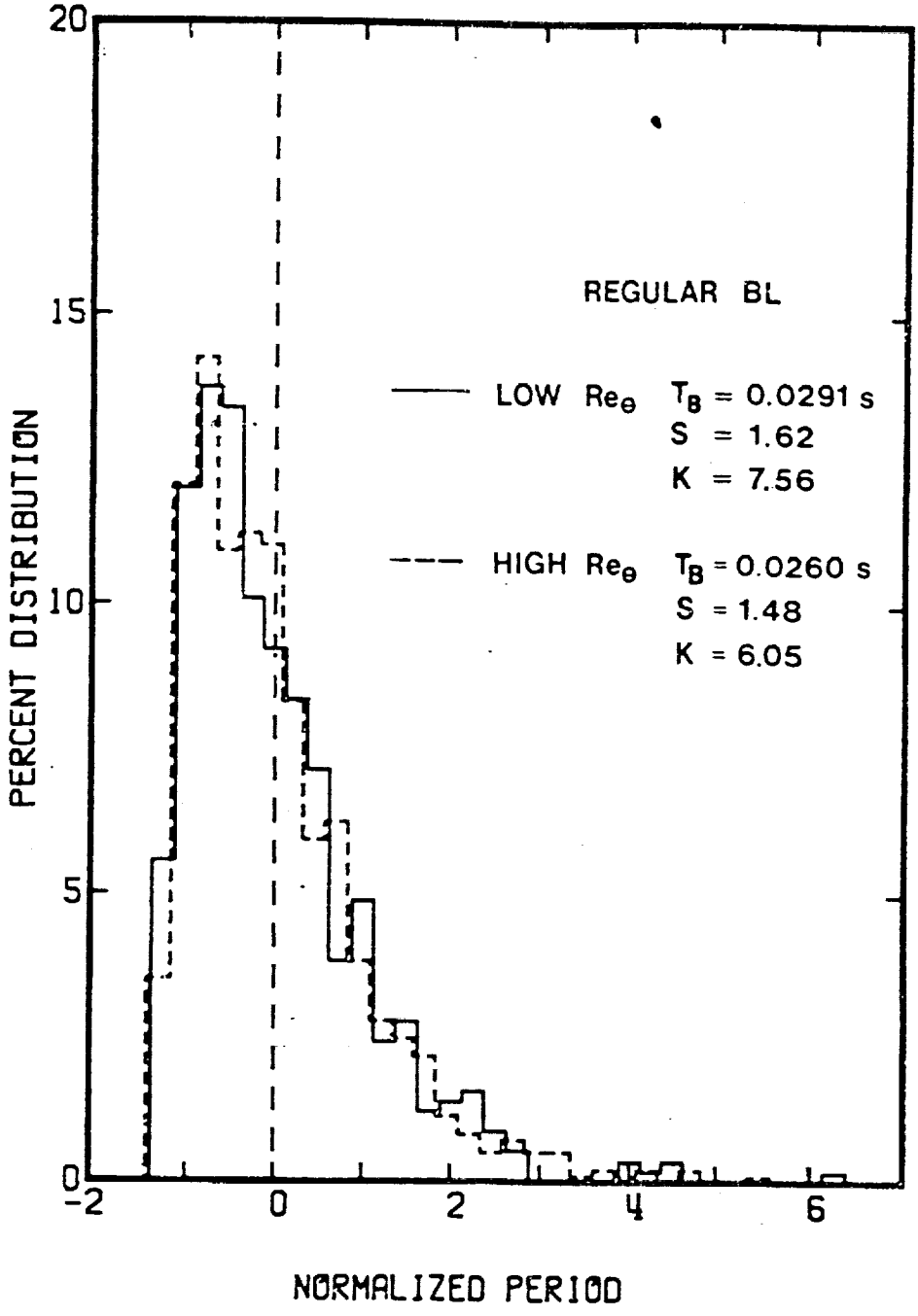

Figure 101. Normalized Probability Distributions of Burst Periods from Match Filter Detection at Both Reynolds Numbers in Regular Boundary Layer

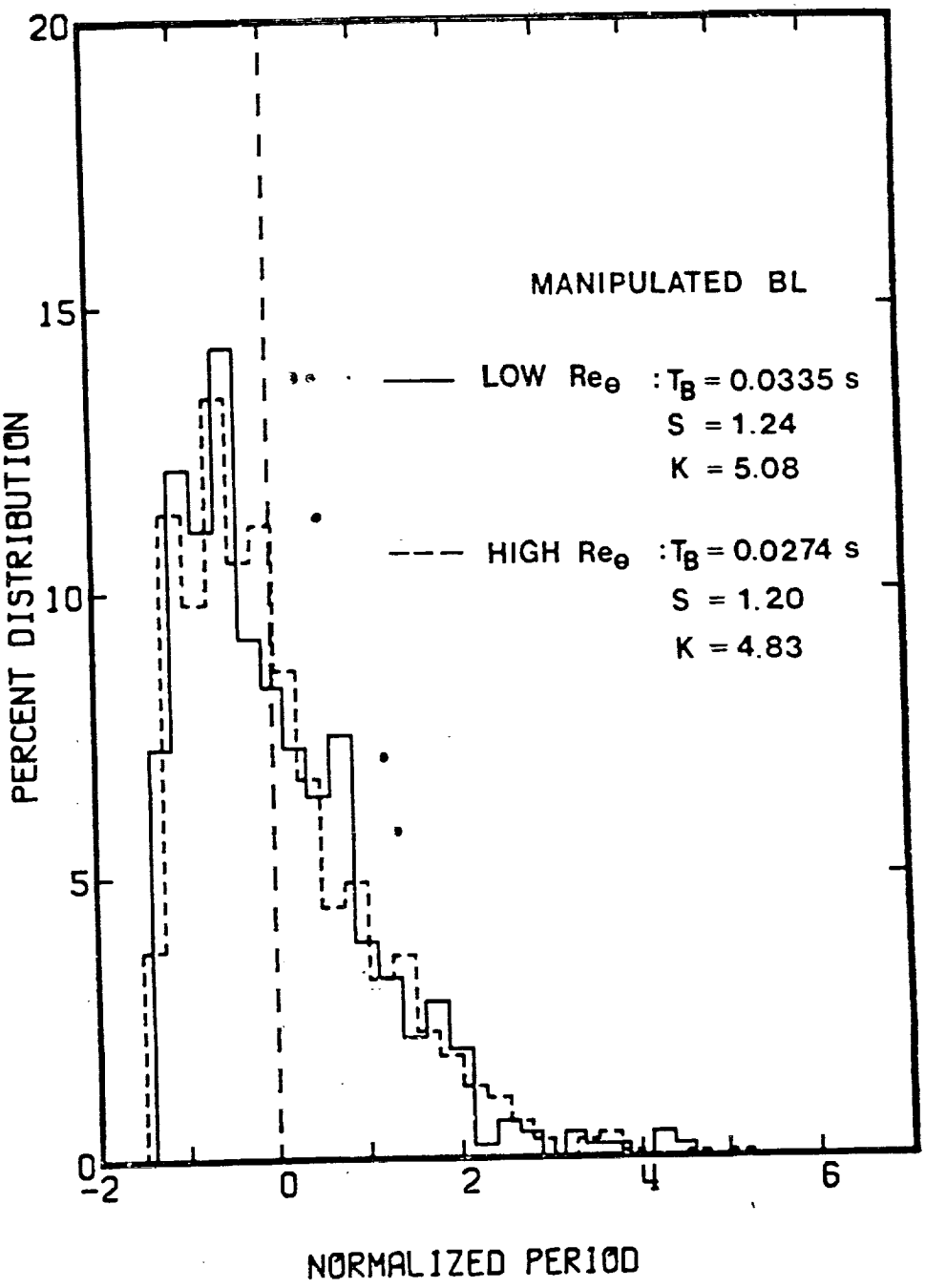

Figure 102. Normalized Probability Distributions of Burst Periods from Match Filter Detection at Both Reynolds Numbers in Manipulated Boundary Layer

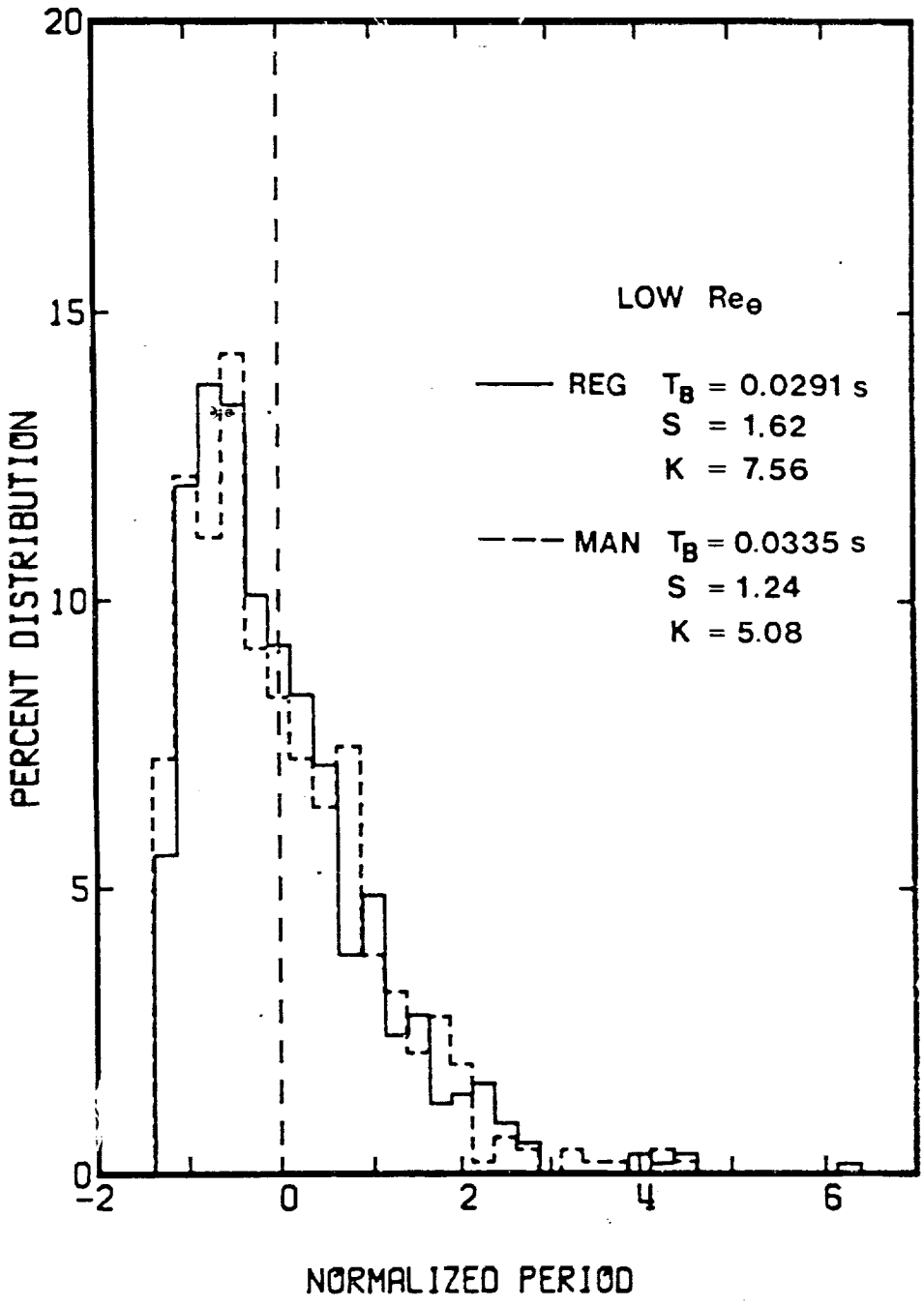

Figure 103. Normalized Probability Distributions of Burst Periods from Match Filter Detection in Regular and Manipulated Boundary Layers at Low Reynolds Number

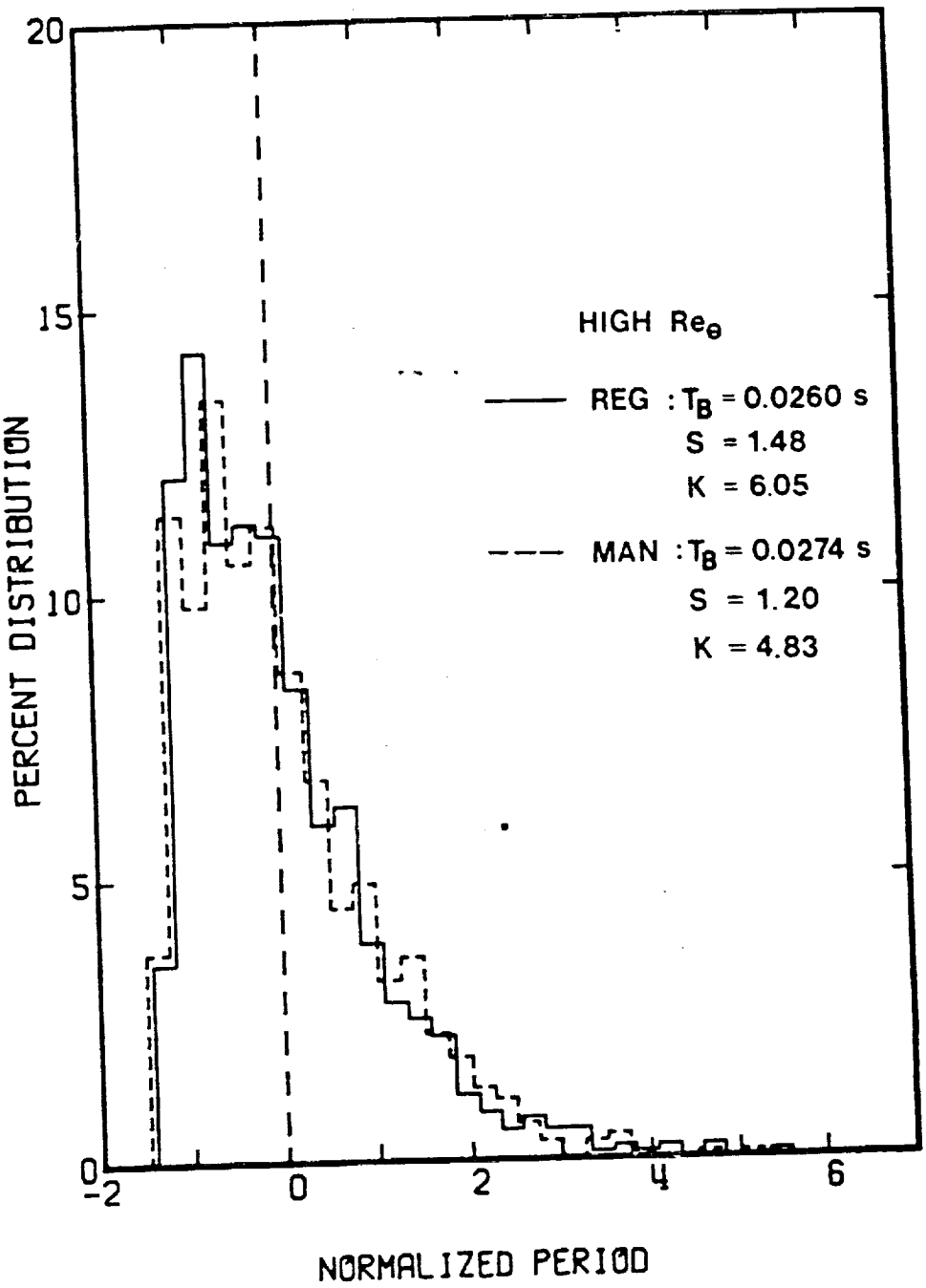

Figure 104. Normalized Probability Distributions of Burst Periods from Match Filter Detection in Regular and Manipulated Boundary Layers at High Reynolds Number

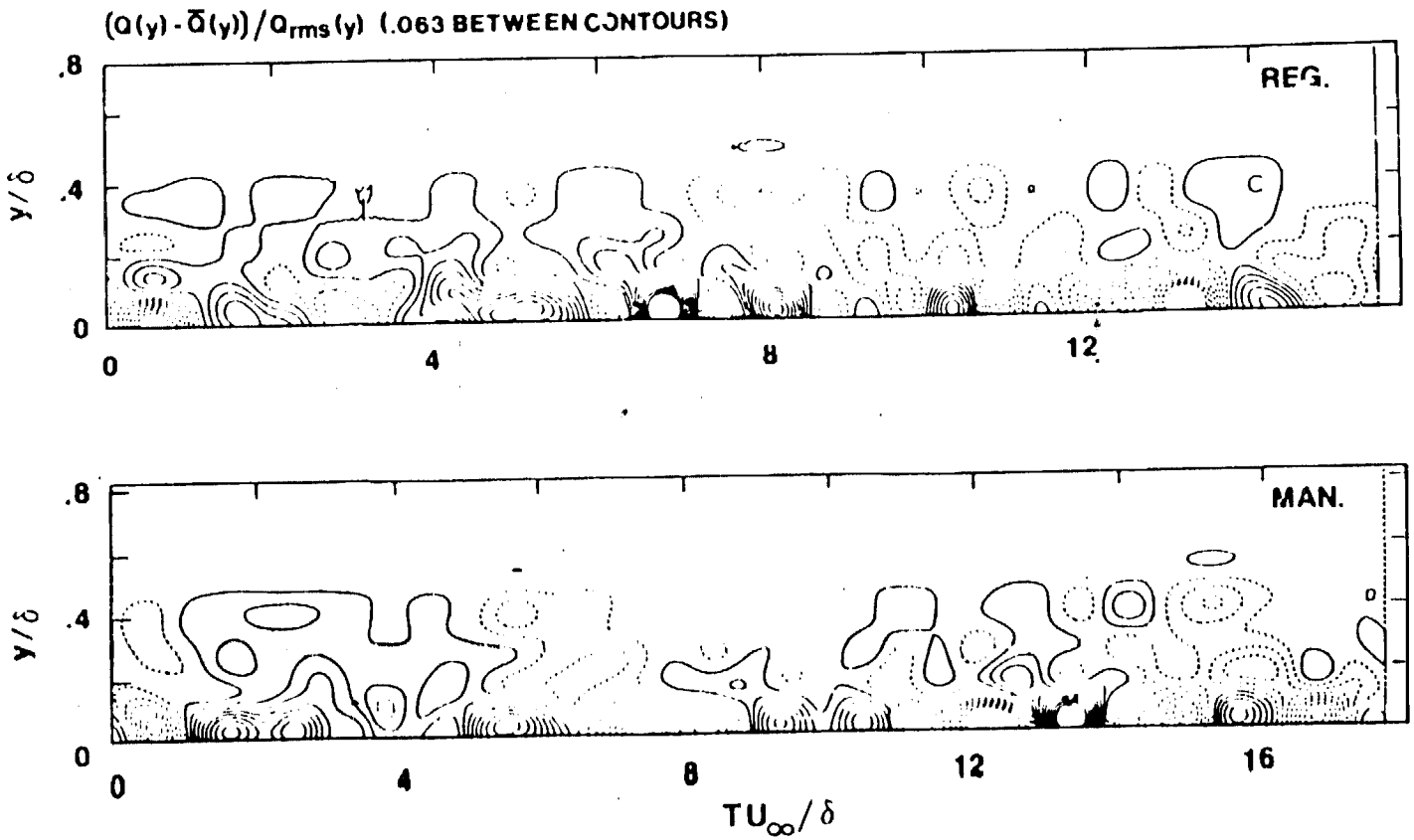

Figure 105. Two-Dimensional Reconstructions of Normalized Streamwise Velocity Time-Series for Regular (Top) and Manipulated (Bottom) Boundary Layers at Low Reynolds Number

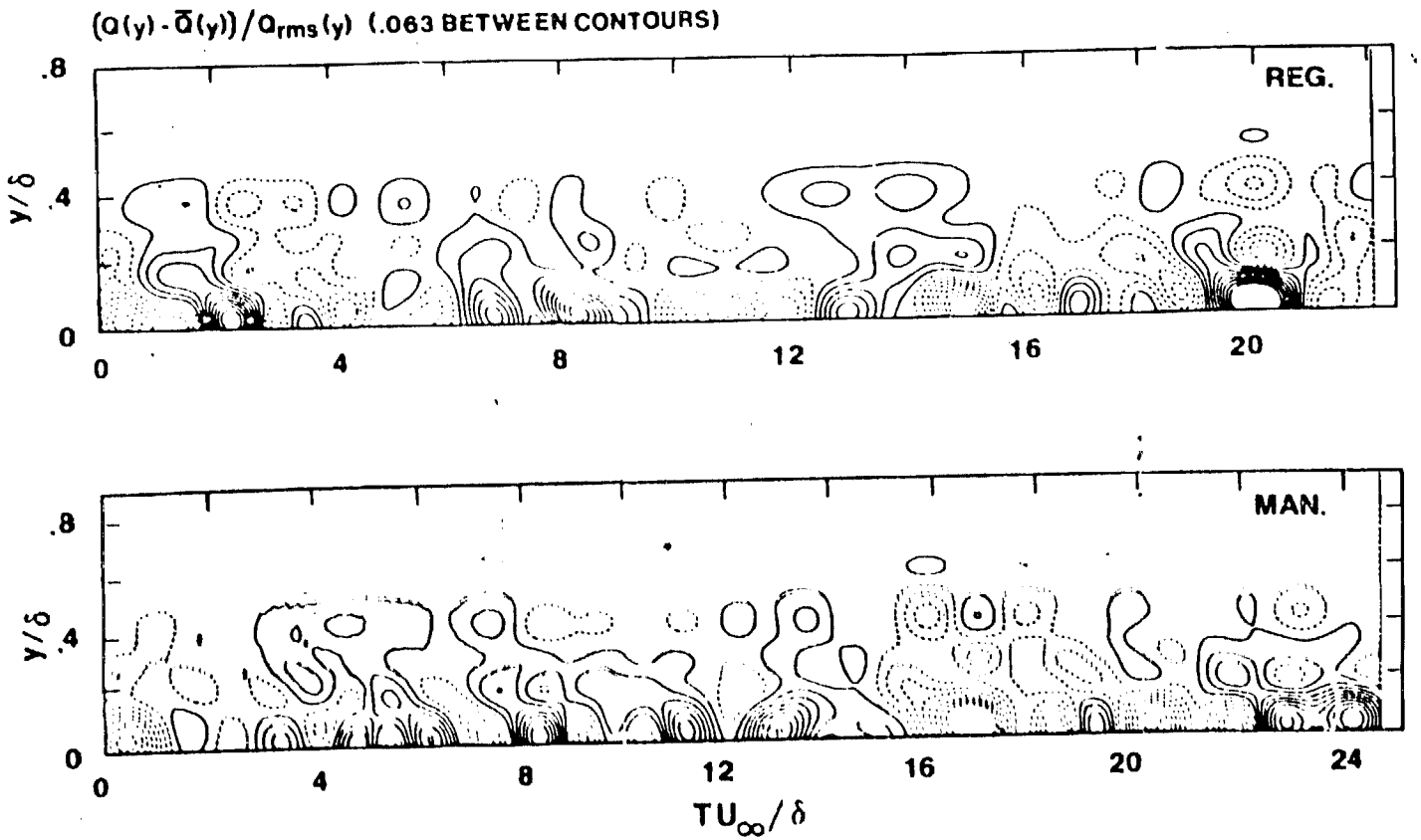

Figure 106. Two-Dimensional Reconstructions of Normalized Streamwise Velocity Time-Series for Regular (Top) and Manipulated (Bottom) Boundary Layers at High Reynolds Number

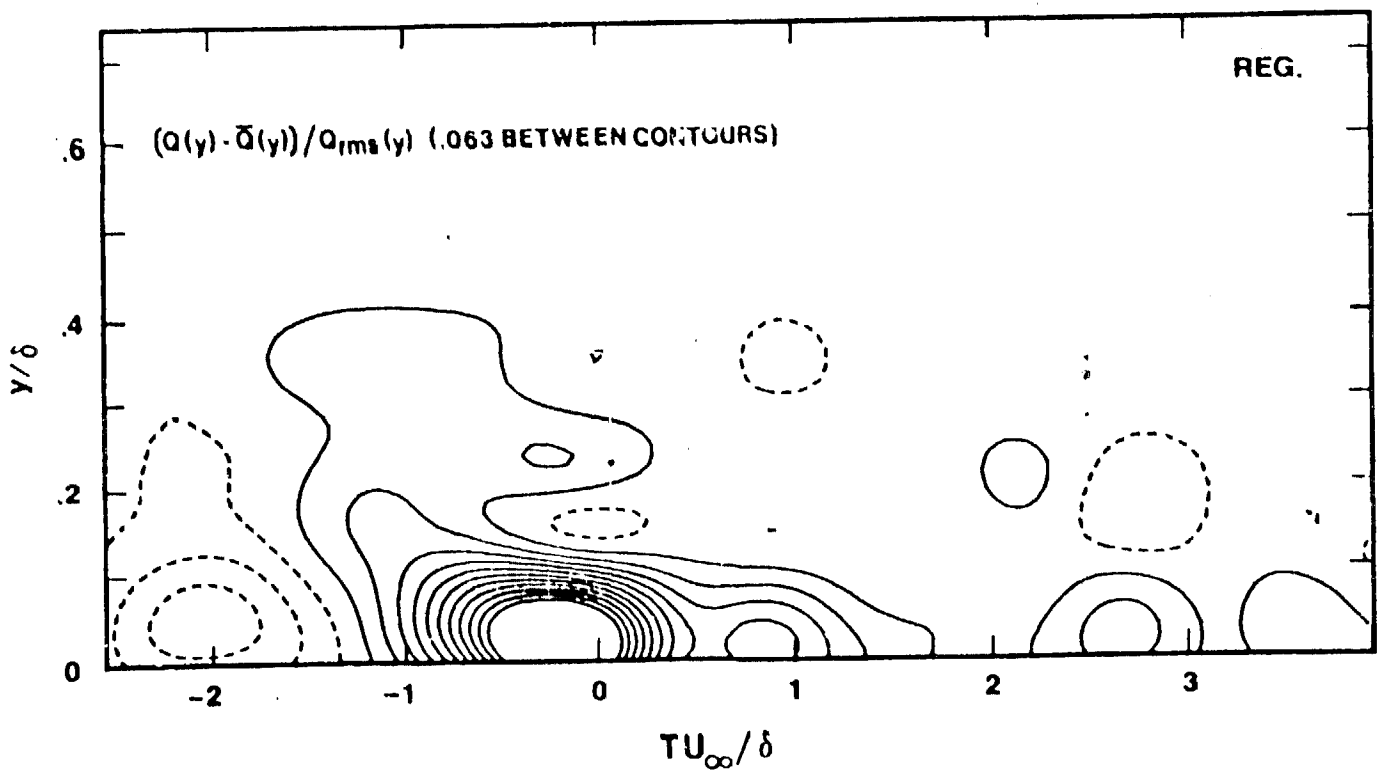

Figure 107. Ensemble Averaged Two-Dimensional Reconstructions of Normalized Streamwise Velocity for Time Instant of Digital Image Acquisition in Regular Boundary Layer

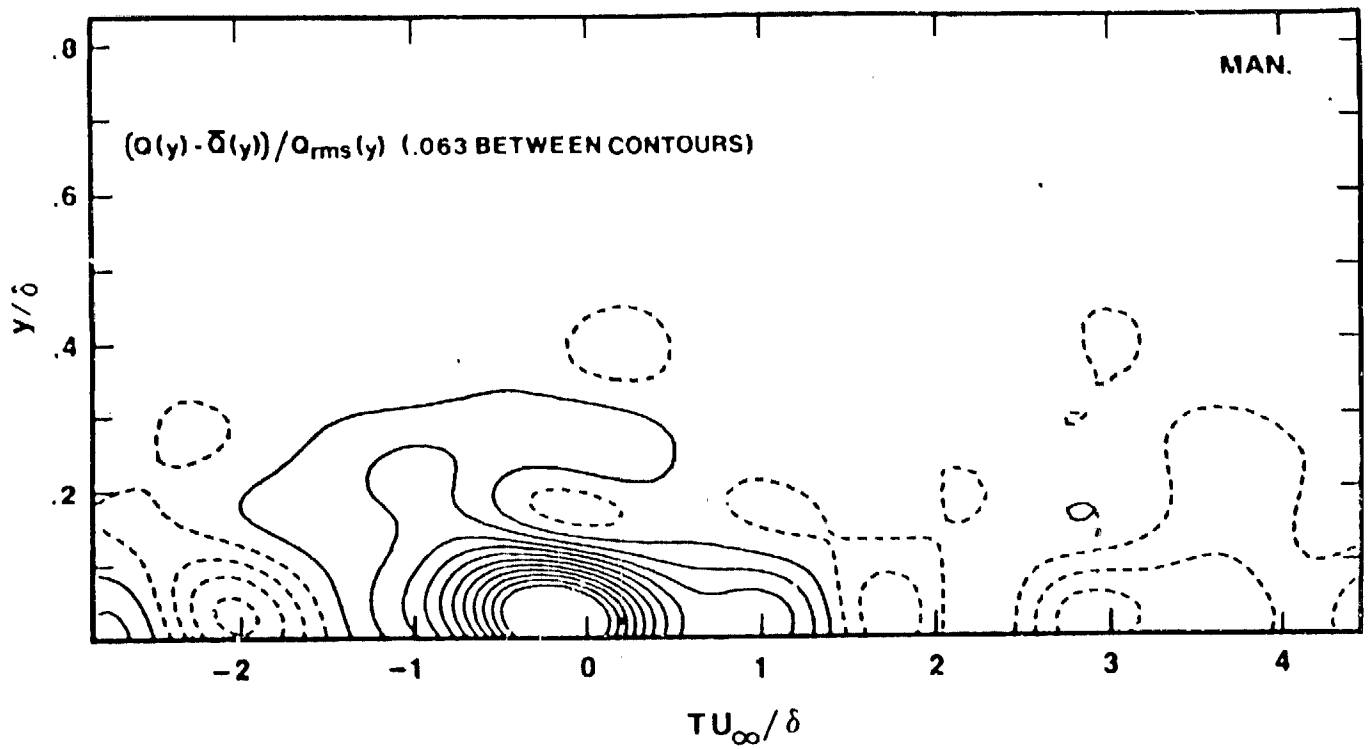

Figure 108. Ensemble Averaged Two-Dimensional Reconstructions of Normalized Streamwise Velocity for Time Instant of Digital Image Acquisition in Manipulated Boundary Layer

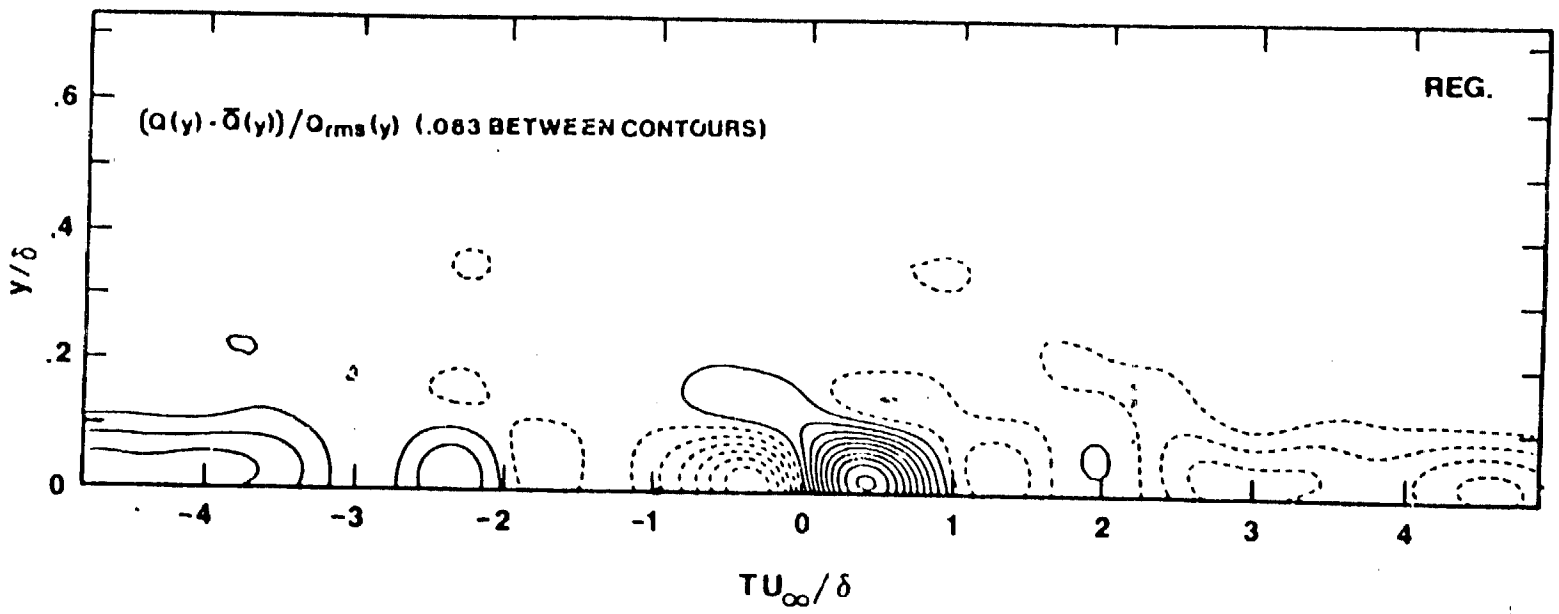

Figure 109. Burst-Conditioned Ensemble Average of Normalized Two-Dimensional Velocity Reconstructions Obtained From Match Filter Detection in Regular Boundary Layer at Low Reynolds Number

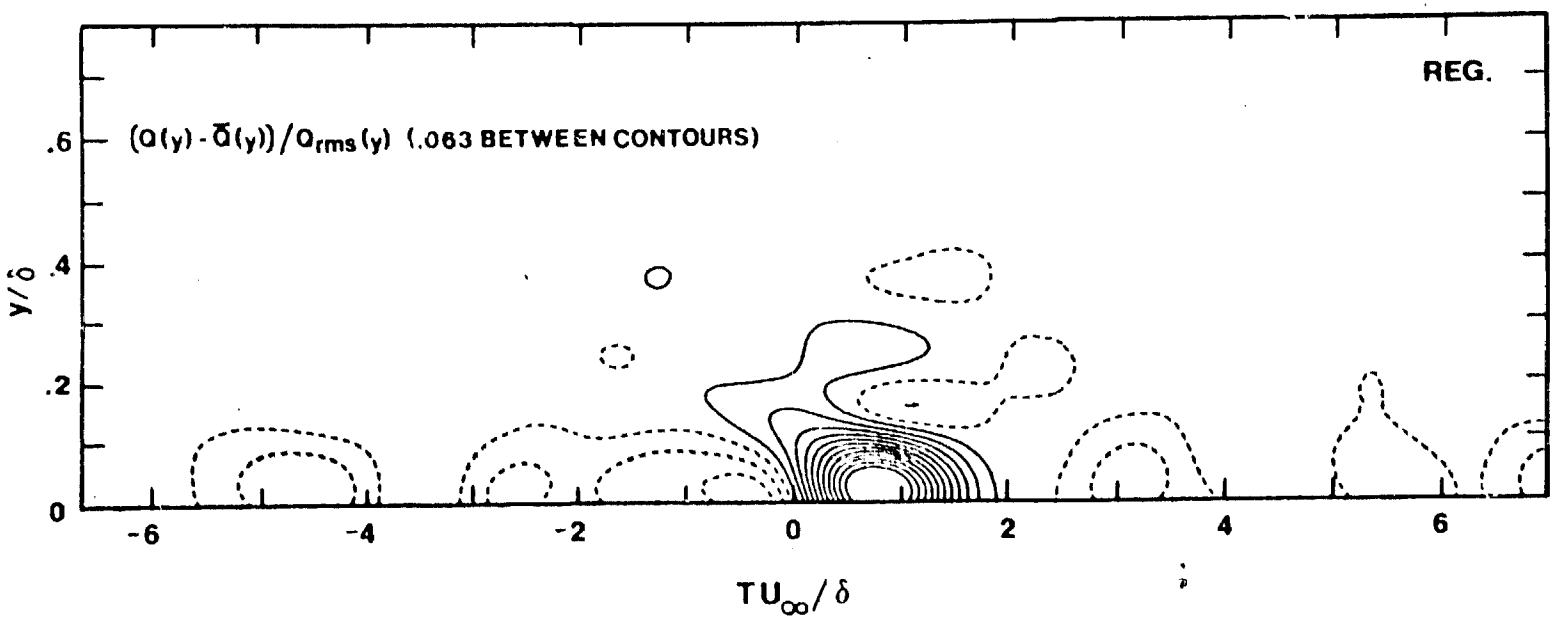

Figure 110. Burst-Conditioned Ensemble Average of Normalized Two-Dimensional Velocity Reconstructions Obtained From Match Filter Detection in Regular Boundary Layer at High Reynolds Number

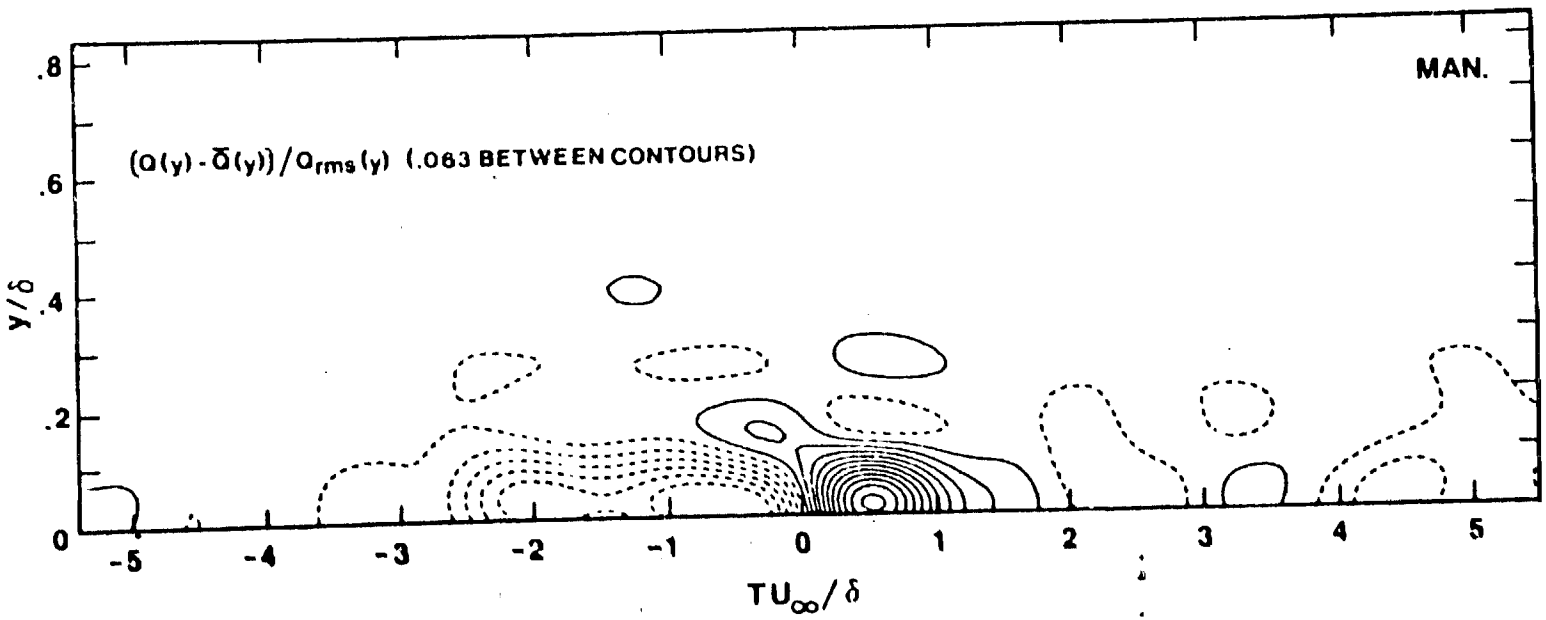

Figure 111. Burst-Conditioned Ensemble Average of Normalized Two-Dimensional Velocity Reconstructions Obtained From Match Filter Detection in Manipulated Boundary Layer at Low Reynolds Number

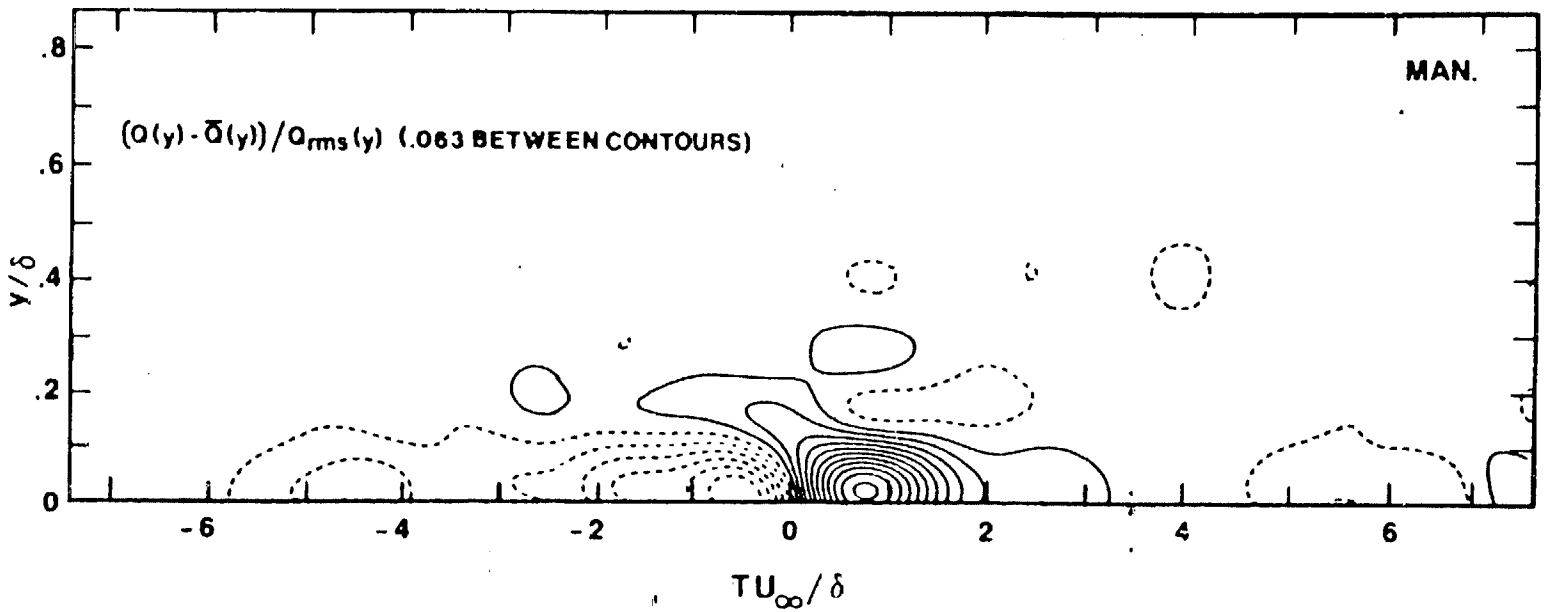

Figure 112. Burst-Conditioned Ensemble Average of Normalized Two-Dimensional Velocity Reconstructions Obtained From Match Filter Detection in Manipulated Boundary Layer at High Reynolds Number

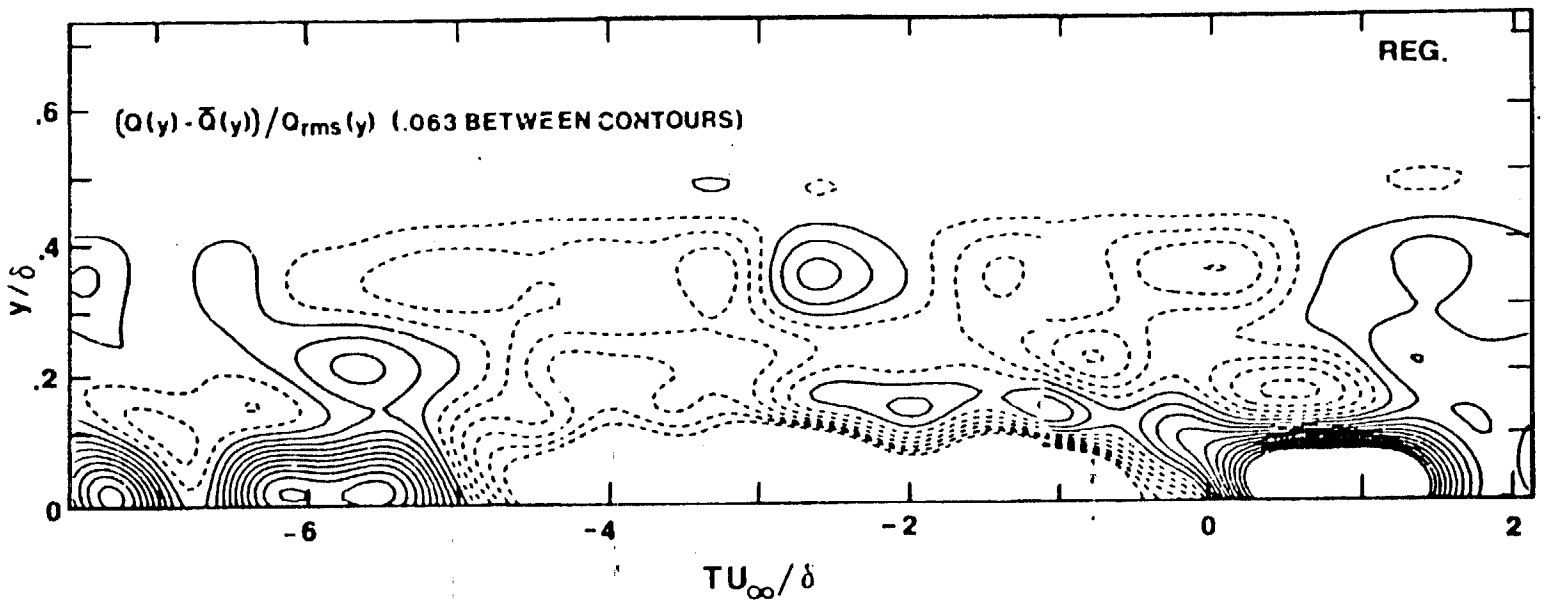

Figure 113. Ensemble Average of Normalized Two-Dimensional Velocity Reconstructions for Events with Periods Greater than Three Standard Deviations from Distribution Mean at Low Reynolds Number

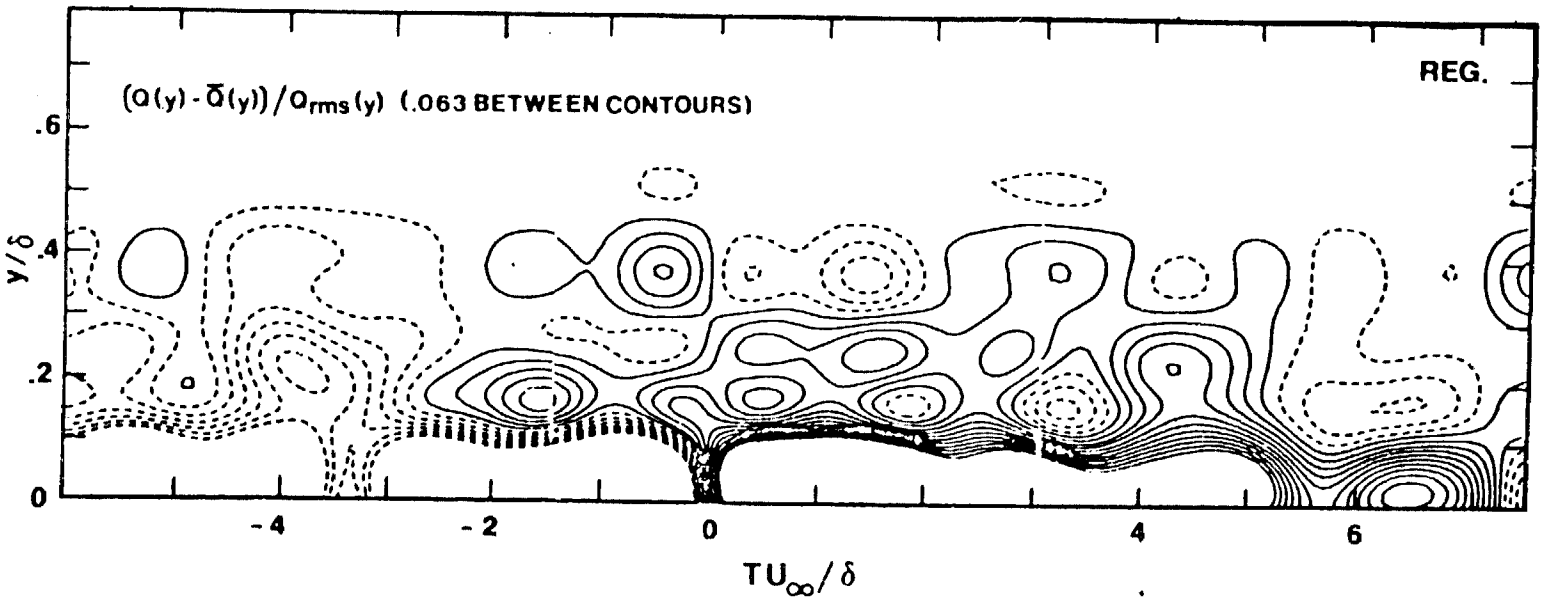

Figure 114. Ensemble Average of Normalized Two-Dimensional Velocity Reconstructions for Events with Periods Greater than Three Standard Deviations from Distribution Mean at High Reynolds Number

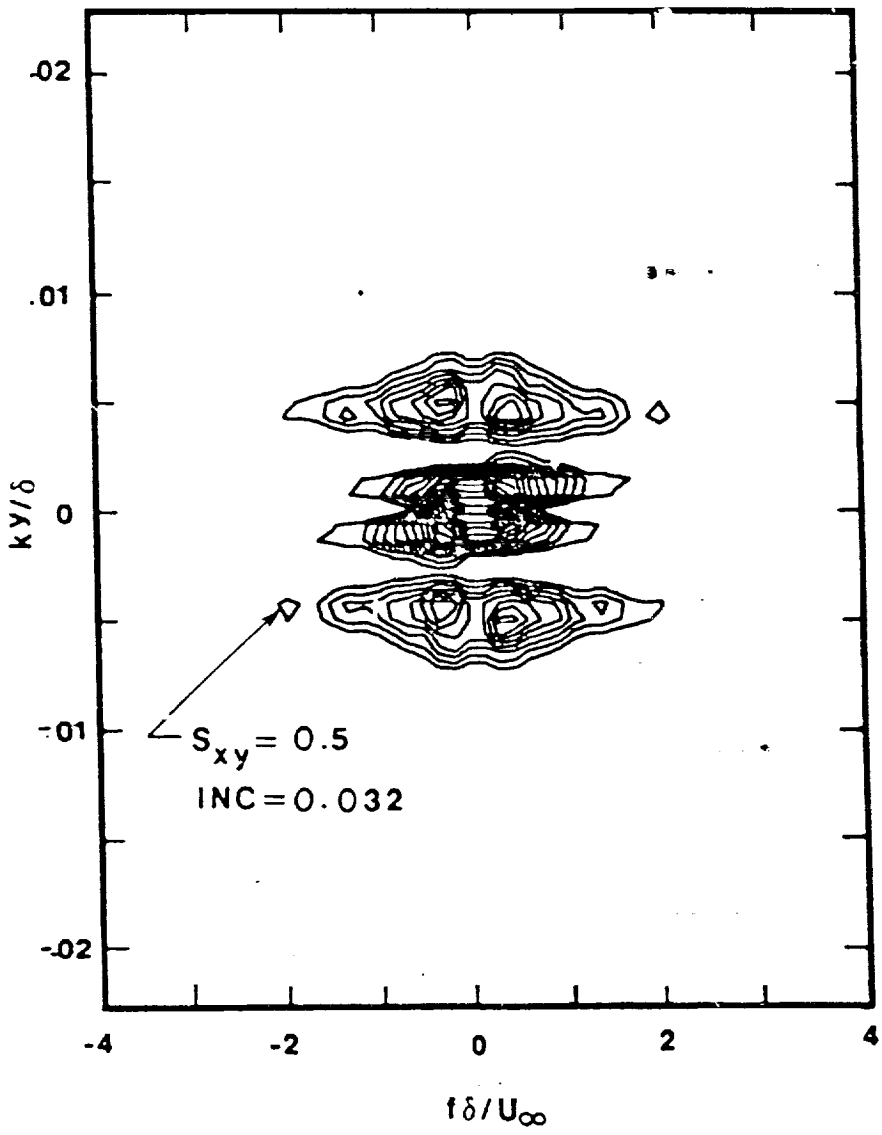

Figure 115. Normalized Two-Dimensional Spectrum of Reconstructed Streamwise Velocity Distributions for Regular Boundary Layer at Low Reynolds Number

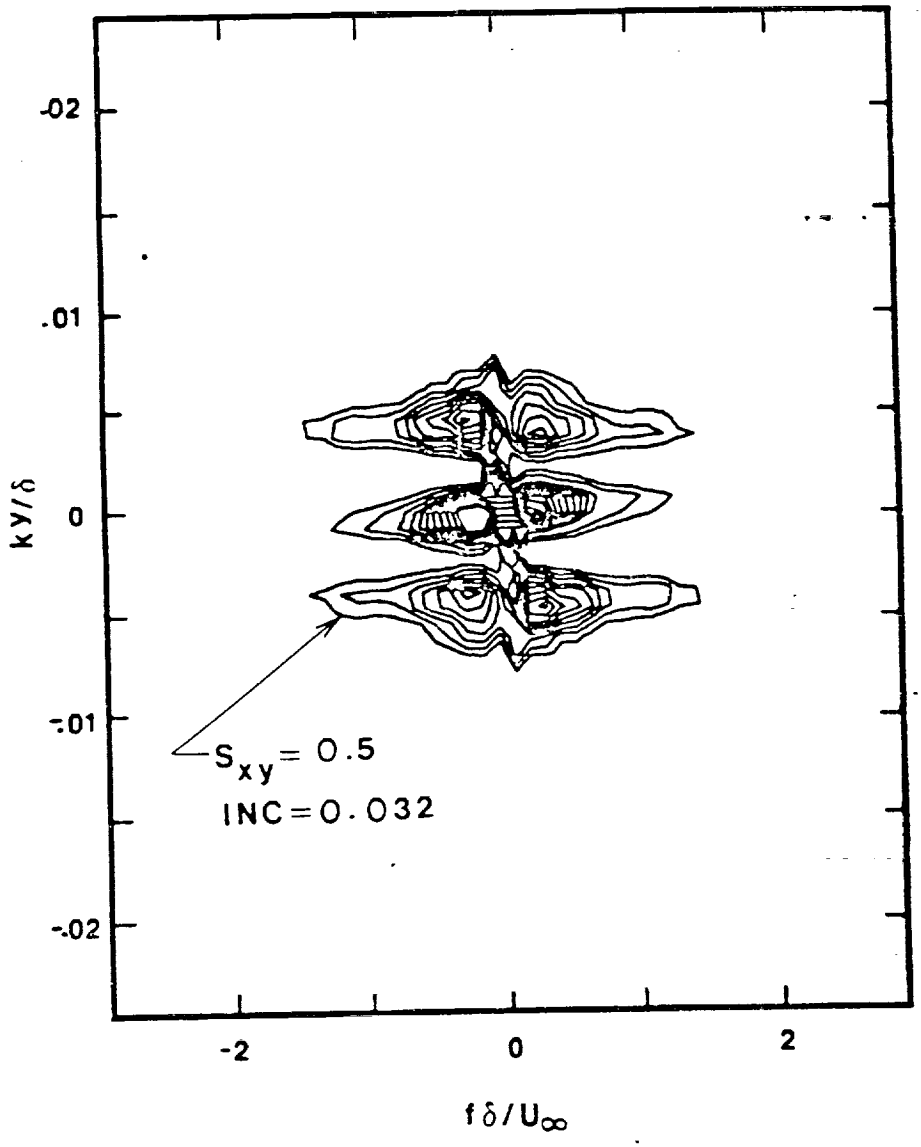

Figure 116. Normalized Two-Dimensional Spectrum of Reconstructed Streamwise Velocity Distributions for Regular Boundary Layer at High Reynolds Number

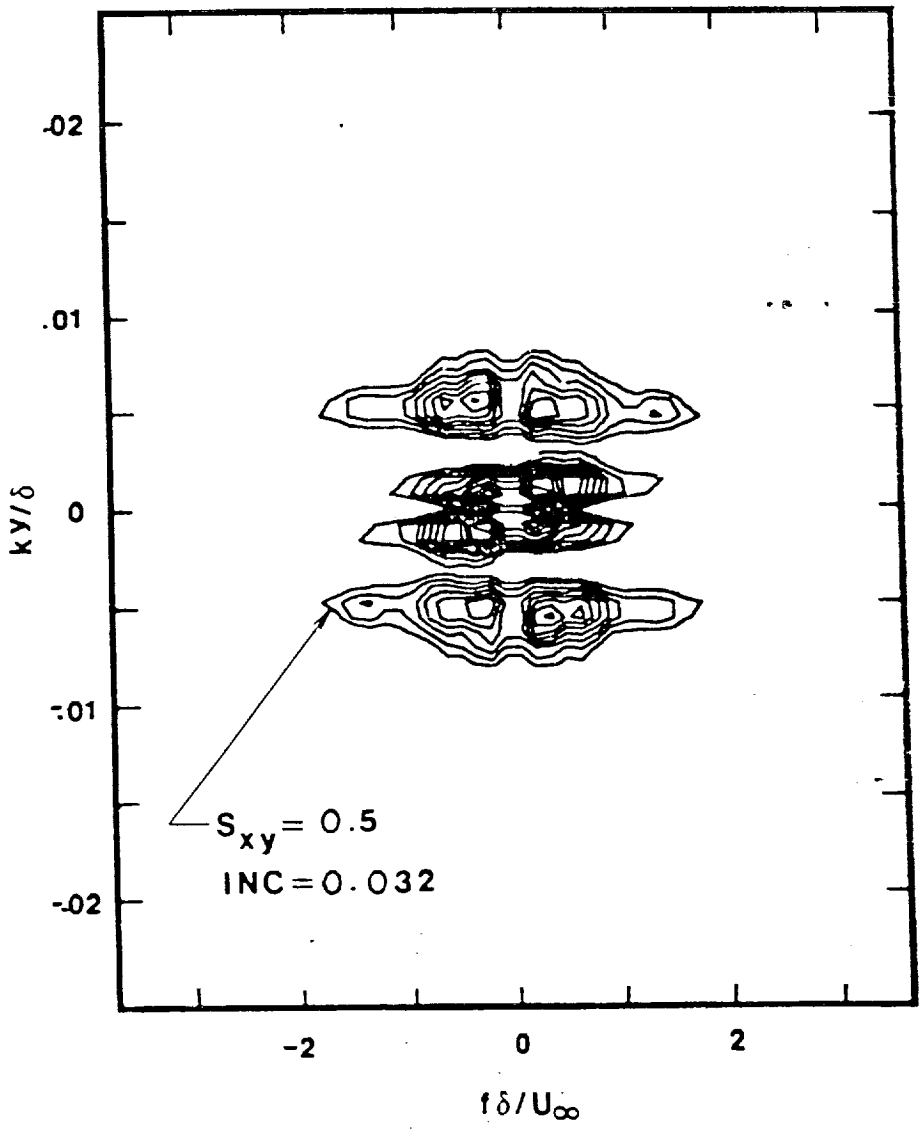

Figure 117. Normalized Two-Dimensional Spectrum of Reconstructed Streamwise Velocity Distributions for Manipulated Boundary Layer at Low Reynolds Number

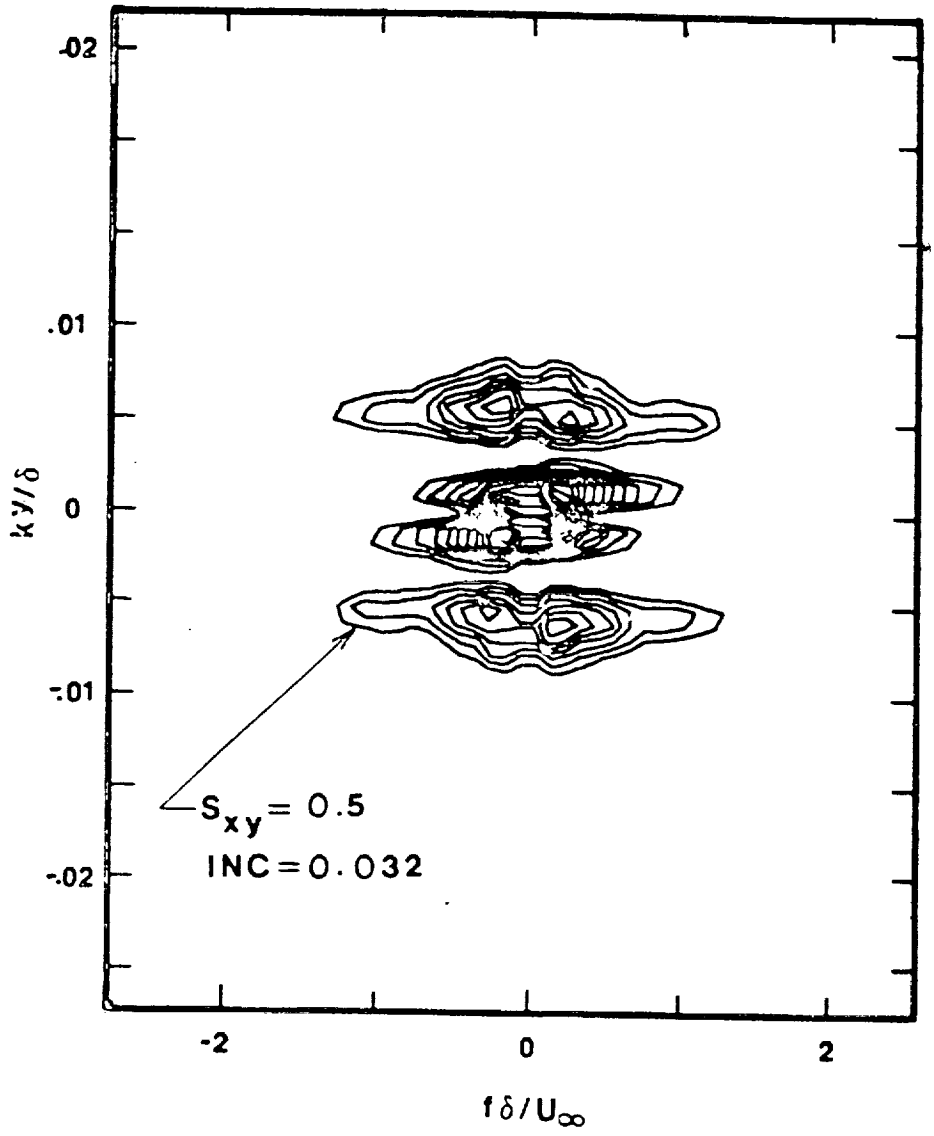

Figure 118. Normalized Two-Dimensional Spectrum of Reconstructed Streamwise Velocity Distributions for Manipulated Boundary Layer at High Reynolds Number

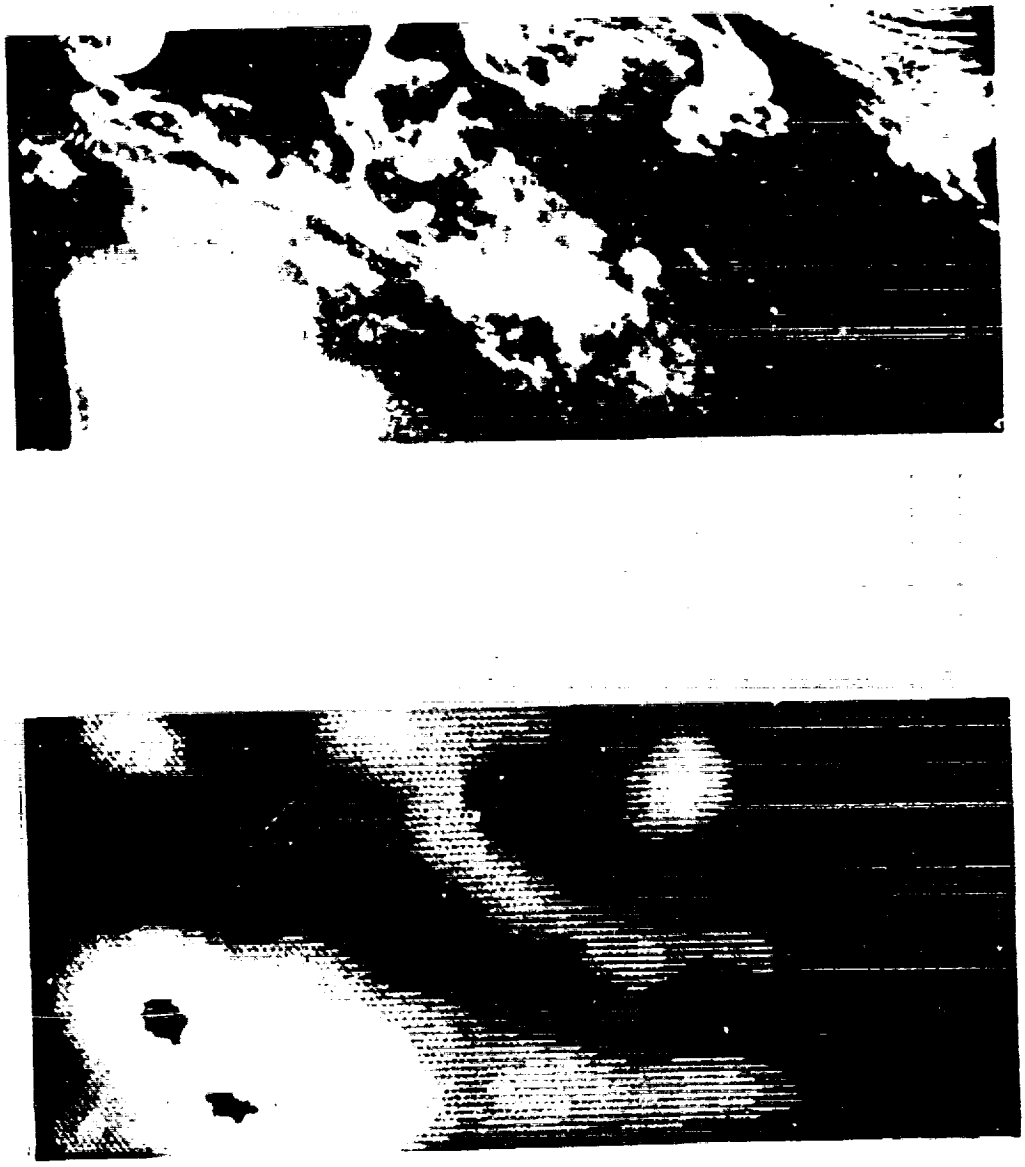

Figure 119. Digitized Realization of Visualized Flow Conditioned on Wall Event (Top) and Corresponding Two-Dimensional Match-Filter Enhancement in Regular Boundary Layer

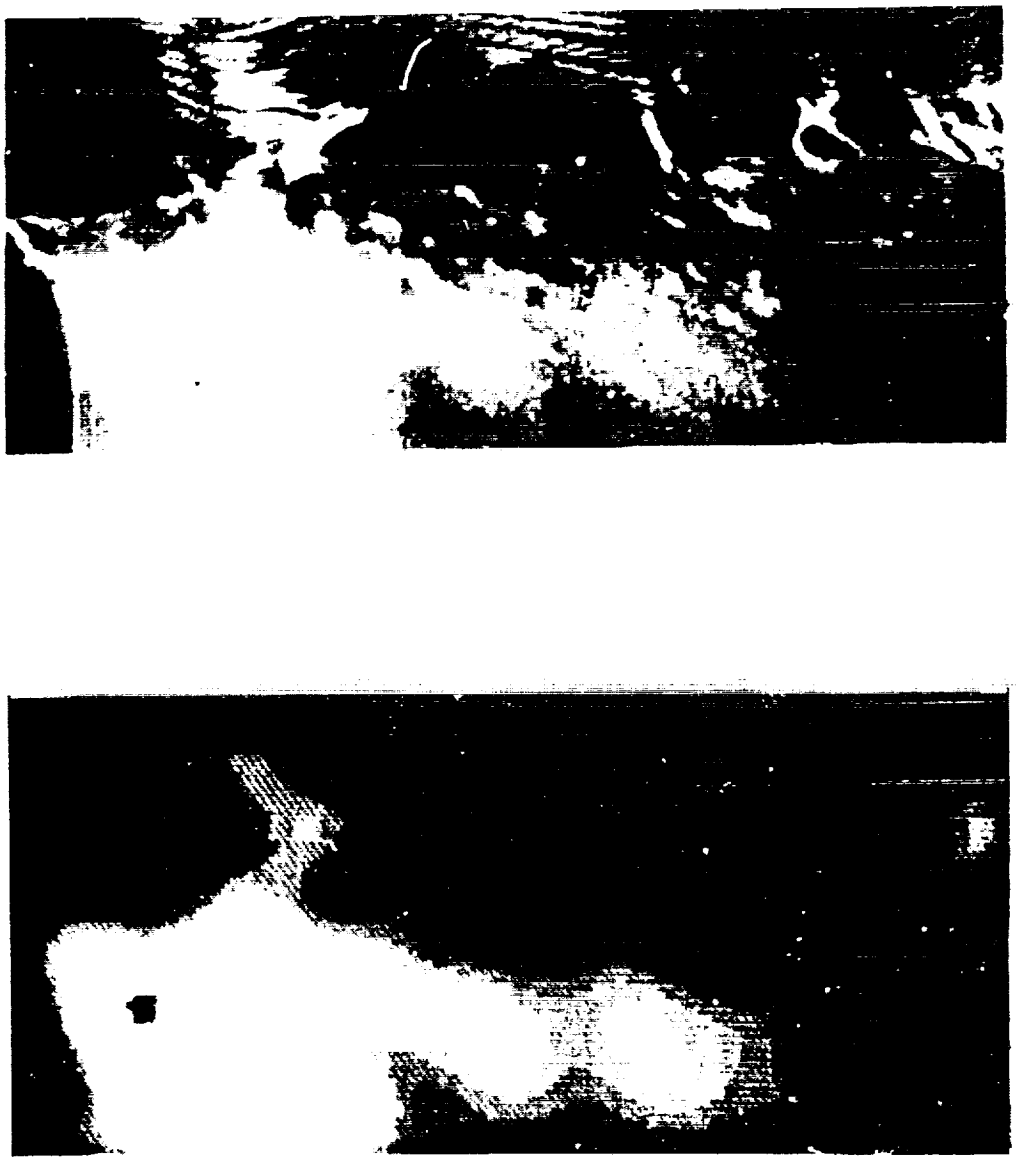

Figure 120. Digitized Realization of Visualized Flow Conditioned on Wall Event (Top) and Corresponding Two-Dimensional Match-Filter Enhancement in Manipulated Boundary Layer

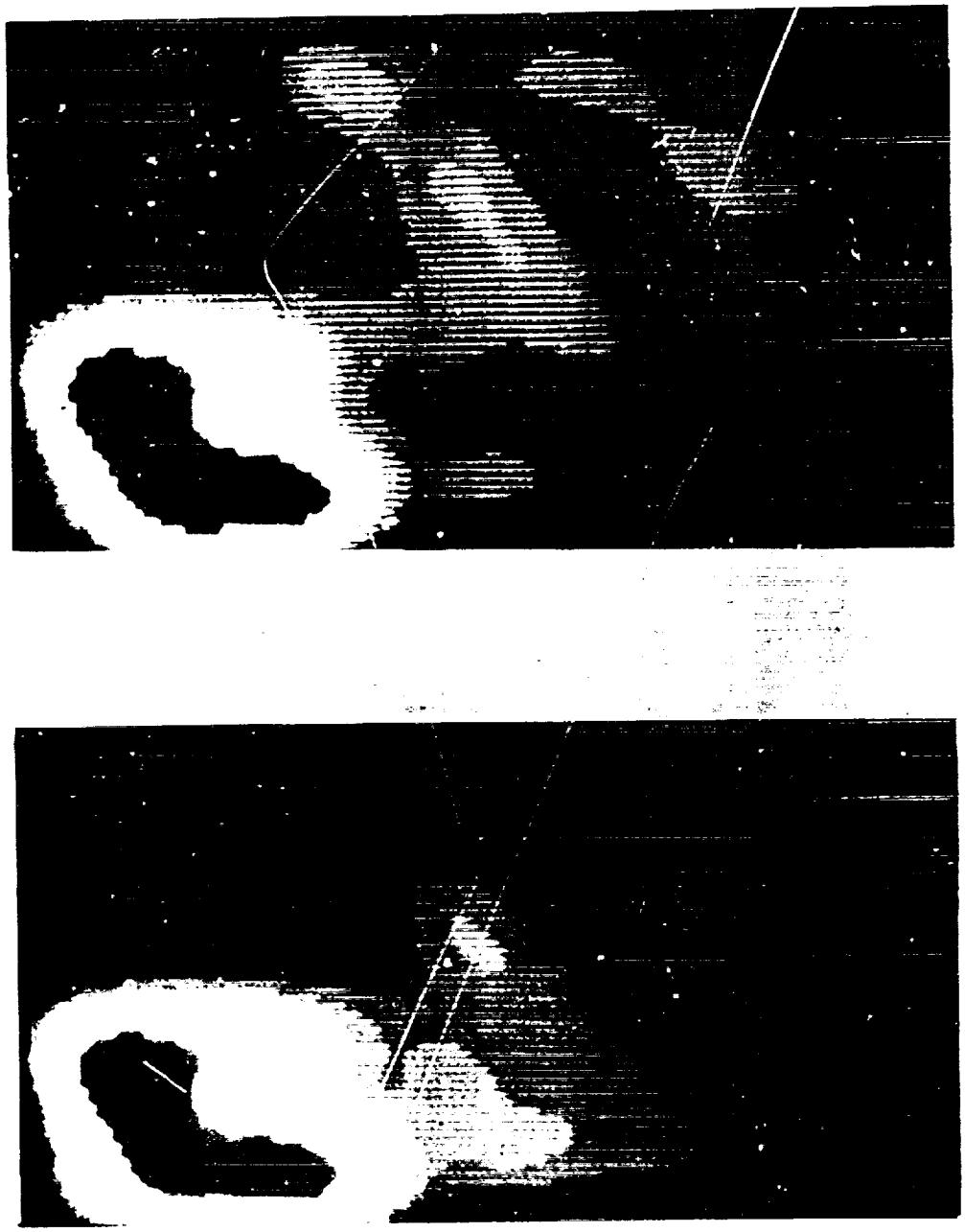

Figure 121. Ensemble Average of Enhanced Images Conditioned on Match Detection in Regular (Top) and Manipulated (Bottom) Boundary Layers

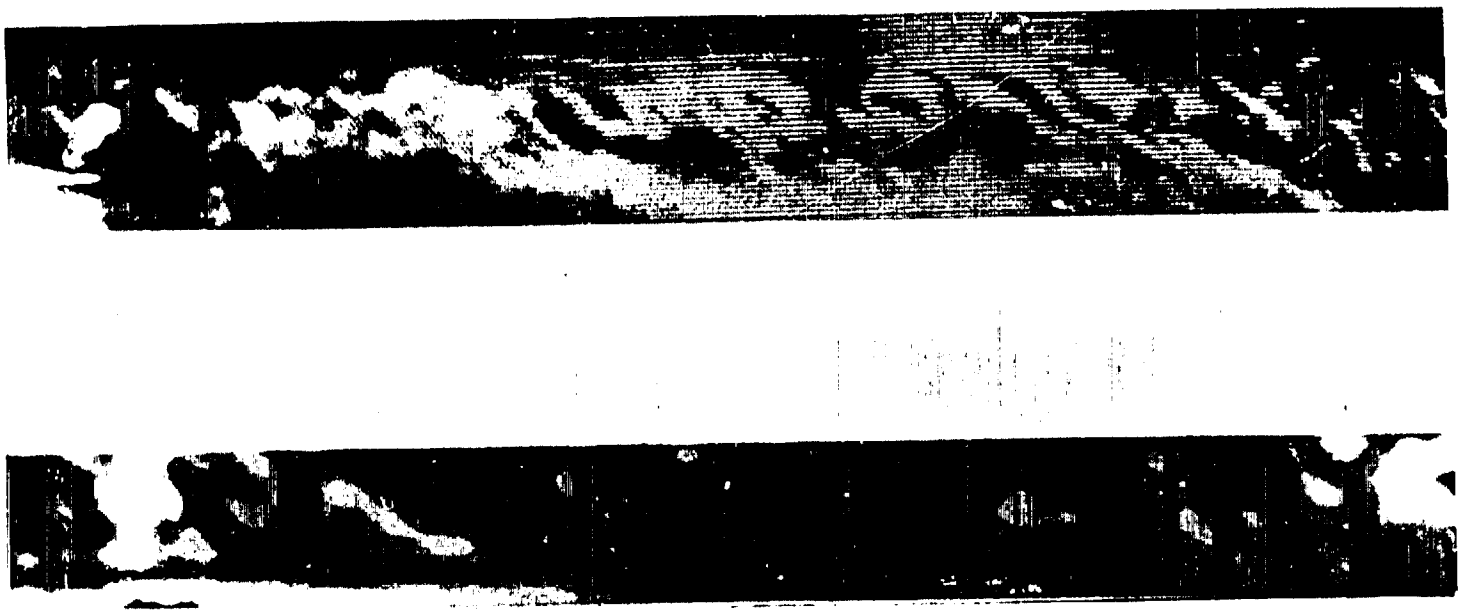

Figure 122. Digitized Realization of Visualized Flow Conditioned on Wall Event (Top) and Corresponding Two-Dimensional Match-Filter Enhancement (Bottom) Viewing 10δ .. Regular Boundary Layer

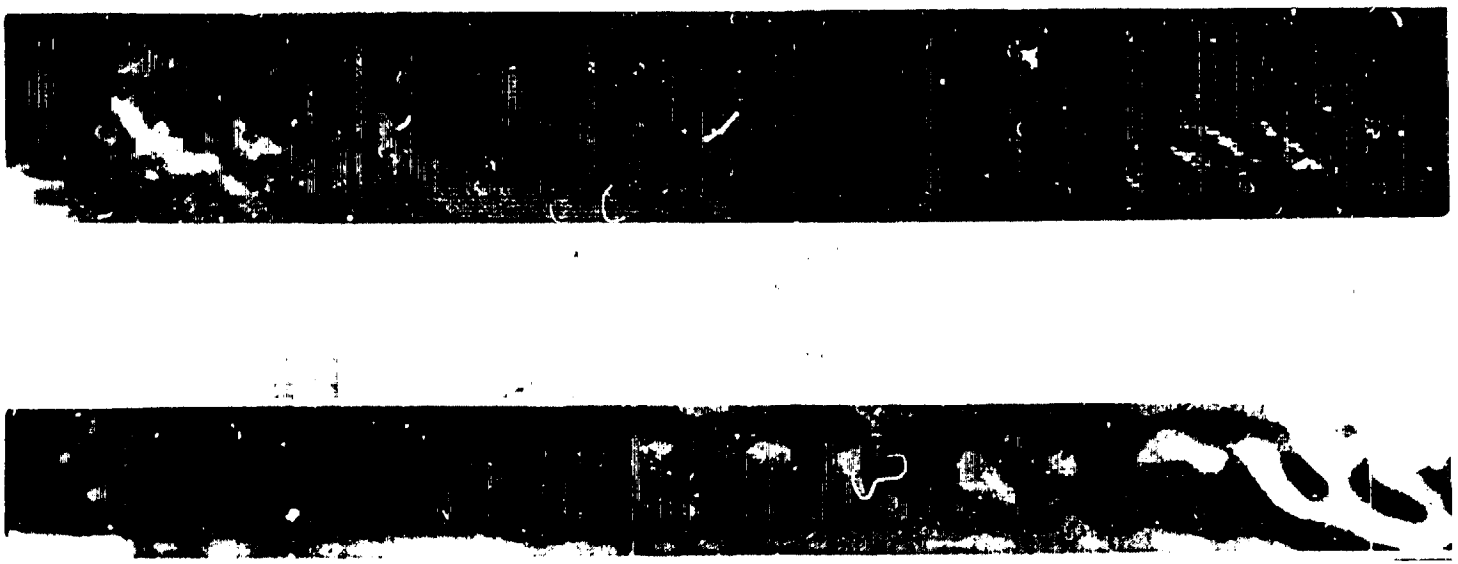

Figure 123. Digitized Realization of Visualized Flow Conditioned on Wall Event (Top) and Corresponding Two-Dimensional Match-Filter Enhancement (Bottom) Viewing 10δ in Manipulated Boundary Layer

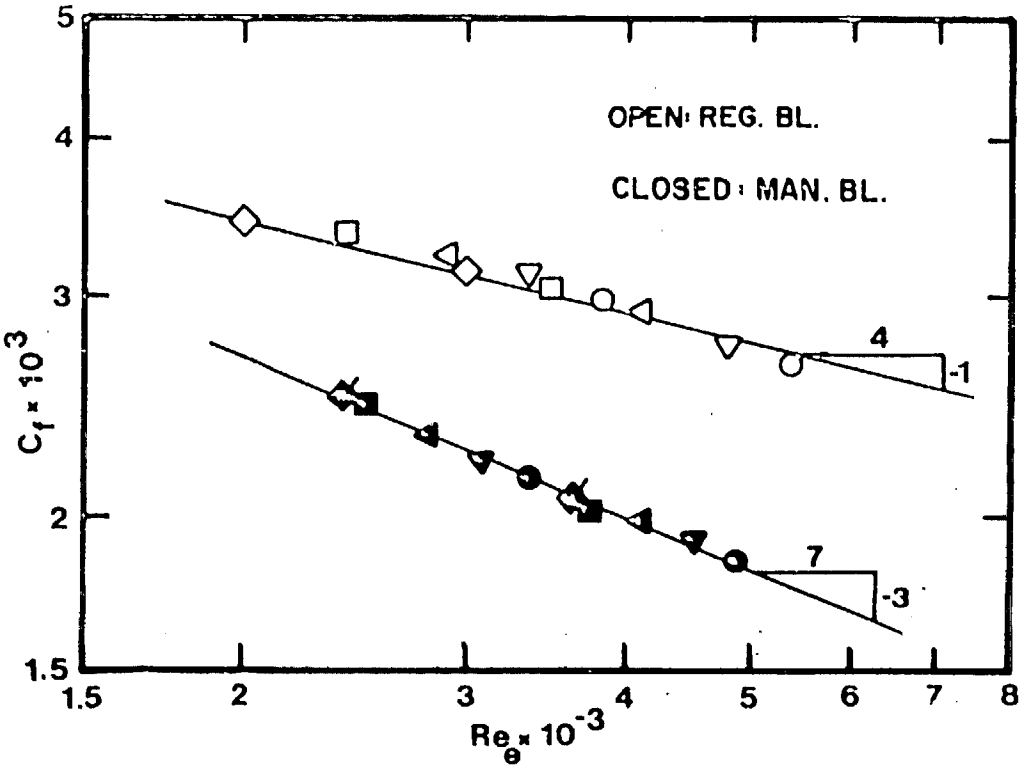

Figure 124. Reynolds Number Dependence of Wall-Friction Coefficients in Regular and Manipulated Boundary Layers

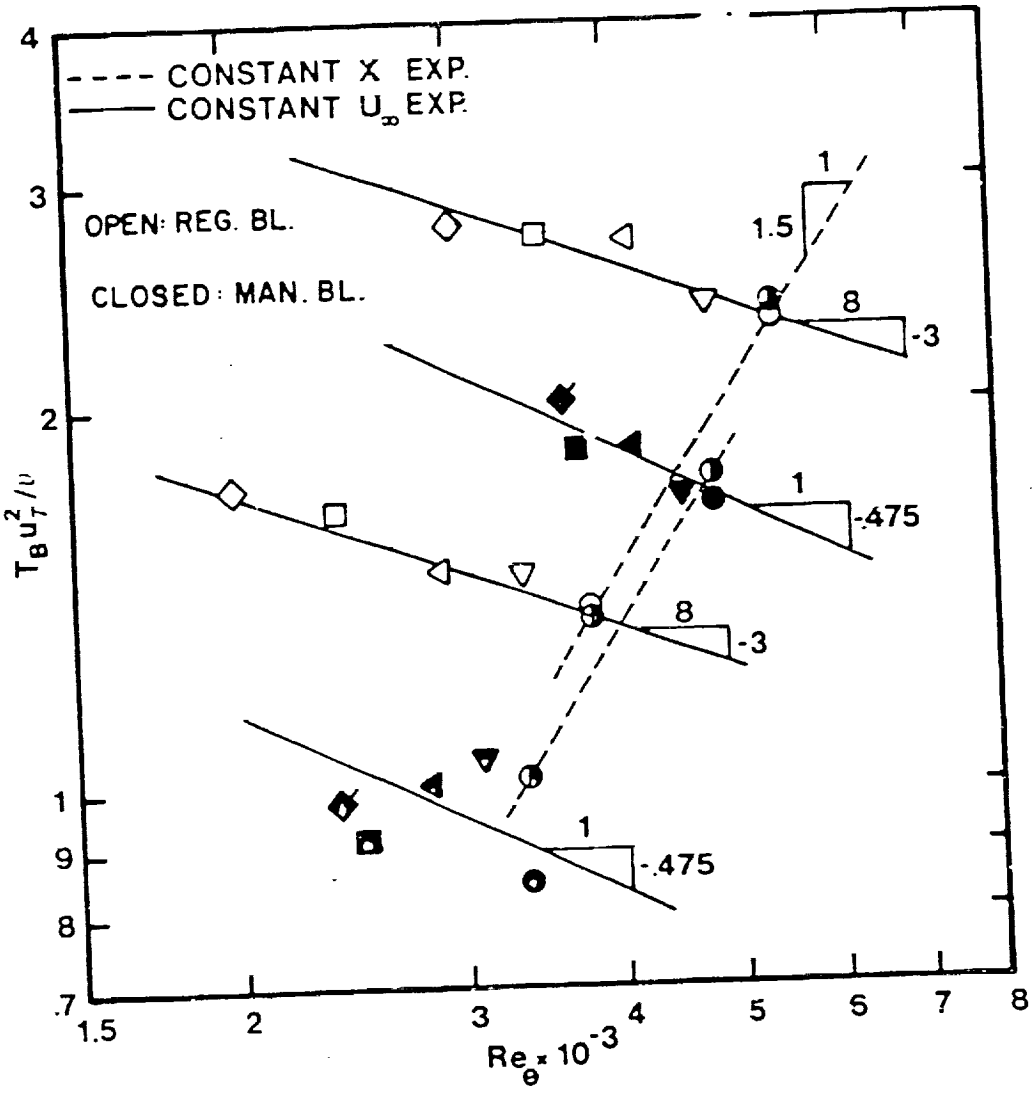

Figure 125. Reynolds Number Dependence of Wall-Layer Strouhal Frequency in Regular and Manipulated Boundary Layers

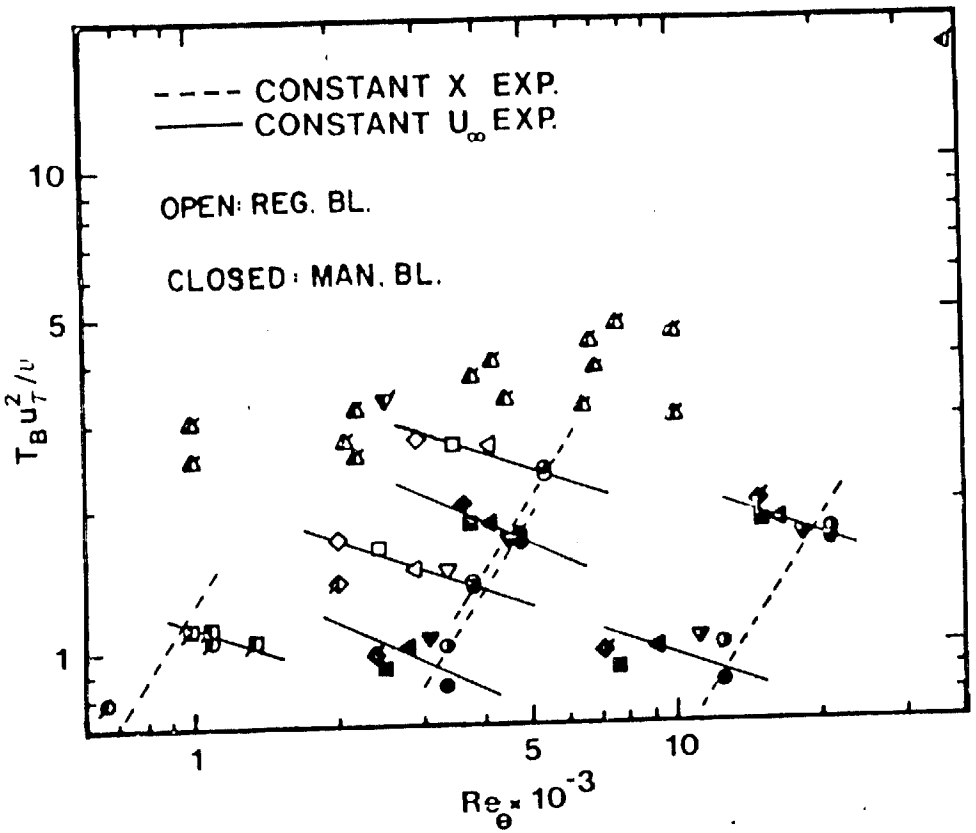

Figure 126. Reynolds Number Dependence of Wall-Layer Strouhal Frequency for Present Investigation and Results of Other Investigations

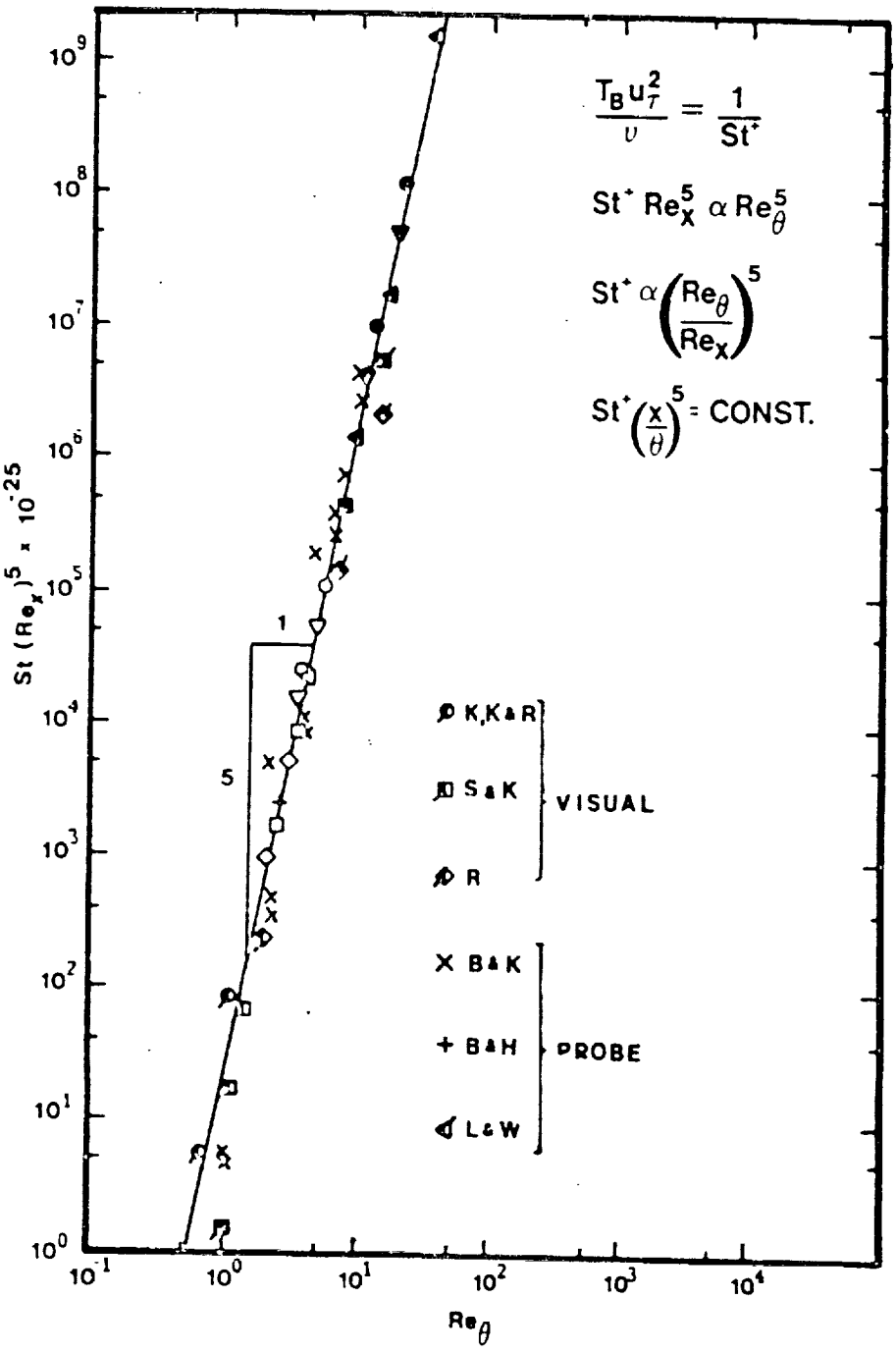

Figure 127. Correlation of Wall-Layer Strouhal Frequency with Reynolds Number for Results in Figure 126.

ORIGINAL PAGE
BLACK AND WHITE PHOTOGRAPH

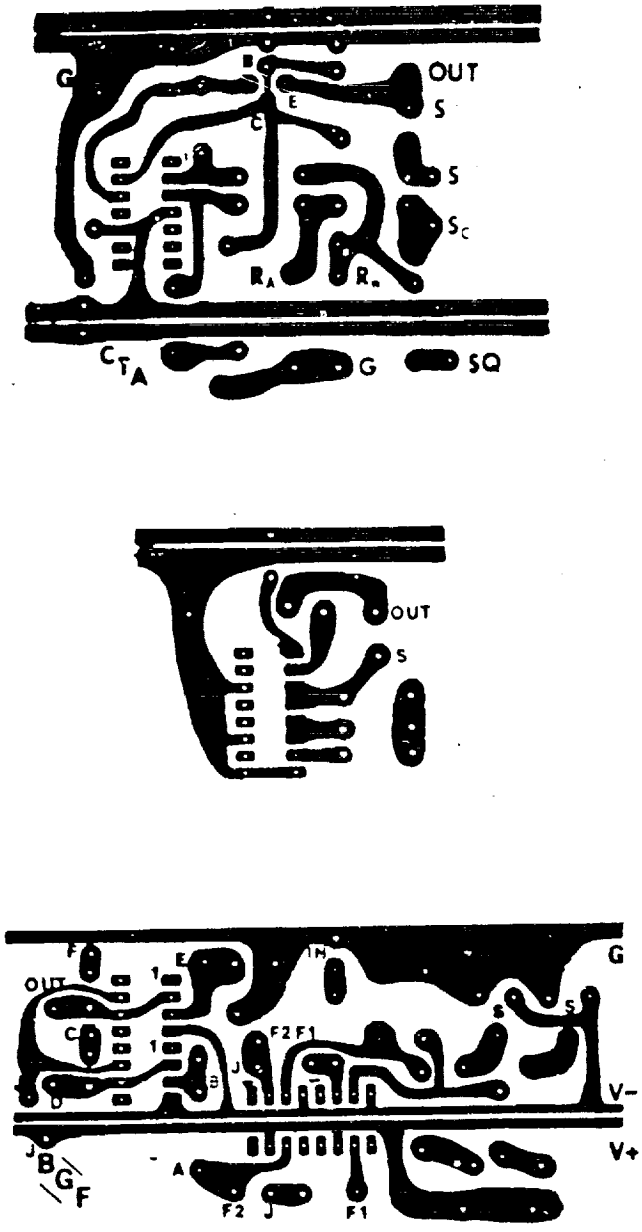

Figure 128. Etch Patterns for Printed Circuits Used in Constructing Constant-Temperature Anemometers (Top), Square-Wave Generator (Middle) and Bias/Filter/Gain Signal Conditioners (Bottom)

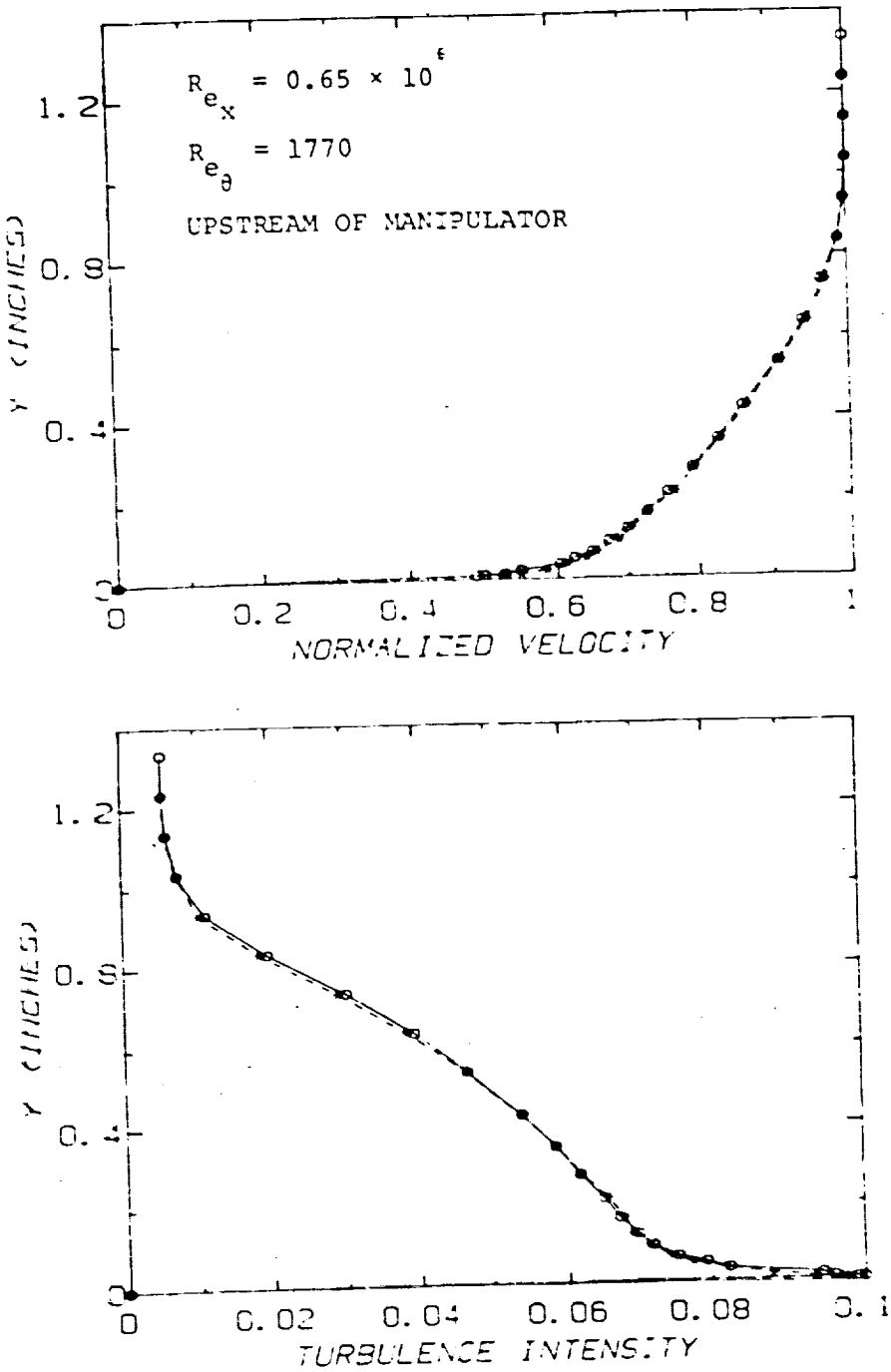

Figure 129. Mean Velocity and Turbulence Intensity Profiles in Regular and Manipulated Boundary Layers Upstream of Device Position

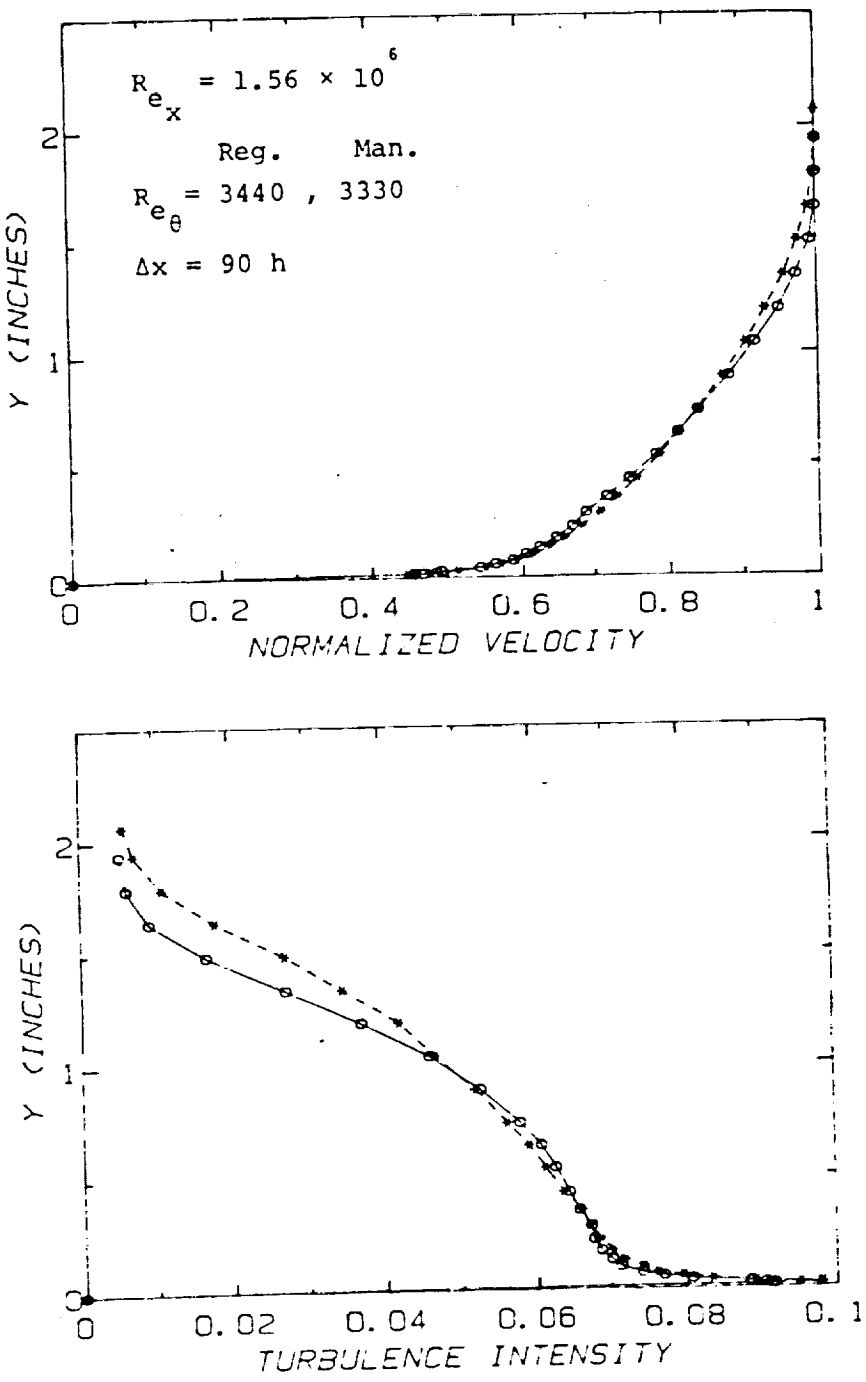

Figure 132. Mean Velocity and Turbulence Intensity Profiles in Regular and Manipulated Boundary Layers at Location Approximately 90 Device Heights Downstream

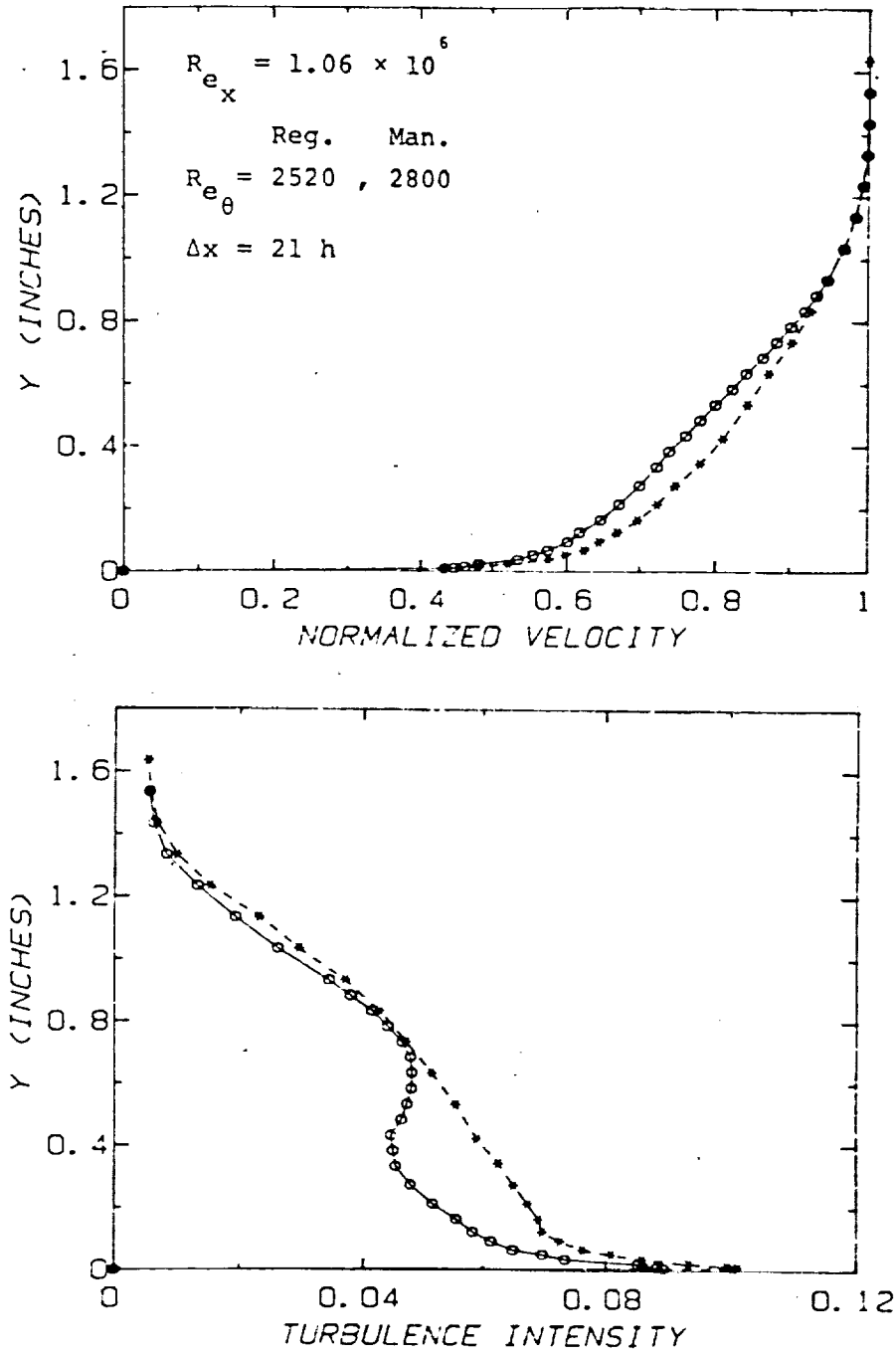

Figure 131. Mean Velocity and Turbulence Intensity Profiles in Regular and Manipulated Boundary Layers at Location Approximately 21 Device Heights Downstream

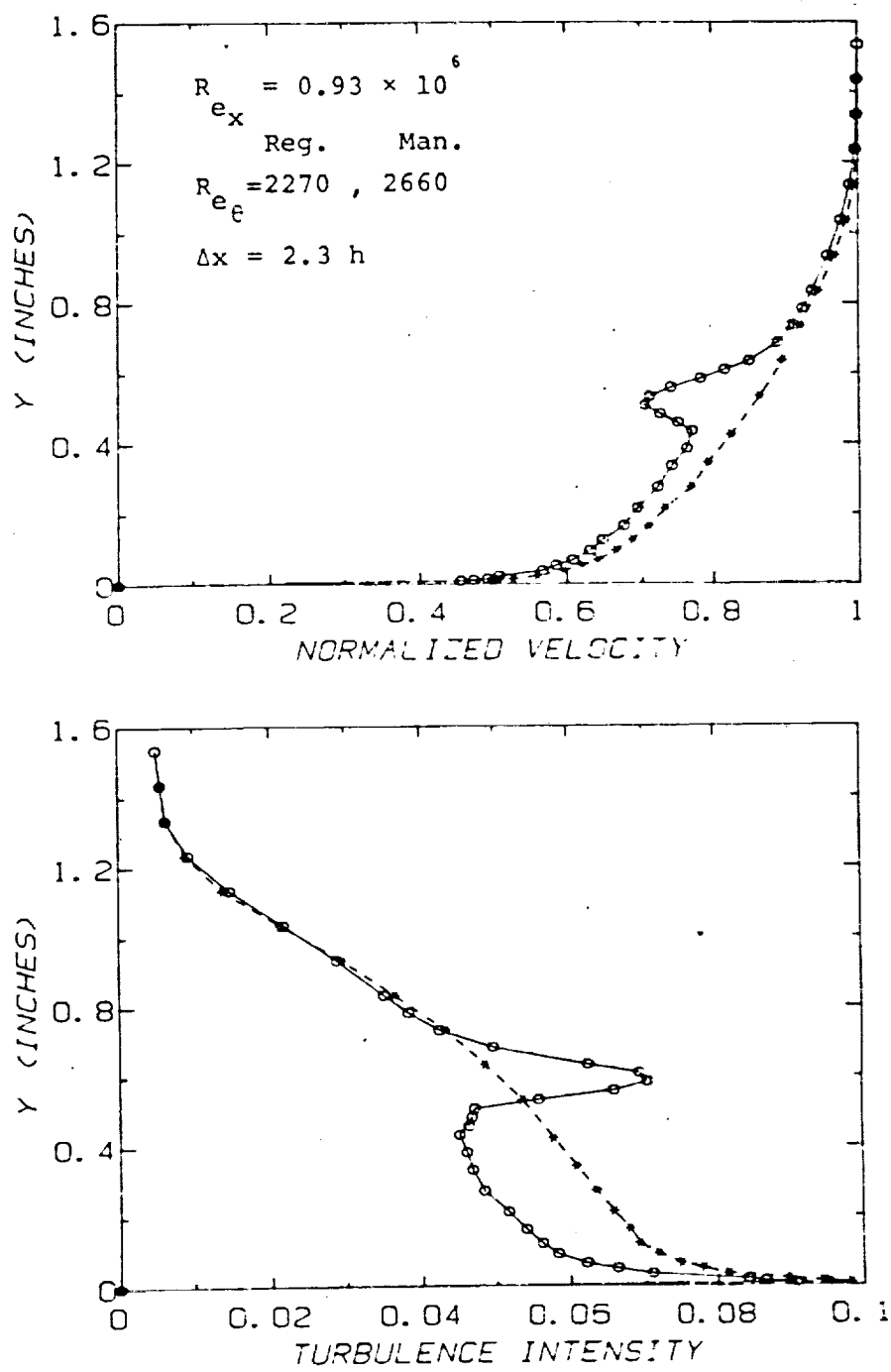

Figure 130. Mean Velocity and Turbulence Intensity Profiles in Regular and Manipulated Boundary Layers at Location Approximately 2 Device Heights Downstream

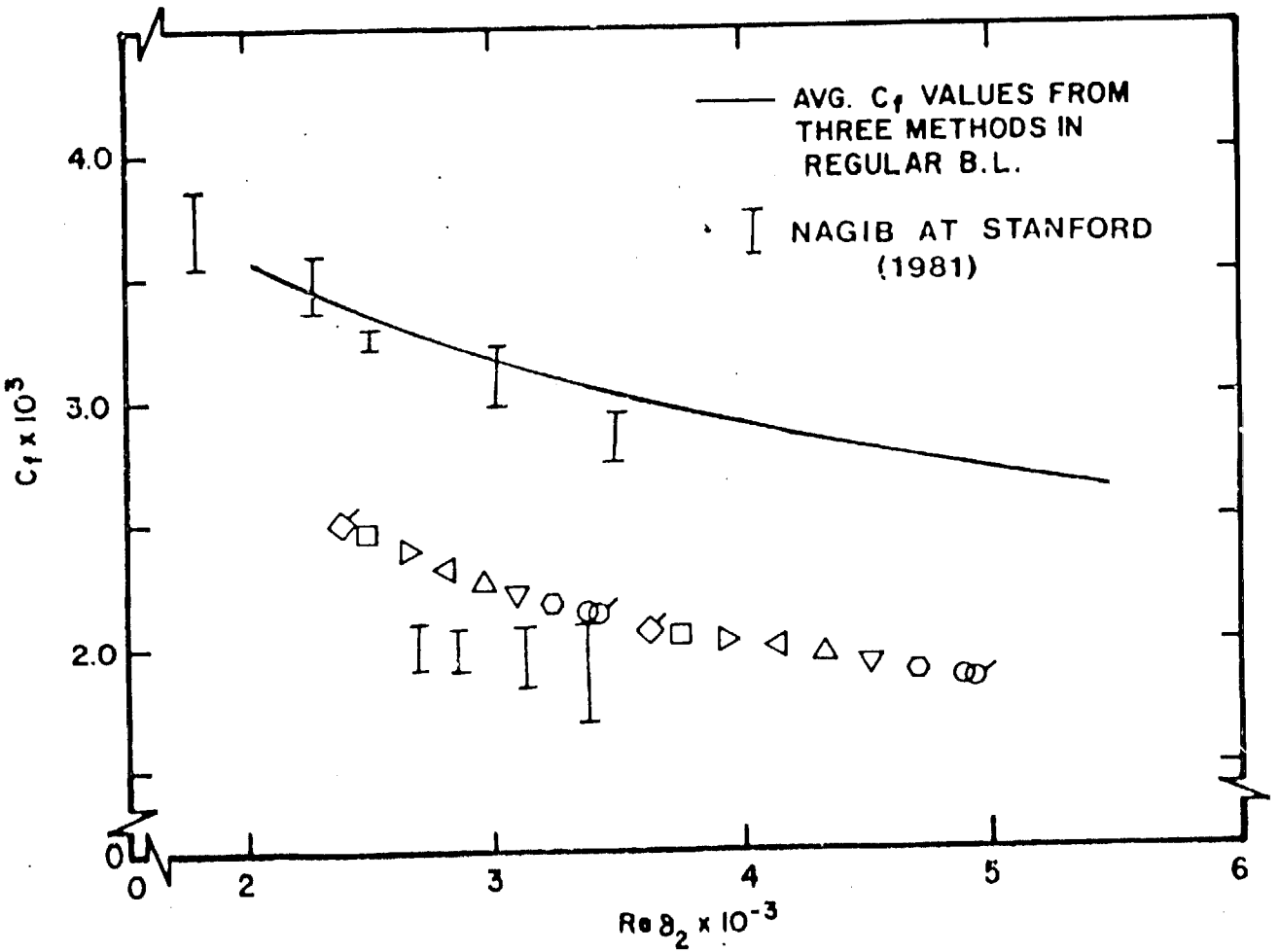

Figure III. Wall-Friction Coefficient Distribution in Regular and Manipulated Boundary Layers and Comparison with Present Results from Figure 60

BIBLIOGRAPHY

Achia, B. V. and Thompson, D. W. 1977. Structure of the Turbulent Boundary Layer in Drag-Reducing Pipe Flow. J. Fluid Mech. Vol. 81, Part 3, pp. 439-464.

Aggarwal, J. K., Duda, R. O., Rosenfeld, A., Ed. 1977. Computer Methods in Image Analysis. IEEE Press, New York.

Antonia, R. A. 1972. Conditional Sampled Measurements Near the Outer Edge of a Turbulent Boundary Layer. J. Fluid Mech. Vol. 56, Part 1, pp. 1-18.

Antonia, R. A. 1981. Conditional Sampling in Turbulence Measurements. Ann. Rev. Fluid Mech. Vol. 13, pp. 131-156.

Bakewell, H. P. and Lumley, J. L. 1967. Viscous Sublayer and Adjacent Wall Region in Turbulent Pipe Flow. Phys. Fluids. Vol. 10, No. 9, pp. 1880-1889.

Bearman, P. W. 1971. Corrections for the Effect of Ambient Temperature Drift on Hot-Wire Measurements in Incompressible Flow. DISA Information. No. 11, pp. 25-30.

Bendat, J. S. and Piersol, A. G. 1971. Random Data: Analysis and Measurement Procedures. Wiley-Interscience, New York.

Bendat, J. S. and Piersol, A. G. 1980. Engineering Applications of Correlation and Spectral Analysis. John Wiley and Sons, New York.

Berner, C. and Schrivener, O. 1980. Drag Reduction and Structure of Turbulence in Dilute Polymer Solutions, Viscous Drag Reduction. G. R. Hough, Ed. Vol. 72. Progress in Astronautics and Aeronautics, pp. 290-299.

Black, T. J. 1966. The Structure of Wall Turbulence. Proc. Heat Transfer and Fluid Mech. Inst., p. 366.

Blackwelder, R. 1970. Large Scale Motion of a Turbulent Boundary Layer With a Zero and Favorable Pressure Gradient. Ph.D. Thesis. The Johns Hopkins University. Baltimore, Maryland.

Blackwelder, R. 1977. On the Role of Phase Information in Conditional Sampling. Phys. Fluids. Vol. 20, No. 10, Pt. 11.

Blackwelder, R. F. and Ecklemann, H. 1979. Streamwise Vortices Associated with the Bursting Phenomenon. J. Fluid Mech. Vol. 94, Part 3, pp. 577-594.

Blackwelder, R. F. and Haritonidis, J. H. 1981. The Bursting Frequency in Turbulent Boundary Layers. To be Published.

Blackwelder, R. F. and Kaplan, R. E. 1976. On the Wall Structure of the Turbulent Boundary Layers. J. Fluid Mech. Vol. 76, Part 1, pp. 89-112.

Blackwelder, R. F. and Kovasznay, L. S. G. 1972. Time Scales and Correlations in a Turbulent Boundary Layer. Phys. Fluids. Vol. 15, No. 9, pp. 1545-1554.

Blackwelder, R. F. and Woo, H. H. W. 1974. Pressure Perturbation of a Turbulent Boundary Layer. Phys. Fluids. Vol. 17, pp. 515-519.

Bogard, D. G. and Tiederman, W. G. 1981. Investigation of Flow Visualization Techniques for Detecting Turbulent Bursts. Conference on Turbulence in Liquids. Rolla, Missouri.

Bradshaw, P. 1967. The Turbulence Structure of Equilibrium Boundary Layers. J. Fluid Mech. Vol. 29, Part 4, pp. 625-645.

Bradshaw, P., Ferriss, D. H. and Atwell, N. P. 1967. Calculation of Boundary-Layer Development Using Turbulent Energy Equation. J. Fluid Mech. Vol. 28, Part 3, pp. 593-616.

Brederode, V. and Bradshaw, P. 1974. A Note on the Empirical Constants Appearing in the Logarithmic Law for Turbulent Wall Flows. I. C. Aero Report 74-03. Imperial College of Science and Technology, Dept. of Aero.

Brown, G. L. and Thomas, A. S. W. 1977. Large Structure in a Turbulent Boundary Layer. Phys. Fluids. Vol. 20, No. 10, Part II, pp. 5243-5252.

Bushnell, D. 1978. Panel Discussion, Coherent Structure of Turbulent Boundary Layers, Lehigh University, Pennsylvania, pp. 507-522.

Bushnell, D. M., Hefner, J. N. and Ash, R. L. 1979. Effect of Compliant Wall Motion on Turbulent Boundary Layers. Phys. Fluids. Vol. 20, No. 10, Part II, pp. 531-548.

Cantwell, B. J. 1981. Organized Motion in Turbulent Flow. Ann. Rev. Fluid Mech. Vol. 13, pp. 457-515.

Chen, P. and Blackwelder, R. F. 1978. Large-Scale Motion in a Turbulent Boundary Layer: A Study Using Temperature Contamination. J. Fluid Mech. Vol. 89, Part 1, pp. 1-31.

Coles, D. 1956. The Law of the Wake in the Turbulent Boundary Layer. J. Fluid Mech. Vol. 1, pp. 191-226.

Coles, D. 1968. Young Person's Guide to Data, Proceedings of Computation of Turbulent Boundary Layers. Stanford University, California.

Coles, D. 1978. A Model for Flow in the Viscous Sublayer, Coherent Structure of Turbulent Boundary Layers. Lehigh University, Pennsylvania, pp. 462-475.

Coles, D. W. and Hirst, D. E., editors. 1968. Proceedings of Computation of Turbulent Boundary Layers. Stanford University, California.

Corino, E. R. and Brodkey, R. S. 1969. A Visual Investigation of the Wall Region in Turbulent Flow. J. Fluid Mech. Vol. 37, Part I, pp. 1-30.

Corke, T. C., Guezennec, Y., Nagib, H. M. 1980. Modification in Drag of Turbulent Boundary Layers Resulting from Manipulation of Large-Scale Structures, Viscous Drag Reduction. G. R. Hough, Ed., Vol. 72. Progress in Astronautics and Aeronautics, pp. 128-143.

Corke, T., Koga, D., Drubka, R. and Nagib, H. 1977. A New Technique for Introducing Controlled Sheets of Smoke Streaklines in Wind Tunnels. IEEE Publication 77-CH 1251-8 AES.

Corrsin, S. and Kistler, A. 1954. The Free Stream Boundaries of Turbulent Flows. NACA Tech. Note No. 3133.

Donohue, G. L., Tiederman, W. G. and Risehman, M. M. 1972. Flow Visualization of the Near-Wall Region in a Drag-Reducing Channel Flow. J. Fluid Mech. Vol. 56, Part 3, pp. 559-575.

Doligalski, T. L., Smith, C. R. and Walker, J. D. A. 1980. Production Mechanism for Turbulent Boundary-Layer Flows, Viscous Drag Reduction. G. R. Hough, Ed., Vol. 72. Progress in Astronautics and Aeronautics, pp. 47-72.

Drubka, R. E., Tan-atichat, J. and Nagib, H. M. 1977. Analysis of Temperature Compensating Circuits for Hot-Wires and Hot-Films. DISA Information No. 22, pp. 5-14.

Drubka, R. E. and Wlezien, R. W. 1979. Efficient Velocity Calibration and Yaw-Relation in Truncation Errors in Hot-Wire Measurements of Turbulents. Bulletin of the American Physical Society, Fluid Dynamics Division. Volume 24, pp. 1142.

Ecklemann, H. 1974. The Structure of the Viscous Sublayer and the Adjacent Wall Region in a Turbulent Channel Flow. J. Fluid Mech. Vol. 65, Part 3, pp. 439-459.

Einstein, H. A. and Li, H. 1956. The Viscous Sublayer Along a Smooth Boundary. ASCE, Proc. 82.

Emmons, H. W. 1951. The Laminar Turbulent Transition in a Boundary Layer. J. Aeronaut. Sci. Vol. 18, pp. 490-498.

Falco, R. E. 1977. Coherent Motions in the Outer Region of Turbulent Boundary Layers. Phys. Fluids. Vol. 20, No. 10, Part II.

Fiedler, H. and Head, M. R. 1966. Intermittency Measurements in the Turbulent Boundary Layer. J. Fluid Mech. Vol. 25, p. 719.

Grant, H. L. 1958. The Large Eddies of Turbulent Motion. J. Fluid Mech. Vol. 4, pp. 149-190.

Grass, A. J. 1971. Structural Features of Turbulent Flow Over Smooth and Rough Boundaries. J. Fluid Mech. Vol. 50, Part 2, pp. 233-255.

Greville, T. N. E. 1969. Introduction to Spline Functions. Theory and Applications of Spline Functions. T. N. E. Greville, ed. Academic Press, pp. 1-35.

Gupta, A. K., Laufer, J. and Kaplan, R. E. 1971. Spatial Structure in the Viscous Sub-layer. J. Fluid Mech. Vol. 50, Part 3, pp. 393-512.

Gupta, A. K. and Kaplan, R. E. 1972. Statistical Characteristics of Reynolds Stress in a Turbulent Boundary Layer. Phys. Fluids. Vol. 15, No. 6, pp. 981-985.

Hanratty, T. J. 1956. J. Am. Inst. Chem. Engrs. Vol. 2, Part 3, pp. 359ff.

Hanratty, T. J., Chorn, L. G. and Harziavramidis, D. T. 1977. Turbulent Fluctuations in the Viscous Wall Region for Newtonian and Drag Reducing Fluids. Phys. Fluids. Vol. 20, No. 10, Part II, pp. S112-S119.

Head, M. R. and Bandyopadhyay, P. 1981. New Aspects of Turbulent Boundary Layer Structure. J. Fluid Mech. Vol. 107, pp. 297-338.

Hefner, J. N., Weinstein, L. M. and Bushnell, D. M. 1980. Large-Eddy Breakup Scheme for Turbulent Viscous Drag Reduction, Viscous Flow Drag Reduction. Progress in Astronautics and Aeronautics. Vol. 72, pp. 110-127.

Hinze, J. O. 1975. Turbulence. McGraw-Hill Book Company, New York, New York.

Hofbauer, M. 1978. Investigation of Coherent Structures in the Velocity Field of a Fully Developed Turbulent Channel Flow Using Flow Visualization and Anemometry. Report #ISSN 0374-1257. Max-Planch-Institut fur Stromungsforshung und der Aerodynamishen Versuchsansalt.

Huffman, G. D. and Bradshaw, P. 1972. A Note on von Karman's Constant in Low Reynolds Number Turbulent Flows. J. Fluid Mech. Vol. 53, Part 1, pp. 45-60.

Kaplan, R. E. and Laufer, J. 1969. The Intermittantly Turbulent Region of the Boundary Layer. Proc. Int. Congr. Mech., 12th, p. 236.

Kim, H. T., Kline, S. J. and Reynolds, W. C. 1971. The Production of Turbulence Near a Smooth Wall in a Turbulent Boundary Layer. J. Fluid Mech. Vol. 50, p. 133.

Klebanoff, P. S. 1954. Characteristics of Turbulence in a Boundary Layer with Zero Pressure Gradient. NACA Tech. Note. No. 3178.

Kline, S. J. 1978. The Role of Visualization in the Study of the Structure of the Turbulent Boundary Layer. Workshop on Coherent Structure of Turbulent Boundary Layers. Lehigh University, pp. 1-26.

Kline, S. J., Reynolds, W. C., Schraub, F. A. and Runstadler, P. W. 1967. The Structure of Turbulent Boundary Layers. J. Fluid Mech. Vol. 30, Part 4, pp. 741-773.

Kovasznay, L. S. G. 1967. Structure of the Turbulent Boundary Layer. Phys. Fluids. Vol. 10, Suppl. pp. S25-S30.

Kovasznay, L. S. G., Kibbens, V. and Blackwelder, R. 1970. Large Scale Motions in the Intermittent Region of a Turbulent Boundary Layer. J. Fluid Mech. Vol. 41, pp. 283-325.

Kreider, J. F. 1973. A Simple Stable Constant Temperature Hot-Wire Anemometer. IEEE Trans. Instrumentation and Measurement, pp. 190-191.

McClenna, J. H., Parks, T. W. and Rabiner, L. R. 1979. FIR Linear Phase Filter Design Program, Programs for Digital Signal Processing, IEEE Press, New York.

Nagib, H. M., Corke, T. C., Way, J. L. and Helland, K. N. 1979. Computer Analysis of Flow Visualization Records Obtained by the Smoke-Wire Technique. Proceedings of the Dynamic Flow Conference 1978. Available from DISA Electronics, Denmark.

Nagib, H. M., Guezennec, Y. and Corke, T. C. 1978. Applications of a Smoke-Wire Visualization Technique to Turbulent Boundary Layers. Workshop on Coherent Structure of Turbulent Boundary Layers. Lehigh University, Pennsylvania.

Nishioka, M., Asai, M. and Iida, S. 1980. Wall Phenomena in the Final Stage of Transition to Turbulence. Symposium on Transition and Turbulence. To be published by Academic Press.

Nychas, S. G., Hershey, H. C. and Brodkey, R. S. 1973. A Visual Study of Turbulent Shear Flow. Manuscript. Also see J. Fluid Mech. Vol. 62, p. 513.

Offen, G. R. and Kline, S. J. 1973. A Comparison and Analysis of Detection Methods for the Measurement of Production in a Boundary Layer. Turb. in Liq. Vol. 3.

Offen, G. R. and Kline, S. J. 1975. A Proposed Model of the Bursting Process in Turbulent Boundary Layers. J. Fluid Mech. Vol. 70, Part 2, pp. 209-228.

Oldaker, D. K. and Tiederman, W. G. 1977. Spatial Structure of the Viscous Sub-Layer in Drag-Reducing Channel Flows. Phys. Fluids. Vol. 20, No. 10, Part II.

Oppenheim, A. V. and Schafer, R. W. 1975. Digital Signal Processing. Prentice-Hall.

Pratt, W. K. 1978. Digital Image Processing. Wiley-Interscience, New York.

Praturi, Ananda K. and Brodkey, Robert S. 1978. A Stereoscopic Visual Study of Coherent Structures in Turbulent Shear Flow. J. Fluid Mech. Vol. 89, Part 2, pp. 251-272.

Purtell, L. P., Klebanoff, P. S. and Buckley, F. T. 1981. Turbulent Boundary Layer at Low Reynolds Numbers. Phys. Fluids. Vol. 24, No. 5, pp. 802-811.

Rajogopalan, J. and Antonia, R. A. 1980. Investigation of Natural Transition in the Inlet Region of a Two-Dimensional Duct Flow. Phys. Fluids. Vol. 23, pp. 1938-1948.

Rao, K., Narasimha, R. and Narayanan, M. A. 1971. The Bursting Phenomenon in a Turbulent Boundary Layer, J. Fluid Mech. Vol. 48, Part 2, pp. 339-352.

Rosenfeld, A., Park, C. M. and Strong, J. P. 1969. Noise Cleansing in Digital Pictures. Proceedings EASCON Convention Record, pp. 269-273.

Rotta, J. 1950. Beitrag zur Berechnung der Turbulenten Grenzschichten. NACA 1344.

Sandborn, V. A. 1971. Evaluation of the Time Dependent Surface Shear Stress in Turbulent Flows. Colorado State University.

Schlichting, H. 1968. Boundary-Layer Theory. McGraw-Hill Book Company, New York.

Schraub, F. A. and Kline, S. J. 1965. A Study of the Structure of the Turbulent Boundary Layer With and Without Longitudinal Pressure Gradients. Report MD-12 Thermo Science Division. Dept. of Mech. Engr., Stanford University.

Schwartz, M. and Shaw, L. 1975. Signal Processing. McGraw-Hill Book Company, New York.

Senda, M. and Suzuki, K. 1981. Pattern Recognition Study of Coherent Motion in a Transpired Turbulent Boundary Layer. Rolla, Missouri.

Spalding, D. B. 1961. A Single Formula for the Law of the Wall. J. Appl. Mech. Vol. 28, pp. 455-457.

Strickland, H. H. and Simpson, R. L. 1973. The Separating Turbulent Boundary Layer: An Experimental Study of an Airfoil Type Flow. Tech. Report WT-2. Southern Methodist University.

Tan-atichat, J., Nagib, H. M. and Loehrke, R. I. 1982. Interaction of Free Stream Turbulence with Screens and Perforated Plates: A Balance Between Turbulence Scales. J. Fluid Mech. Vol. 114, pp. 541-568.

Taneda, S. 1981. Flow Visualization of Turbulent Boundary Layers. J. Flow Vis. Soc. Japan. Vol. 1, Part 1, pp. 50-56.

Taneda, S., Anamoto, H. and Ishi-i, K. 1981. Visual Observations of Artificial Disturbances in Turbulent Boundary Layers. J. Flow. Vis. Soc. Japan. Vol. 1, Part 2, pp. 223-226.

Tennekes, H. 1968. Outline of Second-Order Theory of Turbulent Pipe Flow. AIAA Journal. Vol. 6, No. 9, pp. 1735-1740.

Tennekes, H. and Lumley, J. L. 1972. A First Course in Turbulence. The MIT Press, Cambridge, Massachusetts.

Terrel, T. J. 1980. Introduction to Digital Filters. John Wiley and Sons, New York.

Townsend, A. A. 1956. The Structure of Turbulent Shear Flow. Cambridge University Press.

Townsend, A. A. 1970. Entrainment and the Structure of Turbulent Flow. J. Fluid Mech. Vol. 41, Part 1, pp. 13-46.

Townsend, A. A. 1979. Flow Patterns of Large Eddies in a Wake and in a Boundary Layer. J. Fluid Mech. Vol. 95, Part 3, pp. 515-537.

Wallace, J. M., Ecklemann, H. and Brodkey, R. S. 1972. The Wall Region in Turbulent Shear Flow. J. Fluid Mech. Vol. 54, Part 1, pp. 39-48.

Wallis, R. H. 1976. An Approach for the Space Varient Restoration and Enhancement of Images. Proceedings Symposium on Current Mathematical Problems in Image Science, Monterey, California.

Way, J. L. 1975. Applications in Fluid Mechanics Research of a Portable Data Acquisition and Processing System. Proceedings of 5th Annual ICIASF, Ottowa, Canada.

Wieghardt, K. and Tillmann, W. 1941. Zur Turbulenten Reiburgsschicht bei Druckanstieg, UM6617.

Wigeland, R. A. 1976. Grid Generated Turbulence With and Without Rotation About The Streamwise Direction. Ph.D. Thesis, Illinois Institute of Technology.

Willmarth, W. W. and Lu, S. S. 1972. Structure of the Reynolds Stress Near the Wall. J. Fluid Mech. Vol. 55, Part 1, pp. 65-92.

Willmarth, W. W. and Bogar, T. J. 1977. Survey and New Measurements of Turbulent Structure Near the Wall. Phys. Fluids. Vol. 20, No. 10, Part 11.

Whitfield, D. L. 1979. Analytical Description of the Complete Turbulent Boundary Layer Velocity Profile. AIAA Paper No. 78-1158.

Wlezien, R. W. 1981. The Evolution of the Low Wave Number Structure in a Turbulent Wake. Ph.D. Thesis, Illinois Institute of Technology.

Yaglom, A. M. 1979. Similarity Laws for Constant-Pressure and Pressure-Gradient Turbulent Wall Flows. Ann. Rev. Fluid Mech., Vol. 11, pp. 505-540.

Yajnik, K. S. and Anchorya, M. 1977. Non-equilibrium Effects in a Turbulent Boundary Layer Due to the Destruction of Large Eddies. National Aeronautical Lab, Bangalore, NAL-BL-7.

Zilbermann, M., Wygnanski, I. and Kaplan, R. E. 1977. Transitional Boundary Layer Spot in a Fully Turbulent Environment. Phys. Fluids. Vol. 20, pp. S258-271.